

THESIS

DEVELOPMENT OF A THIRD-ORDER CLOSURE TURBULENCE MODEL
WITH SUBGRID-SCALE CONDENSATION

Submitted by

Grant J. Firl

Department of Atmospheric Science

In partial fulfillment of the requirements

For the Degree of Master of Science

Colorado State University

Fort Collins, Colorado

Fall 2009

COLORADO STATE UNIVERSITY

October 12, 2009

WE HEREBY RECOMMEND THAT THE THESIS PREPARED UNDER OUR SUPERVISION BY GRANT J. FIRL ENTITLED DEVELOPMENT OF A THIRD-ORDER CLOSURE TURBULENCE MODEL WITH SUBGRID-SCALE CONDENSATION BE ACCEPTED AS FULFILLING IN PART REQUIREMENTS FOR THE DEGREE OF MASTER OF SCIENCE.

Committee on Graduate Work

Donald Estep

A. Scott Denning

Advisor: David A. Randall

Department Head: Richard H. Johnson

ABSTRACT OF THESIS

DEVELOPMENT OF A THIRD-ORDER CLOSURE TURBULENCE MODEL
WITH SUBGRID-SCALE CONDENSATION

Boundary layer clouds play an important role in the Earth's climate system due to their local effect on the radiation budget and their expansive geographic extent. Their poor representation within many general circulation models provides motivation for the development of a turbulence parameterization capable of better simulating these clouds and their effect on the turbulent structure of the boundary layer. With this goal in mind, this study presents the development and testing of such a model.

Since most boundary layer clouds result from convective processes, it is important that the new turbulence model be able to accurately predict the growth of the boundary layer in a convective regime. Previous studies have shown that third-order closure models provide sufficient detail for realistic boundary layer growth in such a regime. For this reason, the development of the new turbulence model is based on this level of detail. The current model predicts the evolution of 10 second-order moments and diagnoses the values of 28 third-order moments. Further, a subgrid-scale condensation scheme is utilized to diagnose the cloud fraction and liquid water content. This scheme also allows the diagnosed cloud cover to interact with the turbulence variables by modifying the buoyancy production terms in their predictive equations. Finally, the diagnosed cloud

cover participates in warm rain processes and a novel procedure is used to account for rain falling through partial cloudiness on the subgrid-scale.

The new turbulence model is tested as both a single column model and as a turbulence parameterization within a host three-dimensional mesoscale model. For the single column model, five cases are simulated in order to test the model's ability in different boundary layer regimes: a clear convective case, a stratocumulus-like smoke cloud case, a nocturnal drizzling stratocumulus case, a non-precipitating trade-wind cumulus case with low cloud fraction, and a precipitating trade-wind cumulus case. It is demonstrated that the new model simulates all regimes satisfactorily as the mean and turbulent states of the simulated boundary layer are compared with results from large-eddy simulation intercomparison studies. Finally, the new turbulence model is used as a parameterization within a three-dimensional model and two of the previous cases are run. The results are compared to those from both large-eddy simulation intercomparison studies and the host model run with its standard parameterizations. It is shown that the modified version of the three-dimensional model improves upon the results from the same model with its standard parameterization suite.

Grant J. Firl
Department of Atmospheric Science
Colorado State University
Fort Collins, CO 80523
Fall 2009

ACKNOWLEDGEMENTS

I have had the extreme good fortune of working in an environment including both world-class teachers and supportive, enthusiastic friends. As a result, my graduate education has been shaped by many inspired lectures and thought-provoking discussions. No one has contributed more to my growth as a student and scientist than my advisor, Dr. David A. Randall, for whom I am eternally grateful. Not only has he personally fostered a free exchange of ideas, but has collected a fine group of researchers and students who themselves are invaluable resources. Each member has contributed to an incredibly high standard of work that I have aspired to attain. Of this group, I'd like to particularly thank my officemates Kate Thayer-Calder and Todd Jones for occasional research support and more numerous life-centering digressions.

I'd like to acknowledge the support of my family and my wife, Julia, who have believed in my potential and who have consistently reminded me of what really matters.

I'd further like to thank all members of my thesis committee, Drs. David A. Randall, Scott Denning, and Donald Estep, who have taken the time to review this work.

This research was made possible by funding from the United States Department of Energy's Scientific Discovery through Advanced Computing (SciDAC) grant DE-FC02-06ER64302.

TABLE OF CONTENTS

	SIGNATURE PAGE	ii
	ABSTRACT OF THESIS.....	iii
	ACKNOWLEDGEMENTS.....	v
	TABLE OF CONTENTS	vi
Chapter 1	INTRODUCTION.....	1
Chapter 2	MODEL DEVELOPMENT.....	6
2.1	Introduction to derivation.....	6
2.2	Choice of mean variables and their equations.....	8
2.3	Equations for the second-order moments.....	10
2.4	Equations for the third-order moments.....	14
2.5	Parameterization of the pressure correlation terms.....	18
2.6	Parameterization of the dissipation terms.....	21
2.7	Parameterization of the fourth-order moments.....	24
2.8	Diagnostic third-order moments.....	30
2.9	Parameterization of the buoyancy terms.....	32
2.10	Turbulent timescales.....	33
2.11	Subgrid-scale condensation.....	38
2.11.1	Cloud fraction and liquid water content.....	39

	2.11.2 Liquid water correlations.....	45
2.12	Subgrid-scale microphysics.....	60
2.13	Complete system of governing equations.....	67
2.14	Model discretization.....	70
Chapter 3	ONE-DIMENSIONAL MODEL RESULTS.....	78
3.1	Introduction.....	78
3.2	Daytime clear convective case: Wangara.....	79
	3.2.1 Initial conditions.....	80
	3.2.2 Results.....	83
	3.2.2.1 Mean variables.....	83
	3.2.2.2 Second-order moments and their budgets.....	89
	3.2.2.3 Selected third-order moments.....	101
3.3	Smoke cloud case.....	106
	3.3.1 Initial conditions.....	107
	3.3.2 Results.....	109
	3.3.2.1 Mean quantities and entrainment parameters.....	109
	3.3.2.2 Selected second- and third-order moments.....	119
3.4	Drizzling nocturnal stratocumulus case: DYCOMS II.....	123
	3.4.1 Initial conditions.....	124
	3.4.2 Results.....	127
	3.4.2.1 Mean variables, cloudiness statistics, and precipitation.....	127
	3.4.2.2 Turbulent moments and entrainment.....	132
3.5	Nonprecipitating trade-wind cumulus case: BOMEX.....	140

3.5.1	Case setup	141
3.5.2	Results	143
3.5.2.1	Mean variables and cloudiness statistics.....	143
3.5.2.2	Turbulent moments.....	149
3.6	Precipitating trade-wind cumulus case: RICO	154
3.6.1	Case setup	155
3.6.2	Results	157
3.6.2.1	Mean variables, cloudiness statistics, and precipitation.....	157
3.6.2.2	Turbulent moments.....	162
3.7	Notes on model execution time	166
Chapter 4	THREE-DIMENSIONAL IMPLEMENTATION AND RESULTS.....	167
4.1	Introduction	167
4.2	Vector Vorticity Model (VVM).....	168
4.3	Coupling with VVM	169
4.4	Three-dimensional model results.....	173
4.4.1	Drizzling nocturnal stratocumulus case: DYCOMS II.....	174
4.4.2	Nonprecipitating trade-wind cumulus case: BOMEX.....	182
4.5	Notes on model execution time	189
Chapter 5	CONCLUSION	190
APPENDIX A:	Solving for the explicit diagnostic third-order moments.....	196
APPENDIX B:	Virtual potential temperature as a function of conservative variables	216
REFERENCES	218

Chapter 1

Introduction

One of the key uncertainties in modeling climate with general circulation models (GCMs) has been the role of clouds and the feedbacks they participate in. While computational speed has increased according to Moore's Law over the past several decades, GCM grid sizes are still constrained to a size too large to resolve clouds sufficiently. Deep convection is accounted for with convective parameterizations, and stratiform clouds are represented by grid-scale condensation, but this configuration leaves much room for improvement. For example, boundary layer clouds cover a large areal extent, and due to their considerable effect on the local albedo and radiation budget, have critical importance for the Earth's climate (Slingo 1990, Hartmann et al. 1992). Many GCMs, however, fail to accurately represent boundary layer clouds, underestimating the expansive areal extent of stratocumulus decks off of the western boundaries of continents, and failing to accurately represent the transition from stratocumulus decks to shallow cumulus regimes in trade-wind zones. One way to improve a GCM's ability to simulate boundary layer clouds is to improve its turbulence parameterization so that it is capable of correctly representing cloud-topped boundary layers and their effects.

Models used to study cloud-topped boundary layers have generally fallen into one of three categories (Bougeault 1985, Bechtold et al. 1992). The first consists of three-

dimensional dynamical models utilizing fine resolution and sophisticated microphysics and radiation schemes. Results from such models are known as large-eddy simulations (LESs) and were first produced by Deardorff (1974a). LES models are designed to explicitly resolve the energy-containing eddies, and if a subgrid turbulence scheme is used, it is usually of minor importance. Many authors have successfully used LES to study cloudy boundary layers (e.g., Deardorff 1976b, Sommeria 1976, Klemp and Wilhelmson 1978, Moeng 1986, Redelsperger and Sommeria 1986, Brown et al. 2002, and Stevens et al. 2005). However, this success comes with a high computational cost, rendering the LES strategy unusable for GCMs. In the context of parameterization development, LES is best used to produce reference data for evaluating less computationally expensive models where appropriate data is sparse or missing, as is the case with boundary-layer turbulence.

The second type of model used to study cloud-top boundary layers is the bulk mixed-layer model. These models represent the boundary layer as one well-mixed layer, the properties of which are governed by surface fluxes, the boundary layer depth, and the strength of entrainment at the interface with the free troposphere. Many authors have used these models and have had success representing salient features of cloud-topped mixed layers (e.g., Lilly 1968, Schubert 1976, Deardorff 1976b, and Schubert et al. 1979). Despite these models' extreme computational efficiency and popularity, they are highly parameterized, may provide insufficient detail of the vertical structure of the boundary layer, and lack generality.

The third type of model is the higher-order closure (HOC) turbulence model. Such a model has a domain that includes many layers within the boundary layer and

solves dynamical equations for mean properties and turbulent moments. Initially, HOC models demonstrated success in simulating only clear boundary layers, either convectively driven or shear-driven (e.g., Mellor and Yamada 1974, Zeman and Lumley 1976, André et al 1978, Canuto et al. 1994, Cheng et al. 2005). Subsequently, many authors have extended these models to include subgrid-scale condensation, based on the ideas pioneered by Sommeria and Deardorff (1977). The precise formulation of such a scheme is of critical importance for determining the buoyancy flux and turbulent kinetic energy budget, and is discussed in Section 2.11. With such a parameterization, HOC turbulence models are well suited to study the cloud-topped boundary layer at a much-reduced computational cost relative to LES. Bougeault (1985) outlined three main advantages of using such a model to study cloudy boundary layers. First, HOC models can be used in any type of boundary layer, since the dynamic equations at their core are general. As a caveat, however, their parameterized components are not guaranteed to be general, e.g., the subgrid-scale condensation parameterization. Second, depending on their complexity and which turbulent moments are prognosed, HOC models provide a wealth of information about the boundary layer, including variances of thermodynamic variables, fluxes of heat, moisture, and momentum, and with third-order closure, the transport of the second-order moments. Thirdly, HOC models provide this detail at a computational cost reduced by several orders of magnitude from LES.

HOC turbulence models present modelers with a choice. The derivation of the prognostic equations for the second-order moments reveals that the third-order moments are needed, and the third-order moment equations need the fourth-order moments, etc. At some point, it is necessary to close this loop of dependence, although it is not

immediately obvious how many moments are sufficient. It is computationally impractical and expensive to calculate a higher order of moments than necessary, and, for a given problem, some order of moments may capture the desired detail. For the study of cloudy boundary layers where buoyancy is the main source of turbulent kinetic energy, André et al. (1976b) and Krueger (1988) contend that prognosing the third-order moments, third-order closure (TOC), is necessary and sufficient. They claim that second-order closure (SOC) models cannot adequately predict the growth of the convective boundary layer because the vertical transport of turbulent kinetic energy is too weak (Yamada and Mellor 1975, Wyngaard and Côté 1975, Yamada and Kao 1986). This vertical transport is a third-order moment and is usually treated as down-gradient diffusion in SOC models. Subsequent authors have shown that TOC models give better results due to their more accurate treatment of vertical fluxes of second-order moments (Zeman and Lumley 1976, André et al. 1978). TOC models add significant additional computational cost, however, since they may add more than twenty prognostic equations over those required for SOC. Zeman and Lumley (1976), Canuto et al. (1994), and Cheng et al. (2005) address this high cost by deriving diagnostic algebraic relations for the third-order moments while retaining their models' ability to simulate convective boundary layers. This approach seems to form a good balance between model ability and computational cost, and will be adopted in the current study.

The goal of the current study is to develop a HOC model to be used as a turbulence parameterization in a mesoscale or general circulation model that is not only capable of determining accurate turbulent statistics for a clear boundary layer, but is also general enough for every type of cloudy boundary layer regime. Chapter two provides a

detailed derivation and description of the model. First, the prognostic mean and second-order moment equations and parameterizations required for closure are discussed. Next, the diagnostic third-order moments, non-Gaussian fourth order-moments, and turbulent timescales are covered. Lastly, a discussion of the subgrid-scale condensation and microphysics schemes is given. Chapter three presents results of the model's use as a single column model (SCM). Five test cases are simulated and the results are compared to those from LES intercomparison projects. Chapter four presents results of the model's use as a turbulence parameterization in a new three-dimensional mesoscale model based on the vector vorticity equation (Jung and Arakawa 2008). Finally, chapter five provides a concluding discussion.

Chapter 2

Model Development

2.1 Introduction to derivation

Given the limitations of second-order closure turbulence models and the success of third-order closure turbulence models in simulating convective boundary layers, the development of a turbulence parameterization for the study of cloudy boundary layers should begin with the latter. In a typical GCM that consists of many computation-intensive components in addition to the turbulence parameterization, however, the need for computational efficiency and speed is often a high priority. Solving the additional prognostic equations for the third-order moments can add a high computational cost that may be unacceptable. Turbulence schemes such as those of Canuto et al. (1994) and Cheng et al. (2005) address this problem by deriving algebraic diagnostic relations for the third-order moments. The elimination of the prognostic third-order moments and inclusion of algebraic diagnostic third-order moments significantly reduces the computational cost, yet maintains more realistic third-order moments and the ability to simulate convective boundary layers. For this reason, a scheme such as this is desirable for use in a GCM and is the starting point for the current model's development.

This chapter provides a detailed description and derivation of the current turbulence scheme. The method closely follows the work of Cheng et al. (2005), hereafter

CEA2005, but contains many extensions not found in that work. One notable extension is the addition of more prognostic variables. The model of CEA2005 has prognostic equations for $\bar{\theta}$, $\overline{w'^2}$, $\overline{u'^2}$, $\overline{w'\theta'}$, and $\overline{\theta'^2}$ – a total of one prognostic equation for a mean quantity and four for second-order moments. The current model has prognostic equations for $\bar{\theta}_l$, \bar{q}_l , \bar{u} , \bar{v} , $\overline{u'^2}$, $\overline{v'^2}$, $\overline{w'^2}$, $\overline{w'u'}$, $\overline{w'v'}$, $\overline{w'\theta'_l}$, $\overline{w'q'_l}$, $\overline{\theta_l'^2}$, $\overline{\theta'_l q'_l}$, and $\overline{q_l'^2}$ -- a total of four prognostic equations for mean quantities and ten for second-order moments. Additionally, the model of CEA2005 has six third-order moments whereas the current model has 28.

The inclusion of additional variables adds considerable computational complexity, but is necessary given the scope of this study. In particular, the inclusion of a mean moisture variable is a necessary precondition to simulate boundary layer clouds and their effect on the turbulent structure of the boundary layer. The mean momentum variables are not strictly necessary for a one-dimensional turbulence parameterization, but most models that include turbulence parameterizations almost always include variables to describe the mean momentum. Their inclusion here provides surface wind values needed for the surface flux parameterization for some test cases. The choice of second-order moments mostly follows directly from the choice of mean variables. The turbulent vertical fluxes of momentum, heat, and moisture are critically important for the prediction of their respective mean quantities. The scalar variances and covariances provide richness of description for the turbulent state and are necessary for determining cloud fraction, cloud liquid water content, and buoyancy terms for the scalar fluxes and turbulent kinetic energy components. The turbulent kinetic energy components largely determine how vigorous turbulent processes are in the boundary layer. The vertical

velocity variance in particular plays a critical role in determining the rate at which gradients of the mean variables are mixed.

2.2 Choice of mean variables and their equations

First, the thermodynamic variables chosen for use in the current model are liquid water potential temperature, θ_l , (Betts 1973) and total suspended water specific humidity, q_t . The use of these variables eliminates several difficulties associated with small-scale condensation, since θ_l is conserved under both moist and dry adiabatic processes (Deardorff 1976a). The equivalent potential temperature, θ_e , has this property and the additional advantage of being conserved under precipitation processes. Ultimately, θ_l was chosen over θ_e due to the fact that θ_l reduces to θ in the absence of condensation and θ_l has been the preferred variable for use with subgrid-scale condensation parameterizations. The prognostic equations for momentum, θ_l , and q_t with the Boussinesq approximation are: (Stull 1988)

$$\frac{\partial u_i}{\partial t} = -u_j \frac{\partial u_i}{\partial x_j} + \frac{\theta'_v}{\theta_{v_0}} g_i + f \varepsilon_{ij3} u_j - \frac{1}{\rho_0} \frac{\partial p}{\partial x_i} + \nu \frac{\partial^2 u_i}{\partial x_j^2} \quad (2.1)$$

$$\frac{\partial \theta_l}{\partial t} = -u_j \frac{\partial \theta_l}{\partial x_j} + \nu_{\theta_l} \frac{\partial^2 \theta_l}{\partial x_j^2} - \frac{1}{\rho_0 c_p} \frac{\partial F_j}{\partial x_j} - \frac{L_v}{c_p} \left(\frac{p_0}{p} \right)^{\kappa} \frac{1}{\rho_0} \frac{\partial P}{\partial x_j} \quad (2.2)$$

$$\frac{\partial q_t}{\partial t} = -u_j \frac{\partial q_t}{\partial x_j} + \nu_{q_t} \frac{\partial^2 q_t}{\partial x_j^2} + \left(\frac{\partial q_t}{\partial t} \right)_{MIC} \quad (2.3)$$

where $f = 2\Omega \sin \phi$, ε_{ijk} is the alternating unit tensor, ρ_0 is the reference density, ν is the kinematic molecular viscosity, ν_{θ_l} is the kinematic molecular diffusivity for θ_l , ν_{q_t} is the

kinematic molecular diffusivity for q_l , $\frac{\partial F_j}{\partial x_j}$ is the radiative flux divergence, P is the

precipitation flux ($\text{kg m}^{-2} \text{s}^{-1}$), $\left(\frac{\partial q_l}{\partial t}\right)_{MIC}$ is the tendency of q_l due to microphysics, and

from Betts (1973), $\theta_l = \theta - \left(\frac{\theta}{T} \frac{L_v}{c_p}\right) q_l$, where q_l is the liquid water specific humidity.

Using Reynolds' decomposition, equations (2.1)-(2.3) may be written as

$$\begin{aligned} \frac{\partial(\bar{u}_i + u'_i)}{\partial t} = & -(\bar{u}_j + u'_j) \frac{\partial(\bar{u}_i + u'_i)}{\partial x_j} + \frac{\theta'_v}{\theta_{v_0}} g_i - g_i + f \varepsilon_{ij3} (\bar{u}_j + u'_j) - \frac{1}{\rho_0} \frac{\partial(\bar{p} + p')}{\partial x_i} \\ & + v \frac{\partial^2(\bar{u}_i + u'_i)}{\partial x_j^2} \end{aligned} \quad (2.4)$$

$$\begin{aligned} \frac{\partial(\bar{\theta}_l + \theta'_l)}{\partial t} = & -(\bar{u}_j + u'_j) \frac{\partial(\bar{\theta}_l + \theta'_l)}{\partial x_j} + v_{\theta_l} \frac{\partial^2(\bar{\theta}_l + \theta'_l)}{\partial x_j^2} - \frac{1}{\rho_0 c_p} \frac{\partial(\bar{F}_j + F'_j)}{\partial x_j} \\ & - \frac{L_v}{c_p} \left(\frac{p_0}{p}\right)^{\kappa} \frac{1}{\rho_0} \frac{\partial(\bar{P} + P')}{\partial x_j} \end{aligned} \quad (2.5)$$

$$\frac{\partial(\bar{q}_l + q'_l)}{\partial t} = -(\bar{u}_j + u'_j) \frac{\partial(\bar{q}_l + q'_l)}{\partial x_j} + v_{q_l} \frac{\partial^2(\bar{q}_l + q'_l)}{\partial x_j^2} + \left(\frac{\partial \bar{q}_l}{\partial t}\right)_{MIC} + \left(\frac{\partial q'_l}{\partial t}\right)_{MIC} \quad (2.6)$$

where the overbar denotes a grid-cell mean and primes indicate local deviations from the grid-cell mean. We wish to describe the grid-cell mean properties. In order to derive equations that describe the grid-cell mean state, we may average equations (2.4)-(2.6) to yield

$$\frac{\partial \bar{u}_i}{\partial t} = -\bar{u}_j \frac{\partial \bar{u}_i}{\partial x_j} - \frac{\partial \overline{u'_i u'_j}}{\partial x_j} - g_i + f \varepsilon_{ij3} \bar{u}_j - \frac{1}{\rho_0} \frac{\partial \bar{p}}{\partial x_i} + v \frac{\partial^2 \bar{u}_i}{\partial x_j^2} \quad (2.7)$$

$$\frac{\partial \bar{\theta}_l}{\partial t} = -\bar{u}_j \frac{\partial \bar{\theta}_l}{\partial x_j} - \frac{\partial \bar{u}'_j \bar{\theta}'_l}{\partial x_j} + v_{\theta_l} \frac{\partial^2 \bar{\theta}_l}{\partial x_j^2} - \frac{1}{\rho_0 c_p} \frac{\partial \bar{F}_j}{\partial x_j} - \frac{L_v}{c_p} \left(\frac{p_0}{p} \right)^{\kappa} \frac{1}{\rho_0} \frac{\partial \bar{P}}{\partial x_j} \quad (2.8)$$

$$\frac{\partial \bar{q}_t}{\partial t} = -\bar{u}_j \frac{\partial \bar{q}_t}{\partial x_j} - \frac{\partial \bar{u}'_j \bar{q}'_t}{\partial x_j} + v_{q_t} \frac{\partial^2 \bar{q}_t}{\partial x_j^2} + \left(\frac{\partial \bar{q}_t}{\partial t} \right)_{MIC} \quad (2.9)$$

2.3 Equations for the Second-order Moments

The equations for the mean state variables include the second-order moment terms $\overline{u'_i u'_j}$, $\overline{u'_j \theta'_l}$, and $\overline{u'_j q'_t}$. It is possible to derive prognostic equations for these terms. Subtracting the mean equations, (2.7)-(2.9), from their respective total equations, (2.4)-(2.6), yields equations for the fluctuating variables:

$$\frac{\partial u'_i}{\partial t} = -\bar{u}_j \frac{\partial u'_i}{\partial x_j} - u'_j \frac{\partial \bar{u}_i}{\partial x_j} - u'_j \frac{\partial u'_i}{\partial x_j} + \frac{\partial \overline{u'_i u'_j}}{\partial x_j} + \frac{\theta'_v}{\theta_{v_0}} g_i + f \varepsilon_{ij3} u'_j - \frac{1}{\rho_0} \frac{\partial p'}{\partial x_i} + v \frac{\partial^2 u'_i}{\partial x_j^2} \quad (2.10)$$

$$\frac{\partial \theta'_l}{\partial t} = -\bar{u}_j \frac{\partial \theta'_l}{\partial x_j} - u'_j \frac{\partial \bar{\theta}_l}{\partial x_j} - u'_j \frac{\partial \theta'_l}{\partial x_j} + \frac{\partial \overline{u'_j \theta'_l}}{\partial x_j} + v_{\theta_l} \frac{\partial^2 \theta'_l}{\partial x_j^2} - \frac{1}{\rho_0 c_p} \frac{\partial F'_j}{\partial x_j} - \frac{L_v}{c_p} \left(\frac{p_0}{p} \right)^{\kappa} \frac{1}{\rho_0} \frac{\partial P'}{\partial x_j} \quad (2.11)$$

$$\frac{\partial q'_t}{\partial t} = -\bar{u}_j \frac{\partial q'_t}{\partial x_j} - u'_j \frac{\partial \bar{q}_t}{\partial x_j} - u'_j \frac{\partial q'_t}{\partial x_j} + \frac{\partial \overline{u'_j q'_t}}{\partial x_j} + v_{q_t} \frac{\partial^2 q'_t}{\partial x_j^2} + \left(\frac{\partial q'_t}{\partial t} \right)_{MIC} \quad (2.12)$$

Two more fluctuating variable equations useful for the remainder of the derivation are obtained by substituting another arbitrary momentum component, u'_l or u'_k , for u'_i . The results are

$$\frac{\partial u'_l}{\partial t} = -\bar{u}_j \frac{\partial u'_l}{\partial x_j} - u'_j \frac{\partial \bar{u}_l}{\partial x_j} - u'_j \frac{\partial u'_l}{\partial x_j} + \frac{\partial \overline{u'_i u'_j}}{\partial x_j} + \frac{\theta'_v}{\theta_{v_0}} g_l + f \varepsilon_{ij3} u'_j - \frac{1}{\rho_0} \frac{\partial p'}{\partial x_l} + v \frac{\partial^2 u'_l}{\partial x_j^2} \quad (2.13)$$

$$\frac{\partial u'_k}{\partial t} = -u'_j \frac{\partial u'_k}{\partial x_j} - u'_j \frac{\partial \bar{u}_k}{\partial x_j} - u'_j \frac{\partial u'_k}{\partial x_j} + \overline{\frac{\partial u'_k u'_j}{\partial x_j}} + \frac{\theta'_v}{\theta_{v_0}} g_k + f \varepsilon_{ij3} u'_j - \frac{1}{\rho_0} \frac{\partial p'}{\partial x_k} + v \frac{\partial^2 u'_k}{\partial x_j^2}. \quad (2.14)$$

Next, the second-order moment equations may be constructed by utilizing the product

rule for differentiation, e.g. $\overline{\frac{\partial u'_i u'_i}{\partial t}} = u'_i \frac{\partial u'_i}{\partial t} + u'_i \frac{\partial u'_i}{\partial t}$. Table 2.1 summarizes the

operations to be performed and the results are given in equations (2.15)-(2.20).

Second-order Moment	Operation Performed
$\overline{u'_i u'_i}$	$u'_i * \text{Eq. (2.10)} + u'_i * \text{Eq. (2.13)}$
$\overline{u'_i \theta'_i}$	$u'_i * \text{Eq. (2.11)} + \theta'_i * \text{Eq. (2.10)}$
$\overline{u'_i q'_i}$	$u'_i * \text{Eq. (2.12)} + q'_i * \text{Eq. (2.10)}$
$\overline{\theta'^2}$	$2\theta'_i * \text{Eq. (2.11)}$
$\overline{q'^2}$	$2q'_i * \text{Eq. (2.12)}$
$\overline{\theta'_i q'_i}$	$\theta'_i * \text{Eq. (2.12)} + q'_i * \text{Eq. (2.11)}$

Table 2.1 Operations performed to derive second-order moment equations

$$\begin{aligned} \frac{\partial u'_i u'_i}{\partial t} = & -u'_j \frac{\partial u'_i u'_i}{\partial x_j} - u'_i u'_j \frac{\partial \bar{u}_i}{\partial x_j} - u'_i u'_j \frac{\partial \bar{u}_i}{\partial x_j} - \frac{\partial u'_i u'_i u'_j}{\partial x_j} + u'_i \theta'_v \frac{g_i}{\theta_{v_0}} + u'_i \theta'_v \frac{g_i}{\theta_{v_0}} \\ & + f \varepsilon_{ij3} u'_i u'_j + f \varepsilon_{ij3} u'_i u'_j - \frac{1}{\rho_0} u'_i \frac{\partial p'}{\partial x_i} - \frac{1}{\rho_0} u'_i \frac{\partial p'}{\partial x_i} + u'_i \frac{\partial u'_i u'_j}{\partial x_j} + u'_i \frac{\partial u'_i u'_j}{\partial x_j} \quad (2.15) \\ & + v u'_i \frac{\partial^2 u'_i}{\partial x_j^2} + v u'_i \frac{\partial^2 u'_i}{\partial x_j^2} \end{aligned}$$

$$\begin{aligned}
\frac{\partial u'_i \theta'_l}{\partial t} = & -\overline{u_j} \frac{\partial u'_i \theta'_l}{\partial x_j} - u'_i u'_j \frac{\partial \overline{\theta_l}}{\partial x_j} - u'_j \theta'_l \frac{\partial \overline{u_i}}{\partial x_j} - \frac{\partial u'_i u'_j \theta'_l}{\partial x_j} + \overline{u'_i} \frac{\partial \overline{u'_j \theta'_l}}{\partial x_j} + \overline{\theta'_l} \frac{\partial \overline{u'_i u'_j}}{\partial x_j} \\
& - \frac{u'_i}{\rho_0 c_p} \frac{\partial F'_j}{\partial x_j} - \frac{L_v}{c_p} \left(\frac{p_0}{p} \right)^\kappa \frac{u'_i}{\rho_0} \frac{\partial P'}{\partial x_j} + \theta'_l \theta'_v \frac{g_i}{\theta_{v_0}} + f \varepsilon_{ij3} u'_j \theta'_l - \frac{1}{\rho_0} \theta'_l \frac{\partial p'}{\partial x_i} \\
& + v_{\theta_l} u'_i \frac{\partial^2 \theta'_l}{\partial x_j^2} + v \theta'_l \frac{\partial^2 u'_i}{\partial x_j^2}
\end{aligned} \tag{2.16}$$

$$\begin{aligned}
\frac{\partial u'_i q'_l}{\partial t} = & -\overline{u_j} \frac{\partial u'_i q'_l}{\partial x_j} - u'_i u'_j \frac{\partial \overline{q_l}}{\partial x_j} - u'_j q'_l \frac{\partial \overline{u_i}}{\partial x_j} - \frac{\partial u'_i u'_j q'_l}{\partial x_j} + \overline{u'_i} \frac{\partial \overline{u'_j q'_l}}{\partial x_j} + \overline{q'_l} \frac{\partial \overline{u'_i u'_j}}{\partial x_j} \\
& + q'_l \theta'_v \frac{g_i}{\theta_{v_0}} + f \varepsilon_{ij3} u'_j q'_l - \frac{1}{\rho_0} q'_l \frac{\partial p'}{\partial x_i} + v_{q_l} u'_i \frac{\partial^2 q'_l}{\partial x_j^2} + v q'_l \frac{\partial^2 u'_i}{\partial x_j^2} + u'_i \left(\frac{\partial q'_l}{\partial t} \right)_{MIC}
\end{aligned} \tag{2.17}$$

$$\begin{aligned}
\frac{\partial \theta_l'^2}{\partial t} = & -\overline{u_j} \frac{\partial \theta_l'^2}{\partial x_j} - 2u'_j \theta'_l \frac{\partial \overline{\theta_l}}{\partial x_j} - \frac{\partial u'_j \theta_l'^2}{\partial x_j} - \frac{2\theta'_l}{\rho_0 c_p} \frac{\partial F'_j}{\partial x_j} - \frac{L_v}{c_p} \left(\frac{p_0}{p} \right)^\kappa \frac{2\theta'_l}{\rho_0} \frac{\partial P'}{\partial x_j} \\
& + 2v_{\theta_l} \theta'_l \frac{\partial^2 \theta'_l}{\partial x_j^2} + 2\theta'_l \frac{\partial \overline{u'_j \theta'_l}}{\partial x_j}
\end{aligned} \tag{2.18}$$

$$\begin{aligned}
\frac{\partial q_l'^2}{\partial t} = & -\overline{u_j} \frac{\partial q_l'^2}{\partial x_j} - 2u'_j q'_l \frac{\partial \overline{q_l}}{\partial x_j} - \frac{\partial u'_j q_l'^2}{\partial x_j} + 2v_{q_l} q'_l \frac{\partial^2 q'_l}{\partial x_j^2} + 2q'_l \frac{\partial \overline{u'_j q'_l}}{\partial x_j} + 2q'_l \left(\frac{\partial q'_l}{\partial t} \right)_{MIC}
\end{aligned} \tag{2.19}$$

$$\begin{aligned}
\frac{\partial \theta'_l q'_l}{\partial t} = & -\overline{u_j} \frac{\partial \theta'_l q'_l}{\partial x_j} - u'_j \theta'_l \frac{\partial \overline{q_l}}{\partial x_j} - u'_j q'_l \frac{\partial \overline{\theta_l}}{\partial x_j} - \frac{\partial u'_j \theta'_l q'_l}{\partial x_j} + \overline{\theta'_l} \frac{\partial \overline{u'_j q'_l}}{\partial x_j} + \overline{q'_l} \frac{\partial \overline{u'_j \theta'_l}}{\partial x_j} \\
& + v_{q_l} \theta'_l \frac{\partial^2 q'_l}{\partial x_j^2} + v_{\theta_l} q'_l \frac{\partial^2 \theta'_l}{\partial x_j^2} - \frac{q'_l}{\rho_0 c_p} \frac{\partial F'_j}{\partial x_j} + -\frac{L_v}{c_p} \left(\frac{p_0}{p} \right)^\kappa \frac{q'_l}{\rho_0} \frac{\partial P'}{\partial x_j} + \theta'_l \left(\frac{\partial q'_l}{\partial t} \right)_{MIC}
\end{aligned} \tag{2.20}$$

One may notice that equations (2.18)-(2.20) are for second-order moments that are not needed directly in the mean equations or in the other second-order moment equations (2.15)-(2.17). They are necessary, however, for determining the buoyancy terms in equations (2.15)-(2.17), as discussed in Section 2.9.

The last step is to average equations (2.15)-(2.20) and to make some simplifications. First, advection by the mean wind is neglected. This simplification is valid for a single column model where horizontal advection has no meaning and the vertical velocity is unknown. For a three-dimensional application, these terms should remain. Second, the Coriolis force is insignificant on scales under consideration, and all terms involving the Coriolis parameter are neglected. Third, all terms involving the precipitation flux divergence and radiative flux divergence are neglected. Fourth, equations (2.17), (2.19), and (2.20) contain terms involving the time rate of change of the fluctuating portion of q_t due to microphysics. Presumably, microphysical processes do affect the time rate of change of the second-order moments. For example, autoconversion converts cloud water into rain water, potentially depleting higher values of q_t within a grid cell leading to a decrease in its variance. For the purposes of this study, however, these terms are assumed to be small and are therefore neglected. Using these simplifications yields

$$\begin{aligned} \overline{\frac{\partial u'_i u'_l}{\partial t}} &= \overline{-u'_i u'_j \frac{\partial \bar{u}_i}{\partial x_j}} - \overline{u'_i u'_j \frac{\partial \bar{u}_l}{\partial x_j}} - \overline{\frac{\partial u'_i u'_l u'_j}{\partial x_j}} + \overline{u'_l \theta'_v \frac{g_i}{\theta_{v_0}}} + \overline{u'_i \theta'_v \frac{g_l}{\theta_{v_0}}} \\ &\quad - \frac{1}{\rho_0} \overline{u'_l \frac{\partial p'}{\partial x_i}} - \frac{1}{\rho_0} \overline{u'_i \frac{\partial p'}{\partial x_l}} + \overline{v u'_l \frac{\partial^2 u'_i}{\partial x_j^2}} + \overline{v u'_i \frac{\partial^2 u'_l}{\partial x_j^2}} \end{aligned} \quad (2.21)$$

$$\begin{aligned} \overline{\frac{\partial u'_i \theta'_l}{\partial t}} &= \overline{-u'_i u'_j \frac{\partial \bar{\theta}_l}{\partial x_j}} - \overline{u'_j \theta'_l \frac{\partial \bar{u}_i}{\partial x_j}} - \overline{\frac{\partial u'_i u'_j \theta'_l}{\partial x_j}} + \overline{\theta'_l \theta'_v \frac{g_i}{\theta_{v_0}}} \\ &\quad - \frac{1}{\rho_0} \overline{\theta'_l \frac{\partial p'}{\partial x_i}} + \overline{v_{\theta_l} u'_i \frac{\partial^2 \theta'_l}{\partial x_j^2}} + \overline{v \theta'_l \frac{\partial^2 u'_i}{\partial x_j^2}} \end{aligned} \quad (2.22)$$

$$\begin{aligned} \overline{\frac{\partial u'_i q'_t}{\partial t}} = & \overline{-u'_i u'_j \frac{\partial q'_t}{\partial x_j}} - \overline{u'_j q'_t \frac{\partial u'_i}{\partial x_j}} - \overline{\frac{\partial u'_i u'_j q'_t}{\partial x_j}} + \overline{q'_t \theta'_v \frac{g_i}{\theta_{v_0}}} \\ & - \frac{1}{\rho_0} \overline{q'_t \frac{\partial p'}{\partial x_i}} + \overline{v_{q_i} u'_i \frac{\partial^2 q'_t}{\partial x_j^2}} + \overline{v_{q_i} q'_t \frac{\partial^2 u'_i}{\partial x_j^2}} \end{aligned} \quad (2.23)$$

$$\overline{\frac{\partial \theta'^2_t}{\partial t}} = \overline{-2u'_j \theta'_t \frac{\partial \theta'_t}{\partial x_j}} - \overline{\frac{\partial u'_j \theta'^2_t}{\partial x_j}} + \overline{2v_{\theta_i} \theta'_t \frac{\partial^2 \theta'_t}{\partial x_j^2}} \quad (2.24)$$

$$\overline{\frac{\partial q'^2_t}{\partial t}} = \overline{-2u'_j q'_t \frac{\partial q'_t}{\partial x_j}} - \overline{\frac{\partial u'_j q'^2_t}{\partial x_j}} + \overline{2v_{q_i} q'_t \frac{\partial^2 q'_t}{\partial x_j^2}} \quad (2.25)$$

$$\overline{\frac{\partial \theta'_t q'_t}{\partial t}} = \overline{-u'_j \theta'_t \frac{\partial q'_t}{\partial x_j}} - \overline{u'_j q'_t \frac{\partial \theta'_t}{\partial x_j}} - \overline{\frac{\partial u'_j \theta'_t q'_t}{\partial x_j}} + \overline{v_{q_i} \theta'_t \frac{\partial^2 q'_t}{\partial x_j^2}} + \overline{v_{\theta_i} q'_t \frac{\partial^2 \theta'_t}{\partial x_j^2}}. \quad (2.26)$$

After the simplifying assumptions, equations (2.21)-(2.26) are still not a closed set because there are terms in them that are incalculable from known quantities. Equations (2.21), (2.22), and (2.23) contain unknown terms involving pressure fluctuations and buoyancy, and all of the equations contain unknown terms involving molecular viscosity. In addition, all of the second-order equations contain unknown third-order moments. This demonstrates the turbulence closure problem, namely that equations for nth-order moments contain terms with (n+1)-order moments.

The following sections describe how these terms are parameterized in the present model. Since much of this work is motivated by the success and computational efficiency of the work of CEA2005, the parameterizations follow that work where appropriate, especially for the pressure correlation and third-order moment terms. Deviations from CEA2005 are made for the buoyancy terms and the molecular viscosity, or dissipation, terms. These deviations are necessary since the model of CEA2005 does not include a

moisture variable and therefore does not include the effects of moisture on buoyancy. A rich literature for the buoyancy and dissipation terms guides their choice.

2.4 Equations for the Third-order Moments

As with the second-order moments, prognostic equations may be derived to predict the third-order moments, although it is expected that they will also contain unknown terms including fourth-order moments, pressure correlation terms, molecular viscosity terms, and buoyancy terms. In the derivation of these equations, the product rule

Third-Order Moment	Operation Performed
$\overline{u'_i u'_l u'_k}$	$\overline{u'_i u'_l} * \text{Eq. (2.14)} + \overline{u'_k} * \text{Eq. (2.15)}$
$\overline{u'_i u'_l \theta'_l}$	$\overline{u'_i u'_l} * \text{Eq. (2.11)} + \overline{\theta'_l} * \text{Eq. (2.15)}$
$\overline{u'_i u'_l q'_t}$	$\overline{u'_i u'_l} * \text{Eq. (2.12)} + \overline{q'_t} * \text{Eq. (2.15)}$
$\overline{u'_l \theta'^2_l}$	$\overline{u'_l \theta'_l} * \text{Eq. (2.11)} + \overline{\theta'_l} * \text{Eq. (2.16)}$
$\overline{u'_l q'^2_t}$	$\overline{u'_l q'_t} * \text{Eq. (2.12)} + \overline{q'_t} * \text{Eq. (2.17)}$
$\overline{u'_l \theta'_l q'_t}$	$\overline{u'_l \theta'_l} * \text{Eq. (2.12)} + \overline{q'_t} * \text{Eq. (2.16)}$
$\overline{\theta'^3_l}$	$\overline{3\theta'^2_l} * \text{Eq. (2.11)}$
$\overline{q'^3_t}$	$\overline{3q'^2_t} * \text{Eq. (2.12)}$
$\overline{\theta'^2_l q'_t}$	$\overline{\theta'_l q'_t} * \text{Eq. (2.11)} + \overline{\theta'_l} * \text{Eq. (2.20)}$
$\overline{\theta'_l q'^2_t}$	$\overline{\theta'_l q'_t} * \text{Eq. (2.12)} + \overline{q'_t} * \text{Eq. (2.20)}$

Table 2.2 Operations performed to derive third-order moment equations

for differentiation is key once again, and the equations for the turbulent variables, (2.10)-(2.14), and the unaveraged second-order moment equations, (2.15)-(2.20), are needed. Table 2.2 summarizes the operations to be performed, and the results follow. As with the second-order moment equations, terms involving the mean wind, Coriolis parameter, precipitation flux divergence, radiative flux divergence, and microphysics are neglected.

$$\begin{aligned}
\frac{\overline{\partial u'_i u'_l u'_k}}{\partial t} &= -\overline{u'_j u'_i u'_l} \frac{\partial \bar{u}_k}{\partial x_j} - \overline{u'_j u'_l u'_k} \frac{\partial \bar{u}_i}{\partial x_j} - \overline{u'_j u'_i u'_k} \frac{\partial \bar{u}_l}{\partial x_j} - \overline{\partial u'_j u'_i u'_l u'_k} \\
&\quad + \frac{g_k}{\theta_{v_0}} \overline{u'_i u'_l \theta'_v} + \frac{g_i}{\theta_{v_0}} \overline{u'_l u'_k \theta'_v} + \frac{g_l}{\theta_{v_0}} \overline{u'_i u'_k \theta'_v} \\
&\quad - \frac{1}{\rho_0} \left(\overline{u'_i u'_l} \frac{\partial p'}{\partial x_k} + \overline{u'_l u'_k} \frac{\partial p'}{\partial x_i} + \overline{u'_i u'_k} \frac{\partial p'}{\partial x_l} \right) \\
&\quad + \overline{u'_i u'_l} \frac{\partial \overline{u'_j u'_k}}{\partial x_j} + \overline{u'_l u'_k} \frac{\partial \overline{u'_i u'_j}}{\partial x_j} + \overline{u'_i u'_k} \frac{\partial \overline{u'_j u'_l}}{\partial x_j} \\
&\quad + \overline{v u'_i u'_l} \frac{\partial^2 u'_k}{\partial x_j^2} + \overline{v u'_l u'_k} \frac{\partial^2 u'_i}{\partial x_j^2} + \overline{v u'_i u'_k} \frac{\partial^2 u'_l}{\partial x_j^2}
\end{aligned} \tag{2.27}$$

$$\begin{aligned}
\frac{\overline{\partial u'_i u'_l \theta'_l}}{\partial t} &= -\overline{u'_j u'_i u'_l} \frac{\partial \bar{\theta}_l}{\partial x_j} - \overline{u'_j u'_l \theta'_l} \frac{\partial \bar{u}_i}{\partial x_j} - \overline{u'_j u'_i \theta'_l} \frac{\partial \bar{u}_l}{\partial x_j} - \overline{\partial u'_j u'_i u'_l \theta'_l} \\
&\quad + \frac{g_i}{\theta_{v_0}} \overline{u'_l \theta'_l \theta'_v} + \frac{g_l}{\theta_{v_0}} \overline{u'_i \theta'_l \theta'_v} - \frac{1}{\rho_0} \left(\overline{u'_l \theta'_l} \frac{\partial p'}{\partial x_i} + \overline{u'_i \theta'_l} \frac{\partial p'}{\partial x_l} \right) \\
&\quad + \overline{u'_i u'_l} \frac{\partial \overline{u'_j \theta'_l}}{\partial x_j} + \overline{u'_l \theta'_l} \frac{\partial \overline{u'_i u'_j}}{\partial x_j} + \overline{u'_i \theta'_l} \frac{\partial \overline{u'_j u'_l}}{\partial x_j} \\
&\quad + \overline{v u'_i u'_l} \frac{\partial^2 \theta'_l}{\partial x_j^2} + \overline{v u'_l \theta'_l} \frac{\partial^2 u'_i}{\partial x_j^2} + \overline{v u'_i \theta'_l} \frac{\partial^2 u'_l}{\partial x_j^2}
\end{aligned} \tag{2.28}$$

$$\begin{aligned}
\frac{\overline{\partial u'_i u'_l q'_t}}{\partial t} &= \overline{-u'_j u'_i u'_l} \frac{\partial \bar{q}_t}{\partial x_j} - \overline{u'_j u'_l q'_t} \frac{\partial \bar{u}_i}{\partial x_j} - \overline{u'_j u'_i q'_t} \frac{\partial \bar{u}_l}{\partial x_j} - \frac{\overline{\partial u'_j u'_i u'_l q'_t}}{\partial x_j} \\
&\quad + \frac{g_i}{\theta_{v_0}} \overline{u'_l q'_t \theta'_v} + \frac{g_l}{\theta_{v_0}} \overline{u'_i q'_t \theta'_v} - \frac{1}{\rho_0} \left(\overline{u'_l q'_t} \frac{\partial p'}{\partial x_i} + \overline{u'_i q'_t} \frac{\partial p'}{\partial x_l} \right) \\
&\quad + \overline{u'_i u'_l} \frac{\partial u'_j q'_t}{\partial x_j} + \overline{u'_l q'_t} \frac{\partial u'_i u'_j}{\partial x_j} + \overline{u'_i q'_t} \frac{\partial u'_j u'_l}{\partial x_j} \\
&\quad + \overline{v_{q_t} u'_i u'_l} \frac{\partial^2 q'_t}{\partial x_j^2} + \overline{v u'_l q'_t} \frac{\partial^2 u'_i}{\partial x_j^2} + \overline{v u'_i q'_t} \frac{\partial^2 u'_l}{\partial x_j^2}
\end{aligned} \tag{2.29}$$

$$\begin{aligned}
\frac{\overline{\partial u'_l \theta'_l{}'^2}}{\partial t} &= \overline{-2u'_j u'_l \theta'_l} \frac{\partial \bar{\theta}_l}{\partial x_j} - \overline{u'_j \theta'_l{}'^2} \frac{\partial \bar{u}_l}{\partial x_j} - \frac{\overline{\partial u'_j u'_l \theta'_l{}'^2}}{\partial x_j} + \frac{g_l}{\theta_{v_0}} \overline{\theta'_l{}'^2 \theta'_v} - \frac{1}{\rho_0} \overline{\theta'_l{}'^2} \frac{\partial p'}{\partial x_l} \\
&\quad + \overline{2u'_l \theta'_l} \frac{\partial u'_j \theta'_l}{\partial x_j} + \overline{\theta'_l{}'^2} \frac{\partial u'_l u'_j}{\partial x_j} + \overline{2v_{\theta_l} u'_l \theta'_l} \frac{\partial^2 \theta'_l}{\partial x_j^2} + \overline{v \theta'_l{}'^2} \frac{\partial^2 u'_l}{\partial x_j^2}
\end{aligned} \tag{2.30}$$

$$\begin{aligned}
\frac{\overline{\partial u'_l q'_l{}'^2}}{\partial t} &= \overline{-2u'_j u'_l q'_l} \frac{\partial \bar{q}_t}{\partial x_j} - \overline{u'_j q'_l{}'^2} \frac{\partial \bar{u}_l}{\partial x_j} - \frac{\overline{\partial u'_j u'_l q'_l{}'^2}}{\partial x_j} + \frac{g_l}{\theta_{v_0}} \overline{q'_l{}'^2 \theta'_v} - \frac{1}{\rho_0} \overline{q'_l{}'^2} \frac{\partial p'}{\partial x_l} \\
&\quad + \overline{2u'_l q'_l} \frac{\partial u'_j q'_l}{\partial x_j} + \overline{q'_l{}'^2} \frac{\partial u'_l u'_j}{\partial x_j} + \overline{2v_{q_t} u'_l q'_l} \frac{\partial^2 q'_l}{\partial x_j^2} + \overline{v q'_l{}'^2} \frac{\partial^2 u'_l}{\partial x_j^2}
\end{aligned} \tag{2.31}$$

$$\begin{aligned}
\frac{\overline{\partial u'_l \theta'_l q'_l}}{\partial t} &= \overline{-u'_j u'_l \theta'_l} \frac{\partial \bar{q}_t}{\partial x_j} - \overline{u'_j u'_l q'_l} \frac{\partial \bar{\theta}_l}{\partial x_j} - \overline{u'_j \theta'_l q'_l} \frac{\partial \bar{u}_l}{\partial x_j} - \frac{\overline{\partial u'_j u'_l \theta'_l q'_l}}{\partial x_j} \\
&\quad + \frac{g_l}{\theta_{v_0}} \overline{\theta'_l q'_l \theta'_v} - \frac{1}{\rho_0} \overline{\theta'_l q'_l} \frac{\partial p'}{\partial x_l} + \overline{u'_l \theta'_l} \frac{\partial u'_j q'_l}{\partial x_j} + \overline{\theta'_l q'_l} \frac{\partial u'_l u'_j}{\partial x_j} + \overline{u'_l q'_l} \frac{\partial u'_j \theta'_l}{\partial x_j} \\
&\quad + \overline{v_{\theta_l} u'_l q'_l} \frac{\partial^2 \theta'_l}{\partial x_j^2} + \overline{v \theta'_l q'_l} \frac{\partial^2 u'_l}{\partial x_j^2} + \overline{v_{q_t} u'_l \theta'_l} \frac{\partial^2 q'_l}{\partial x_j^2}
\end{aligned} \tag{2.32}$$

$$\frac{\overline{\partial \theta'_l{}'^3}}{\partial t} = \overline{-3u'_j \theta'_l{}'^2} \frac{\partial \bar{\theta}_l}{\partial x_j} - \frac{\overline{\partial u'_j \theta'_l{}'^3}}{\partial x_j} + \overline{3\theta'_l{}'^2} \frac{\partial u'_j \theta'_l}{\partial x_j} + \overline{3v_{\theta_l} \theta'_l{}'^2} \frac{\partial^2 \theta'_l}{\partial x_j^2} \tag{2.33}$$

$$\frac{\overline{\partial q'_l{}'^3}}{\partial t} = \overline{-3u'_j q'_l{}'^2} \frac{\partial \bar{q}_t}{\partial x_j} - \frac{\overline{\partial u'_j q'_l{}'^3}}{\partial x_j} + \overline{3q'_l{}'^2} \frac{\partial u'_j q'_l}{\partial x_j} + \overline{3v_{q_t} q'_l{}'^2} \frac{\partial^2 q'_l}{\partial x_j^2} \tag{2.34}$$

$$\begin{aligned} \frac{\overline{\partial \theta_l'^2 q_t'}}{\partial t} = & \overline{-u_j' \theta_l'^2} \frac{\partial \overline{q_t}}{\partial x_j} - \overline{2u_j' \theta_l' q_t'} \frac{\partial \overline{\theta_l}}{\partial x_j} - \overline{\frac{\partial u_j' \theta_l'^2 q_t'}{\partial x_j}} + \overline{\theta_l'^2} \frac{\partial \overline{u_j' q_t'}}{\partial x_j} + \overline{2\theta_l' q_t'} \frac{\partial \overline{u_j' \theta_l'}}{\partial x_j} \\ & + \overline{2v_{\theta_l} \theta_l' q_t'} \frac{\partial^2 \overline{\theta_l'}}{\partial x_j^2} + \overline{v_{q_t} \theta_l'^2} \frac{\partial^2 \overline{q_t'}}{\partial x_j^2} \end{aligned} \quad (2.35)$$

$$\begin{aligned} \frac{\overline{\partial \theta_l' q_t'^2}}{\partial t} = & \overline{-u_j' q_t'^2} \frac{\partial \overline{\theta_l}}{\partial x_j} - \overline{2u_j' \theta_l' q_t'} \frac{\partial \overline{q_t}}{\partial x_j} - \overline{\frac{\partial u_j' \theta_l' q_t'^2}{\partial x_j}} + \overline{q_t'^2} \frac{\partial \overline{u_j' \theta_l'}}{\partial x_j} + \overline{2\theta_l' q_t'} \frac{\partial \overline{u_j' q_t'}}{\partial x_j} \\ & + \overline{2v_{q_t} \theta_l' q_t'} \frac{\partial^2 \overline{q_t'}}{\partial x_j^2} + \overline{v_{\theta_l} q_t'^2} \frac{\partial^2 \overline{\theta_l'}}{\partial x_j^2} \end{aligned} \quad (2.36)$$

2.5 Parameterization of the pressure correlation terms

Pressure correlations in CEA2005 are parameterized following the work of Zeman and Lumley (1979) and Canuto (1992). They consist of a return-to-isotropy term that acts on longer timescales to restore isotropic turbulence when anisotropic turbulence is present, and a “fast term” that acts on shorter timescales and effectively damps the moments governed by the equations in which they appear. The pressure correlations in equations (2.21), (2.22), (2.27), (2.28), and (2.30) are taken directly from CEA2005, except where the parameterizations include buoyancy terms. In these terms, θ_v' is substituted for θ' to account for the effects of water vapor and liquid water on buoyancy. Pressure correlations in equations (2.23), (2.29), (2.31), and (2.32), where the total water specific humidity appears, are obtained analogously to those found in equations (2.22), (2.28) and (2.30), respectively. In addition, the leading coefficient two's for terms involving c_4, c_6, c_8 , and c_9 found in CEA2005 are included in the coefficients themselves, in accordance with other works (Bougeault 1981b, Golaz et al. 2002a, André

et al. 1978). The parameterizations are summarized in Table 2.3. For reference, δ is the Kronecker delta, g is the acceleration of gravity, and $\alpha = \frac{1}{\theta_{v_0}}$ is the thermal expansion coefficient, $\bar{e} = \frac{1}{2} \left(\overline{u'^2} + \overline{v'^2} + \overline{w'^2} \right)$ is the turbulence kinetic energy, τ_1 and τ_2 are the turbulent timescales, and the c_n are model constants. The constants are discussed in Section 2.6 and turbulent timescales are discussed in Section 2.10.

Equation	Pressure Correlation	Parameterization
2.21	$\frac{1}{\rho_0} \left(\overline{u'_i \frac{\partial p'}{\partial x_i}} + \overline{u'_i \frac{\partial p'}{\partial x_l}} \right)$	$\frac{c_4}{\tau_1} \left(\overline{u'_i u'_i} - \frac{2}{3} \overline{e \delta_{il}} \right) + c_5 g \alpha \left(\overline{u'_i \theta'_v \delta_{3l}} + \overline{u'_l \theta'_v \delta_{3i}} - \frac{2}{3} \overline{\delta_{il} w' \theta'_v} \right)$
2.22	$\frac{1}{\rho_0} \overline{\theta'_l \frac{\partial p'}{\partial x_i}}$	$\frac{c_6}{\tau_2} \overline{u'_i \theta'_l} + c_7 g \alpha \overline{\theta'_l \theta'_v \delta_{3i}}$
2.23	$\frac{1}{\rho_0} \overline{q'_t \frac{\partial p'}{\partial x_i}}$	$\frac{c_6}{\tau_2} \overline{u'_i q'_t} + c_7 g \alpha \overline{q'_t \theta'_v \delta_{3i}}$
2.27	$\frac{1}{\rho_0} \left(\overline{u'_i u'_l \frac{\partial p'}{\partial x_k}} + \overline{u'_l u'_k \frac{\partial p'}{\partial x_i}} + \overline{u'_i u'_k \frac{\partial p'}{\partial x_l}} \right)$	$\frac{c_8}{\tau_1} \overline{u'_i u'_l u'_k} + c_{11} g \alpha \left(\overline{u'_i u'_l \theta'_v \delta_{3k}} + \overline{u'_l u'_k \theta'_v \delta_{3i}} + \overline{u'_i u'_k \theta'_v \delta_{3l}} \right)$
2.28	$\frac{1}{\rho_0} \left(\overline{u'_i \theta'_l \frac{\partial p'}{\partial x_i}} + \overline{u'_i \theta'_l \frac{\partial p'}{\partial x_l}} \right)$	$\frac{c_8}{\tau_1} \left(\overline{u'_i u'_l \theta'_l} - \frac{1}{3} \overline{\delta_{il} u'_k u'_k \theta'_l} \right) + c_{11} g \alpha \left(\overline{u'_i \theta'_l \theta'_v \delta_{3l}} + \overline{u'_l \theta'_l \theta'_v \delta_{3i}} \right) - \frac{c_9}{\tau_1} \overline{\delta_{il} u'_k u'_k \theta'_l}$
2.29	$\frac{1}{\rho_0} \left(\overline{u'_i q'_t \frac{\partial p'}{\partial x_i}} + \overline{u'_i q'_t \frac{\partial p'}{\partial x_l}} \right)$	$\frac{c_8}{\tau_1} \left(\overline{u'_i u'_l q'_t} - \frac{1}{3} \overline{\delta_{il} u'_k u'_k q'_t} \right) + c_{11} g \alpha \left(\overline{u'_i q'_t \theta'_v \delta_{3l}} + \overline{u'_l q'_t \theta'_v \delta_{3i}} \right) - \frac{c_9}{\tau_1} \overline{\delta_{il} u'_k u'_k q'_t}$
2.30	$\frac{1}{\rho_0} \overline{\theta'^2_l \frac{\partial p'}{\partial x_l}}$	$\frac{c_8}{\tau_1} \overline{u'_l \theta'^2_l} + c_{11} g \alpha \overline{\theta'^2_l \theta'_v \delta_{3l}}$
2.31	$\frac{1}{\rho_0} \overline{q'^2_t \frac{\partial p'}{\partial x_l}}$	$\frac{c_8}{\tau_1} \overline{u'_l q'^2_t} + c_{11} g \alpha \overline{q'^2_t \theta'_v \delta_{3l}}$
2.32	$\frac{1}{\rho_0} \overline{\theta'_l q'_t \frac{\partial p'}{\partial x_l}}$	$\frac{c_8}{\tau_1} \overline{u'_l \theta'_l q'_t} + c_{11} g \alpha \overline{\theta'_l q'_t \theta'_v \delta_{3l}}$

Table 2.3 Pressure correlation parameterizations

2.6 Parameterization of the dissipation terms

Each molecular viscosity term can be split into two separate terms using the product rule and the chain rule, e.g. $\overline{vA \frac{\partial^2 B}{\partial x^2}} + \overline{vB \frac{\partial^2 A}{\partial x^2}} = \overline{v \frac{\partial^2 AB}{\partial x^2}} - 2\overline{v \frac{\partial A}{\partial x} \frac{\partial B}{\partial x}}$. The first term on the right-hand side represents diffusion by molecular processes and the second term on the right-hand side represents dissipation. Using a scaling argument, Stull (1988) argues that the molecular diffusion term is several orders of magnitude smaller than other terms in the second- and third-order moment equations and can be neglected. The dissipation term needs to be retained, however.

For most moments, CEA2005 parameterize the dissipation as simple damping whose magnitude is controlled by a constant and the turbulent timescale. This same

Equation	Molecular Viscosity Term	Parameterization
2.21	$\overline{v u_i' \frac{\partial^2 u_i'}{\partial x_j^2}} + \overline{v u_i' \frac{\partial^2 u_i'}{\partial x_j^2}}$	$-\overline{c_1 \delta_{ij} \frac{u_i' u_i'}{\tau_1}}$
2.22	$\overline{v_{\theta_i} u_i' \frac{\partial^2 \theta_i'}{\partial x_j^2}} + \overline{v_{\theta_i} \theta_i' \frac{\partial^2 u_i'}{\partial x_j^2}}$	0
2.23	$\overline{v_{q_i} u_i' \frac{\partial^2 q_i'}{\partial x_j^2}} + \overline{v_{q_i} q_i' \frac{\partial^2 u_i'}{\partial x_j^2}}$	0
2.24	$\overline{2v_{\theta_i} \theta_i' \frac{\partial^2 \theta_i'}{\partial x_j^2}}$	$-\overline{c_2 \frac{\theta_i'^2}{\tau_1}}$
2.25	$\overline{2v_{q_i} q_i' \frac{\partial^2 q_i'}{\partial x_j^2}}$	$-\overline{c_2 \frac{q_i'^2}{\tau_1}}$
2.26	$\overline{v_{q_i} \theta_i' \frac{\partial^2 q_i'}{\partial x_j^2}} + \overline{v_{\theta_i} q_i' \frac{\partial^2 \theta_i'}{\partial x_j^2}}$	$-\overline{c_2 \frac{\theta_i' q_i'}{\tau_1}}$

Table 2.4 Second-order moment dissipation parameterizations

Equation	Molecular Viscosity Term	Parameterization
2.27	$\overline{v u_i' u_l' \frac{\partial^2 u_k'}{\partial x_j^2}} + \overline{v u_l' u_k' \frac{\partial^2 u_i'}{\partial x_j^2}} + \overline{v u_i' u_k' \frac{\partial^2 u_l'}{\partial x_j^2}}$	0
2.28	$\overline{v_{\theta_i} u_i' u_l' \frac{\partial^2 \theta_l'}{\partial x_j^2}} + \overline{v u_l' \theta_l' \frac{\partial^2 u_i'}{\partial x_j^2}} + \overline{v u_i' \theta_l' \frac{\partial^2 u_l'}{\partial x_j^2}}$	$-\frac{c_{10}}{3\tau_1} \overline{\delta_{il} u_k' u_k' \theta_l'}$
2.29	$\overline{v_{q_t} u_i' u_l' \frac{\partial^2 q_t'}{\partial x_j^2}} + \overline{v u_l' q_t' \frac{\partial^2 u_i'}{\partial x_j^2}} + \overline{v u_i' q_t' \frac{\partial^2 u_l'}{\partial x_j^2}}$	$-\frac{c_{10}}{3\tau_1} \overline{\delta_{il} u_k' u_k' q_t'}$
2.30	$\overline{2v_{\theta_i} u_l' \theta_l' \frac{\partial^2 \theta_l'}{\partial x_j^2}} + \overline{v \theta_l'^2 \frac{\partial^2 u_l'}{\partial x_j^2}}$	0
2.31	$\overline{2v_{q_t} u_l' q_t' \frac{\partial^2 q_t'}{\partial x_j^2}} + \overline{v q_t'^2 \frac{\partial^2 u_l'}{\partial x_j^2}}$	0
2.32	$\overline{v_{\theta_i} u_l' q_t' \frac{\partial^2 \theta_l'}{\partial x_j^2}} + \overline{v \theta_l' q_t' \frac{\partial^2 u_l'}{\partial x_j^2}} + \overline{v_{q_t} u_l' \theta_l' \frac{\partial^2 q_t'}{\partial x_j^2}}$	0
2.33	$\overline{3v_{\theta_i} \theta_l'^2 \frac{\partial^2 \theta_l'}{\partial x_j^2}}$	$-\frac{c_{10}}{\tau_1} \overline{\theta_l'^3}$
2.34	$\overline{3v_{q_t} q_t'^2 \frac{\partial^2 q_t'}{\partial x_j^2}}$	$-\frac{c_{10}}{\tau_1} \overline{q_t'^3}$
2.35	$\overline{2v_{\theta_i} \theta_l' q_t' \frac{\partial^2 \theta_l'}{\partial x_j^2}} + \overline{v_{q_t} \theta_l'^2 \frac{\partial^2 q_t'}{\partial x_j^2}}$	$-\frac{c_{10}}{\tau_1} \overline{\theta_l'^2 q_t'}$
2.36	$\overline{2v_{q_t} \theta_l' q_t' \frac{\partial^2 q_t'}{\partial x_j^2}} + \overline{v_{\theta_i} q_t'^2 \frac{\partial^2 \theta_l'}{\partial x_j^2}}$	$-\frac{c_{10}}{\tau_1} \overline{\theta_l' q_t'^2}$

Table 2.5 Third-order moment dissipation parameterizations

parameterization is used in the current model, except for the dissipation in the turbulent

kinetic energy components. CEA2005 assume that the dissipation of $\overline{u_i'^2}$ is proportional to

the total turbulent kinetic energy, i.e. $-\frac{1}{3} \frac{TKE}{\tau}$. This differs from the dissipation

parameterization of the other second-order moments where a tunable constant is used,

e.g. $-c_i \frac{SOM}{\tau}$, where *SOM* stands for any second-order moment. In the current model, the latter form is used for the dissipation of the turbulent kinetic energy components as is done in the work of Golaz et al. (2002a). A noteworthy deviation from that work, however, is the absence of an ad hoc diffusion term. The parameterizations of the dissipation terms for the second- and third-order moments used in this model are given in Tables 2.4 and 2.5.

The nondimensional constants $c_1, c_2, c_4, c_5, c_6, c_7, c_8, c_{10}$, and c_{11} used in the parameterization of the pressure correlation and dissipation terms are presented in Table 2.6. The first two, c_1 and c_2 , appear in the dissipation terms of the second-order moments. Their values in the current model are somewhat smaller than those used in previous turbulence models, but this does not necessarily indicate that dissipation is weaker in the current model. The turbulence timescale discussed in Section 2.10 factors into this term heavily, and its parameterization differs from previous models. The constants c_4, c_5, c_6 , and c_7 appear in the return-to-isotropy portion of the pressure correlation terms in the second-order moments. Their values are the same or very similar to those used in the models of Bougeault (1981b) and Golaz (2002a). Finally, the constants c_8, c_{10} , and c_{11} appear in the return-to-isotropy and dissipation terms of the third-order moments. Previous models have inflated the values of these constants to help control unrealistically large third-order moments and its associated effect on model stability. Large values for these constants were found to be unnecessary with the current model.

c_1	c_2	c_4	c_5	c_6	c_7	c_8	c_{10}	c_{11}
0.5	0.5	4.5	0.0	4.0	0.6	3.0	$2c_2$	0.4

Table 2.6 Constants used in the parameterizations

2.7 Parameterization of the fourth-order moments

At this point, the system is closed except for parameterizing the fourth-order moments and buoyancy terms. Many authors have assumed that the fourth-order moments have a joint Gaussian distribution allowing the fourth-order moments to be parameterized as $\overline{a'b'c'd'} = \overline{a'b'} * \overline{c'd'} + \overline{a'c'} * \overline{b'd'} + \overline{a'd'} * \overline{b'c'}$ (André et al. 1978; Canuto et al. 1994; Canuto 1992; Bougeault 1981b; Zeman and Lumley 1976). This assumption leads to unphysical and destabilizing values of the third-order moments, causing many authors to adopt the “clipping approximation” realizability constraint (André et al. 1976a,b; André et al. 1978) or another form of damping unrealistic growth of the third-order moments. In addition, Moeng and Randall (1984) discovered “spurious oscillations” in their simulations of the boundary layer with a third-order closure turbulence model and found them to be associated with the mean gradient terms in the third-order moment equations, even with the use of the clipping approximation and other damping terms. CEA2005 developed a new parameterization for the fourth-order moments that includes nonzero fourth-order cumulants based on large-eddy simulation results. Use of this new parameterization has been shown to obviate the use of the clipping approximation and to avoid the spurious oscillations associated with the mean gradients in the third-order moment equations. CEA2005’s procedure is outlined here, but as in the rest of the model, is extended to include the moist conservative variables.

The fourth-order moment closure of CEA2005 splits the fourth-order moments into a component modeled by the quasi-normal approximation (QN) and a nonzero cumulant (NC) component that is parameterized from large-eddy simulation data, e.g.

$$\begin{aligned}
\frac{\overline{\partial a'b'c'd'}}{\partial z} &= \left. \frac{\partial \overline{a'b'c'd'}}{\partial z} \right|_{QN} + \left. \frac{\partial \overline{a'b'c'd'}}{\partial z} \right|_{NC} \\
&= \frac{\partial}{\partial z} (\overline{a'b' * c'd'} + \overline{a'c' * b'd'} + \overline{a'd' * b'c'}) + \left. \frac{\partial \overline{a'b'c'd'}}{\partial z} \right|_{NC}
\end{aligned} \tag{2.37}$$

The quasi-normal approximations for the fourth-order moments in equations (2.27)-(2.36) are listed in Table 2.7 for reference, although only the vertical dimension is listed.

From equations (2.27) – (2.36), the dynamic equations for the third-order moments can be described in the following way:

$$\begin{aligned}
TOM \text{ tendency} &= (\text{mean gradient production terms}) + (\text{buoyancy terms}) \\
&\quad + (\text{pressure correlation terms}) + (SOM \text{ gradient production terms}) \\
&\quad + (\text{dissipation terms}) + (FOM \text{ terms})
\end{aligned} \tag{2.38}$$

Using the fourth-order moment closure of CEA2005, the (*FOM* terms) are split into two terms according to Equation (2.37), a QN part and a NC part. If one assumes stationarity and neglects the time tendency of the TOMs, one can algebraically solve for the NC part of the fourth-order moments:

$$\begin{aligned}
FOM_{NC} &= (\text{mean gradient production terms}) + (\text{buoyancy terms}) \\
&\quad + (\text{pressure correlation terms}) + (SOM \text{ gradient production terms}) \\
&\quad + (\text{dissipation terms}) + FOM_{QN}
\end{aligned} \tag{2.39}$$

The first set of terms on the right hand side of equations (2.40) – (2.49) show the results of this algebraic manipulation. The equations are reduced to the vertical dimension and parameterizations for the pressure correlation, dissipation, and QN terms from Tables 2.3, 2.5, and 2.7 have been substituted for the exact terms from equations (2.27) – (2.36). The second set of terms on the right-hand side of equations (2.40) – (2.49) show how the NC terms are parameterized according to CEA2005. The vertical derivatives of nonzero cumulants are assumed to be linear combinations of the third-order moments with tunable

coefficients. The terms with tunable coefficients labeled with p 's combine with the return-to-isotropy portion of the pressure correlations and dissipation parameterizations to damp the growth of the third-order moments.

Equation	Term	Quasi-normal fourth-order moment vertical derivative
2.27	$\left. \frac{\partial \overline{w'u_i' u_i' u_k'}}{\partial z} \right _{QN}$	$\overline{w'u_i'} \frac{\partial \overline{u_i' u_k'}}{\partial z} + \overline{u_i' u_k'} \frac{\partial \overline{w'u_i'}}{\partial z} + \overline{w'u_i'} \frac{\partial \overline{u_i' u_k'}}{\partial z} + \overline{u_i' u_k'} \frac{\partial \overline{w'u_i'}}{\partial z} + \overline{w'u_k'} \frac{\partial \overline{u_i' u_i'}}{\partial z} + \overline{u_i' u_i'} \frac{\partial \overline{w'u_k'}}{\partial z}$
2.28	$\left. \frac{\partial \overline{w'u_i' u_i' \theta_i'}}{\partial z} \right _{QN}$	$\overline{w'u_i'} \frac{\partial \overline{u_i' \theta_i'}}{\partial z} + \overline{u_i' \theta_i'} \frac{\partial \overline{w'u_i'}}{\partial z} + \overline{w'u_i'} \frac{\partial \overline{u_i' \theta_i'}}{\partial z} + \overline{u_i' \theta_i'} \frac{\partial \overline{w'u_i'}}{\partial z} + \overline{w'\theta_i'} \frac{\partial \overline{u_i' u_i'}}{\partial z} + \overline{u_i' u_i'} \frac{\partial \overline{w'\theta_i'}}{\partial z}$
2.29	$\left. \frac{\partial \overline{w'u_i' u_i' q_i'} \right _{QN}$	$\overline{w'u_i'} \frac{\partial \overline{u_i' q_i'}}{\partial z} + \overline{u_i' q_i'} \frac{\partial \overline{w'u_i'}}{\partial z} + \overline{w'u_i'} \frac{\partial \overline{u_i' q_i'}}{\partial z} + \overline{u_i' q_i'} \frac{\partial \overline{w'u_i'}}{\partial z} + \overline{w'q_i'} \frac{\partial \overline{u_i' u_i'}}{\partial z} + \overline{u_i' u_i'} \frac{\partial \overline{w'q_i'}}{\partial z}$
2.30	$\left. \frac{\partial \overline{w'u_i' \theta_i'^2} \right _{QN}$	$\overline{w'u_i'} \frac{\partial \overline{\theta_i'^2}}{\partial z} + \overline{\theta_i'^2} \frac{\partial \overline{w'u_i'}}{\partial z} + 2\overline{w'\theta_i'} \frac{\partial \overline{u_i' \theta_i'}}{\partial z} + 2\overline{u_i' \theta_i'} \frac{\partial \overline{w'\theta_i'}}{\partial z}$
2.31	$\left. \frac{\partial \overline{w'u_i' q_i'^2} \right _{QN}$	$\overline{w'u_i'} \frac{\partial \overline{q_i'^2}}{\partial z} + \overline{q_i'^2} \frac{\partial \overline{w'u_i'}}{\partial z} + 2\overline{w'q_i'} \frac{\partial \overline{u_i' q_i'}}{\partial z} + 2\overline{u_i' q_i'} \frac{\partial \overline{w'q_i'}}{\partial z}$
2.32	$\left. \frac{\partial \overline{w'u_i' \theta_i' q_i'} \right _{QN}$	$\overline{w'u_i'} \frac{\partial \overline{\theta_i' q_i'}}{\partial z} + \overline{\theta_i' q_i'} \frac{\partial \overline{w'u_i'}}{\partial z} + \overline{w'\theta_i'} \frac{\partial \overline{u_i' q_i'}}{\partial z} + \overline{u_i' q_i'} \frac{\partial \overline{w'\theta_i'}}{\partial z} + \overline{w'q_i'} \frac{\partial \overline{u_i' \theta_i'}}{\partial z} + \overline{u_i' \theta_i'} \frac{\partial \overline{w'q_i'}}{\partial z}$
2.33	$\left. \frac{\partial \overline{w'\theta_i'^3} \right _{QN}$	$3\overline{w'\theta_i'} \frac{\partial \overline{\theta_i'^2}}{\partial z} + 3\overline{\theta_i'^2} \frac{\partial \overline{w'\theta_i'}}{\partial z}$
2.34	$\left. \frac{\partial \overline{w'q_i'^3} \right _{QN}$	$3\overline{w'q_i'} \frac{\partial \overline{q_i'^2}}{\partial z} + 3\overline{q_i'^2} \frac{\partial \overline{w'q_i'}}{\partial z}$
2.35	$\left. \frac{\partial \overline{w'\theta_i'^2 q_i'} \right _{QN}$	$\overline{w'q_i'} \frac{\partial \overline{\theta_i'^2}}{\partial z} + \overline{\theta_i'^2} \frac{\partial \overline{w'q_i'}}{\partial z} + 2\overline{w'\theta_i'} \frac{\partial \overline{\theta_i' q_i'}}{\partial z} + 2\overline{\theta_i' q_i'} \frac{\partial \overline{w'\theta_i'}}{\partial z}$
2.36	$\left. \frac{\partial \overline{w'\theta_i' q_i'^2} \right _{QN}$	$\overline{w'\theta_i'} \frac{\partial \overline{q_i'^2}}{\partial z} + \overline{q_i'^2} \frac{\partial \overline{w'\theta_i'}}{\partial z} + 2\overline{w'q_i'} \frac{\partial \overline{\theta_i' q_i'}}{\partial z} + 2\overline{\theta_i' q_i'} \frac{\partial \overline{w'q_i'}}{\partial z}$

Table 2.7 Quasi-normal components of fourth-order moment vertical derivatives

(Note: Equations (2.41) and (2.42) should contain a term with a coefficient of

$\left(\frac{c_8}{3} + c_9 - \frac{c_{10}}{3}\right)$, but CEA2005 point out that for realizability, this coefficient must

evaluate to zero. Using the values of c_8 and c_{10} in Table 2.6, to satisfy realizability the

value of c_9 must be $-\frac{2}{3}$. For this reason, this term has been left out.)

$$\begin{aligned}
\left. \frac{\overline{\partial w' u'_i u'_k}}{\partial z} \right|_{NC} &= -\overline{w' u'_i} \frac{\overline{\partial u'_i u'_k}}{\partial z} - \overline{w' u'_l} \frac{\overline{\partial u'_i u'_k}}{\partial z} - \overline{w' u'_k} \frac{\overline{\partial u'_i u'_l}}{\partial z} - \frac{c_8}{\tau_1} \overline{u'_i u'_l u'_k} \\
&\quad + \lambda \left(\overline{u'_i u'_l \theta'_v} \delta_{3k} + \overline{u'_i u'_k \theta'_v} \delta_{3l} + \overline{u'_l u'_k \theta'_v} \delta_{3i} \right) \\
&\quad - \overline{w' u'_i u'_l} \frac{\overline{\partial u'_k}}{\partial z} - \overline{w' u'_l u'_k} \frac{\overline{\partial u'_i}}{\partial z} - \overline{w' u'_i u'_k} \frac{\overline{\partial u'_l}}{\partial z} \\
&\approx \frac{P_n}{\tau_1} \overline{u'_i u'_l u'_k} - d_m \overline{w' u'_i u'_l} \frac{\overline{\partial u'_k}}{\partial z} - d_m \overline{w' u'_l u'_k} \frac{\overline{\partial u'_i}}{\partial z} - d_m \overline{w' u'_i u'_k} \frac{\overline{\partial u'_l}}{\partial z}
\end{aligned} \tag{2.40}$$

$$\begin{aligned}
\left. \frac{\overline{\partial w' u'_i u'_l \theta'_l}}{\partial z} \right|_{NC} &= -\overline{w' u'_i u'_l} \frac{\overline{\partial \theta'_l}}{\partial z} - \overline{w' u'_i \theta'_l} \frac{\overline{\partial u'_l}}{\partial z} - \overline{w' u'_l \theta'_l} \frac{\overline{\partial u'_i}}{\partial z} - \overline{w' u'_i} \frac{\overline{\partial u'_l \theta'_l}}{\partial z} \\
&\quad - \overline{w' u'_l} \frac{\overline{\partial u'_i \theta'_l}}{\partial z} - \overline{w' \theta'_l} \frac{\overline{\partial u'_i u'_l}}{\partial z} - \frac{c_8}{\tau_1} \overline{u'_i u'_l \theta'_l} + \lambda \left(\overline{u'_l \theta'_l \theta'_v} \delta_{3i} + \overline{u'_i \theta'_l \theta'_v} \delta_{3l} \right) \\
&\approx \frac{P_n}{\tau_1} \overline{u'_i u'_l \theta'_l} - d_m \overline{w' u'_i u'_l} \frac{\overline{\partial \theta'_l}}{\partial z} - d_m \overline{w' u'_i \theta'_l} \frac{\overline{\partial u'_l}}{\partial z} - d_m \overline{w' u'_l \theta'_l} \frac{\overline{\partial u'_i}}{\partial z}
\end{aligned} \tag{2.41}$$

$$\begin{aligned}
\left. \frac{\overline{\partial w' u'_i u'_l q'_t}}{\partial z} \right|_{NC} &= -\overline{w' u'_i u'_l} \frac{\overline{\partial q'_t}}{\partial z} - \overline{w' u'_i q'_t} \frac{\overline{\partial u'_l}}{\partial z} - \overline{w' u'_l q'_t} \frac{\overline{\partial u'_i}}{\partial z} - \overline{w' u'_i} \frac{\overline{\partial u'_l q'_t}}{\partial z} \\
&\quad - \overline{w' u'_l} \frac{\overline{\partial u'_i q'_t}}{\partial z} - \overline{w' q'_t} \frac{\overline{\partial u'_i u'_l}}{\partial z} - \frac{c_8}{\tau_1} \overline{u'_i u'_l q'_t} + \lambda \left(\overline{u'_l q'_t \theta'_v} \delta_{3i} + \overline{u'_i q'_t \theta'_v} \delta_{3l} \right) \\
&\approx \frac{P_n}{\tau_1} \overline{u'_i u'_l q'_t} - d_m \overline{w' u'_i u'_l} \frac{\overline{\partial q'_t}}{\partial z} - d_m \overline{w' u'_i q'_t} \frac{\overline{\partial u'_l}}{\partial z} - d_m \overline{w' u'_l q'_t} \frac{\overline{\partial u'_i}}{\partial z}
\end{aligned} \tag{2.42}$$

$$\begin{aligned}
\left. \frac{\partial \overline{w'u'_i \theta_i'^2}}{\partial z} \right|_{NC} &= -\overline{2w'u'_i \theta_i'} \frac{\partial \overline{\theta_i}}{\partial z} - \overline{w'\theta_i'^2} \frac{\partial \overline{u_i}}{\partial z} - \overline{2w'\theta_i'} \frac{\partial \overline{u_i \theta_i'}}{\partial z} - \overline{w'u_i'} \frac{\partial \overline{\theta_i'^2}}{\partial z} \\
&\quad - \frac{c_8}{\tau_1} \overline{u_i' \theta_i'^2} + \overline{\lambda \theta_i'^2 \theta_v' \delta_{3i}} \\
&\approx \frac{p_n}{\tau_1} \overline{u_i' \theta_i'^2} - \overline{d_m w'u_i' \theta_i'} \frac{\partial \overline{\theta_i}}{\partial z} - \overline{d_m w'\theta_i'^2} \frac{\partial \overline{u_i}}{\partial z}
\end{aligned} \tag{2.43}$$

$$\begin{aligned}
\left. \frac{\partial \overline{w'u'_i q_i'^2}}{\partial z} \right|_{NC} &= -\overline{2w'u'_i q_i'} \frac{\partial \overline{q_i}}{\partial z} - \overline{w'q_i'^2} \frac{\partial \overline{u_i}}{\partial z} - \overline{2w'q_i'} \frac{\partial \overline{u_i q_i'}}{\partial z} - \overline{w'u_i'} \frac{\partial \overline{q_i'^2}}{\partial z} \\
&\quad - \frac{c_8}{\tau_1} \overline{u_i' q_i'^2} + \overline{\lambda q_i'^2 \theta_v' \delta_{3i}} \\
&\approx \frac{p_n}{\tau_1} \overline{u_i' q_i'^2} - \overline{d_m w'u_i' q_i'} \frac{\partial \overline{q_i}}{\partial z} - \overline{d_m w'q_i'^2} \frac{\partial \overline{u_i}}{\partial z}
\end{aligned} \tag{2.44}$$

$$\begin{aligned}
\left. \frac{\partial \overline{w'u'_i \theta_i' q_i'}}{\partial z} \right|_{NC} &= -\overline{w'u_i' \theta_i'} \frac{\partial \overline{q_i}}{\partial z} - \overline{w'u_i' q_i'} \frac{\partial \overline{\theta_i}}{\partial z} - \overline{w'\theta_i' q_i'} \frac{\partial \overline{u_i}}{\partial z} - \overline{w'\theta_i'} \frac{\partial \overline{u_i' q_i'}}{\partial z} \\
&\quad - \overline{w'u_i'} \frac{\partial \overline{\theta_i' q_i'}}{\partial z} - \overline{w'q_i'} \frac{\partial \overline{u_i' \theta_i'}}{\partial z} - \frac{c_8}{\tau_1} \overline{u_i' \theta_i' q_i'} + \overline{\lambda \theta_i' q_i' \theta_v' \delta_{3i}} \\
&\approx \frac{p_n}{\tau_1} \overline{u_i' \theta_i' q_i'} - \overline{d_m w'u_i' \theta_i'} \frac{\partial \overline{q_i}}{\partial z} - \overline{d_m w'u_i' q_i'} \frac{\partial \overline{\theta_i}}{\partial z} - \overline{d_m w'\theta_i' q_i'} \frac{\partial \overline{u_i}}{\partial z}
\end{aligned} \tag{2.45}$$

$$\begin{aligned}
\left. \frac{\partial \overline{w'\theta_i'^3}}{\partial z} \right|_{NC} &= -\overline{3w'\theta_i'^2} \frac{\partial \overline{\theta_i}}{\partial z} - \overline{3w'\theta_i'} \frac{\partial \overline{\theta_i'^2}}{\partial z} - \frac{c_{10}}{\tau_1} \overline{\theta_i'^3} \\
&\approx \frac{p_n}{\tau_1} \overline{\theta_i'^3} - \overline{d_m w'\theta_i'^2} \frac{\partial \overline{\theta_i}}{\partial z}
\end{aligned} \tag{2.46}$$

$$\begin{aligned}
\left. \frac{\partial \overline{w'q_i'^3}}{\partial z} \right|_{NC} &= -\overline{3w'q_i'^2} \frac{\partial \overline{q_i}}{\partial z} - \overline{3w'q_i'} \frac{\partial \overline{q_i'^2}}{\partial z} - \frac{c_{10}}{\tau_1} \overline{q_i'^3} \\
&\approx \frac{p_n}{\tau_1} \overline{q_i'^3} - \overline{d_m w'q_i'^2} \frac{\partial \overline{q_i}}{\partial z}
\end{aligned} \tag{2.47}$$

$$\begin{aligned}
\left. \frac{\overline{\partial w' \theta_i'^2 q_i'}}{\partial z} \right|_{NC} &= -\overline{2w' \theta_i' q_i'} \frac{\partial \bar{\theta}_i}{\partial z} - \overline{w' \theta_i'^2} \frac{\partial \bar{q}_i}{\partial z} - \overline{2w' \theta_i'} \frac{\partial \overline{\theta_i' q_i'}}{\partial z} - \overline{w' q_i'} \frac{\partial \overline{\theta_i'^2}}{\partial z} \\
&\quad - \frac{c_{10}}{\tau_1} \overline{\theta_i'^2 q_i'} \\
&\approx \frac{p_n}{\tau_1} \overline{\theta_i'^2 q_i'} - d_m \overline{w' \theta_i' q_i'} \frac{\partial \bar{\theta}_i}{\partial z} - d_m \overline{w' \theta_i'^2} \frac{\partial \bar{q}_i}{\partial z}
\end{aligned} \tag{2.48}$$

$$\begin{aligned}
\left. \frac{\overline{\partial w' \theta_i' q_i'^2}}{\partial z} \right|_{NC} &= -\overline{w' q_i'^2} \frac{\partial \bar{\theta}_i}{\partial z} - \overline{2w' \theta_i' q_i'} \frac{\partial \bar{q}_i}{\partial z} - \overline{2w' q_i'} \frac{\partial \overline{\theta_i' q_i'}}{\partial z} - \overline{w' \theta_i'} \frac{\partial \overline{q_i'^2}}{\partial z} \\
&\quad - \frac{c_{10}}{\tau_1} \overline{\theta_i' q_i'^2} \\
&\approx \frac{p_n}{\tau_1} \overline{\theta_i' q_i'^2} - d_m \overline{w' q_i'^2} \frac{\partial \bar{\theta}_i}{\partial z} - d_m \overline{w' \theta_i' q_i'} \frac{\partial \bar{q}_i}{\partial z}
\end{aligned} \tag{2.49}$$

The specification of the p_n and d_m coefficients are all that remain for closed fourth-order moments. CEA2005 determine these coefficients for six fourth-order moments by best-fit analysis from large-eddy simulation data. Perhaps coincidentally, the best fit for the p_n and d_m coefficients eliminates the mean gradient terms in the third-order moment equations. CEA2005 point out that mean gradient terms in the third-order moment equations have been assumed to be zero before by Zeman and Lumley (1976), but these authors rationalized this simplification by arguing that these terms are small. CEA2005 present an argument using LES data that shows the mean gradient terms in the third-order moment equations are effectively canceled out by the non-zero cumulant portion of the fourth-order moments. Regardless, the elimination of the mean gradient terms constitutes a welcome simplification and solves the “spurious oscillation” problem discovered by Moeng and Randall (1984).

In the current model, p_n and d_m need to be determined for 28 fourth-order moments. I postulate that the appropriate p_n coefficients for the fourth-order moments not covered in CEA2005 can be determined by analogy; e.g. the p_n for $\overline{w'^2 q_t'^2}$ will be the same as the p_n for $\overline{w'^2 \theta'^2}$, the p_n for $\overline{w'^3 q_t'}$ will be the same as the p_n for $\overline{w'^3 \theta'}$, and so on, since the equations for each pair are derived in the same way with analogous matching terms. As with other constants, the p_n are left as free parameters in the model so that they may be easily changed if future research warrants. The d_m for the 28 fourth-order moments are determined in the same way, and in each fourth-order moment equation, the choice of d_m eliminates any dependence on mean gradient terms. Specific values for p_n and d_m are given in Appendix A.

2.8 Diagnostic third-order moments

With the closure of the fourth-order moments, they may be substituted back into the third-order moment equations. Following Zeman and Lumley (1976), Canuto et al. (1994), and Cheng et al. (2005), stationarity will be assumed, leaving diagnostic relations for the third-order moments. This reduces computational complexity by eliminating the need to time-step and, as shown by the authors above, produces satisfactory simulations of the convective boundary layer. The diagnostic third-order relations with the pressure correlation, dissipation, and fourth-order moment parameterizations included are given by

$$\begin{aligned} \frac{c_8 + p_n}{\tau_1} \overline{u'_i u'_i u'_k} &= -\overline{w' u'_i} \frac{\partial \overline{u'_i u'_k}}{\partial z} - \overline{w' u'_l} \frac{\partial \overline{u'_i u'_k}}{\partial z} - \overline{w' u'_k} \frac{\partial \overline{u'_i u'_l}}{\partial z} \\ &+ \lambda \left(\overline{u'_i u'_l \theta'_v} \delta_{3k} + \overline{u'_i u'_k \theta'_v} \delta_{3l} + \overline{u'_i u'_k \theta'_v} \delta_{3i} \right) \end{aligned} \quad (2.50)$$

$$\frac{c_8 + p_n}{\tau_1} \overline{u'_i u'_i \theta'_l} = -\overline{w' u'_i} \frac{\partial \overline{u'_i \theta'_l}}{\partial z} - \overline{w' u'_l} \frac{\partial \overline{u'_i \theta'_l}}{\partial z} - \overline{w' \theta'_l} \frac{\partial \overline{u'_i u'_l}}{\partial z} + \lambda \left(\overline{u'_i \theta'_l \theta'_v} \delta_{3l} + \overline{u'_l \theta'_l \theta'_v} \delta_{3i} \right) \quad (2.51)$$

$$\frac{c_8 + p_n}{\tau_1} \overline{u'_i u'_i q'_l} = -\overline{w' u'_i} \frac{\partial \overline{u'_i q'_l}}{\partial z} - \overline{w' u'_l} \frac{\partial \overline{u'_i q'_l}}{\partial z} - \overline{w' q'_l} \frac{\partial \overline{u'_i u'_l}}{\partial z} + \lambda \left(\overline{u'_i q'_l \theta'_v} \delta_{3l} + \overline{u'_l q'_l \theta'_v} \delta_{3i} \right) \quad (2.52)$$

$$\frac{c_8 + p_n}{\tau_1} \overline{u'_i \theta'^2_l} = -\overline{w' u'_i} \frac{\partial \overline{\theta'^2_l}}{\partial z} - 2\overline{w' \theta'_l} \frac{\partial \overline{u'_i \theta'_l}}{\partial z} + \lambda \overline{\theta'^2_l \theta'_v} \delta_{3l} \quad (2.53)$$

$$\frac{c_8 + p_n}{\tau_1} \overline{u'_i q'^2_l} = -\overline{w' u'_i} \frac{\partial \overline{q'^2_l}}{\partial z} - 2\overline{w' q'_l} \frac{\partial \overline{u'_i q'_l}}{\partial z} + \lambda \overline{q'^2_l \theta'_v} \delta_{3l} \quad (2.54)$$

$$\frac{c_8 + p_n}{\tau_1} \overline{u'_i \theta'_l q'_l} = -\overline{w' u'_i} \frac{\partial \overline{\theta'_l q'_l}}{\partial z} - \overline{w' \theta'_l} \frac{\partial \overline{u'_i q'_l}}{\partial z} - \overline{w' q'_l} \frac{\partial \overline{u'_i \theta'_l}}{\partial z} + \lambda \overline{\theta'_l q'_l \theta'_v} \delta_{3l} \quad (2.55)$$

$$\frac{c_{10} + p_n}{\tau_1} \overline{\theta'^3_l} = -3\overline{w' \theta'_l} \frac{\partial \overline{\theta'^2_l}}{\partial z} \quad (2.56)$$

$$\frac{c_{10} + p_n}{\tau_1} \overline{q'^3_l} = -3\overline{w' q'_l} \frac{\partial \overline{q'^2_l}}{\partial z} \quad (2.57)$$

$$\frac{c_{10} + p_n}{\tau_1} \overline{\theta'^2_l q'_l} = -2\overline{w' \theta'_l} \frac{\partial \overline{\theta'_l q'_l}}{\partial z} - \overline{w' q'_l} \frac{\partial \overline{\theta'^2_l}}{\partial z} \quad (2.58)$$

$$\frac{c_{10} + p_n}{\tau_1} \overline{\theta'_l q'^2_l} = -2\overline{w' q'_l} \frac{\partial \overline{\theta'_l q'_l}}{\partial z} - \overline{w' \theta'_l} \frac{\partial \overline{q'^2_l}}{\partial z} \quad (2.59)$$

Even with elimination of the mean gradient terms due to the specification of the d_m constants, equations (2.50) – (2.59) are not yet a closed set since the buoyancy terms

contain third-order moments. They do, however, represent a system of 28 equations with 28 unknowns, and it is possible to explicitly solve for the third-order moments in one of two ways. First, one can solve a system of linear equations for the 28 unknowns each time step within the model. Alternatively, one can solve the system symbolically as Canuto et al. (1994) and CEA2005 have done using a symbolic algebra program. The latter method has some important advantages. First, the latter method is more computationally simple and efficient. The system needs only to be solved once rather than every time step. Second, it becomes trivial to simplify the diagnostic third-order moments. Canuto et al. (1994) point out that the third-order moments can be reverted to simple down-gradient diffusion by setting a select few coefficients to zero. Due to these advantages, the latter method is employed. Appendix A outlines the exact procedure, and the explicit algebraic third-order moments are given in equations (A29) – (A56). Each third-order moment becomes a linear combination of the vertical derivatives of the second-order moments with extensive coefficients. These coefficients are given in Table A4 in Appendix A.

2.9 Parameterization of the buoyancy terms

The final closure involves the determination of the buoyancy terms in both the second-order moment equations and the third-order moment relations. As mentioned in the works of Bougeault (1981a) and Golaz et al. (2002a) and shown in Appendix B, the virtual potential temperature, θ_v , may be expressed in terms of moist conservative variables as

$$\theta_v = \theta_l + \frac{(1 - \varepsilon_0)}{\varepsilon_0} \theta_0 q_t + \left[\frac{L_v}{c_p} \left(\frac{p_0}{p} \right)^\kappa - \frac{\theta_0}{\varepsilon_0} \right] q_t \quad (2.60)$$

where ε_0 is the ratio of the dry air gas constant to the water vapor gas constant, and θ_0 is a reference potential temperature. This allows all buoyancy terms that need to be parameterized to be written in general form as

$$\overline{\chi' \theta'_v} = \overline{\chi' \theta'_l} + C_{T_0} \overline{\chi' q'_t} + D(z) \overline{\chi' q'_l}, \quad (2.61)$$

where χ' represents any of w' , θ'_l , q'_t , w'^2 , u'^2 , $w' \theta'_l$, $w' q'_t$, θ'^2_l , q'^2_t , $\theta'_l q'_t$,

$C_{T_0} = \frac{(1 - \varepsilon_0)}{\varepsilon_0} \theta_0$, and $D(z) = \left[\frac{L_v}{c_p} \left(\frac{p_0}{p(z)} \right)^\kappa - \frac{\theta_0}{\varepsilon} \right]$. This effectively shifts the closure to

finding liquid water correlations, which may be accomplished from a subgrid condensation scheme discussed in Section 2.11.2.

2.10 Turbulent timescales

Turbulent timescales play a key role in higher-order closure turbulence models due to their influence in the dissipation and pressure-correlation terms in both the second- and third-order moments. The importance of their parameterization is even greater in the current model because of the use of diagnostic third-order moments. The turbulent time scale appears in each coefficient of every third-order moment relation and therefore helps to determine the magnitudes of all third-order moments.

A common way to model turbulent, or dissipation, timescales is

$$\tau = \frac{L}{\sqrt{e}} \quad (2.62)$$

where L is the “eddy length scale” or the “dissipation length scale.” Parameterizations for this length scale vary greatly in the literature, and are often chosen to best match a particular turbulence scheme to observations (Stull 1998, Lenderink and Holtslag 2004). Further, their formulations have often been dependent on the type of boundary layer that the author’s model is intended to simulate. Some work well in buoyancy-driven boundary layers and others work well for shear-driven boundary layers. The formulation of the length scale given in CEA2005 is shown to work well in clear buoyancy-driven mixed layers. It is calculated as an average of three length scales: one based on the depth of the mixed layer, one applicable to the surface layer, and one that is determined by local buoyancy. Its calculation loosely follows the work of Nakanishi (2001), wherein the constants used to determine the surface length scale are dependent on tuning for various boundary layer regimes.

While the eddy length scale formulation from CEA2005 works well for dry convective boundary layer cases, its use in testing led to instability for cloudy boundary layer cases, especially for boundary layers capped by strong inversions like those found in stratocumulus-topped boundary layer regimes. Rather than continuing the practice of tuning the eddy length scale to fit observations, or calculating it by averaging several other length scales designed for various scenarios, it is appropriate to seek a length scale based on simple physical properties that is general in nature and will work well in any given boundary layer regime. Bougeault and André (1986) developed a new eddy length scale that has shown promise in meeting those criteria. It has been used extensively in turbulence parameterizations to model many different boundary layer regimes, including

clear convective cases, shallow cumulus cases, stratocumulus cases, broken cumulus cases, and even orography-induced turbulence above the boundary layer (e.g., Bougeault and André 1986, Bougeault and Lacarrere 1989, Bechtold et al. 1992, Cuxart et al. 2000, and Golaz et al. 2002a).

The length scale parameterization of Bougeault and André (1986) is formed from an average of two length scales, L_{up} and L_{down} that are defined by

$$\int_z^{z+L_{up}} \frac{g}{\theta_{v_0}} [\bar{\theta}_v(z') - \bar{\theta}_v(z)] dz' = \bar{e}(z) \quad (2.63)$$

and

$$\int_{z-L_{down}}^z \frac{g}{\theta_{v_0}} [\bar{\theta}_v(z) - \bar{\theta}_v(z')] dz' = \bar{e}(z). \quad (2.64)$$

The length scales can be interpreted as the “upward free path” and the “downward free path,” respectively (Bougeault and André 1986). The upward (downward) free path of a given level is determined by a parcel originating at that level given an initial kinetic energy equal to the mean turbulence kinetic energy at that level. The parcel may travel upward (downward) until the accumulated buoyancy accelerations exhaust the parcel’s kinetic energy. Figure 2.1 is taken from Cuxart et al. 2000 and illustrates the concept. The averaging operation used to combine L_{up} and L_{down} is important and has caused debate within the literature. Bougeault and André (1986) initially used a harmonic average

$$L = 2 \left(\frac{1}{L_{up}} + \frac{1}{L_{down}} \right)^{-1},$$

but Bougeault and Lacarrere (1989), Cuxart et al. (2000), and

Golaz et al. (2002a), used the geometric average $L = \sqrt{L_{up}L_{down}}$. Since shorter eddy length scales create more turbulence dissipation and the geometric average is smaller than

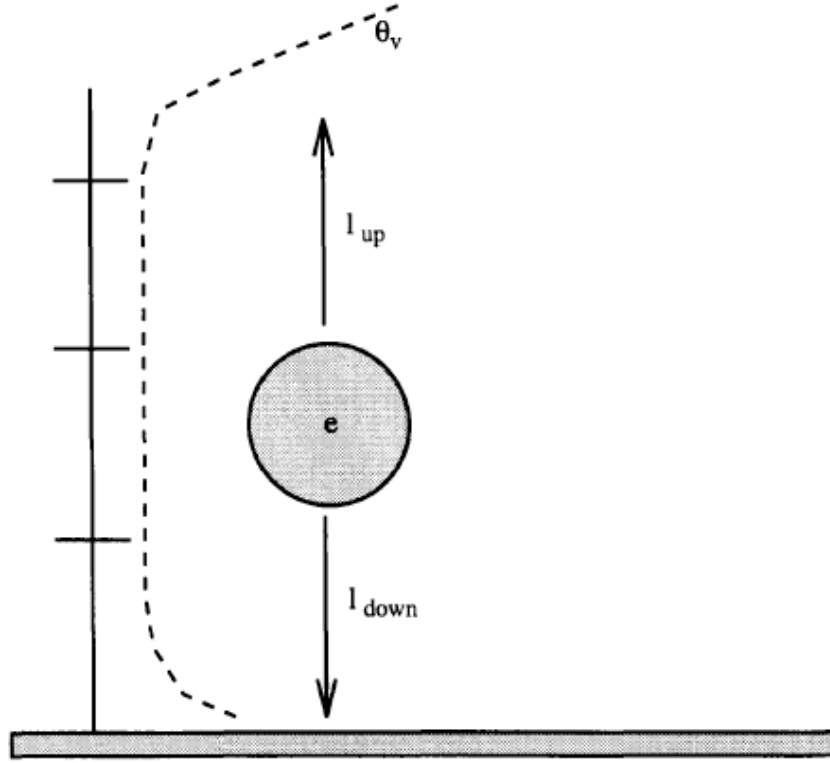


Figure 2.1 Upward and downward free path illustration {from Cuxart et al. (2000)}

the harmonic average, using the geometric average results in more turbulence dissipation. The geometric average is used in the current study.

Cuxart et al (2000) recognized the need to include lateral entrainment into the parcel, but did not modify the length scale to include it since it was deemed less important for the cases they were studying. Golaz et al. (2002a) found that for cumulus regimes, the omission of lateral entrainment caused the upward free path to be underestimated. To improve this deficiency, they included the effects of lateral entrainment by modifying L_{up} in the following way:

$$\int_z^{z+L_{up}} \frac{g}{\theta_{v_0}} [\overline{\theta_v}(z') - \overline{\theta_{v,parcel}}(z')] dz' = \bar{e}(z) \quad (2.65)$$

The virtual potential temperature of the parcel changes due to lateral entrainment at each level. They assumed a constant fractional entrainment rate of

$$\mu = \frac{1}{M} \frac{dM}{dz} = 6.0 \times 10^{-4} \text{ m}^{-1}. \text{ The change in the virtual potential temperature with height}$$

is then given by $\frac{d\overline{\theta_{v,parcel}}}{dz} = -\mu(\overline{\theta_{v,parcel}} - \overline{\theta_v})$. In addition, although this formulation of

the eddy length scale is nonlocal, Golaz et al. (2002a) further modify L_{up} and L_{down} to

better represent the nonlocal nature of cumulus layers. They note that a parcel originating at a certain level above the ground may only ascend a small distance, while a parcel

originating from lower in the column may ascend to greater heights. Likewise, a parcel at

a given level may not descend as far as a parcel that originates above it. To account for

this, the following modification is made to L_{up} and L_{down} . As L_{up} is calculated level by

level from the surface, the maximum level reached by all parcels originating below the current level is recorded, z_{max} . If $z_{max} > z + L_{up}(z)$, then L_{up} is set to $z_{max} - z$. L_{down} is

modified analogously. Both the entrainment modification and the nonlocalizing

procedure are retained in the current study. To prevent instabilities, Golaz et al. (2002a)

restrain the eddy length scale to an interval. A lower limit equal to the vertical grid size

and a 400 m upper limit are used for all length scales except for those involved in the

return-to-isotropy terms of the scalar fluxes. There, an upper limit of 2000 m is used.

The strengths of this formulation for the length scale are many. The original motivation for using this length scale in Bougeault and André (1986) was to eliminate unstable oscillations discovered by Moeng and Randall (1984) that developed near the inversion of stratocumulus-topped boundary layers. That work has shown that the shorter length scales calculated from this formulation near the inversion do, in fact, eliminate

those errors, in addition to being more physically realistic. In addition, the nonlocal nature of the formulation guarantees that physical boundaries, such as inversions and the surface, are properly accounted for. Finally, several authors (e.g., Bougeault and André 1986, Bougeault and Lacarrere 1989, Bechtold et al. 1992, Cuxart et al. 2000) have pointed out that in layers with constant stratifications, this length scale reduces to be proportional to the buoyancy length scale proposed by Deardorff (1980),

$$L = \sqrt{e} \left[\frac{g}{\theta_{v_0}} \frac{\partial \overline{\theta}_v}{\partial z} \right]^{-1/2} .$$

2.11 Subgrid-scale condensation

The traditional approach to determining cloud cover within an atmospheric model is to determine whether condensation occurs on the grid-scale using grid mean variables and traditional microphysics. When using a large grid size as in a general circulation model, however, the assumption that a box several kilometers wide and hundreds of meters tall becomes saturated at once is both physically unfounded and computationally problematic. A better approach was pioneered by Sommeria and Deardorff (1977), hereafter SD77, where condensation is allowed to occur on the subgrid scale. By parameterizing cloud fraction and liquid water on scales smaller than the grid, a smooth transition from a clear grid cell to a cloudy one is made possible. In addition, areas featuring lower cloud fractions like trade-wind or fair-weather cumulus can more properly be represented with such a scheme. In addition to cloud fraction and liquid water, a subgrid-scale condensation scheme is able to diagnose liquid water correlations that are important for buoyancy terms in a higher-order closure model. A discussion of

the cloud fraction and liquid water content is given first, followed by the liquid water correlations.

2.11.1 Cloud fraction and liquid water content

The scheme of SD77 uses a statistical approach to determine cloud fraction and liquid water content. If one considers a large grid cell containing some portion of clouds, variables such as θ_l and q_l may vary considerably within. SD77 assume that the variation in these variables can be represented by a joint-Gaussian distribution. If $\overline{\theta_l}$, $\overline{q_l}$, $\overline{\theta_l'^2}$, $\overline{q_l'^2}$, and $\overline{\theta_l'q_l'}$ are all known, the precise joint-Gaussian distribution is determined. Further, SD77 demonstrate that the saturation specific humidity can be obtained from θ_l , q_l , and p to a good approximation. With this information, it is possible to obtain the cloud fraction by integrating over the part of the probability distribution function (PDF) where values of θ_l and q_l indicate a parcel is saturated. Similarly, the cloud liquid water can be obtained with the use of $q_l = q_l - q_s$. Fig. 2.2, taken from SD77, illustrates the concept, and in general, cloud fraction and cloud liquid water content can be expressed by

$$R = \int_{-\infty}^{\infty} \int_{q_s}^{\infty} G dq_l d\theta_l \quad \text{and} \quad (2.66)$$

$$\overline{q_l} = \int_{-\infty}^{\infty} \int_{q_s}^{\infty} (q_l - q_s) G dq_l d\theta_l \quad (2.67)$$

where G is the joint probability density function for θ_l and q_l .

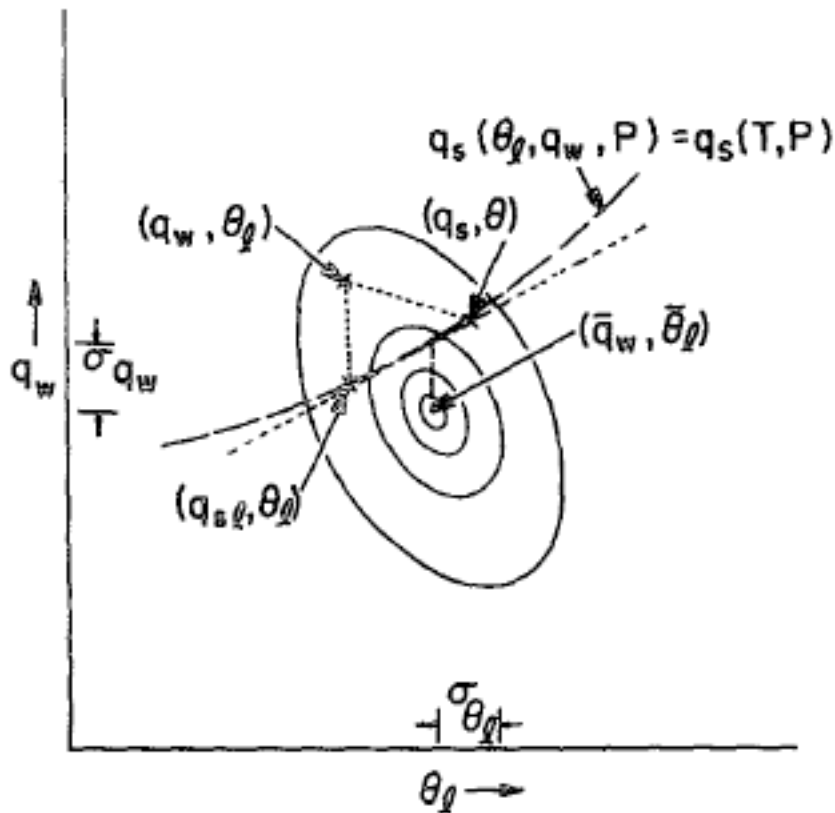


Figure 2.2 - (from SD77, Figure 1) Contours represent the probability of a particular θ_l and q_l pair, given their mean values, variances, and the covariance between them. The long-dashed line represents the actual saturation specific humidity curve, while the short-dashed line represents the approximation given in SD77. Cloud fraction can be computed by integrating this PDF above the saturation specific humidity line.

Subsequent authors have questioned the use of the joint-Gaussian assumption for the PDF of θ_l and q_l . Using a subgrid-scale condensation scheme to model trade-wind cumulus, Bougeault (1981a), hereafter B81a, noted that the tails of the distribution are extremely important for the development for cumulus and that a better PDF to use for this regime is an exponential distribution or a simple positively skewed one. An attempt to generalize to all cloudy regimes was made in Bougeault (1982), where a gamma distribution was utilized to study both cumulus and stratocumulus cases. Tompkins

(2002) reduces the subgrid-scale condensation scheme to defining a PDF for only q_t , arguing that temperature fluctuations are smaller and less important than those of q_t . He then assumes a beta distribution for q_t to calculate cloud fraction, liquid water content, and liquid water correlations. Other authors have extended the subgrid-scale condensation scheme to include fluctuations in vertical velocity as well, and have assumed bimodal distributions (Lewellen and Yoh 1993; Golaz et al. 2002a; Larson et al. 2002).

Given the spread of PDFs used and the apparent inability of one particular PDF to describe all cloudy boundary layers, another approach was taken by Cuijpers and Bechtold (1995), hereafter CB95. They studied boundary layers containing cloud fractions from zero to one using a large eddy simulation with a goal of finding a simple subgrid-scale condensation parameterization for all cloudy boundary layers without assuming a joint PDF for the thermodynamic variables a priori. They found that the cloud fraction and liquid water content could be parameterized by a simple function of the “normalized saturation deficit, Q_1 .” The quantity Q_1 also appears in previous implementations of SD77-type schemes and is given by

$$Q_1 = \frac{\bar{s}}{\sigma_s} \quad (2.68)$$

where $\sigma_s = \sqrt{s'^2}$ is the standard deviation of s ,

$$s = aq_t' - b\theta_t' + c, \quad a = \left(1 + \frac{L_v}{c_p} \frac{\partial \bar{q}_{sl}}{\partial T_t}\right)^{-1}, \quad b = a \left(\frac{\bar{T}}{\bar{\theta}}\right) \frac{\partial \bar{q}_{sl}}{\partial T_t}, \quad c = a(\bar{q}_t - \bar{q}_{sl}),$$

$$\bar{T}_l = \left(\frac{\bar{T}}{\bar{\theta}} \right) \bar{\theta}_l, \quad \bar{q}_{sl} = q_s(\bar{T}_l), \quad \text{and} \quad \frac{\partial \bar{q}_{sl}}{\partial \bar{T}_l} = \frac{\bar{q}_s L_v}{R_v \bar{T}_l^2}. \quad \text{Given this nomenclature, a new variable}$$

is constructed following Mellor (1977a) and Bechtold et al. (1995), $t = \frac{S}{\sigma_s}$, so that the

double integrals for cloud fraction and liquid water content can be converted to single integrals and can be evaluated easier. The integrals become

$$R = \int_0^\infty G(t) dt \quad \text{and} \quad (2.69)$$

$$\frac{\bar{q}_l}{\sigma_x} = \int_0^\infty t G(t) dt. \quad (2.70)$$

Assuming a joint-Gaussian distribution in SD77, the cloud fraction is found to be

$$R = \frac{1}{2} \left[1 + \operatorname{erf} \left(\frac{Q_1}{\sqrt{2}} \right) \right], \quad (2.71)$$

whereas in B81a a simple positively skewed PDF is assumed and cloud fraction is given by a piece-wise function

$$R = \begin{cases} e^{Q_1^{-1}} & Q_1 \leq 1 \\ 1 & Q_1 > 1 \end{cases}. \quad (2.72)$$

The original scheme of SD was found to underestimate cloud fraction for low values of Q_1 including cumulus regimes, but performed well for high values of Q_1 including stratocumulus regimes. The scheme of B81a was found to be well suited for low values of Q_1 , but admittedly inadequate for high values of Q_1 . The scheme of CB95 is given by the simple function

$$R = \max \left\{ 0.0, \min \left[1.0, 0.5 + 0.36 \arctan(1.55 Q_1) \right] \right\} \quad (2.73)$$

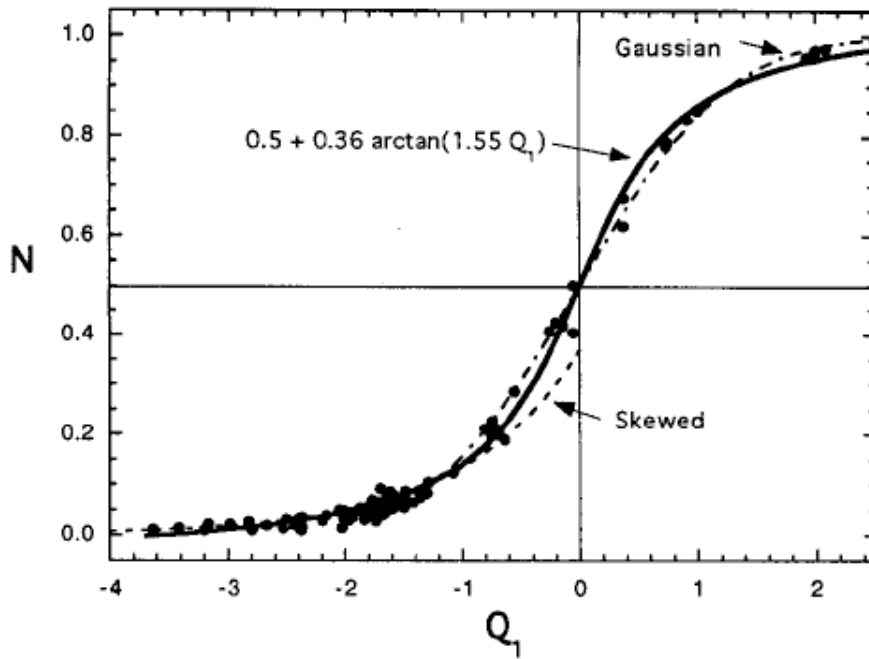


Figure 2.3 Solid line -- CB95; "Gaussian" -- SD; "Skewed" -- Bougeault (1981a) {from Bougeault (1981a), Figure 3}

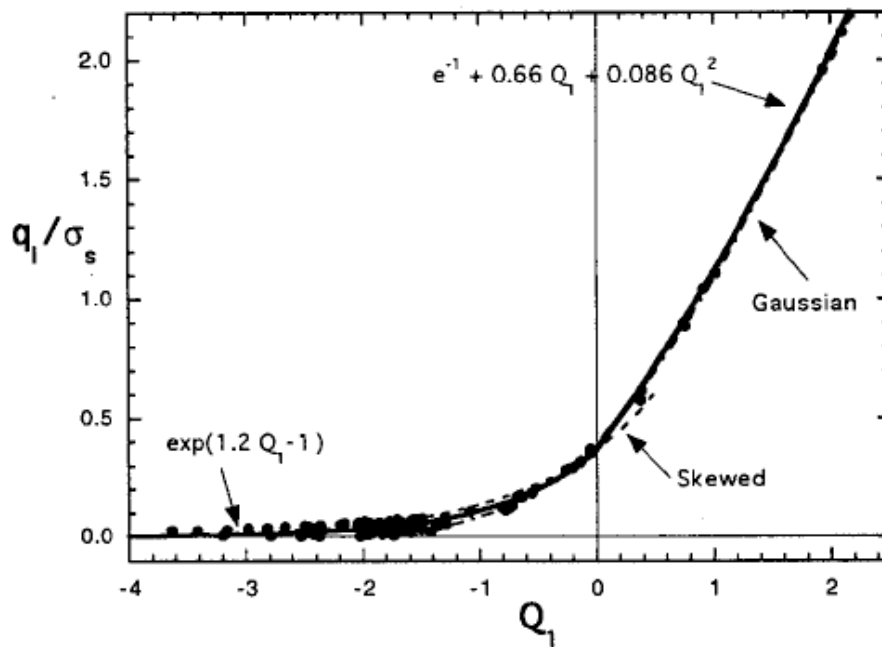


Figure 2.4 As in Figure 2.3 {from Bougeault (1981a), Figure 4}

and is shown to resemble SD77 for high values of Q_1 and B81a for low values of Q_1 (See Figure 2.3). It is therefore found to be a useful general parameterization for cloud fraction.

A similar discussion applies to liquid water content, with the SD77 scheme giving

$$\bar{q}_l = \sigma_s \left(RQ_1 + \frac{e^{-Q_1^2/2}}{\sqrt{2\pi}} \right), \quad (2.74)$$

the B81a scheme giving

$$\bar{q}_l = \sigma_s \begin{cases} e^{Q_1-1} & Q_1 \leq 1 \\ Q_1 & Q_1 > 1 \end{cases}, \quad (2.75)$$

and the scheme of CB95 giving

$$\bar{q}_l = \sigma_s \begin{cases} e^{-1} + 0.66Q_1 + 0.086Q_1^2 & Q_1 < 0 \\ e^{1.2Q_1-1} & Q_1 \geq 0 \end{cases}. \quad (2.76)$$

See Figure 2.4 for plots of the different schemes' liquid water contents. The generality and simplicity of the CB95 scheme make it an attractive one to use, and it has been adopted by many authors (e.g., Bechtold and Siebesma 1998, Lenderink and Holtslag 2004) and is the scheme used in the current model.

Just as it is possible to integrate over the joint PDF to diagnose the liquid water content, it is also possible to integrate over the same PDF to diagnose the amount of liquid water that exists in concentrations over some threshold value. Such a quantity is of interest for the autoconversion process of many microphysics schemes, including the one used in the current model described in Section 2.12. One can define a quantity called “autoconversion-eligible” cloud water as $q_l = (q_t - q_s) - q_{l,THRESHOLD}$ where the threshold value is the cloud water specific humidity above which the autoconversion process

becomes efficient. As with the total liquid water content, this quantity can be diagnosed as in equation (2.67) from the joint PDF of θ_l and q_l using

$$\overline{q_{l,AUTO}} = (\overline{q_l} - \overline{q_s}) - q_{l,THRESHOLD} = \int_{-\infty}^{\infty} \int_{q_s}^{\infty} [(q_l - q_s) - q_{l,THRESHOLD}] G dq_l d\theta_l. \quad (2.77)$$

Using the same logic as for the total liquid water content, one can use the scheme of CB95 to diagnose the autoconversion-eligible liquid water content as

$$\overline{q_{l,AUTO}} = \sigma_s \begin{cases} e^{-1} + 0.66Q_{1,r} + 0.086Q_{1,r}^2 & Q_{1,r} < 0 \\ e^{1.2Q_{1,r} - 1} & Q_{1,r} \geq 0 \end{cases} \quad (2.78)$$

where the normalized saturation deficit, $Q_{1,r}$, has been modified to

$$Q_{1,r} = \frac{a[(\overline{q_l} - \overline{q_{sl}}) - q_{l,THRESHOLD}]}{\sigma_s}. \quad (2.79)$$

2.11.2 Liquid water correlations

The other important aspect of a subgrid condensation scheme is the diagnosis of liquid water correlations. As demonstrated in Section 2.9, liquid water correlations have an important role to play in the turbulent second- and third-order turbulent moments. Perhaps most importantly, the vertical liquid water flux is a major part of the vertical buoyancy flux term and is consequently quite important for accurately predicting turbulent kinetic energy in cloudy boundary layers. SD77 includes a brief discussion of the buoyancy flux in partly cloudy layers, but do not mention the liquid water flux or other liquid water correlations. Mellor (1977a,b) fills in the gap left by SD77 and includes a logical extension to address the liquid water correlations in a joint-Gaussian

framework. If one assumes that any variable, m , has a joint-Gaussian distribution with the variable s , then the liquid water correlation $\overline{m'q_l'}$ may be calculated as

$$\overline{m'q_l'} = \overline{m's'} \left(\frac{\overline{sq_l'}}{\sigma_s^2} \right) \quad (2.80)$$

where $\left(\frac{\overline{sq_l'}}{\sigma_s^2} \right) = \int_0^\infty (t - Q_l) t G(t) dt$ following Bechtold et al. (1995). Notice that the

evaluation of $\left(\frac{\overline{sq_l'}}{\sigma_s^2} \right)$ depends on the assumed PDF. For the joint-Gaussian PDF,

$$\left(\frac{\overline{sq_l'}}{\sigma_s^2} \right) = \frac{1}{2} \left[1 + \operatorname{erf} \left(\frac{Q_l}{\sqrt{2}} \right) \right] = R. \quad (2.81)$$

As with the cloud fraction and liquid water content, many authors have questioned the validity of the joint-Gaussian assumption for determining liquid water correlations. Some authors continue to use an explicitly assumed PDF for the conserved variables, but vary the particular PDF based on the type of boundary layer regime under consideration (e.g., Bougeault 1981a and Bougeault 1982). Others have added vertical velocity as another variable in the PDF and assumed a bimodal double Gaussian distribution (e.g., Lewellen and Yoh 1993 and Golaz et al. 2002a). Still others have dropped the use of an analytic PDF for the conserved variables and have used LES data to develop a general form for the liquid water correlations (e.g., Bechtold et al. 1995, Cuijpers and Bechtold 1995, and Bechtold and Siebesma 1998). All approaches have demonstrated some measure of success, but each has flaws and no particular one has proven general and simple enough to render the others obsolete.

An excellent discussion of alternative distributions for the conservative variables can be found in B81a, Bougeault (1982), and Bechtold et al. (1995), hereafter BEA95, wherein distributions are compared according to the skewness of s . Bougeault (1982) points out that a cumulus boundary layer contains thin updrafts of fast moving cloudy air and wide downdrafts of slowly descending clear air. One would expect that the actual distribution in such a case would be have a strong positive skewness of s . Within a stratocumulus regime, though, updrafts and downdrafts take up roughly the same area, and the skewness of s for the actual distribution would be closer to zero, like for the Gaussian distribution. In his study, Bougeault (1982) used a gamma distribution with variable skewness of s , and made plots of the resultant cloud fraction, liquid water

content, and $\left(\frac{\overline{sq'_l}}{\sigma_s^2}\right)$ as functions of Q_1 , shown here as Figure 2.5. Immediately evident

from the plots is that cloud fraction and liquid water content are almost independent of

the skewness of s for $Q_1 > -1$, and $\left(\frac{\overline{sq'_l}}{\sigma_s^2}\right)$ is almost independent of Q_1 for $Q_1 > 0$. For

values of Q_1 lower than those values, however, all three quantities strongly depend on the skewness of s . This result helps one to draw the conclusion, as BEA95 did, that the stratocumulus boundary layer regime can be appropriately represented by any reasonable PDF, but that cumulus boundary layer regimes are very sensitive to the choice. B81a and B81b show that a simple positively skewed PDF with skewness of s of 2 is adequate for use in simulating a trade-wind cumulus regime. Given this choice, the integration over the PDF for the liquid water correlations results in the piecewise function

$$\left(\frac{sq'_l}{\sigma_s^2}\right) = \begin{cases} (2 - Q_1)e^{Q_1-1} & Q_1 \leq 1 \\ 1 & Q_1 > 1 \end{cases}. \quad (2.82)$$

Without assuming a joint Gaussian PDF, however, B81a points out that it is intractable to find an exact form for $\overline{m'q'_l}$ as is done for the joint Gaussian case demonstrated in equation (2.88). He assumes, however, that all variables are well correlated inside the cloud layer, and that the liquid water correlations may be written

$$\left(\overline{\frac{sq'_l}{\sigma_s^2}}\right) = \frac{\overline{w'q'_l}}{\sigma_w\sigma_s} = \frac{\overline{q'_lq'_l}}{\sigma_{q_l}\sigma_s} = -\frac{\overline{\theta'_lq'_l}}{\sigma_{\theta_l}\sigma_s}. \quad (2.83)$$

This assumption is equivalent to saying that w' , θ'_l , and q'_l are all correlated with liquid water in exactly the same way within a cloud, which may seem like a strange assumption to make. Using LES data, however, B81a shows that equation (2.83) is a much better assumption than equation (2.80) for cumulus regimes. It should be noted that many subsequent authors continue to use equation (2.80), despite it having been derived for the special case of a joint Gaussian PDF for lack of a better assumption. (Bougeault 1982, Bechtold et al. 1995, Cuijpers and Bechtold 1995, Bechtold and Siebesma 1998).

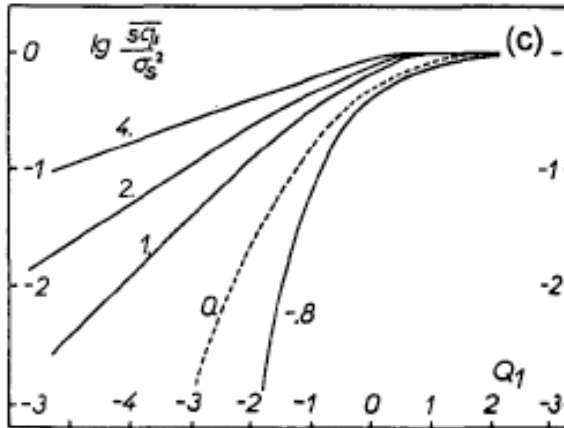
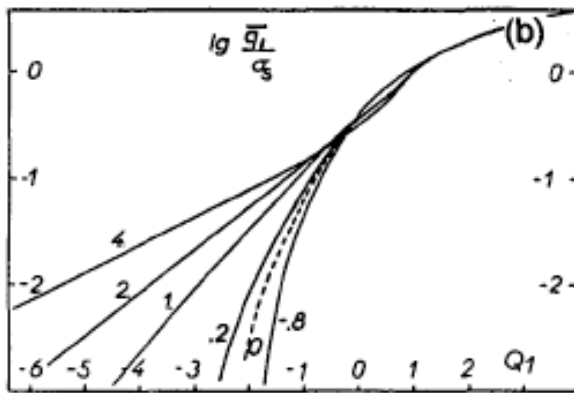
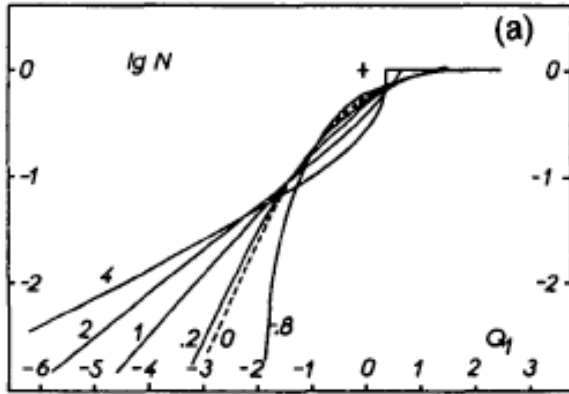


Figure 2.5 Cloud fraction, liquid water content, and $\left(\frac{s q_l'}{\sigma_s^2}\right)$ as functions of Q_1 . The labels indicate skewness of s ; the dashed "0" line is the Gaussian scheme. {from BEA95 after Bougeault (1982)}

Alternatively, a new line of parameterizations begins with BEA95 and drops the notion that one analytic PDF for the conserved variables must be assumed a priori. They keep the Gaussian integration for liquid water correlations as in equation (2.80), but add γ , a “proportionality coefficient”:

$$\overline{m'q_l'} = \gamma \overline{m's'} \left(\overline{\frac{sq_l'}{\sigma_s^2}} \right). \quad (2.84)$$

BEA95 acknowledge that γ can take values of one to five, depending on the value of Q_1 , with higher values of γ for lower values of Q_1 . However, they keep γ at unity, and

instead opt to change the parameterization of $\left(\overline{\frac{sq_l'}{\sigma_s^2}} \right)$ to reflect increases in liquid water

correlations in cumulus regimes with low values of Q_1 . They use

$$\left(\overline{\frac{sq_l'}{\sigma_s^2}} \right) = RF_{NG} \quad (2.85)$$

where F_{NG} is the “non-Gaussian transport factor” given by the piecewise function

$$F_{NG} = \begin{cases} 1 & Q_1 > 0 \\ 1 - 1.5Q_1 & -2 \leq Q_1 \leq 0 \\ 2 - Q_1 & Q_1 < -2 \end{cases}. \quad (2.86)$$

When Q_1 is greater than zero, the formulas for the liquid water correlations revert back to the Gaussian formulas of Mellor (1977a,b), but for values less than zero, the non-Gaussian transport factor increases to greater than five (see Figure 2.6).

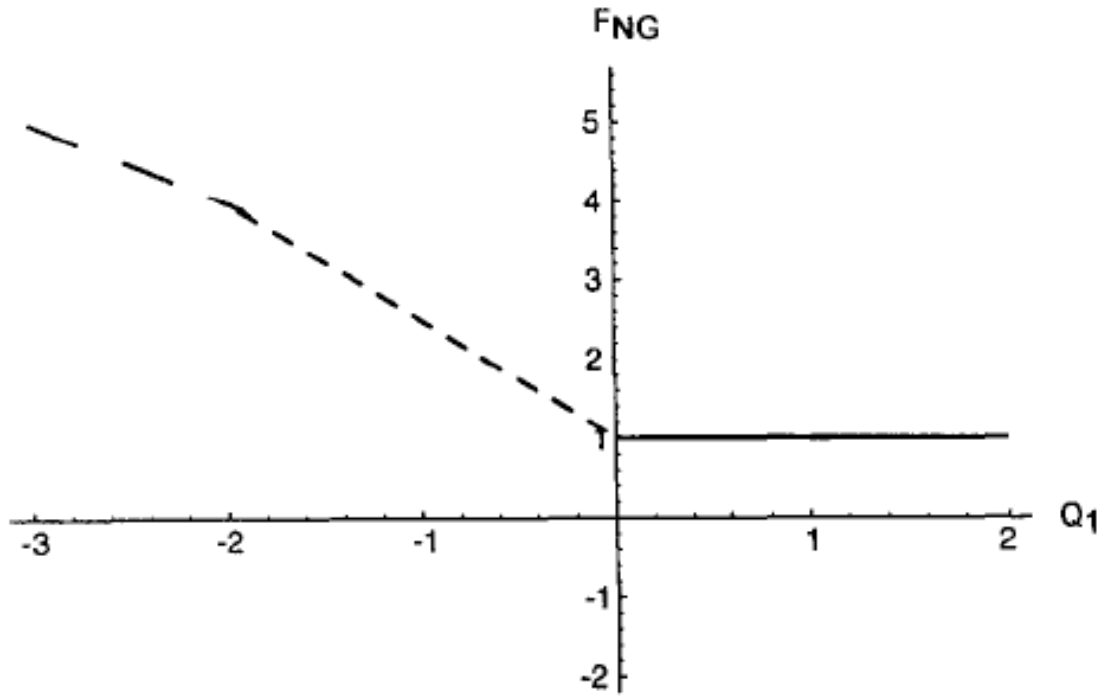


Figure 2.6 Non-Gaussian transport factor as a function of Q_1 {from BEA95}

CB95 extend the ideas of BEA95 by using LES to determine the non-Gaussian transport factor. Using this method, a PDF for liquid water potential temperature and total water specific humidity is not explicitly assumed. Instead, LES results from various cloudy boundary layer regimes help to determine a general formula for the liquid water correlations. Figures 2.7 and 2.8 show the non-Gaussian transport factor determined from LES and the best fit from the LES data. Figure 2.7 shows that the non-Gaussian transport factor increases exponentially as Q_1 decreases according to

$$F_{NG} = \begin{cases} 1 & Q_1 \geq 0 \\ e^{-1.4Q_1} & Q_1 < 0 \end{cases} \quad (2.87)$$

Equation (2.87) is the best fit given the wide range of values of skewness of s for all cloudy boundary layer regimes. Figure 2.8 shows that the skewness of s near the cloud

base tends toward zero and therefore the non-Gaussian transport factor tends toward one there.

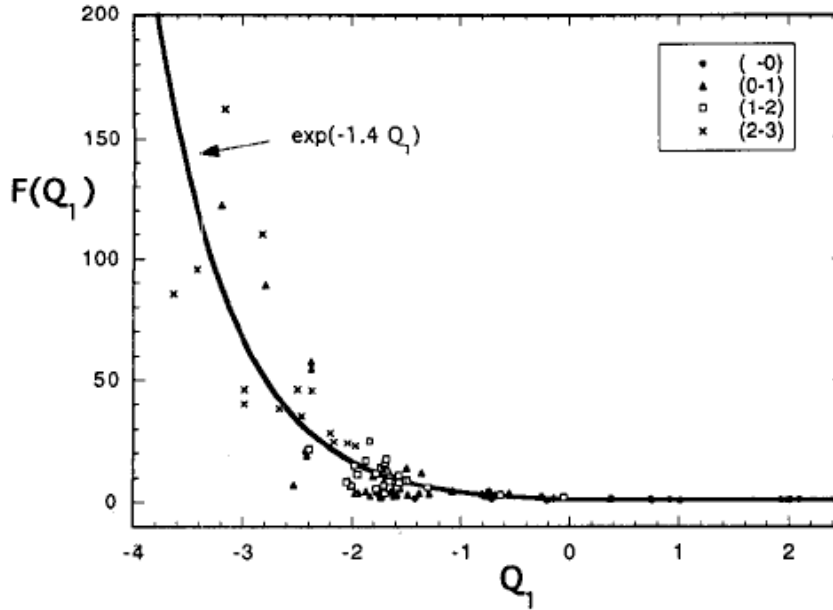


Figure 2.7 Non-Gaussian transport factor determined from LES. The symbols in the legend indicate values of skewness of s . {from CB95}

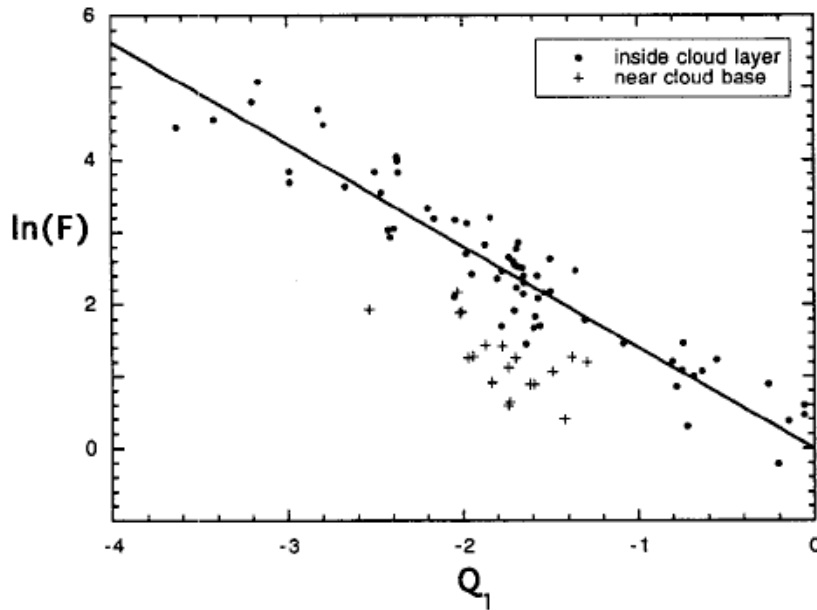


Figure 2.8 Non-Gaussian transport factor determined from LES {from CB95}

Bechtold and Siebesma (1998), hereafter BS98, continue along this same line of parameterization. They use equations (2.84) and (2.85) to determine liquid water correlations, but determine the non-Gaussian transport factor using a mass-flux approach. They determine that

$$F_{NG} = \frac{1}{R} \frac{q_{l,c}}{[a(q_s(T) - q_l) + q_{l,c}]} \quad (2.88)$$

where $q_{l,c} = \frac{\overline{q_l}}{R}$ is the in-cloud liquid water content. BS98 show that equation (2.96) is an accurate formula for calculating liquid water correlations for many boundary layer cloud regimes. Figure 2.9 shows the non-Gaussian transport factor for various cloudy boundary layer cases. Their results are consistent with BEA95 and CB95 in that the non-Gaussian transport factor increases strongly for values of Q_1 less than zero. BS98 further show the mean buoyancy flux in cloudy boundary layer has two maxima – one for cumulus regimes and one for stratocumulus regimes (see figure 2.10). This last result is consistent with the findings of Randall (1987).

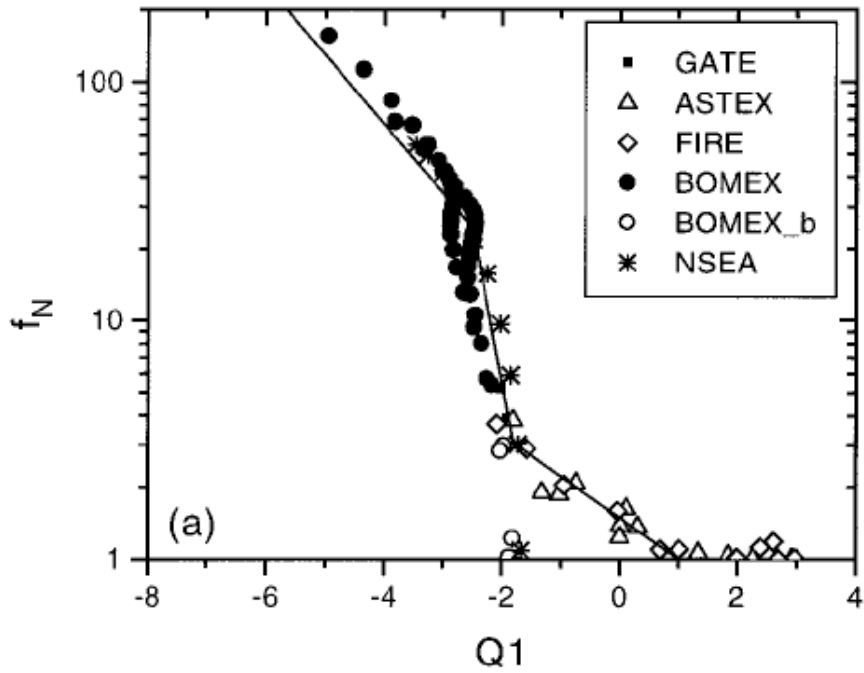


Figure 2.9 Non-Gaussian transport factor calculated from the mass-flux approach in BS98 for various cloudy boundary layer regimes {from BS98}

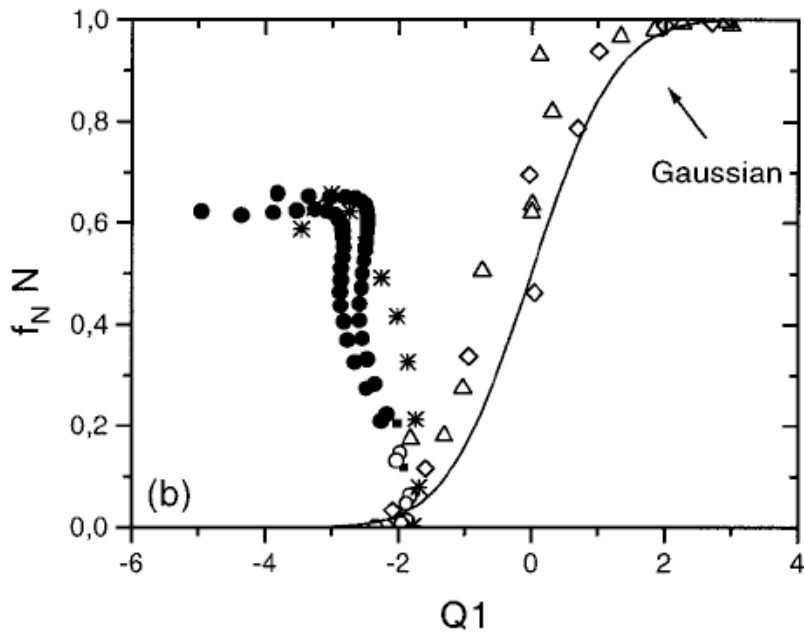


Figure 2.10 Non-Gaussian transport factor multiplied by cloud fraction – this product is the same as $\left(\frac{\overline{sq'_l}}{\sigma_s^2} \right)$ for the BS98 framework. {from BS98}

Even though the schemes of BEA95, CB95, and SB98 have increasing sophistication in determining the non-Gaussian transport factor, their use in testing was found to be inadequate to produce satisfactory results for boundary layers containing cumulus clouds. In particular, the vertical liquid water flux was found to be too small, which resulted in a buoyancy flux that was not sufficient to generate or maintain enough turbulent kinetic energy for a trade-wind cumulus boundary layer. On the other hand, the scheme of B81a that was developed specifically for trade-wind cumulus boundary layers worked well in the current model for this type of boundary layer, although it predictably generated too much turbulent kinetic energy for the stratocumulus cases. For the stratocumulus cases, the scheme based on the Gaussian PDF was found to work well. Unfortunately, none of the schemes mentioned in this study worked well for all cloudy boundary layers. This provides motivation and means to create a new scheme that will work well for any cloudy boundary layer.

One way to create such a scheme is to combine two schemes that work in the limiting cases, when Q_1 is small as in cumulus boundary layers and when Q_1 is large as in stratocumulus boundary layers. This approach has been used for the cloud fraction and liquid water content in BEA95 and in Abdella and McFarlane (2001), but never for the liquid water correlations. For the current model, this idea is adopted for all liquid water correlations. The scheme of B81a is used to determine liquid water correlations for low values of Q_1 and the Gaussian scheme of M77 is used for high values of Q_1 . For intermediate values of Q_1 , a linear interpolation between the two schemes is used. The limits of Q_1 that determine where one scheme switches to the other are somewhat

arbitrary and tunable, but are guided by the information obtained from the non-Gaussian transport factor found in BEA95, CB95, and SB98.

Since Q_1 is calculated at each level to determine the mean cloudiness statistics, the simplest implementation of the Q_1 -based liquid water correlation idea is to simply use the value of Q_1 at each level to determine which liquid water correlation scheme to use for that level. This approach allows for differing cloud schemes within the same column, and may be useful for situations where a stratocumulus deck is eroded by a growing cumulus layer below. However, it was found during testing that when used in a typical stratocumulus regime, while most of the cloud layer consists of levels with high cloud fraction, the cloud base and cloud top levels often had only a small cloud fraction and values of Q_1 that fell in the cumulus regime. The result was a stratocumulus layer bounded by thin cumulus layers and led to unrealistic profiles of the buoyancy flux and TKE.

To eliminate this problem, the following procedure was used. Given the mean cloud fraction diagnosed as in section 2.11.1, one can also diagnose the cloud type using some artificial means. In the current model, a simple formulation based on the maximum cloud fraction found in the column is used:

$$\begin{aligned}
 R_{\max} \leq R_{cu} &: && \text{cumulus regime} \\
 R_{cu} < R_{\max} \leq R_{sc} &&& \text{transitional regime} \\
 R_{\max} > R_{sc} &&& \text{stratocumulus regime}
 \end{aligned}$$

where R_{\max} is the maximum cloud fraction in the column. When determined to be in the cumulus regime, liquid water correlations are calculated according to B81a and when determined to be in the stratocumulus regime, the M77 scheme is used. If it is determined that the cloud regime falls between the cumulus regime and stratocumulus regime, linear

interpolation is used to calculate the liquid water correlations from the two limiting schemes.

Explicitly, the liquid water correlations are calculated as follows:

$$\overline{w'q'_{l\ cu}} = 0.8 * \sigma_w \sigma_s \left(\frac{\overline{sq'_l}}{\sigma_s^2} \right) \quad (2.89)$$

$$\overline{\theta'_l q'_{l\ cu}} = -1.2 * \sigma_{\theta_l} \sigma_s \left(\frac{\overline{sq'_l}}{\sigma_s^2} \right) \quad (2.90)$$

$$\overline{q'_t q'_{l\ cu}} = 1.2 * \sigma_{q_t} \sigma_s \left(\frac{\overline{sq'_l}}{\sigma_s^2} \right) \quad (2.91)$$

$$\overline{w'q'_{l\ sc}} = R \left(\overline{aw'q'_t} - \overline{bw'\theta'_l} \right) \quad (2.92)$$

$$\overline{\theta'_l q'_{l\ sc}} = R \left(\overline{a\theta'_l q'_t} - \overline{b\theta'_l{}^2} \right) \quad (2.93)$$

$$\overline{q'_t q'_{l\ sc}} = R \left(\overline{aq'_t{}^2} - \overline{b\theta'_l q'_t} \right) \quad (2.94)$$

$$\text{where } \left(\frac{\overline{sq'_l}}{\sigma_s^2} \right) = (2 - Q_1) e^{Q_1 - 1}. \quad (2.95)$$

Then, liquid water correlations are calculated according to

$$\overline{\chi'q'_l} = \begin{cases} \overline{\chi'q'_{l\ cu}} & \text{cumulus regime} \\ \left(1 - \frac{Q_1 - Q_{1\ cu}}{Q_{1\ sc} - Q_{1\ cu}} \right) \overline{\chi'q'_{l\ cu}} + \left(\frac{Q_1 - Q_{1\ cu}}{Q_{1\ sc} - Q_{1\ cu}} \right) \overline{\chi'q'_{l\ sc}} & \text{transitional regime} \\ \overline{\chi'q'_{l\ sc}} & \text{stratocumulus regime} \end{cases} \quad (2.96)$$

where $Q_{1_{cu}} = \frac{\tan\left[\frac{(R_{cu} - 0.5)}{0.36}\right]}{1.55}$, and $Q_{1_{sc}} = \frac{\tan\left[\frac{(R_{sc} - 0.5)}{0.36}\right]}{1.55}$. R_{cu} and R_{sc} are cloud

fraction thresholds that determine which liquid water correlation scheme is used for a given cloud fraction. Experimental values for the current model are $R_{cu} = 0.25$ and $R_{sc} = 0.5$.

The third-order moment liquid water correlations are handled in a similar way:

$$\overline{u'_i u'_j q'_l}_{cu} = \sigma_{u_i} \sigma_{u_j} \sigma_s \left(\frac{\overline{s^2 q'_l}}{\sigma_s^3} \right)_{cu} \quad (2.97)$$

$$\overline{u'_i \theta'_l q'_l}_{cu} = -\sigma_{u_i} \sigma_{\theta_l} \sigma_s \left(\frac{\overline{s^2 q'_l}}{\sigma_s^3} \right)_{cu} \quad (2.98)$$

$$\overline{u'_i q'_t q'_l}_{cu} = \sigma_{u_i} \sigma_{q_t} \sigma_s \left(\frac{\overline{s^2 q'_l}}{\sigma_s^3} \right)_{cu} \quad (2.99)$$

$$\overline{\theta_l'^2 q'_l}_{cu} = \sigma_{\theta_l}^2 \sigma_s \left(\frac{\overline{s^2 q'_l}}{\sigma_s^3} \right)_{cu} \quad (2.100)$$

$$\overline{\theta'_l q'_t q'_l}_{cu} = -\sigma_{\theta_l} \sigma_{q_t} \sigma_s \left(\frac{\overline{s^2 q'_l}}{\sigma_s^3} \right)_{cu} \quad (2.101)$$

$$\overline{q_t'^2 q'_l}_{cu} = \sigma_{q_t}^2 \sigma_s \left(\frac{\overline{s^2 q'_l}}{\sigma_s^3} \right)_{cu} \quad (2.102)$$

$$\text{where } \left(\frac{\overline{s^2 q'_l}}{\sigma_s^3} \right)_{cu} = (Q_1^2 - 4Q_1 + 5)R, \quad (2.103)$$

$$\overline{u'_i u'_j q'_l}_{sc} = \left(\overline{au'_i u'_j q'_l} - \overline{bu'_i u'_j \theta'_l} \right) \left(\frac{\overline{s^2 q'_l}}{\sigma_s^3} \right)_{sc} \quad (2.104)$$

$$\overline{u'_i \theta'_l q'_l}_{sc} = \left(\overline{au'_i \theta'_l q'_l} - \overline{bu'_i \theta'_l{}^2} \right) \left(\frac{\overline{s^2 q'_l}}{\sigma_s^3} \right)_{sc} \quad (2.105)$$

$$\overline{u'_i q'_l q'_l}_{sc} = \left(\overline{au'_i q'_l{}^2} - \overline{bu'_i \theta'_l q'_l} \right) \left(\frac{\overline{s^2 q'_l}}{\sigma_s^3} \right)_{sc} \quad (2.106)$$

$$\overline{\theta'_l{}^2 q'_l}_{sc} = \left(\overline{a\theta'_l{}^2 q'_l} - \overline{b\theta'_l{}^3} \right) \left(\frac{\overline{s^2 q'_l}}{\sigma_s^3} \right)_{sc} \quad (2.107)$$

$$\overline{\theta'_l q'_l q'_l}_{sc} = \left(\overline{a\theta'_l q'_l{}^2} - \overline{b\theta'_l{}^2 q'_l} \right) \left(\frac{\overline{s^2 q'_l}}{\sigma_s^3} \right)_{sc} \quad (2.108)$$

$$\overline{q'_l{}^2 q'_l}_{sc} = \left(\overline{aq'_l{}^3} - \overline{b\theta'_l q'_l{}^2} \right) \left(\frac{\overline{s^2 q'_l}}{\sigma_s^3} \right)_{sc} \quad (2.109)$$

$$\text{where } \left(\frac{\overline{s^2 q'_l}}{\sigma_s^3} \right)_{sc} = \begin{cases} (e^{-1} + 0.66Q_1 + 0.086Q_1^2) - RQ_1 & Q_1 \geq 0 \\ (e^{1.2Q_1 - 1}) - RQ_1 & Q_1 < 0 \end{cases} \quad (2.110)$$

Then, liquid water correlations are calculated according to

$$\overline{\chi' \psi' q'_l} = \begin{cases} \overline{\chi' \psi' q'_l}_{cu} & \text{cumulus regime} \\ \left(1 - \frac{Q_1 - Q_{1,cu}}{Q_{1,sc} - Q_{1,cu}} \right) \overline{\chi' \psi' q'_l}_{cu} + \left(\frac{Q_1 - Q_{1,cu}}{Q_{1,sc} - Q_{1,cu}} \right) \overline{\chi' \psi' q'_l}_{sc} & \text{transitional regime} \\ \overline{\chi' \psi' q'_l}_{sc} & \text{stratocumulus regime} \end{cases} \quad (2.111)$$

2.12 Subgrid-scale microphysics

The use of a subgrid-scale condensation parameterization makes it necessary to handle precipitation processes in a non-traditional way. Traditional microphysics schemes assume an entire grid box is either saturated or unsaturated and calculate precipitation processes and their effects on the thermodynamics accordingly. A different approach that takes into account partial cloudiness within a grid cell is needed instead. For example, precipitation that is generated by autoconversion at some height above the surface may fall through cloudy areas where collection and other processes may enhance the precipitation, or through clear areas where evaporation diminishes the precipitation. With grid cells containing partial cloudiness, it is not clear whether the precipitation falls through the cloudy or clear portions or which microphysical processes should be applied since the subgrid-scale condensation scheme does not provide any information about the spatial arrangement of the partial cloudiness.

One way to account for partial cloudiness in a microphysics scheme is to define two rain water variables: one to keep track of in-cloud rain water and one for rain water falling through clear air. Using a cloud overlap assumption, it is possible to keep track of the conversion of cloudy rain water to clear rain water (and vice versa) as it falls through a partly cloudy column. The microphysics processes that one wishes to include only affects one species of rain water. For the current model, only warm rain processes are considered. Autoconversion and collection of cloud water by rain drops provide a source of cloudy rain water, and evaporation provides a sink of clear rain water.

The dynamic equations governing each rain water species are given by

$$\frac{\partial \overline{q_{r,CLD}}}{\partial t} = \frac{1}{\rho_0} \frac{\partial P}{\partial z} + \frac{\partial \overline{q_r}}{\partial t}_{AUTO} + \frac{\partial \overline{q_r}}{\partial t}_{ACCR} \quad (2.112)$$

$$\frac{\partial \overline{q_{r,CLR}}}{\partial t} = \frac{1}{\rho_0} \frac{\partial P}{\partial z} + \frac{\partial \overline{q_r}}{\partial t}_{EVAP} \quad (2.113)$$

where the rain flux divergence term accounts for the rain falling into and out of cloudy and clear areas. The parameterization of the warm rain processes follows Khairoutdinov and Randall (2003). The tendency of cloudy rain water due to autoconversion is given by

$$\frac{\partial \overline{q_r}}{\partial t}_{AUTO} = R * \max[0, \alpha \overline{q_{l,AUTO}}] \quad (2.114)$$

where R , the cloud fraction, is added to account for the fact that autoconversion only occurs within the cloudy area of a grid cell, α is the autoconversion rate coefficient, and $\overline{q_{l,AUTO}}$ is the autoconversion-eligible cloud water diagnosed from the subgrid-scale

condensation scheme. The tendency of cloudy rain water due to accretion is give by

$$\frac{\partial \overline{q_r}}{\partial t}_{ACCR} = a_{P,CLD} A_{ar} \frac{\overline{q_{l,CLD}} \overline{q_{r,CLD}}^{3+b_r}}{4} \quad (2.115)$$

where

$$A_{ar} = \frac{\pi}{4} a_r N_{0r} E_{rc} \Gamma(3 + b_r) \left(\frac{\rho_{ref}}{\rho_0} \right)^{0.5} \left(\frac{\rho_0}{\pi \rho_r N_{0r}} \right)^{\frac{3+b_r}{4}},$$

$a_{P,CLD}$ is the area containing cloudy rain water,

and $\overline{q_{l,CLD}} = \frac{\overline{q_l}}{R}$. The tendency of clear rain water due to evaporation is given by

$$\frac{\partial \overline{q_r}}{\partial t}_{EVAP} = a_{P,CLR} \frac{2\pi C_r N_{0r}}{\rho_0 (A+B)} \left[A_{er} \overline{q_{r,CLR}}^{-0.5} + B_{er} \overline{q_{r,CLR}}^{\frac{5+b_r}{8}} \right] (S-1) \quad (2.116)$$

where

$$A_{er} = a_{fr} \left(\frac{\rho_0}{\pi \rho_r N_{0r}} \right)^{0.5}, \quad B_{er} = b_{fr} \left(\frac{\rho_0 a_r}{\mu} \right)^{0.5} \Gamma \left(\frac{5 + b_r}{2} \right) \left(\frac{\rho_{ref}}{\rho_0} \right)^{0.25} \left(\frac{\rho_0}{\pi \rho_r N_{0r}} \right)^{\frac{5+b_r}{8}},$$

$$A = \frac{L_v}{K_a T} \left(\frac{L_v}{R_v T} - 1 \right), \quad B = \frac{R_v R_d}{D_a e^{sat}}, \quad S = \frac{q_v}{q_{sat}}, \quad \text{and } a_{P,CLR} \text{ is the area containing clear rain}$$

water. Table 2.8 lists the unspecified constants.

Symbol	Description	Value	Units
a_r	constant in fall speed formula for rain	842	$m^{1-b} s^{-1}$
a_{fr}	constant in ventilation factor for rain	0.78	
b_r	exponent in fall speed for rain	0.8	
b_{fr}	constant in ventilation factor for rain	0.31	
C_r	rain shape factor	1.0	
D_a	diffusion coefficient of water vapor at 0°C	2.210×10^{-5}	$m^2 s^{-1}$
E_{rc}	collection efficiency of rain for cloud water	1.0	
N_{0r}	intercept parameter for rain	8.0×10^6	m^4
K_a	thermal conductivity of air at 0°C	2.4×10^{-2}	$J m K^{-1} s^{-1}$
α	autoconversion rate	0.001	s^{-1}
ρ_{ref}	reference air density	1.29	$kg m^{-3}$
ρ_r	density of rain	1000	$kg m^{-3}$
μ	dynamic viscosity of air at 0°C	1.717×10^{-5}	$kg m^{-1} s^{-1}$

Table 2.8 Constants used in the microphysics parameterization.

Yet to be determined are the precipitation flux divergence terms. Given the possibility of rain falling from cloudy air into clear air and vice versa, these terms must account for these transitions. For the cloudy rain water, the flux divergence term is given by

$$\frac{1}{\rho_0} \frac{\partial P}{\partial z} = \frac{1}{\rho_0 \Delta z} \left[\underbrace{\left(P_{CLD,k+1 \rightarrow CLD,k} + P_{CLR,k+1 \rightarrow CLD,k} \right)}_{\text{Flux Falling Into Cloud}} - \underbrace{\left(P_{CLD,k \rightarrow CLD,k-1} + P_{CLD,k \rightarrow CLR,k-1} \right)}_{\text{Flux Falling Out Of Cloud}} \right] \quad (2.117)$$

where the terms in the first parentheses on the right-hand side represent the rain flux falling into the cloudy rain area from both cloudy and clear area of the level directly above, and the terms in the second parentheses represent the rain flux falling out of the

cloudy rain area into either cloudy or clear area of the level below. Similarly, the flux divergence term for the clear rain water is given by

$$\frac{1}{\rho_0} \frac{\partial P}{\partial z} = \frac{1}{\rho_0 \Delta z} \left[\underbrace{\left(P_{CLR,k+1 \rightarrow CLR,k} + P_{CLD,k+1 \rightarrow CLR,k} \right)}_{\text{Flux Falling Into Clear Air}} - \underbrace{\left(P_{CLR,k \rightarrow CLD,k-1} + P_{CLR,k \rightarrow CLR,k-1} \right)}_{\text{Flux Falling Out Of Clear Air}} \right]. \quad (2.118)$$

Next, one needs to calculate $P_{CLD,k+1 \rightarrow CLD,k}$, $P_{CLR,k+1 \rightarrow CLD,k}$, $P_{CLD,k+1 \rightarrow CLR,k}$, and

$P_{CLR,k+1 \rightarrow CLR,k}$, the rain flux falling from cloud above into cloud below, the rain flux falling from clear sky above into cloud below, the rain flux falling from cloud above into clear sky below, and the rain flux falling from clear sky above into clear sky below, respectively, for each model level. To do so, one must make an assumption about how the partial cloudiness overlaps in the vertical dimension.

The work of Jakob and Klein (2000), hereafter JK2000, provides an intuitive and convenient choice for the cloud overlap assumption and the framework to use it in. The cloud overlap assumption of JK2000 is taken from the ECMWF model. At each level, k , they define the area covered by clouds from all levels above, C_k , as:

$$C_k = 1 - (1 - C_{k+1}) \frac{1 - \max(R_k, R_{k+1})}{1 - \min(R_{k+1}, 1 - \delta)} \quad (2.119)$$

where levels increase upward and $\delta = 1 \times 10^{-6}$ to prevent division by zero.

C_k can be thought of as the area of the shadow generated by optically opaque clouds from a light source at nadir. This expression “gives maximum overlap for clouds in adjacent levels with cloud fraction monotonically increasing or decreasing with height, and random overlap for clouds either separated by clear levels or for levels of changing sign in the vertical gradient of cloud fraction” (JK2000). Given C_k , it is then possible to determine the portion of clouds at level k that has no clouds above it: $\Delta C_k = C_k - C_{k+1}$. In

the JK2000 scheme, this quantity represents the cloud fraction that cannot possibly have precipitation falling into it from above, and is instrumental in determining areas of cloudy and clear precipitation flux.

Next, one needs to use the cloud overlap assumption to determine the areas of cloudy precipitation flux and clear precipitation flux. Figure 2.11 taken from JK2000 demonstrates the concept. They identify four possibilities for the precipitation flux that can happen at the interface between two levels (see Figure 1):

1. Cloudy precipitation flux falling into cloudy sky:
2. Cloudy precipitation flux falling into clear sky
3. Clear precipitation flux falling into cloudy sky
4. Clear precipitation flux falling into clear sky.

In order to calculate these precipitation fluxes, one needs to know the total precipitation flux and the areas of cloudy and clear precipitation flux. The areas of cloudy and clear precipitation flux as well as the areas of transition are calculated as follows.

- For each level starting from the top, if $\overline{q_{r,CLR}}$ and $\overline{q_{r,CLD}}$ are zero, then the areas of cloudy and clear precipitation flux, $a_{P,CLD}$ and $a_{P,CLR}$, are zero.
- If $\overline{q_{r,CLR}} + \overline{q_{r,CLD}} > 0$, then the rain must occupy some area and the areas of cloudy and clear precipitation for the first level containing rain water are determined by

$$\begin{aligned}
 a_{P,CLD_k} &= \begin{cases} R_k & \text{if } \overline{q_{r,CLD}} > 0 \\ 0 & \text{if } \overline{q_{r,CLD}} = 0 \end{cases} \\
 a_{P,CLR_k} &= \begin{cases} 1 - R_k & \text{if } \overline{q_{r,CLR}} > 0 \\ 0 & \text{if } \overline{q_{r,CLR}} = 0 \end{cases}
 \end{aligned} \tag{2.120}$$

- For each level below the topmost level of rainfall, the areas of cloudy and clear precipitation flux are calculated as

$$a_{P,CLD_k} = \begin{cases} R_k & \text{if } R_k > 0.01 \text{ and } \overline{q_{l,AUTO}} > 0 \\ a_{P,CLD_{k+1}} + \Delta a_{P,CLR \rightarrow CLD_k} - \Delta a_{P,CLD \rightarrow CLR_k} & \text{otherwise} \end{cases} \quad (2.121)$$

$$a_{P,CLR_k} = a_{P,CLR_{k+1}} - \Delta a_{P,CLR \rightarrow CLD_k} + \Delta a_{P,CLD \rightarrow CLR_k}$$

where

$$\Delta a_{P,CLR \rightarrow CLD_k} = \max\left[0, \min\left(a_{P,CLR_{k+1}}, R_k - \Delta C_k -_{k+1}\right)\right]$$

$$\Delta a_{P,CLD \rightarrow CLR_k} = a_{P,CLD_{k+1}} - \min\left(R_k - \Delta C_k, a_{P,CLD_{k+1}}\right)$$

The quantities $\Delta a_{P,CLR \rightarrow CLD_k}$ and $\Delta a_{P,CLD \rightarrow CLR_k}$ represent the areas containing precipitation flux where precipitation is falling from a cloudy region to a clear region and from a clear region to a cloudy one, respectively.

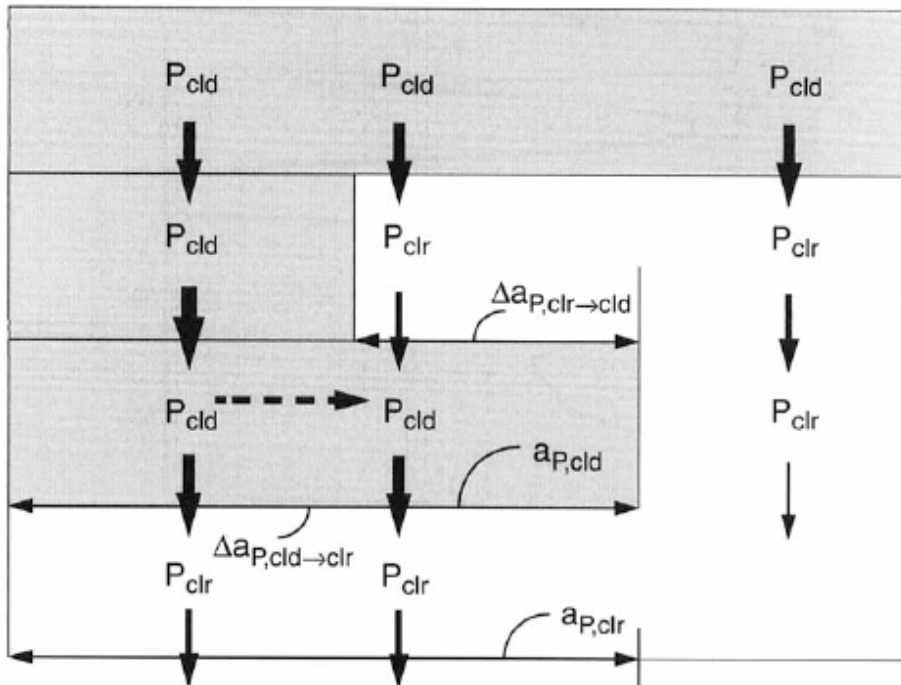


Figure 2.11 Illustration of precipitation fluxes and their areas {from JK2000}

With the areas of cloudy and clear precipitation flux and the areas of transition calculated, it is now possible to calculate the four possible types of precipitation fluxes. First, the total precipitation flux is calculated according to Khairoutdinov and Randall (2003) as

$$P_{TOTAL_k} = \frac{a_r \Gamma(4 + b_r)}{6} (\pi \rho_r N_{0r})^{-b_r} \left(\frac{\rho_{ref}}{\rho_0} \right)^{0.5} \left[\rho_0 (\overline{q_{r,CLD}} + \overline{q_{r,CLR}}) \right]^{1 + \frac{b_r}{4}} \quad (2.122)$$

The total precipitation flux is then divided into a cloudy and clear part according to

$$P_{CLD_k} = \left(\frac{a_{P,CLD_k}}{a_{P,CLD_k} + a_{P,CLR_k}} \right) P_{TOTAL_k} \quad (2.123)$$

$$P_{CLR_k} = \left(\frac{a_{P,CLR_k}}{a_{P,CLD_k} + a_{P,CLR_k}} \right) P_{TOTAL_k}$$

From these two fluxes, the four possible precipitation fluxes are calculated according to

$$P_{CLD_k \rightarrow CLR_{k-1}} = \left(\frac{\Delta a_{P,CLD \rightarrow CLR_{k-1}}}{a_{P,CLD_k}} \right) P_{CLD_k}$$

$$P_{CLD_k \rightarrow CLD_{k-1}} = P_{CLD_k} - P_{CLD_k \rightarrow CLR_{k-1}} \quad (2.124)$$

$$P_{CLR_k \rightarrow CLD_{k-1}} = \left(\frac{\Delta a_{P,CLR \rightarrow CLD_{k-1}}}{a_{P,CLR_k}} \right) P_{CLR_k}$$

$$P_{CLR_k \rightarrow CLR_{k-1}} = P_{CLR_k} - P_{CLR_k \rightarrow CLD_{k-1}}$$

To discretize the predictive equations for the two rain water species, the simple forward-in-time scheme is used for the microphysics terms. The precipitation flux divergence terms, however, constitute advection and should be treated differently. Since the precipitation flux is always in one direction, the upstream scheme is prudent to use. The discretized form of equations (2.112) and (2.113) are given by

$$\begin{aligned}
\overline{q_{r,CLD}}^{i+1} &= \overline{q_{r,CLD}}^i + \Delta t \left[\frac{1}{\rho_0} \frac{(P_{CLD_{k+1} \rightarrow CLD_k} + P_{CLR_{k+1} \rightarrow CLD_k}) - (P_{CLD_k \rightarrow CLD_{k-1}} + P_{CLD_k \rightarrow CLR_{k-1}})}{\tilde{z}_{k+1} - \tilde{z}_k} \right. \\
&\quad \left. + \frac{\partial \overline{q_r}}{\partial t}_{AUTO_k} + \frac{\partial \overline{q_r}}{\partial t}_{ACCR_k} \right] \\
\overline{q_{r,CLR}}^{i+1} &= \overline{q_{r,CLR}}^i + \Delta t \left[\frac{1}{\rho_0} \frac{(P_{CLR_{k+1} \rightarrow CLR_k} + P_{CLD_{k+1} \rightarrow CLR_k}) - (P_{CLR_k \rightarrow CLR_{k-1}} + P_{CLR_k \rightarrow CLD_{k-1}})}{\tilde{z}_{k+1} - \tilde{z}_k} \right. \\
&\quad \left. + \frac{\partial \overline{q_r}}{\partial t}_{EVAP_k} \right]
\end{aligned} \tag{2.125}$$

Since the upstream scheme is conditionally stable, certain conditions must be enforced.

The conditional stability criterion for the upstream scheme is given by $\frac{c\Delta t}{\Delta z} \leq 1$, where c

is the advecting speed. Since the precipitation flux is given by $P = \rho_0 q_r V_i$, the advecting

speed is then $c = V_i = \frac{P}{\rho_0 q_r}$. For stability, one must enforce $\frac{V_i \Delta t}{\Delta z} = \frac{P \Delta t}{\rho_0 q_r \Delta z} \leq 1$ or

$\frac{P}{\rho_0 q_r} \leq \frac{\Delta z}{\Delta t}$. Since Δz and Δt are fixed in the model and P is a function of q_r , the

stability criterion effectively puts a maximum limit on q_r .

2.13 Complete system of governing equations

At this point, the closure of the model is complete. The turbulent variables predicted or diagnosed are included in Table 2.9. When used as a turbulence parameterization, ten prognostic second-order moment equations and 28 algebraic third-order moments are solved. When used as a one-dimensional model, an additional 4 equations for the mean variables are included. Finally, if the microphysics scheme is used, an additional two prognostic equations are solved. The mean equations are

$$\frac{\partial \bar{\theta}_l}{\partial t} = -\frac{\partial \overline{w'\theta'_l}}{\partial z} - \frac{1}{\rho c_p} \frac{\partial \bar{F}}{\partial z} - \frac{L_v}{c_p} \left(\frac{p_0}{p} \right)^\kappa \frac{1}{\rho_0} \frac{\partial \bar{P}}{\partial z} - \overline{w_{LS}} \frac{\partial \bar{\theta}_l}{\partial z} + ADV_{H,\theta_l} \quad (2.126)$$

$$\frac{\partial \bar{q}_l}{\partial t} = -\frac{\partial \overline{w'q'_l}}{\partial z} - \overline{w_{LS}} \frac{\partial \bar{q}_l}{\partial z} + ADV_{H,q_l} - \frac{\partial q_r}{\partial t}_{AUTO} - \frac{\partial q_r}{\partial t}_{ACCR} + \frac{\partial q_r}{\partial t}_{EVAP} \quad (2.127)$$

$$\frac{\partial \bar{u}}{\partial t} = -f(\bar{v}_g - \bar{v}) - \frac{\partial \overline{w'u'}}{\partial z} \quad (2.128)$$

$$\frac{\partial \bar{v}}{\partial t} = f(\bar{u}_g - \bar{u}) - \frac{\partial \overline{w'v'}}{\partial z} \quad (2.129)$$

where the microphysics terms are given in Section 2.12.

Mean Variables	Second-order Moments	Third-order Moments
		$\overline{w'^3}, \overline{w'u'^2}, \overline{w'v'^2}, \overline{w'^2u'}, \overline{w'^2v'}$,
		$\overline{u'^2\theta'_l}, \overline{v'^2\theta'_l}, \overline{w'^2\theta'_l}, \overline{u'^2q'_l}, \overline{v'^2q'_l}, \overline{w'^2q'_l}$,
	$\overline{u'^2}, \overline{v'^2}, \overline{w'^2}$,	
$\bar{\theta}_l, \bar{q}_l, \bar{u}, \bar{v}$	$\overline{w'u'}, \overline{w'v'}, \overline{w'\theta'_l}, \overline{w'q'_l}$,	$\overline{w'u'\theta'_l}, \overline{w'u'q'_l}, \overline{w'v'\theta'_l}, \overline{w'v'q'_l}$,
$\left(\begin{array}{c} q_{r,CLD} \\ q_{r,CLR} \end{array} \right)$	$\overline{\theta_l'^2}, \overline{\theta_l'q_l'}, \overline{q_l'^2}$	$\overline{u'\theta_l'^2}, \overline{v'\theta_l'^2}, \overline{w'\theta_l'^2}, \overline{u'q_l'^2}, \overline{v'q_l'^2}, \overline{w'q_l'^2}$,
		$\overline{u'\theta_l'q_l'}, \overline{v'\theta_l'q_l'}, \overline{w'\theta_l'q_l'}$,
		$\overline{\theta_l'^3}, \overline{\theta_l'^2q_l'}, \overline{\theta_l'q_l'^2}, \overline{q_l'^3}$

Table 2.9 Main variables

The second-order moment equations with the included parameterizations are

$$\frac{\partial \overline{u'^2}}{\partial t} = -\frac{\partial \overline{w'u'^2}}{\partial z} - 2\overline{w'u'} \frac{\partial \bar{u}}{\partial z} - \frac{c_4}{\tau_1} \left(\overline{u'^2} - \frac{2}{3} \bar{e} \right) + \frac{2c_5}{3} g\alpha \overline{w'\theta'_v} - c_1 \frac{\overline{u'^2}}{\tau_1} \quad (2.130)$$

$$\frac{\partial \overline{v'^2}}{\partial t} = -\frac{\partial \overline{w'v'^2}}{\partial z} - 2\overline{w'v'} \frac{\partial \bar{v}}{\partial z} - \frac{c_4}{\tau_1} \left(\overline{v'^2} - \frac{2}{3} \bar{e} \right) + \frac{2c_5}{3} g\alpha \overline{w'\theta'_v} - c_1 \frac{\overline{v'^2}}{\tau_1} \quad (2.131)$$

$$\frac{\partial \overline{w'^2}}{\partial t} = -\frac{\partial \overline{w'^3}}{\partial z} - \frac{c_4}{\tau_1} \left(\overline{w'^2} - \frac{2}{3} \overline{e} \right) + \left(2 - \frac{4c_5}{3} \right) g \alpha \overline{w' \theta'_v} - c_1 \frac{\overline{w'^2}}{\tau_1} \quad (2.132)$$

$$\frac{\partial \overline{w' u'}}{\partial t} = -\frac{\partial \overline{w'^2 u'}}{\partial z} - \overline{w'^2} \frac{\partial \overline{u}}{\partial z} - \frac{c_4}{\tau_1} \overline{w' u'} \quad (2.133)$$

$$\frac{\partial \overline{w' v'}}{\partial t} = -\frac{\partial \overline{w'^2 v'}}{\partial z} - \overline{w'^2} \frac{\partial \overline{v}}{\partial z} - \frac{c_4}{\tau_1} \overline{w' v'} \quad (2.134)$$

$$\frac{\partial \overline{w' \theta'_l}}{\partial t} = -\frac{\partial \overline{w'^2 \theta'_l}}{\partial z} - \overline{w'^2} \frac{\partial \overline{\theta}_l}{\partial z} - \frac{c_6}{\tau_2} \overline{w' \theta'_l} + (1 - c_7) g \alpha \overline{\theta'_l \theta'_v} \quad (2.135)$$

$$\frac{\partial \overline{w' q'_l}}{\partial t} = -\frac{\partial \overline{w'^2 q'_l}}{\partial z} - \overline{w'^2} \frac{\partial \overline{q}_l}{\partial z} - \frac{c_6}{\tau_2} \overline{w' q'_l} + (1 - c_7) g \alpha \overline{q'_l \theta'_v} \quad (2.136)$$

$$\frac{\partial \overline{\theta_l'^2}}{\partial t} = -\frac{\partial \overline{w' \theta_l'^2}}{\partial z} - 2 \overline{w' \theta'_l} \frac{\partial \overline{\theta}_l}{\partial z} - c_2 \frac{\overline{\theta_l'^2}}{\tau_1} \quad (2.137)$$

$$\frac{\partial \overline{\theta'_l q'_l}}{\partial t} = -\frac{\partial \overline{w' \theta'_l q'_l}}{\partial z} - \overline{w' \theta'_l} \frac{\partial \overline{q}_l}{\partial z} - \overline{w' q'_l} \frac{\partial \overline{\theta}_l}{\partial z} - c_2 \frac{\overline{\theta'_l q'_l}}{\tau_1} \quad (2.138)$$

$$\frac{\partial \overline{q_l'^2}}{\partial t} = -\frac{\partial \overline{w' q_l'^2}}{\partial z} - 2 \overline{w' q'_l} \frac{\partial \overline{q}_l}{\partial z} - c_2 \frac{\overline{q_l'^2}}{\tau_1} \quad (2.139)$$

The explicit algebraic third-order moments are given in equations (A29) – (A56) in the appendix. The buoyancy terms in equations (2.130) – (2.139) are calculated according to sections 2.9 and 2.11. The turbulent timescales are discussed in section 2.10.

2.14 Discretization

To discretize the continuous equations, one must choose how to place variables on a grid, how to calculate spatial derivatives, how to calculate time derivatives, and whether to enforce realizability constraints. The choice of variable placement on a grid is guided by many factors. First is the desire to limit computational dispersion or diffusion. Since the goal of the model is to calculate turbulent properties of the boundary layer, it is important that any diffusion in the model be the result of physical turbulence and not unrealistic computational dispersion error. Second, for computational speed, spatial derivatives should contain as few terms as possible. Third, the order of accuracy should be maximized given the number of grid levels used. One way to address all issues is to use a staggered grid, centered spatial differences, and only two grid levels in each derivative. Since the third-order moments only contain derivatives of the second-order moments and the second-order moments contain both derivatives of first- and third-order moments, it makes sense to stagger the second- and third-order moments on different levels. The mean quantities fit with the third-order moments since they contain derivatives of the second-order moments. With the variables placed on the grid in this way, no averaging needs to be done for the spatial derivatives and the space-differencing can be done with a two-level, centered-difference scheme that is second-order accurate. If the variables were placed on an unstaggered grid and the simplest centered difference form was used for the spatial derivatives as shown in Figure 2.12, you would essentially have two groups of variables that don't interact with each other. The red variables are all that are needed to calculate spatial derivatives for each other and the black variables are all that are needed for their respective derivatives. The placement of variables upon the



Figure 2.12 An example of an unstaggered grid. Arrows denote spatial derivative dependence. Colors are used to point out that two distinct noninteractive groups of variables exist on a grid like this.

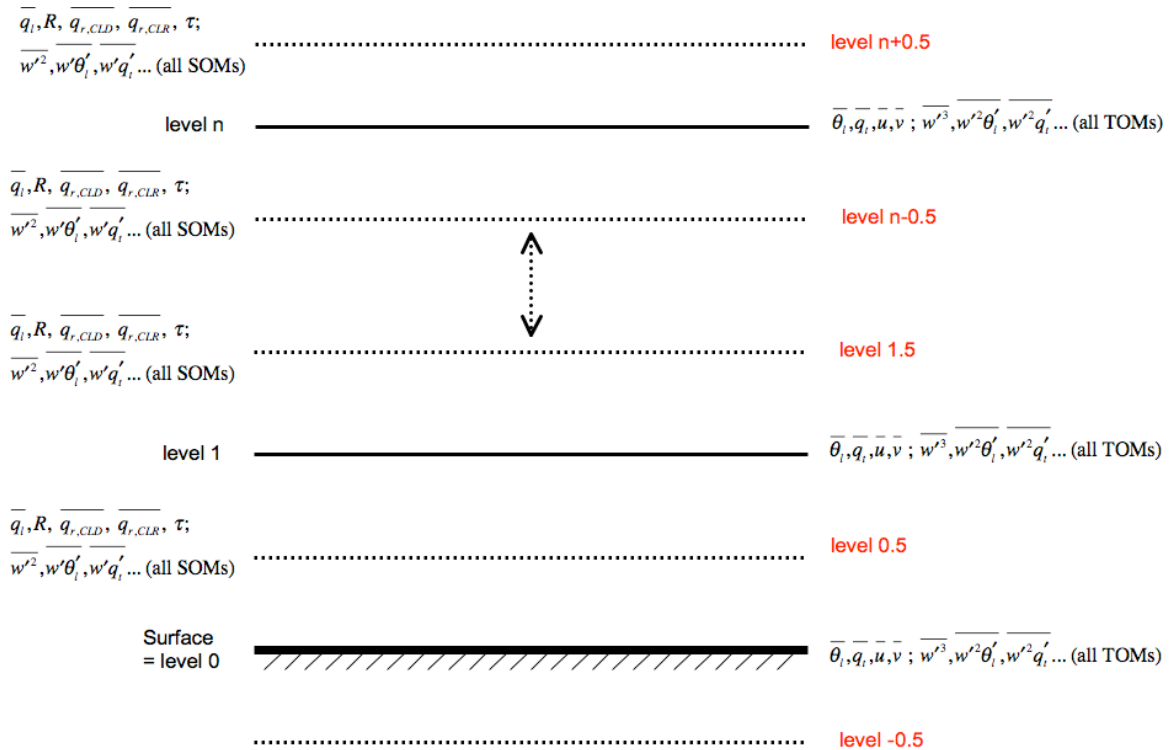


Figure 2.13 Depiction of the arrangement of variables upon the grid

staggered grid is shown in Figure 2.13. Notice that the variables line up so that no averaging must be done to calculate vertical derivatives and there is no redundancy of information.

As mentioned in the discussion about variables on the grid, all spatial derivatives are performed using the simplest centered difference quotient with the exception of the precipitation flux divergence terms in the microphysics parameterization. The precipitation flux and the mean prognostic rain variables reside on the same grid level. Since it is assumed that the precipitation flux is always downward, it is prudent to use the “upstream” scheme for these terms, where only information from the “upwind” side is utilized to calculate the flux divergence.

Many authors have utilized the second-order accurate centered-in-space spatial discretization scheme with a staggered grid for higher-order closure turbulence models (e.g., André et al. 1978, Sun and Ogura 1980, Krueger 1988, Canuto et al. 1994, Cheng et al. 2005). The time-stepping scheme used with this spatial discretization scheme has varied in the literature, however. AEA78 utilized the Euler-backward scheme, Krueger (1988) utilized many different time-stepping schemes depending on the individual terms in the equations, and Sun and Ogura (1980), Canuto et al. (1994), and Cheng et al. (2005) all utilized the simple forward Euler scheme. For ease of implementation and to maintain continuity with the model of Cheng et al. (2005), the forward Euler scheme was used in the current model.

For an example of the complete discretized form of the first-, second-, and third-order moments, the equations for $\overline{\theta}_l$, $\overline{w'\theta'_l}$, and $\overline{w'^2\theta'_l}$ are shown below. All other discretized equations can be written by analogy.

$$\begin{aligned} \overline{\theta'}_{l,k}^{t+1} = \overline{\theta'}_{l,k}^t + \Delta t \left\{ - \frac{\overline{w'\theta'}_{l,k+1/2}^t - \overline{w'\theta'}_{l,k-1/2}^t}{\overline{z}_{k+1/2} - \overline{z}_{k-1/2}} - \overline{w}_k \frac{\overline{\theta'}_{l,k+1}^t - \overline{\theta'}_{l,k-1}^t}{\overline{z}_{k+1} - \overline{z}_{k-1}} - \frac{1}{\rho_{0,k}} \frac{F_{k+1/2} - F_{k-1/2}}{\overline{z}_{k+1/2} - \overline{z}_{k-1/2}} \right. \\ \left. + ADV_{H,\theta_l} - \frac{L_v}{c_p} \left(\frac{p_0}{p_k} \right)^{\kappa} \frac{1}{\rho_{0,k}} \frac{P_{TOTAL,k+1/2} - P_{TOTAL,k-1/2}}{\overline{z}_{k+1/2} - \overline{z}_{k-1/2}} \right\} \end{aligned} \quad (2.140)$$

$$\begin{aligned} \overline{w'\theta'}_{l,k+1/2}^{t+1} = \overline{w'\theta'}_{l,k+1/2}^t + \Delta t \left\{ - \frac{\overline{w'^2\theta'}_{l,k+1}^t - \overline{w'^2\theta'}_{l,k}^t}{\overline{z}_{k+1} - \overline{z}_k} - c_6 \frac{\overline{w'\theta'}_{l,k+1/2}^t}{\tau_{2,k+1/2}} - \overline{w'^2}_{k+1/2} \frac{\overline{\theta'}_{l,k+1}^t - \overline{\theta'}_{l,k}^t}{\overline{z}_{k+1} - \overline{z}_k} \right. \\ \left. + (1 - c_7) \frac{g}{\theta_0} \overline{\theta'}_{l,v,k+1/2}^t \right\} \end{aligned} \quad (2.141)$$

$$\begin{aligned} \overline{w'^2\theta'}_{l,k}^t = -A_{2.3} \frac{\overline{w'^2}_{k+1/2}^t - \overline{w'^2}_{k-1/2}^t}{\overline{z}_{k+1/2} - \overline{z}_{k-1/2}} - A_{2.6} \frac{\overline{w'\theta'}_{l,k+1/2}^t - \overline{w'\theta'}_{l,k-1/2}^t}{\overline{z}_{k+1/2} - \overline{z}_{k-1/2}} - A_{2.7} \frac{\overline{w'q'}_{l,k+1/2}^t - \overline{w'q'}_{l,k-1/2}^t}{\overline{z}_{k+1/2} - \overline{z}_{k-1/2}} \\ - A_{2.8} \frac{\overline{\theta'^2}_{l,k+1/2}^t - \overline{\theta'^2}_{l,k-1/2}^t}{\overline{z}_{k+1/2} - \overline{z}_{k-1/2}} - A_{2.9} \frac{\overline{\theta'_l q'}_{l,k+1/2}^t - \overline{\theta'_l q'}_{l,k-1/2}^t}{\overline{z}_{k+1/2} - \overline{z}_{k-1/2}} - A_{2.10} \frac{\overline{q'^2}_{l,k+1/2}^t - \overline{q'^2}_{l,k-1/2}^t}{\overline{z}_{k+1/2} - \overline{z}_{k-1/2}} + L_2 \end{aligned} \quad (2.142)$$

where the $A_{m,n}$ are calculated at level k using the arithmetic mean for quantities that must be interpolated.

Given the complexity of the model, the exact computational stability criterion is difficult to obtain. A good estimate can be obtained by consideration of the physical processes captured in the individual terms of the model. The second-order moment equations involve common terms: a transport term characterized by the divergence of the third-order moments, a mechanical production term involving second-order moments and mean variable gradients, a return-to-isotropy term that somewhat acts as a smoothing operator, a buoyancy production term, and damping terms in the form of dissipation or part of the pressure correlation. Of these terms, the transport term involving the third-order moments has been responsible for computational instability most often in the

literature. One can gain a good idea of model stability by examining these terms.

Excluding all but the transport term, the second-order moments may be written in discrete form as

$$\frac{SOM_{k+1/2}^{t+1} - SOM_{k+1/2}^t}{\Delta t} = -\frac{TOM_{k+1}^t - TOM_k^t}{\Delta z} \quad (2.143)$$

The discretized form of the third-order moments may be substituted to obtain

$$\begin{aligned} \frac{SOM_{n,k+1/2}^{t+1} - SOM_{n,k+1/2}^t}{\Delta t} = & -\frac{1}{\Delta z} \left\{ \left(-A_{n,1,k+1} \frac{SOM_{1,k+3/2}^t - SOM_{1,k+1/2}^t}{\Delta z} \right. \right. \\ & \left. \left. - \left(-A_{n,1,k} \right) \frac{SOM_{1,k+1/2}^t - SOM_{1,k-1/2}^t}{\Delta z} \right) \right. \\ & + \left(-A_{n,2,k+1} \frac{SOM_{2,k+3/2}^t - SOM_{2,k+1/2}^t}{\Delta z} \right. \\ & \left. \left. - \left(-A_{n,2,k} \right) \frac{SOM_{2,k+1/2}^t - SOM_{2,k-1/2}^t}{\Delta z} \right) \right. \\ & \left. + \dots \right\} \quad (2.144) \end{aligned}$$

This formulation shows that each second-order moment, SOM_n , is dependent on the “diffusion” of many second-order moments, SOM_1, SOM_2, SOM_3 , etc. For each second-order moment, however, it is important to notice that it is dependent on the diffusion of itself as well. Equation (2.144) can be rewritten

$$\begin{aligned} \frac{SOM_{n,k+1/2}^{t+1} - SOM_{n,k+1/2}^t}{\Delta t} = & -\frac{1}{\Delta z} \left\{ \left(-A_{n,n,k+1} \frac{SOM_{n,k+3/2}^t - SOM_{n,k+1/2}^t}{\Delta z} \right. \right. \\ & \left. \left. - \left(-A_{n,n,k} \right) \frac{SOM_{n,k+1/2}^t - SOM_{n,k-1/2}^t}{\Delta z} \right) \right\} \quad (2.145) \\ & + \text{diffusion of the other } SOMs \end{aligned}$$

Considering that for each second-order moment, the dominant portion of the third-order moment transport term is the diffusion of the second-order moment itself, one can approximate equation (2.145) by neglecting the diffusion of the other second-order

moments. If one does, it is easy to recognize that equation (2.145) constitutes the simplest forward-in-time centered-in-space scheme for the diffusion equation. While this scheme is unconditionally unstable for advection, it is conditionally stable for diffusion with the condition for stability given by

$$\frac{A\Delta t}{(\Delta z)^2} \leq \frac{1}{2} \quad (2.146)$$

where A represents the maximum value of the “diffusion coefficient” calculated in the model. Since the diffusion of the other second-order moments was neglected, this stability criterion is really only a general guideline. This guideline has proven to be useful, however. A simple test was performed with the model where the maximum A for the third-order moments was determined to be 100. Using a 25 m grid size, the maximum allowable time step is calculated from equation (2.146) as 3.125 seconds. In practice, it was found that a time step of 3.2 seconds was usable, whereas the integration of the model was destroyed by computational instability when 3.3 seconds was used as the time step.

Recognizing that the diffusion of the second-order moments is the most likely culprit for computational instability, one may question whether it is prudent to calculate the divergence of the third-order moments in another way that allows a longer time step. The Dufort-Frankel scheme is unconditionally stable for the diffusion equation, so this would seem to be a good replacement candidate. Indeed, there is precedent for using this scheme. An early second-order closure turbulence model of Wyngaard and Coté (1974) used the Dufort-Frankel scheme with success. Using the same parameterization of the third-order moments as done in the current model, one could implement the Dufort-

Frankel scheme by changing how the transport term in the second-order moment equations is discretized. It could be discretized as

$$\begin{aligned}
\frac{SOM_{n,k+1/2}^{t+1} - SOM_{n,k+1/2}^{t-1}}{2\Delta t} = & -\frac{1}{\Delta z} \left\{ \left(-A_{n,1,k+1}^t \frac{SOM_{1,k+3/2}^t - SOM_{1,k+1/2}^{t+1}}{\Delta z} \right. \right. \\
& \left. \left. - \left(-A_{n,1,k}^t \right) \frac{SOM_{1,k+1/2}^{t-1} - SOM_{1,k-1/2}^t}{\Delta z} \right) \right. \\
& + \left(-A_{n,2,k+1}^t \frac{SOM_{2,k+3/2}^t - SOM_{2,k+1/2}^{t+1}}{\Delta z} \right. \\
& \left. \left. - \left(-A_{n,2,k}^t \right) \frac{SOM_{2,k+1/2}^{t-1} - SOM_{2,k-1/2}^t}{\Delta z} \right) \right. \\
& \left. + \dots \right\} \tag{2.147}
\end{aligned}$$

One must be careful when choosing the time step if the Dufort-Frankel scheme is used because it is known to be an inconsistent scheme. The ratio $\frac{\Delta t}{\Delta z}$ must go to zero as the grid is refined or else a different partial differential equation is solved than the diffusion equation. That is, the time step must decrease faster than the grid size.

Lastly, some realizability constraints are implemented in the model. The variances of horizontal velocity, vertical velocity, liquid water potential temperature, and total water specific humidity are positive-definite quantities. They are enforced to be greater than zero in the model. These variances are not guaranteed to be conserved, so they are simply set to zero if a negative value is calculated. Other positive-definite quantities including temperature and moisture variables are not enforced to be greater than zero since it was not required for the cases considered. One future improvement of the model would be to include a conservative scheme to maintain these positive-definite quantities. Many previous models included the ‘‘clipping approximation’’ of André et al. (1976) to

prevent the growth of unrealistic third-order moments (André et al. 1978, Krueger 1988).

Such an approximation was not necessary for the current model.

Chapter 3

One-Dimensional Model Results

3.1 Introduction

For testing and validation of the new turbulence model, five cases were simulated and compared with LES results. The first case is based on daytime data from day 33 of the Wangara experiment in Hay, Australia (Clarke et al. 1971). This particular day is noteworthy for its clear skies and weak large-scale forcing and is widely used as a test case for models studying the clear convective boundary layer. The Wangara case is used to test how well the new turbulence model works in the absence of complicating factors like clouds, precipitation, radiation, and strong shear. The final four cases are all taken from those performed by the GCSS Boundary Layer Cloud Working Group (BLCWG). The second case is the “smoke cloud” case that features a typical stratocumulus thermodynamic profile with a radiatively-active smoke cloud beneath the inversion. It is designed to test how the model handles stratocumulus cloud-top entrainment, without the complications arising from condensation and precipitation. The third case from the GCSS BLCWG also features a typical stratocumulus thermodynamic state but includes activated condensation and microphysics schemes. The initial and boundary conditions are adapted from the DYCOMS field campaign. The final two cases from the GCSS BLCWG feature

Case Name	Environment	Goal
Wangara (Section 3.2)	Clear convective boundary layer with weak large-scale forcing	Test first-, second-, and third-order moments without complications due to clouds, precipitation, or radiation
Smoke Cloud (Section 3.3)	Boundary layer with strong thermal inversion initially filled with radiatively-active smoke	Test stratocumulus-like cloud top entrainment without complications due to clouds and precipitation
DYCOMS RF02 (Section 3.4)	Nocturnal stratocumulus-topped boundary layer with drizzle	Test performance of complete model for a drizzling stratocumulus regime
BOMEX (Section 3.5)	Nonprecipitating daytime trade-wind cumulus boundary layer	Test performance of complete model without microphysics for a cumulus regime
RICO (Section 3.6)	Precipitating daytime trade-wind cumulus boundary layer	Test performance of complete model for a precipitating cumulus regime

Table 3.2 One-dimensional cases run by the SCM.

trade-wind cumulus. One case features a very low cloud amount without precipitation adapted from the BOMEX field campaign and the other features a slightly higher cloud fraction with light precipitation and is adapted from the RICO field campaign.

3.2 Daytime clear convective case: Wangara

This case is based on the evolution of a clear convective boundary layer over Hay, Australia on August 16, 1967, also known as day 33 of the Wangara Experiment. Observations show a very shallow initial mixed layer about 100 m deep after sunrise that deepens throughout the day from dry convection to roughly 1300 m at its greatest height before sunset. Although sunrise occurred at 7:12 a.m., the model is initialized with observations from 9:00 a.m. local time, and the experiment spans 8 daytime hours to 5:00

p.m. The model is configured with a constant grid size of 50 m and utilizes 40 levels to cover the 2 km domain. A time step of 5 s is used.

3.2.1 Initial conditions

To initialize the model, profiles of the mean quantities and second-order moments must be specified. The profiles of mean quantities are initialized according to observations and are shown in Figure 3.1. The initial potential temperature profile shows a very shallow mixed layer with its top near 100 m. Above the shallow mixed layer is an inversion of approximately 4 K, topped by a residual mixed layer from about 400 m to 700 m. Above the residual mixed layer, the atmosphere is stably stratified. The initial profile of specific humidity shows a less well-mixed layer to approximately 700 m, above which the specific humidity drops almost linearly from 3 g kg^{-1} to less than 1 g kg^{-1} at 1400 m. The initial wind profiles show that both the easterly and northerly components of the wind were light, although the easterly wind was between -3 and -2 m s^{-1} above the ground, decreasing somewhat linearly to calm above 1500 m. The northerly wind profile

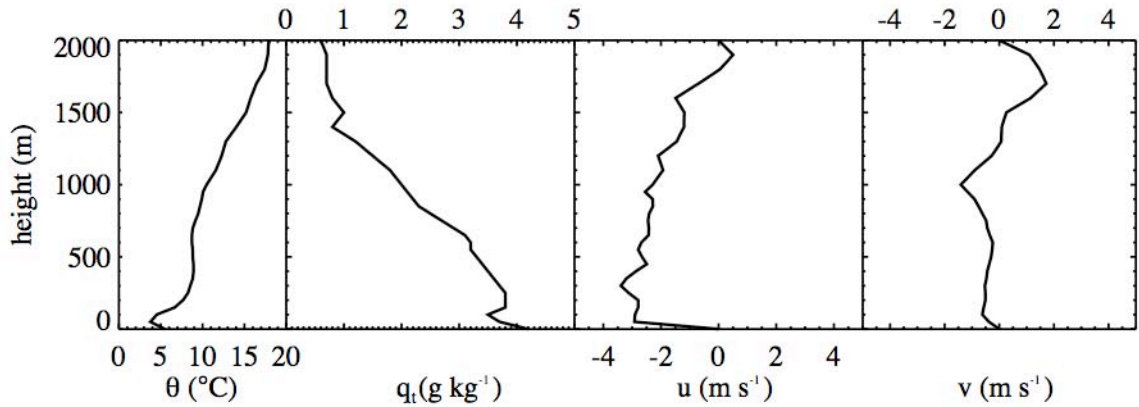


Figure 3.14 Initial profiles of potential temperature, specific humidity, easterly wind speed, and northerly wind speed for the Wangara case

features speeds generally less than 1 m s^{-1} , although a direction change occurs above 1500 m.

Initially, all second-order moments and third-order moments are set equal to zero above the surface layer. Values of the second-order moments at the surface layer are calculated according to Monin-Obukhov similarity theory as set forth in André et al.

(1978), hereafter AEA78. They are given by:

$$\overline{u'^2}_s = \overline{v'^2}_s = \begin{cases} 4u_*^2 + 0.3w_*^2 & \overline{w'\theta'_{l_s}} > 0 \\ 4u_*^2 & \overline{w'\theta'_{l_s}} < 0 \end{cases} \quad (3.1)$$

$$\overline{w'^2}_s = \begin{cases} \left[1.75 + 2(-\zeta)^{\frac{2}{3}} \right] u_*^2 & \zeta < 0 \\ 1.75u_*^2 & \zeta > 0 \end{cases} \quad (3.2)$$

$$\overline{w'u'}_s = \begin{cases} -u_*^2 & \overline{u_s} \geq 0 \\ u_*^2 & \overline{u_s} < 0 \end{cases} \quad (3.3)$$

$$\overline{w'v'}_s = \begin{cases} -u_*^2 & \overline{v_s} \geq 0 \\ u_*^2 & \overline{v_s} < 0 \end{cases} \quad (3.4)$$

$$\overline{\theta'^2}_{l_s} = \begin{cases} 4(1 - 8.3\zeta)^{-\frac{2}{3}} \left(\frac{\overline{w'\theta'_{l_s}}^2}{u_*^2} \right) & \zeta < 0 \\ 4 \left(\frac{\overline{w'\theta'_{l_s}}^2}{u_*^2} \right) & \zeta > 0 \end{cases} \quad (3.5)$$

$$\overline{\theta'q'_{l_s}} = \begin{cases} 4(1 - 8.3\zeta)^{-\frac{2}{3}} \left(\frac{\overline{w'\theta'_{l_s} w'q'_{l_s}}}{u_*^2} \right) & \zeta < 0 \\ 4 \left(\frac{\overline{w'\theta'_{l_s} w'q'_{l_s}}}{u_*^2} \right) & \zeta > 0 \end{cases} \quad (3.6)$$

$$\overline{q'_{t,s}} = \begin{cases} 4(1 - 8.3\zeta)^{-\frac{2}{3}} \left(\frac{\overline{w'q'_{t,s}}}{u_*^2} \right) & \zeta < 0 \\ 4 \left(\frac{\overline{w'q'_{t,s}}}{u_*^2} \right) & \zeta > 0 \end{cases} \quad (3.7)$$

where $\zeta = \frac{z}{L}$ is the nondimensional height, $L = \frac{-u_*^3}{0.35 \frac{g}{\theta_0} \overline{w'\theta'_{l,s}}}$ is the Monin-Obukhov

length, $w_* = \left(\frac{g}{\theta_0} \overline{w'\theta'_{l,s}} z_i \right)^{\frac{1}{3}}$ is the convective velocity, z_i is the boundary layer height, and

u_* , $\overline{w'\theta'_{l,s}}$, and $\overline{w'q'_{t,s}}$ are the friction velocity, surface heat flux, and surface specific

humidity flux, respectively. The final three quantities are specified according to AEA78 as well and are plotted in Figure 3.2. The surface heat flux is given by a sine curve with a half period of 10 hours and a maximum of 0.18 K m s^{-1} at hour 12.5. The moisture flux is calculated from the same curve with a proportionality coefficient:

$$\overline{w'\theta'_{l,s}}(t) = 0.18 \sin\left(\frac{\pi}{10}t - \frac{3\pi}{4}\right) \quad (3.8)$$

$$\overline{w'q'_{t,s}} = (1.3 \times 10^{-4} \text{ K}^{-1}) \cdot \overline{w'\theta'_{l,s}} \quad (3.9)$$

where t is the local time in hours and the units for the heat flux and moisture flux are K m s^{-1} and $(\text{g g}^{-1}) \text{ m s}^{-1}$, respectively. The friction velocity is calculated by linear interpolation from hourly values. Finally, to include the effects of a large-scale pressure gradient force, the geostrophic wind is specified according to Figure 3.3.

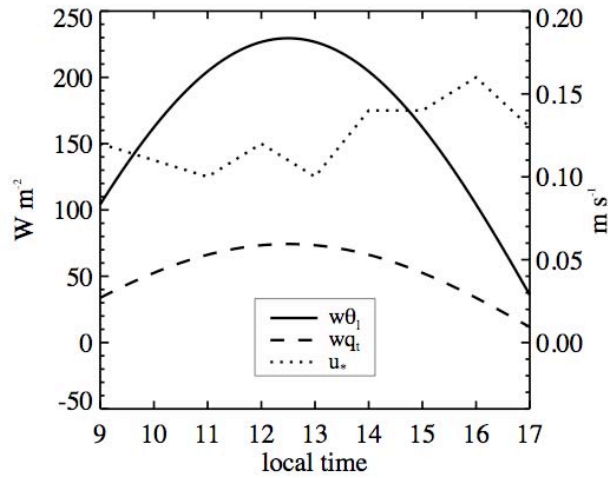


Figure 3.15 Specified time series of the surface heat flux (solid), the surface moisture flux (dashed), and the friction velocity (dotted) -- Note: The left axis is for the two surface fluxes and the right axis is for the friction velocity.

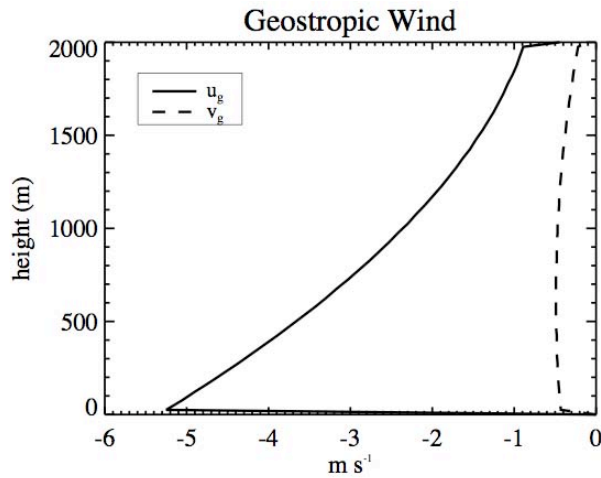


Figure 3.16 Profiles of the components of the geostrophic wind; easterly (solid); northerly (dashed).

3.2.2 Results

3.2.2.1 Mean variables

The output of the current model is compared with large-eddy simulation (LES) output from Deardorff (1974a) and (1974b), hereafter D74a and D74b, and observations from the measurement-intensive Wangara experiment, where available. Additional useful

comparisons can be made with the output from other single-column turbulence models, such as the models of Wyngaard and Coté (1974), Yamada and Mellor (1975), AEA78 and Sun and Ogura (1980). Shown in Figure 3.4 is the evolution of potential temperature. Instantaneous profiles are given for 9:00, 10:00, 11:00, 13:00, 15:00, and 17:00 local time and the position of the boundary layer top is indicated for each time by a labeled horizontal line. From the initial conditions (9:00), it is clear that a shallow mixed layer exists from the surface to roughly 100 m, above which a residual mixed layer is found that extends from about 300 to 700 m. Above the residual mixed layer to the top of the domain, potential temperature increases monotonically upward, indicating a stably stratified layer. By hour 10, the temperature close to the surface has warmed by about 2 K and the mixed layer has grown to about 200 m. The warming and mixing of the surface layer have yet to reach the residual mixed layer above at this time. By hour 11, however, the surface mixed layer has integrated the residual mixed layer above it, and the boundary

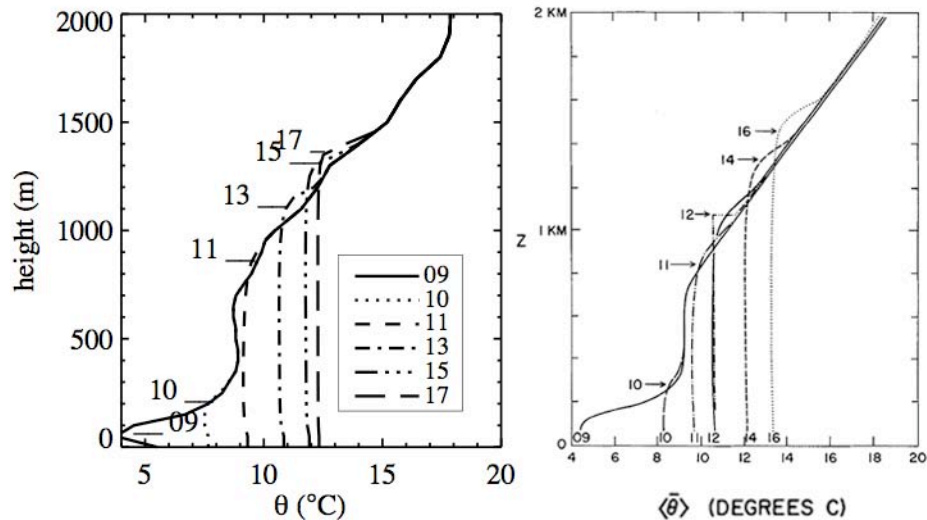


Figure 3.17 Evolution of the potential temperature from the current model (left) and Deardorff's LES (right). Labeled horizontal lines in both plots indicate the height of the boundary layer top at the indicated time.

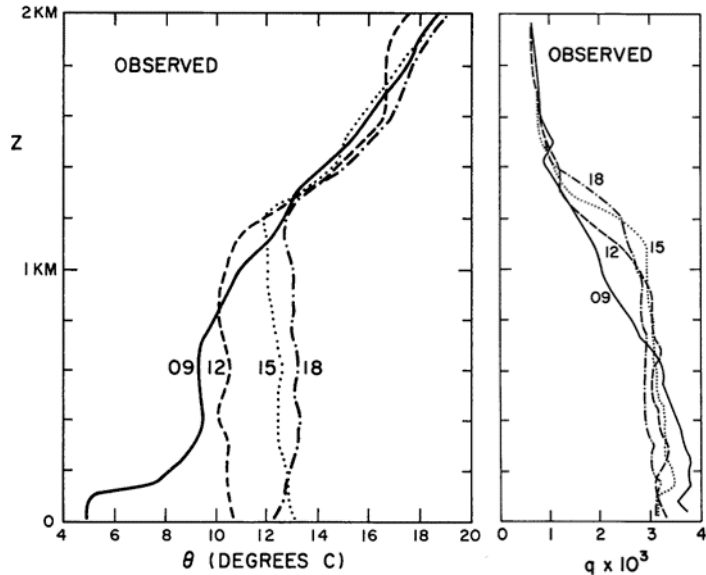


Figure 3.18 Observations of potential temperature and specific humidity at 09:00, 12:00, 15:00, and 18:00. {taken from Deardorff (1974a), figures 1b and 2b}

layer depth grew considerably from just above 200 m to about 900 m in one hour's time.

The profiles at times 13:00, 15:00, and 17:00 show continued growth of the mixed layer, albeit at a slower pace. By the final hour of the simulation, the potential temperature profile shows an almost constant value all the way to the boundary layer top at 1375 m.

The LES results show a very similar evolution, although the boundary layer increases in depth at a quicker pace after 12:00 (also see Figure 3.7). In addition, the LES shows the potential temperature of the layer increases to about 13.5 °C by 16:00, whereas the current single column model shows the boundary layer only warming to 12.4 °C by 17:00, a nontrivial difference of 1.1 °C. The observations (Figure 3.5) show that while not completely mixed, the boundary layer reaches an average value of about 13 °C, between the values of the two models.

Figure 3.6 shows profiles of the specific humidity for both the current model and Deardorff's LES, and the evolution is very similar to that of the potential temperature. As

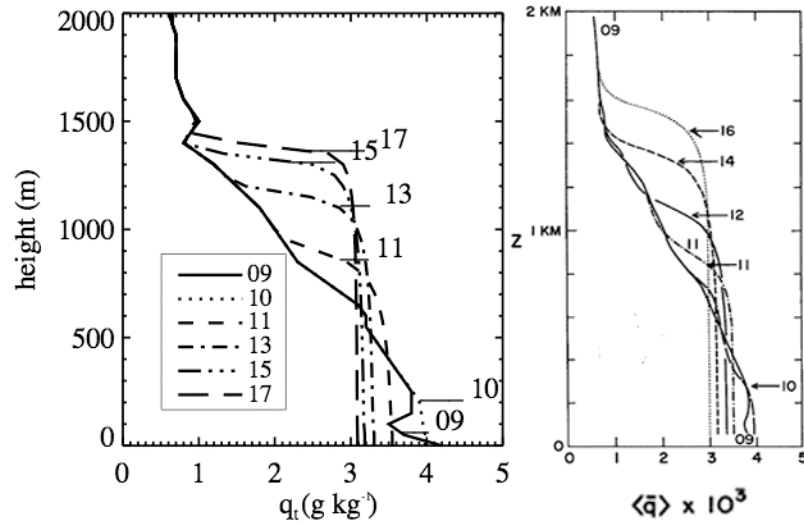


Figure 3.19 As in Figure 3.4, but for specific humidity.

the mixed layer grows, the dry air above the boundary layer gets mixed with relatively moist air near the surface. The result is a mixed layer that gets successively dryer throughout the day. As noted in AEA78 and Mahrt (1976), a small negative gradient in specific humidity is maintained throughout the mixed layer due to the much dryer air above the boundary layer and insufficient turbulence to create a perfectly mixed profile. In comparison with Deardorff's LES, it is once again evident that the LES-computed boundary layer becomes about 200 m deeper than observations suggest. In addition, the LES-computed boundary layer shows more drying than either the observations or the single column model.

Figure 3.7 shows the time evolution of the boundary layer height, calculated as the level of minimum heat flux, for both models. The boundary layer height estimated from the observed potential temperature and specific humidity profiles is shown with symbols. The single column model seems to represent the boundary layer depth better than Deardorff's LES, as the LES shows the boundary layer growing too fast after 12:00

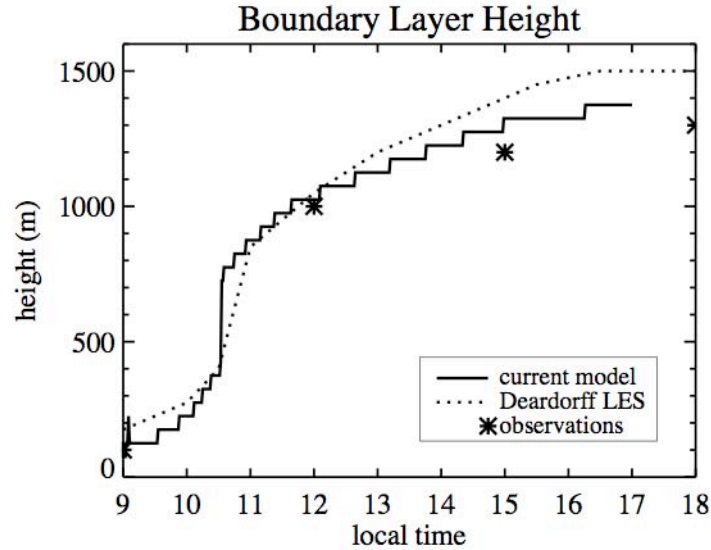


Figure 3.20 Time evolution of the boundary layer height for the current model (solid), Deardorff's LES (dotted), and observations (asterisk).

to about 16:00. By the end of the simulation, the LES boundary layer is 200 m, or about 15% too deep, while the single column model boundary layer is only 75 m, or about 6% too deep. D74a attributes the overestimation to a combination of factors including the lack of large-scale subsidence and the possible overestimation of surface fluxes, although the absence of large-scale subsidence in the current single-column model suggests that it may not be the primary reason.

The profiles of the mean easterly and northerly wind components as well as total wind speed are given in Figure 3.8. The easterly component shows an almost constant wind speed in the mixed layer that increases in time. Above the mixed layer, the easterly component is generally reduced by about 2 m s^{-1} . The northerly component oscillates around zero in the mixed layer and deviates between -1 and 1 m s^{-1} above it with a clear trend toward the geostrophic value. The wind speed profile shows minor changes, but in general, the initial wind speed profile is increased by about 1 m s^{-1} over the 8 hours of the simulation, except next to the surface where the wind speed only increases by about 0.5

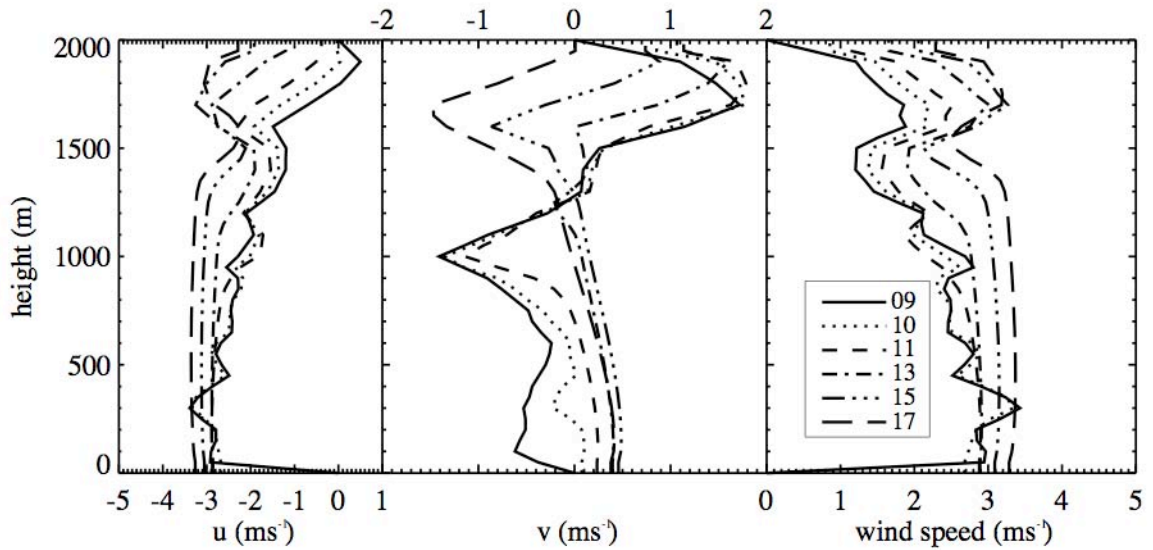


Figure 3.21 Profiles of the easterly and northerly components of the mean wind and the mean wind speed.

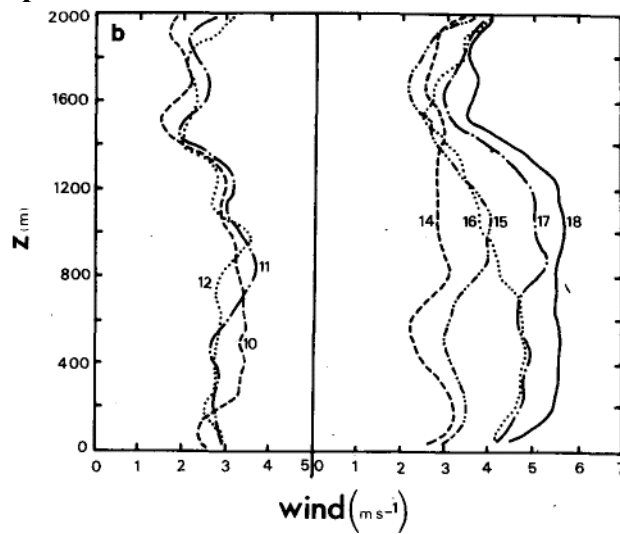


Figure 3.22 Observations of the wind speed {taken from Andre et al. (1978) figure 6b}.

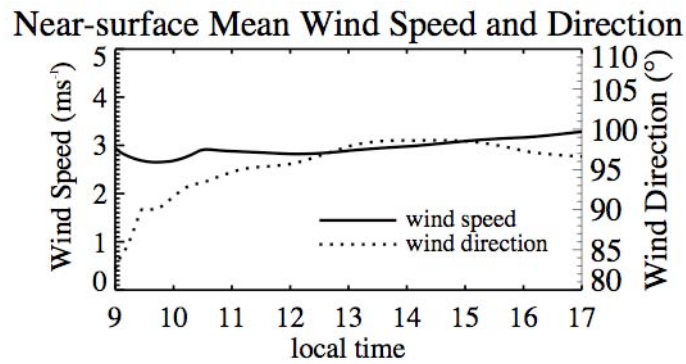


Figure 3.23 Near-surface wind speed (left axis) and direction (right axis)

m s^{-1} . The computed profiles of the wind speed compare favorably with the observations shown in Figure 3.9. The shape and evolution of the profiles are in general agreement, but the computed values underestimate the observed values of the wind speed in the later hours of the simulation. The near-surface wind speed and direction are given in Figure 3.10. As the profiles in figure 3.8 suggest, there is little notable change in the time series as well. The mean surface wind speed increases slowly throughout the day, from about 3.0 to 3.4 m s^{-1} , and the direction, while mostly from the east, switches from slightly from the east-northeast to slightly from the east-southeast, in good agreement with both observations and previous models.

3.2.2.2 Second-order moments and their budgets

The evolution of the sensible heat flux is shown in Figure 3.11. Given a mixed layer that changes temperature almost uniformly throughout the layer, the governing equation for the potential temperature, equation (2.59), mandates that the sensible heat flux profile is linear, and the slope of the line is dictated by the surface sensible heat flux and the boundary layer top height. The plots in Figure 3.11 demonstrate these characteristics. Furthermore, near the top of the boundary layer, a region of negative, or downward, sensible heat flux is present at nearly every time. These negative values are associated with the entrainment process, whereby air with high turbulent kinetic energy near the boundary layer top overshoots the temperature inversion and forces the warmer air above the inversion downward. Through this process, the boundary layer can grow in depth. The ratio of the downward heat flux to the surface heat flux is an important quantity and is an indicator of the strength of the entrainment. Sun and Ogura (1980) present a valuable discussion of this quantity, and they determine that observations

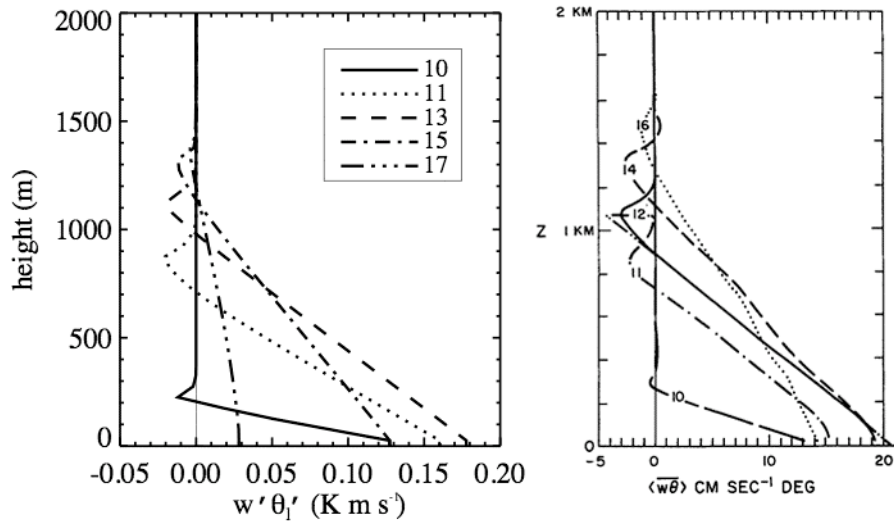


Figure 3.24 Evolution of the sensible heat flux from the current model (left) and Deardorff's LES (right). (Note the difference in units between the two plots.)

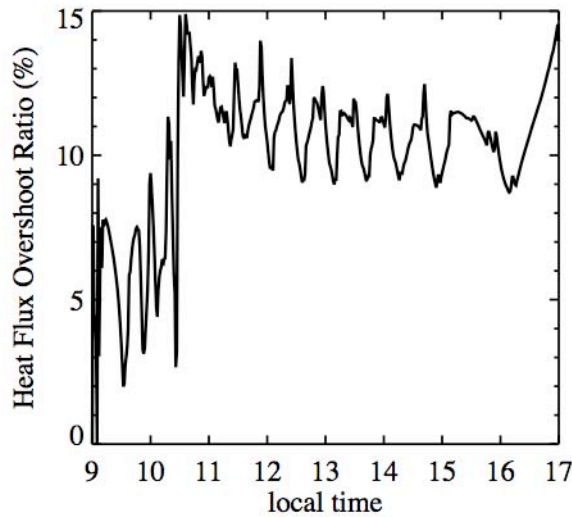


Figure 3.25 Evolution of the sensible heat flux overshoot ratio.

suggest that the ratio is around 5-8% in convective boundary layers. Much larger values of around 15-20% are seen in many models, including Deardorff's LES and the third order closure model of AEA78. Figure 3.12 shows the time series of this ratio for the current model. During the morning hours, the ratio oscillates around 6%, but increases to

oscillations around 11% in the afternoon. In general, these values align well with the observational record.

For more detailed analysis of the sensible heat flux, consider its nondimensional budget given in Figure 3.13. Each profile represents the individual terms in equation

(2.68): “T” is the transport (third-order moment) term given by $-\overline{\frac{\partial w'^2 \theta'_l}{\partial z}}$; “M” is the

mechanical production term given by $-\overline{w'^2} \frac{\partial \overline{\theta}_l}{\partial z}$; “P” is the pressure correlation term

given by $-\frac{c_6}{\tau_2} \overline{w' \theta'_l} - c_7 g \alpha \overline{\theta'_l \theta'_v}$; “B” is the buoyancy term given by $g \alpha \overline{\theta'_l \theta'_v}$; “D” is the

dissipation (diffusion) term given by $v_6 \overline{\frac{\partial^2 w' \theta'_l}{\partial z^2}}$. Even though the budget is shown for a

particular moment in time (14:00), the nondimensional representation changes little throughout the day, so it is sufficient to present a particular moment in time. The budget

resembles those presented in D74b and AEA78 and may be explained intuitively. The

positive heat flux near the ground is generated by two processes. Firstly, there are many

parcels near the ground that are warmer than their surroundings. This contributes to the

greater potential temperature variance and therefore the buoyancy term. Secondly, there

is a shallow superadiabatic layer where the potential temperature decreases with height.

This layer is mixed by turbulent eddies forcing warm parcels upward and contributes to

the positive mechanical production term. The transport profile shows divergence near the

surface and slight convergence around $\frac{z}{z_i} = 0.8 - 0.9$, signifying upward transport of the

heat flux generated near the ground by the preceding processes. Throughout much of the

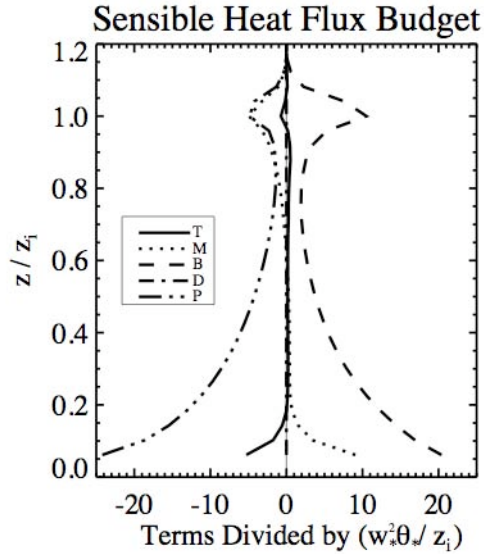


Figure 3.26 Terms in the sensible heat flux equation for hour 14 made nondimensional by $\frac{w_*^2 \theta_*}{z_i}$. See text for explanation of terms.

layer, the heat flux that is generated by buoyancy is countered by the return-to-isotropy portion of the pressure correlation term. Near the inversion, three terms become dominant. The heat flux is generated by the buoyancy term since there is increased potential temperature variance near the inversion, but this is countered by turbulent eddies forcing warmer air downward (mechanical term) and the influence of gravity on the pressure correlation term.

The evolution of the moisture flux profiles is given in Figure 3.14. Qualitative agreement of how the moisture flux evolves throughout the day is satisfactory upon comparison with LES, although the magnitudes differ considerably. The shape of the profiles during most of the day makes intuitive sense, given the evolution of the mean specific humidity. One would expect a linear profile from equation (2.60) since the evolution of the specific humidity profile shows a mostly mixed layer with nearly uniform moisture content. Since the layer is growing into dryer air above, there is upward

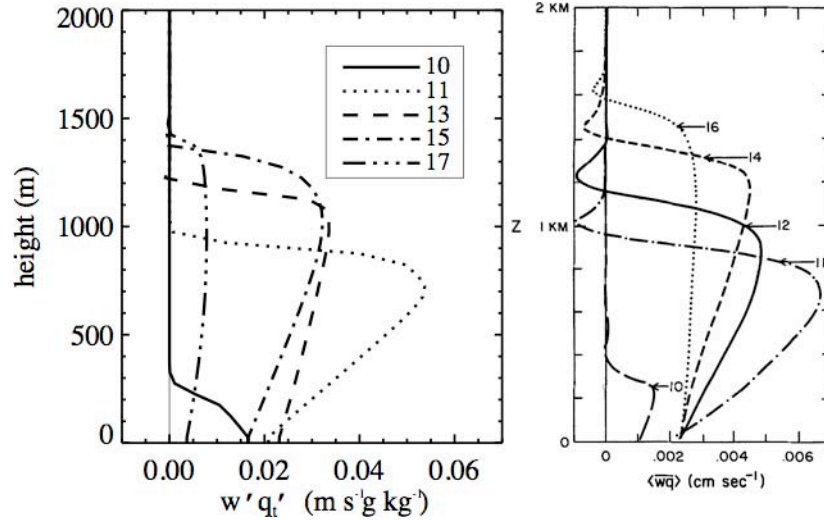


Figure 3.27 Evolution of the moisture flux from the current model (left) and Deardorff's LES (right) (Note the difference in units between the plots.)

moisture flux near the boundary layer top. The slope is then determined by the surface moisture flux. Since the surface moisture flux is less than the upward moisture flux occurring at the boundary layer top, the moisture flux increases linearly with height to the boundary layer top. A consequence of more moisture being fluxed out of the boundary layer than is being replenished from the surface is that the boundary layer becomes uniformly drier, as is shown in Figure 3.6.

As discussed in D74a, Wyngaard and Cote (1974), and AEA78, anomalous negative moisture flux appears near the boundary layer top in many turbulence models. This feature is not observed in nature, and its source has been traced to the parameterization of the pressure correlation term in the moisture flux equation, i.e. (2.69). The current model nearly eliminates this anomaly, although a hint of negative moisture flux near the inversion exists. The reason for this improvement can be seen by examining the moisture flux budget shown in Figure 3.15. Near the inversion, the buoyancy term, $\overline{g\alpha q'_v \theta'_v}$, is large and negative. The mechanical production and pressure correlation terms

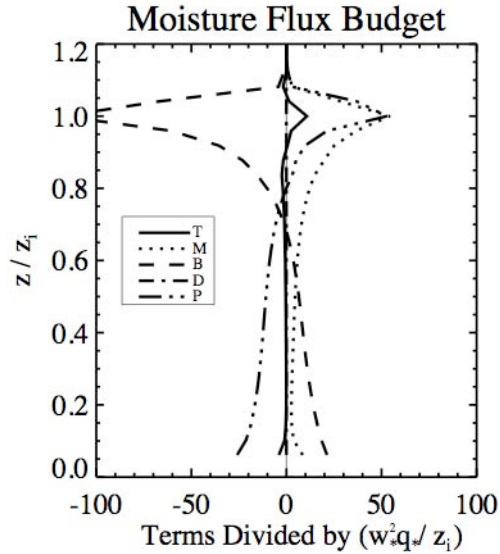


Figure 3.28 Terms in the moisture flux equation made nondimensional by $\frac{w_*^2 q_*}{z_i}$.

act almost equally to balance the large negative buoyancy term, with a small positive contribution from the transport term as well.

The evolutions of the easterly and northerly momentum fluxes are shown in Figure 3.16. Plots from Deardorff's LES are not shown because they use a coordinate system oriented with the surface wind that makes direct comparison difficult. Agreement is satisfactory with studies of the Wangara boundary layer that utilize the conventional coordinate orientation, such as AEA78 and Sun and Ogura (1980) (not shown). The easterly momentum flux profiles show positive values near the surface and a nearly linear decrease to a negative value near the boundary layer top. Since the mean easterly wind is negative (from the east), positive values of the easterly wind flux near the surface indicate a downward flux of easterly momentum and is consistent with the surface acting as a drag on the wind. As discussed in AEA78, the linear shape to the boundary layer top can be explained by differentiation of equation (2.61) with height. If easterly momentum

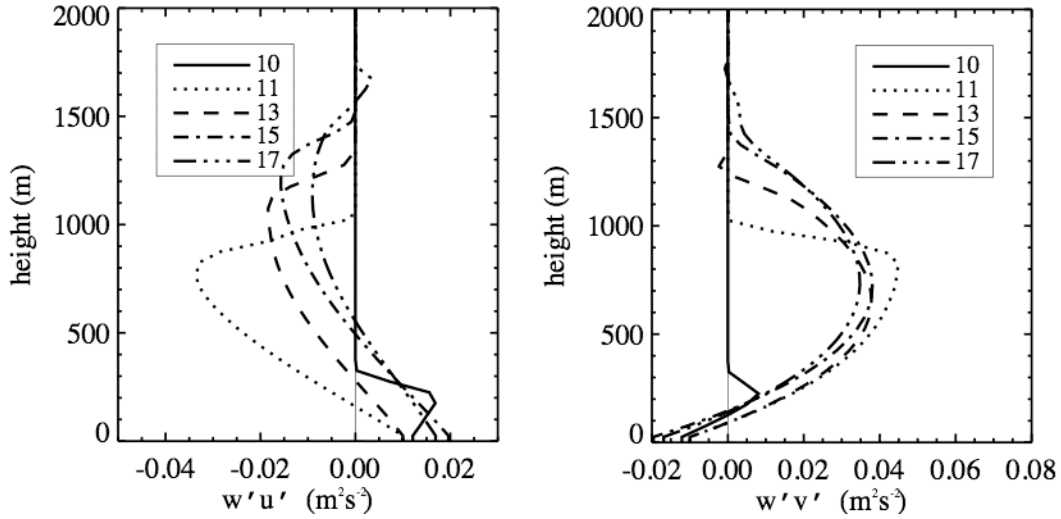


Figure 3.29 Evolution of easterly (left) and northerly (right) momentum fluxes.

is mostly well-mixed in the boundary layer and the northerly geostrophic wind is mostly

constant with height (see Figure 3.3), differentiation yields $\frac{\partial^2 \overline{w'u'}}{\partial z^2} \approx 0$, or a linear

profile. A similar analysis applies to the northerly momentum flux profiles. The negative values near the surface indicate a downward flux of northerly momentum, and a drag on the northerly wind. Differentiation of equation (2.62) with height demonstrates why the

northerly momentum flux profiles exhibit a parabolic shape: $\frac{\partial^2 \overline{w'v'}}{\partial z^2} = f \frac{\partial \overline{u_g}}{\partial z} = \text{constant}$.

The easterly component of the horizontal velocity variance is shown in Figure 3.17, and the vertical velocity variance is shown in Figure 3.18. The dimensionless horizontal velocity variance is nearly stationary throughout the day, but is overestimated from $\frac{z}{z_i} = 0.2 - 0.8$ compared with Deardorff's LES. The dimensionless vertical velocity variance is also nearly stationary throughout the integration period. As discussed in D74b, AEA78, and Sun and Ogura (1980), the vertical velocity variance exhibits a shape well-known and expected in buoyancy driven boundary layers; it increases

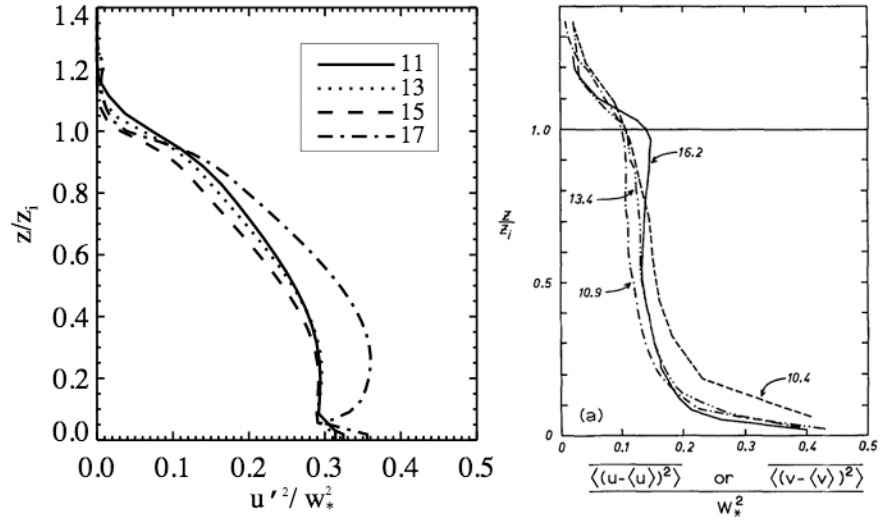


Figure 3.30 Evolution of the easterly component of the horizontal velocity variance from the current model (left) and Deardorff's LES (right).

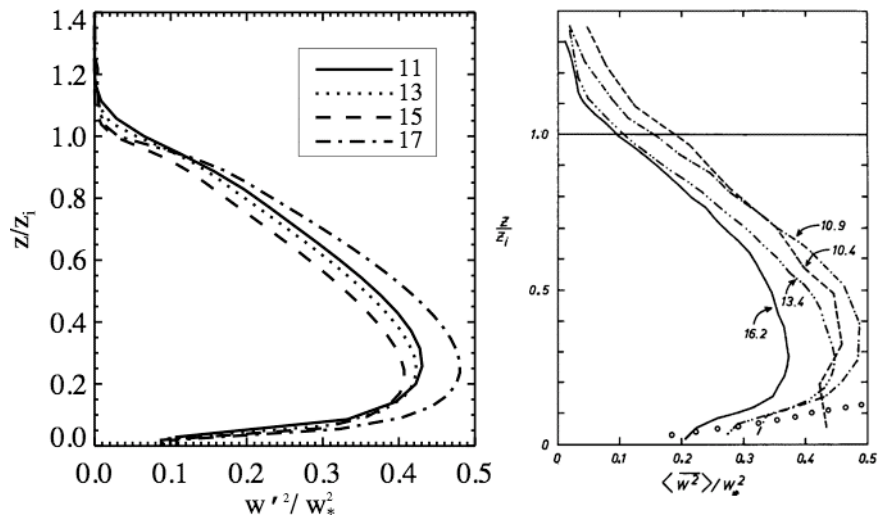


Figure 3.31 Evolution of the vertical velocity variance for the current model for the current model (left) and Deardorff's LES (right).

smoothly from the surface to roughly $\frac{z}{z_i} \approx \frac{1}{3}$ and decreases steadily to zero at a height above the boundary layer top. Positive vertical velocity variance above the boundary layer top is associated with the strength of the entrainment. The fact that Deardorff's LES exhibits more vertical velocity variance above the boundary layer top reinforces the notion that entrainment is too strong in that model, leading to a slightly warmer and dryer

boundary layer, and more negative heat flux near the inversion, as already discussed. The discrepancy in vertical velocity variance magnitude between the two models is minor, with the current model slightly underestimating this quantity compared to the LES. Comparison with other studies suggests Deardorff's LES gives a slight overestimate, suggesting that the underestimate in the current model constitutes improvement.

The turbulent kinetic energy (TKE) is one of the most useful quantities for studying the boundary layer since it provides a simple measure of how strong turbulence is. It plays an integral role in coupling the surface with the free atmosphere by partially determining fluxes of heat, moisture, and momentum (Stull 1988). A time-height cross-section is presented in Figure 3.19 and its budget is presented in Figure 3.20. The budget shows that there are three dominating terms: a positive buoyancy term throughout most of the boundary layer to about $z/z_i = 0.9$, a negative dissipation term that cancels out much of the buoyancy term, and a transport term that fluxes TKE from near the surface to near the inversion. The mechanical production term plays a minor positive role near the inversion and even less so near the surface. Even though initially there is only TKE at the surface, it increases to fill the depth of the boundary layer due to buoyant production and upward vertical transport spinning up turbulence faster than it is being dissipated. At about 10:30, there is a dramatic increase in TKE associated with the surface mixed layer combining with the residual mixed layer from the previous day. The TKE continues to increase in magnitude to about 13:00, roughly coinciding with the maximum surface heat flux and maximum buoyancy production. Thereafter, the magnitude of the TKE starts to slowly decrease throughout much of the layer, and the rate at which the boundary layer

deepens decreases as well. By about 15:30, dissipation of TKE dominates until the end of the simulation where very little turbulence remains in the mixed layer.

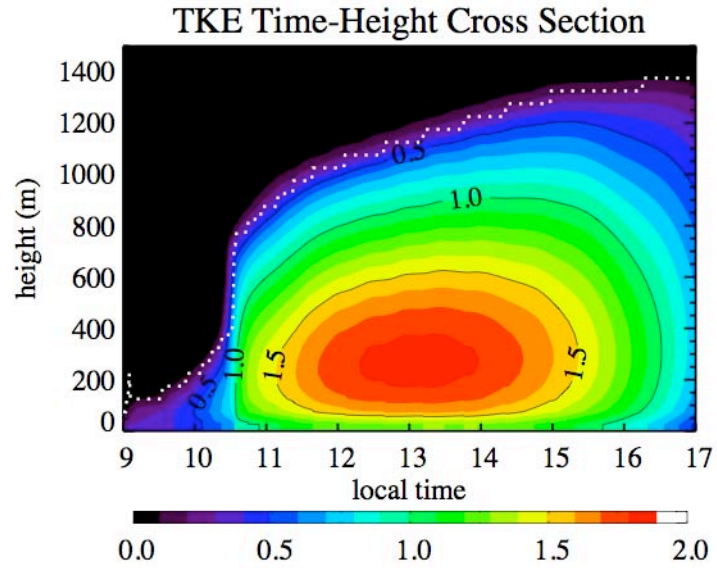


Figure 3.32 Time-height cross-section of the turbulent kinetic energy (m^2s^{-2}). The white dotted line indicates the boundary layer top height.

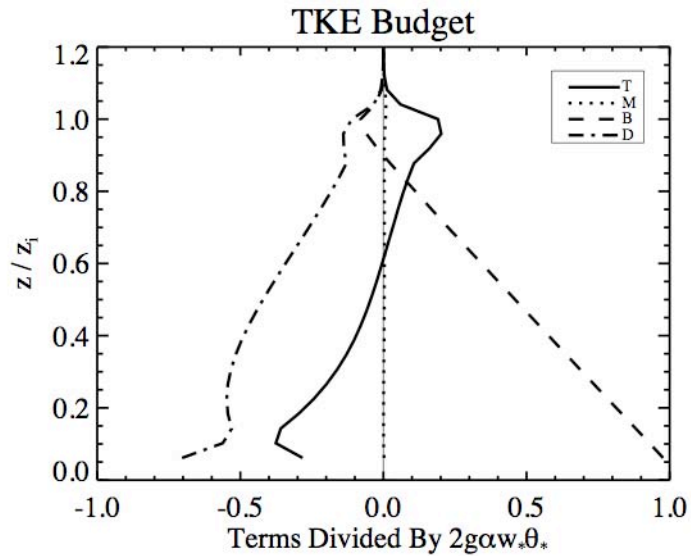


Figure 3.33 Terms in the turbulent kinetic energy equation made dimensionless by $2g\alpha w_*\theta_*$.

The evolution of potential temperature variance and its budget are given in Figures 3.21 and 3.22, respectively. Two maxima are evident in the profiles of potential temperature variance. The lower maximum is associated with numerous warm thermals originating near the surface. The upper maximum near the inversion is associated with entrainment. Turbulence near the inversion forces relatively cool mixed layer air upward into the stable layer above, and warm air above the inversion is forced downward. The magnitude of the potential temperature variance in the current model matches well with Deardorff's LES, but the shape of the peak is narrower in the current model than the LES. This is probably a consequence of weaker entrainment in the current model compared with LES. The potential temperature variance budget shows that production is accomplished by the mechanical production term near the surface and at the inversion, and is transported upward from the surface and downward from the inversion by the transport term.

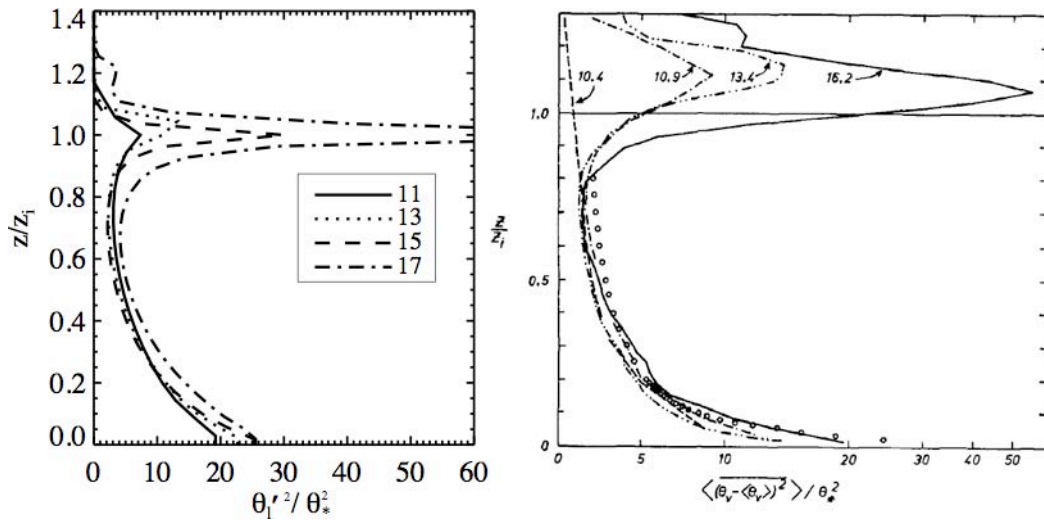


Figure 3.34 Evolution of potential temperature variance for the current model (left) and Deardorff's LES (right).

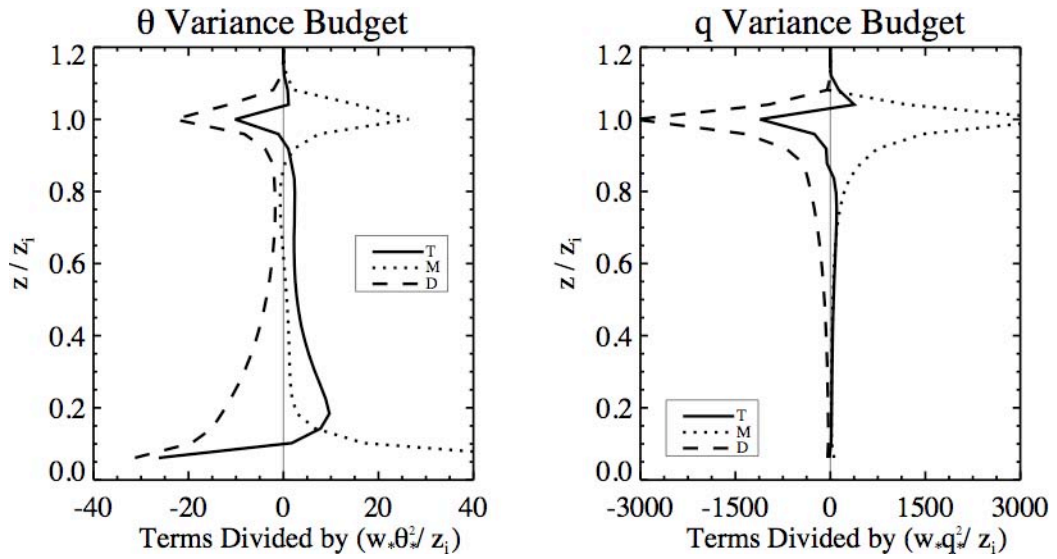


Figure 3.35 The budgets of potential temperature variance (left) and specific humidity variance (right).

The final two second-order moments to be discussed are the specific humidity variance and the covariance of potential temperature and specific humidity. Figures 3.23 and 3.24 show their evolution, and Figure 3.22 shows the budget for specific humidity variance. The profiles of specific humidity variance show very little variance near the surface increasing to a single maximum at the inversion. This makes intuitive sense and

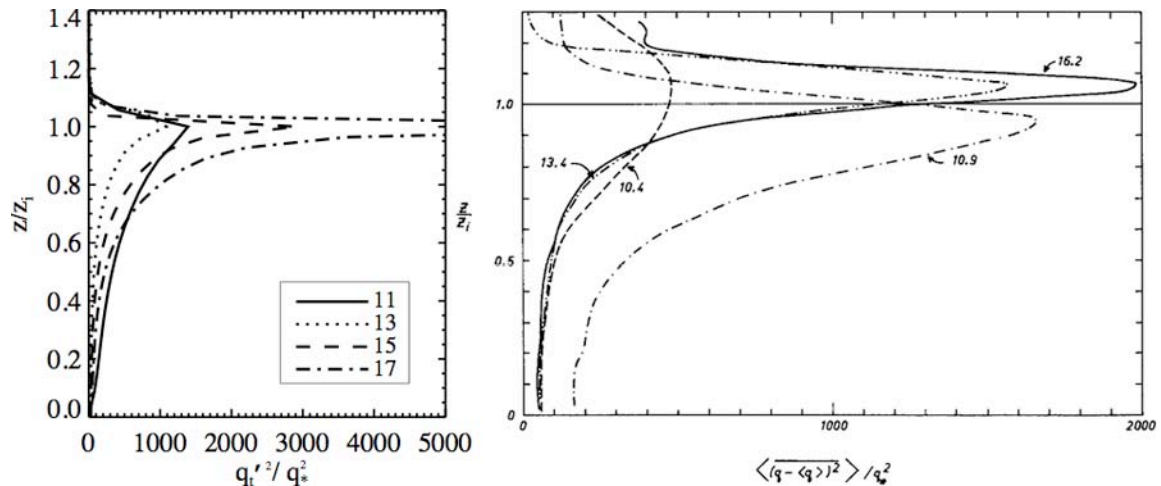


Figure 3.36 Evolution of the specific humidity variance for the current model (left) and Deardorff's LES (right).

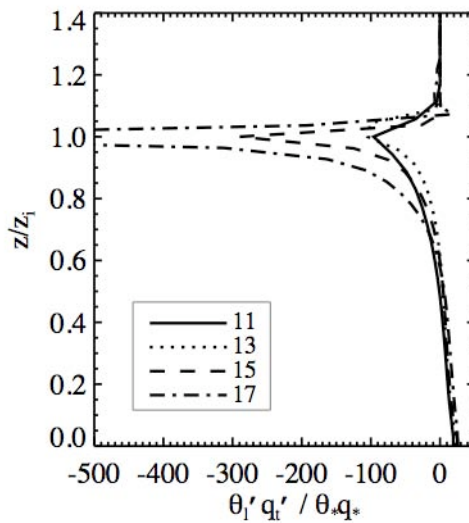


Figure 3.37 Evolution of the covariance of potential temperature and specific humidity for the current model.

agrees with both observations and other models. Parcels near the surface are mostly uniformly moist. Near the inversion, however, entrainment mixes the relatively dry air above the inversion with the relatively moist air below. The variance budget reinforces this concept, since the two terms of most importance are the mechanical production and associated dissipation at the inversion. The profiles of the covariance of potential temperature and specific humidity are also in good agreement with observations and models. Positive values near the surface indicate that parcels are both warm and moist, having been in contact with the surface and modified by surface heat and moisture fluxes. Negative values are present near the inversion as relatively cool and moist boundary layer air is forced into the drier and warmer air above the inversion, and vice versa.

3.2.2.3 Selected third-order moments

Shown in Figure 3.24 are the nondimensional profiles of the flux of turbulent kinetic energy from the current model and from the fully prognostic third-order closure model of AEA78. The laboratory experiment of Willis and Deardorff (1974) shows that

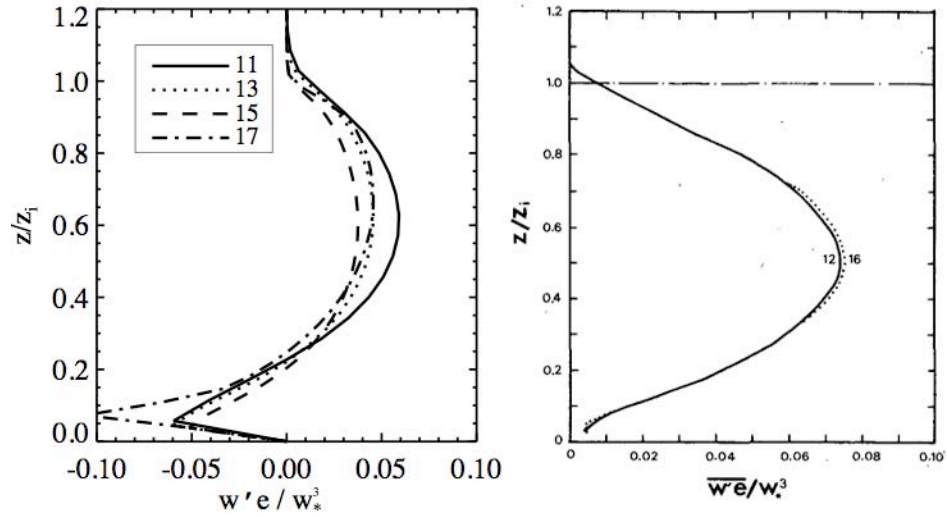


Figure 3.38 Evolution of the flux of turbulent kinetic energy for the current model (left) and Andre et al. (1978) (right).

the flux of turbulent kinetic energy has a nearly parabolic shape with a maximum near

$\frac{z}{z_i} \approx 0.5$ and a value near 0.12, and the aircraft observations found in that study roughly

agree with the laboratory results (not shown). The numerical model of AEA78 generates

a TKE flux profile of a similar shape that remains constant through the daytime of their

simulation and has a maximum value near 0.07. The current model generates profiles for

the TKE flux that are not as constant throughout the simulation. The maximum TKE flux

decreases from 11:00 to 15:00 and increases to 17:00. The TKE flux profile has a near

parabolic shape with a maximum in the middle of the boundary layer with a value near

0.05, but it also exhibits a negative “tail” below $\frac{z}{z_i} = 0.2$, which is not found AEA78’s

profiles. The negative values of TKE flux near the surface have been reproduced in the

laboratory experiment of Willis and Deardorff (1974) and the model of Sun and Ogura

(1980). The transport terms in the equations for the TKE components are flux divergence

terms, so that the vertical derivative of the TKE flux is what is important. The negative

values of TKE flux help to create the correct TKE flux divergence, so even though the

TKE flux peak magnitude is reduced compared to the model of AEA78, the flux divergence terms end up being similar.

AEA78 point out that correctly calculating the divergence of the vertical flux of turbulent kinetic energy, $\frac{1}{2}(\overline{w'u'^2} + \overline{w'v'^2} + \overline{w'^3})$, is a key requirement for simulating convective boundary layers since the turbulent kinetic energy needed for entrainment is not produced near the inversion (see the TKE budget, Figure 3.20). It must be transported from where it is produced by buoyancy lower in the layer to the boundary layer top. Indeed, AEA78 justify their use of fully prognostic third-order moments for this very reason. They argue that the reason a second-order closure model like the one used in Yamada and Mellor (1975) underpredicts the height of the boundary layer and that a fully prognostic third-order closure model accurately simulates boundary layer growth is that not enough TKE is transported to the boundary layer top to support rigorous entrainment in the simpler model, whereas transport is sufficient in the higher-order closure model. Although the shape of the TKE flux profile differs from the profile produced by the fully prognostic third-order closure of AEA78, they produce very similar TKE flux divergence profiles, and the transport term in the TKE budget profile for both of the models matches reasonably well. For this reason, both models produce realistic and satisfactory growth of the boundary layer.

The evolution of four other third-order moments is presented in Figure 3.26. The upper left portion shows the vertical flux of the sensible heat flux. It shows that the flux of the heat flux is almost always upward, which is consistent with the fact that most of the heat flux is generated by the buoyancy production term in the lower half of the boundary layer according to its budget (Figure 3.13). Upon comparison with

observational values and other numerical studies found in Sun and Ogura (1980) and shown from that work in Figure 3.27 (left panel), it appears that the current model's results align better with the observations than the previous models. The vertical flux of potential temperature variance in the lower left panel, indicates that there is an upward vertical flux of potential temperature variance. This result also follows intuitively from the potential temperature variance budget (Figure 3.22) that shows most of the production of variance is from mechanical means near the surface. This variance is transported upward with the buoyant thermals. Comparison with observations in Figure 3.27 (right panel) shows good agreement with observations except very close to the surface. This discrepancy arises due to the imposition of zero boundary conditions in the current model.

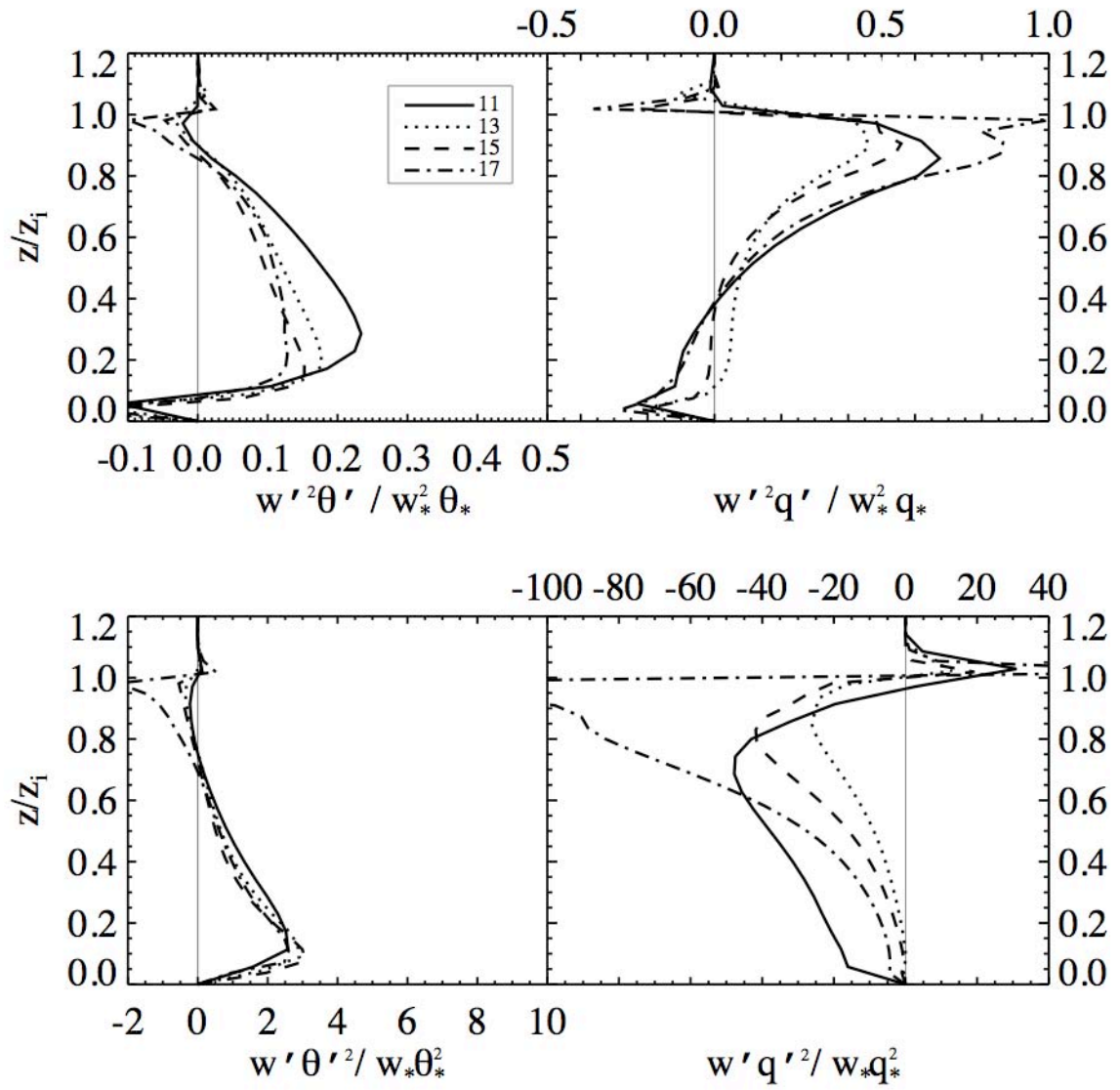


Figure 3.39 Evolution of the vertical fluxes of the sensible heat flux (upper left), moisture flux (upper right), potential temperature variance (lower left), and specific humidity variance (lower right).

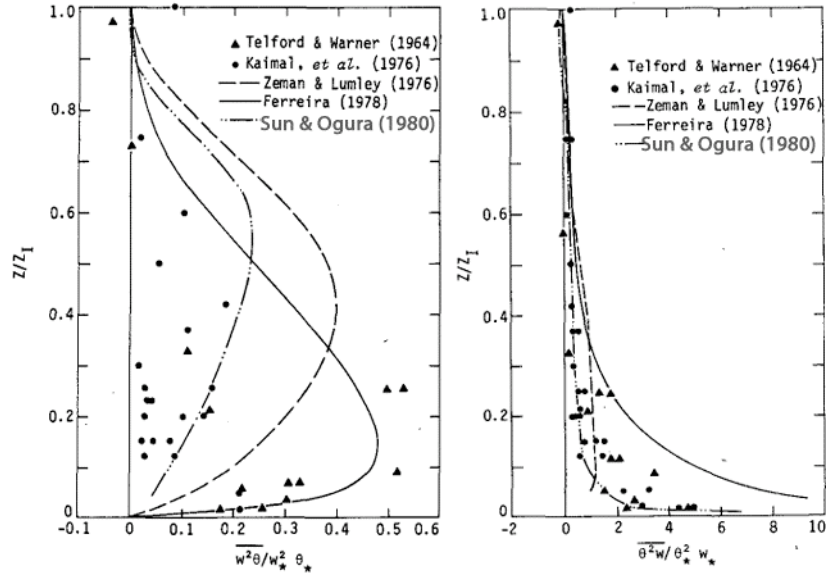


Figure 3.40 Profiles of the fluxes of sensible heat flux (left) and potential temperature variance (right) from Sun and Ogura (1980) and other studies found within that work. Symbols represent data from observational studies, whereas lines indicate model results.

3.3 Smoke cloud case

The first case study of the GCSS BLCWG featured a stratocumulus-topped boundary layer and demonstrated that many different LES codes could successfully represent the general structure of such a layer. It also highlighted the fact that the different codes differed markedly in their calculated entrainment velocity. Since the entrainment process in models is affected by a variety of factors, including the dynamics core, turbulence, radiation, and microphysics, it was impossible to ascertain the cause of the entrainment velocity discrepancy (Moeng et al. 1996). As a result, the second case of the GCSS BLCWG was developed with the goal of isolating the impacts of the dynamics core and the turbulence scheme on the entrainment process. This was accomplished by eliminating liquid clouds and replacing them with a radiatively-active smoke layer. This smoke layer was given properties such that the radiative cooling at the top resembled that of a typical stratocumulus cloud. In this way, it was found possible to study how the

entrainment velocity differs from model to model based solely on its representation of boundary layer dynamics and turbulence (Bretherton et al. 1999). This case was simulated with the current model and its output is compared with the participating GCSS BLCWG models.

3.3.1 Initial conditions

The initial conditions for this case are specified in Bretherton et al. (1999) and are as follows. The profiles of potential temperature and smoke concentration, S , are given by

$$\theta = \begin{cases} 288 & z \leq 687.5 \\ 288 + 0.28(z - 687.5) & 687.5 < z < 712.5 \\ 295 + 1 \times 10^{-4}(z - 712.5) & z \geq 712.5 \end{cases} \quad (3.10)$$

and

$$S = \begin{cases} 1 & z \leq 687.5 \\ 1 - 0.04(z - 687.5) & 687.5 < z < 712.5 \\ 0 & z \geq 712.5 \end{cases} \quad (3.11)$$

These profiles form a well-mixed layer below 687.5 m with a uniform smoke concentration of 1. A thin transitional layer separates the well-mixed and smoke-filled boundary layer from a slightly statically stable clear layer above. Initially, there is zero mean wind. The TKE is initialized to $1 \text{ m}^2 \text{ s}^{-2}$ everywhere below 700 m, and this TKE is assumed to be isotropic, meaning that all three components of the TKE contain an equal share of the total. All other second-order moments and third-order moments are initialized to zero. The initial potential temperature profile is modified by including a random perturbation of $[-0.1 \text{ K}, 0.1 \text{ K}]$ below the inversion (700 m). The surface pressure is initialized to 1000 hPa, and the profiles of pressure and density are generated assuming

hydrostatic equilibrium and an isentropic profile with $\theta_0 = 291.5$ K . Since the current model is prone to erroneous negative tracer flux above the inversion (see section 3.2.2.2), a global multiplicative hole-filler is employed to ensure positive smoke concentration values.

Finally, to make the smoke radiatively-active, the longwave radiation flux is defined as

$$F_{k+\frac{1}{2}} = F_0 \exp\left(-K_a \sum_{l=k+1}^{l=ktop} \rho_l S_l \Delta z\right) \quad (3.12)$$

where $F_0 = 60 \text{ Wm}^{-2}$ is the longwave flux exiting the top of the domain, $K_a=0.02 \text{ m}^2 \text{ kg}^{-1}$ is the absorptivity of the smoke, and the quantity in sigma notation represents the smoke path, or the amount of smoke above the current level that the longwave flux must travel through. The subscript of the flux indicates that it is calculated at half levels, between the levels where the mean quantities “reside.” Given this profile of the flux of longwave radiation, its divergence is calculated to determine the time rate of change of potential temperature due to radiation:

$$\frac{\partial \theta}{\partial t}_k = \frac{-\left(F_{k+\frac{1}{2}} - F_{k-\frac{1}{2}}\right)}{\rho_k C_p \Delta z}. \quad (3.13)$$

According to Bretherton et al. (1999), this specification of the smoke layer generates radiative cooling of about 4 K h^{-1} at the top of the boundary layer, which is inline with typical values for stratocumulus-topped boundary layers. Fifty layers are used at an even spacing of 25 m for a total domain depth of 1250 m. The simulation is run for 3 simulated hours with a time step of 0.5 s.

3.3.2 Results

3.3.2.1 Mean quantities and entrainment parameters

Bretherton et al. (1999) compiled model output from several codes that were used to simulate the smoke cloud case and performed an intercomparison. They presented results from many model configurations, including one-dimensional (1D) single-column models, two-dimensional (2D) models, and three-dimensional (3D) LES. For further analysis, they also divided their three-dimensional results into groups that submitted finer-resolution results (as fine as 5 m in the vertical), and those that used monotone or non-monotone advection schemes. They found that the finer-resolution three-dimensional LES models produced the most realistic results and best represented the entrainment process, and for this reason, these results may be used as a proxy for observations in their absence.

Profiles of potential temperature and smoke concentration are given in Figures 3.28 and 3.29 for the current model and the high-resolution 3D LES from Bretherton et al. (1999). The initial profiles are shown as dotted lines, but all others represent an average profile from hours 2-3. The initial potential temperature profile shows a well-mixed layer (except for small random perturbations) with a strong 7 K inversion at 700 m. The averaged profile from the last hour of the simulation shows that the mixed layer has cooled by about 0.5 K and that the inversion has been elevated by about 25 m.

Comparison with the LES results shows that the current model reproduces the average temperature and structure of the mixed layer well. The slight curvature at the top of the mixed layer indicative of radiative cooling that is evident in the LES results is absent in the current model's profile, however. The smoke concentration profile from the current

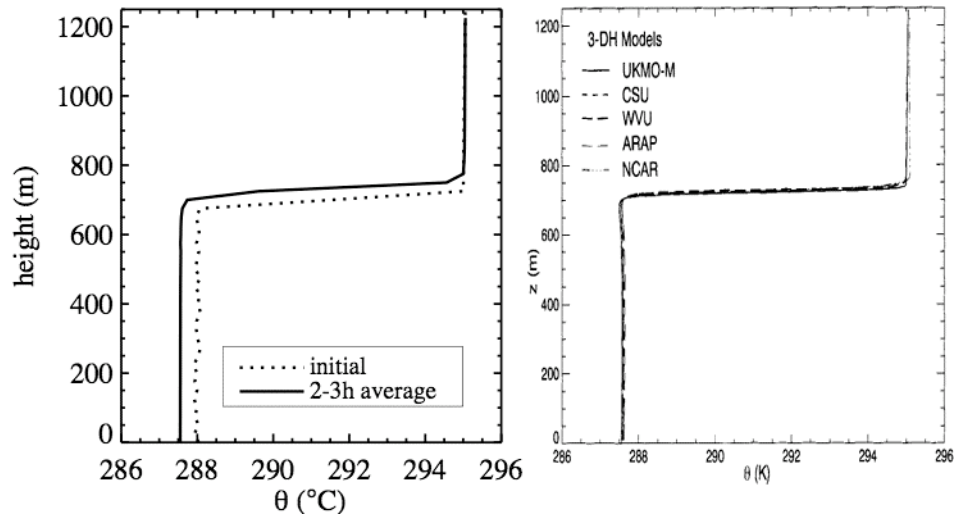


Figure 3.28 Profiles of potential temperature for the current model (left) and fine resolution three-dimensional LES from Bretherton et al. (1999); all profiles except the one labeled "initial" are averages from hours 2-3.

model demonstrates similar characteristics as the potential temperature profiles. Namely, the mean smoke concentration and the structure of profiles match LES well, but the sharpness of the inversion is reduced compared to the LES results. Further, the smoke profile of the current model is not as uniformly mixed as the LES results, and shows a steady decrease with height. While the average values of smoke concentration of the

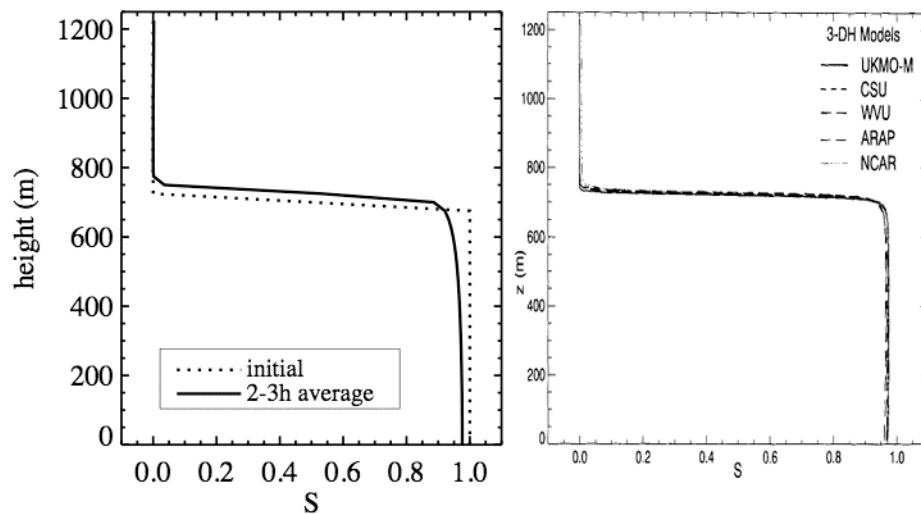


Figure 3.29 As in Figure 3.27 but for the smoke concentration.

models may be similar, the current model produces a smoke concentration that is slightly too high near the surface and too low near the inversion.

Bretherton et al. (1999) discuss the effect of vertical resolution on the structure of the inversion and conclude that the standard resolution of this case (25 m in the vertical) is insufficient to resolve the needed variability at the inversion, but that the finer resolution (5 m vertical resolution) models show a marked improvement. This conclusion was based on the fact that the inversion thickness, defined as the distance between the $S=0.1$ and $S=0.9$ contours, was almost always less than or equal to $2\Delta z$ in the standard resolution models, but that the inversion thickness in the high-resolution models was almost always greater than $2\Delta z$, often in the range of $2\Delta z$ to $6\Delta z$. Further, Bretherton et al. (1999) note that the average inversion thickness is three times as large in the standard resolution models versus the high-resolution models, 50 m to about 17 m. The time-height cross-section of the smoke concentration for the current model is shown in Figure

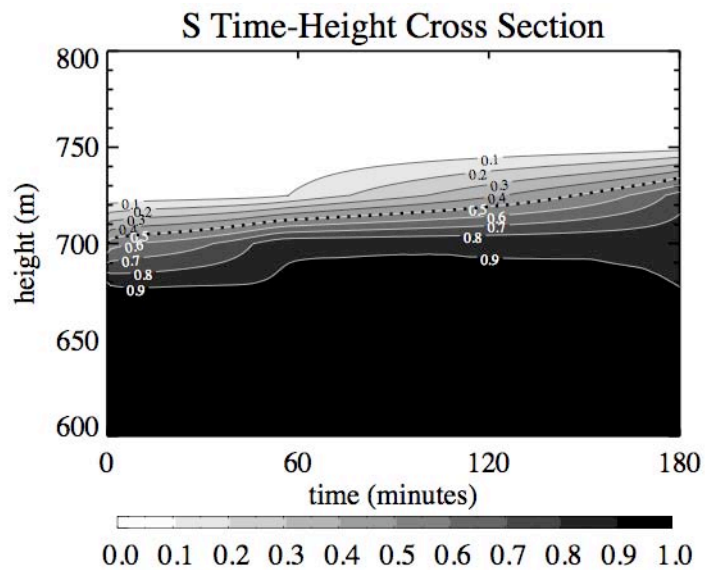


Figure 3.30 Time-height cross-section of the smoke concentration for the current model.

3.30. Initially, the inversion thickness is about 50 m ($2\Delta z$), but grows to about 75 m ($3\Delta z$) by the end of the simulation. These results suggest that, like the standard resolution 3D LES models, the current model's resolution is insufficient to represent the inversion in a realistic way since only two or three grid levels define the inversion.

For this case, the boundary layer depth, z_i , is defined as the height where the smoke concentration is exactly one half. Due to the relative coarseness of resolution, this value is calculated by linear interpolation. Figure 3.31 shows the evolution of the mixed layer depth for the different types of models participating in the GCSS intercomparison and for the current model. The high-resolution 3D LES models show almost a linear increase in mixed layer depth to about 730 m by the end of the simulation and this is considered the benchmark. The standard resolution 3D LES models are split according to their advection scheme, monotone ("3-DM") and non-monotone ("3-DN"). The monotone 3D models also show a linear increase with time that averages about 730 m by the end of the simulation, but there is more spread among the models. The non-monotone 3D models show a nonlinear accelerating increase in mixed layer depth through time, and the final depth reached is generally less than the other two 3D model categories. Both the 2D and 1D models calculate a higher rate of increase with the mixed layer depth growing to about 740 m and greater than 750 m, respectively. The current 1D model shows a mixed layer depth increase that is markedly less than the other 1D models and has a somewhat nonlinear shape. In addition, the final mixed layer depth calculated from the current model (734 m) agrees well with the monotone 3D models, a considerable improvement from the other 1D and even 2D models.

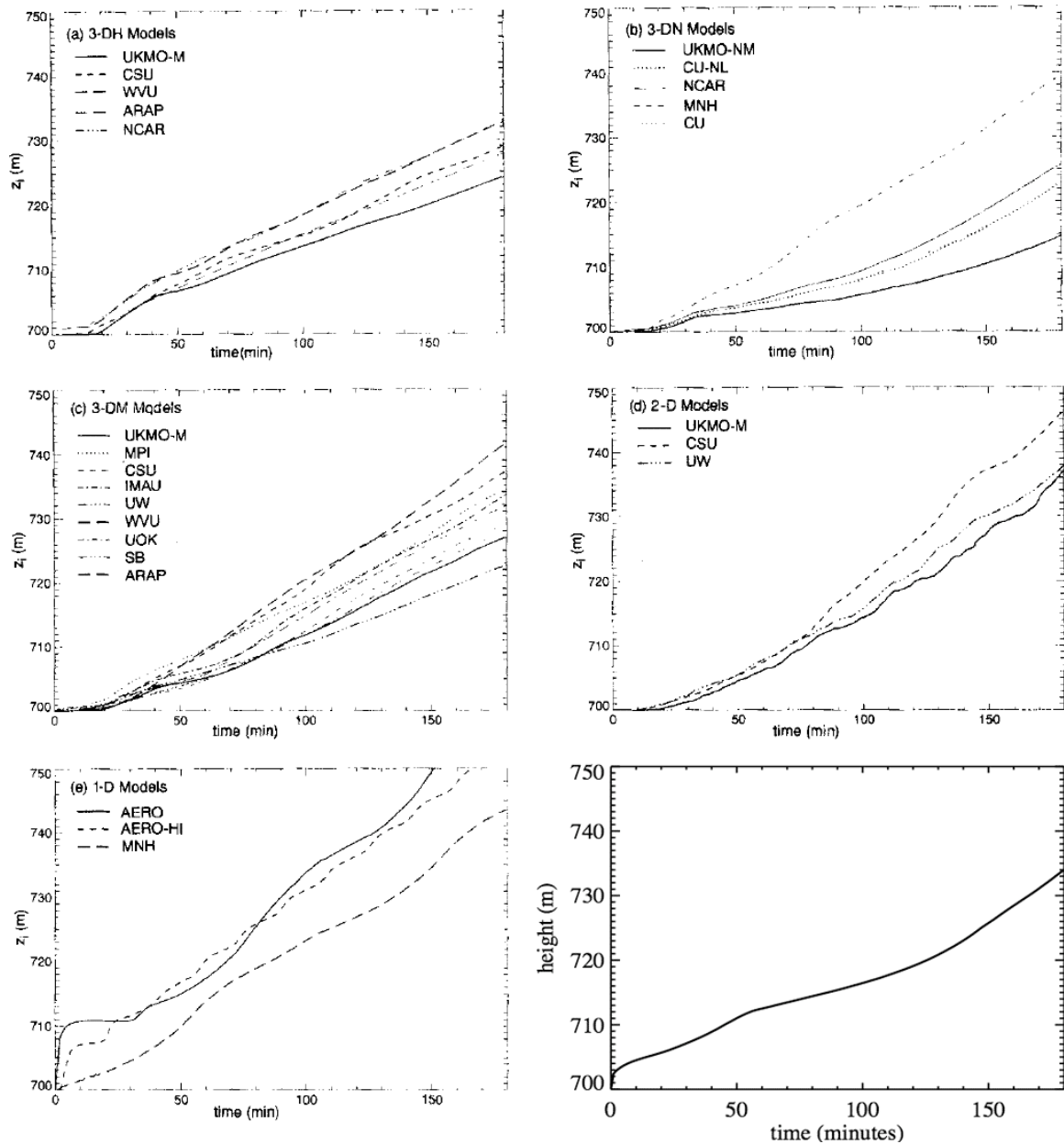


Figure 3.31 Time series of mixed layer depth for different models participating in the GCSS intercomparison; high-resolution 3D LES (upper left), standard resolution non-monotone advection 3D LES (upper right), standard resolution monotone advection 3D LES (center left), 2D (center right), 1D (lower left), current model (lower right).

The rate of growth of the mixed layer is determined by entrainment, and the differing rates of growth among the models suggest that there are discernible differences in how well they represent this process. Bretherton et al. (1999) examine the entrainment

process in the intercomparison models by comparing some key parameters including the boundary layer average TKE, entrainment rate, w_e , convective velocity, w_* , and entrainment efficiency, A . For a buoyancy-dominated boundary layer, the last three quantities are defined according to Bretherton et al. (1999) as:

$$w_e = \frac{dz_i}{dt} \quad (3.14)$$

$$w_*^3 = 2.5 \int_0^{z_i} \overline{w'b'} dz \quad (3.15)$$

$$A = \frac{z_i w_e \Delta b}{w_*^3} \quad (3.16)$$

where $\overline{w'b'} = \frac{g}{\theta_0} \overline{w'\theta'}$ and Δb is the buoyancy jump across the inversion. These

parameters were calculated for the current model and compared with results from the GCSS intercomparison.

The evolution of boundary layer average TKE is shown in Figure 3.32 for the various intercomparison models and the current one. There are fundamental differences in how many of the intercomparison models handle TKE. Some use a first order closure diffusion scheme, while others explicitly predict its evolution. The case specifications called for models that predict TKE to be initialized with $1 \text{ m}^2\text{s}^{-2}$ in the boundary layer while those using a first order scheme are initialized to zero. This difference is obvious in Figure 3.32, with the first-order closure models showing very small quantities of TKE in the beginning while the others start out with their maximum values. In all 3D and 2D models, oscillations are present for the first couple of hours, but mostly dampen by the last hour. The current model displays behavior similar to the 1D models of the

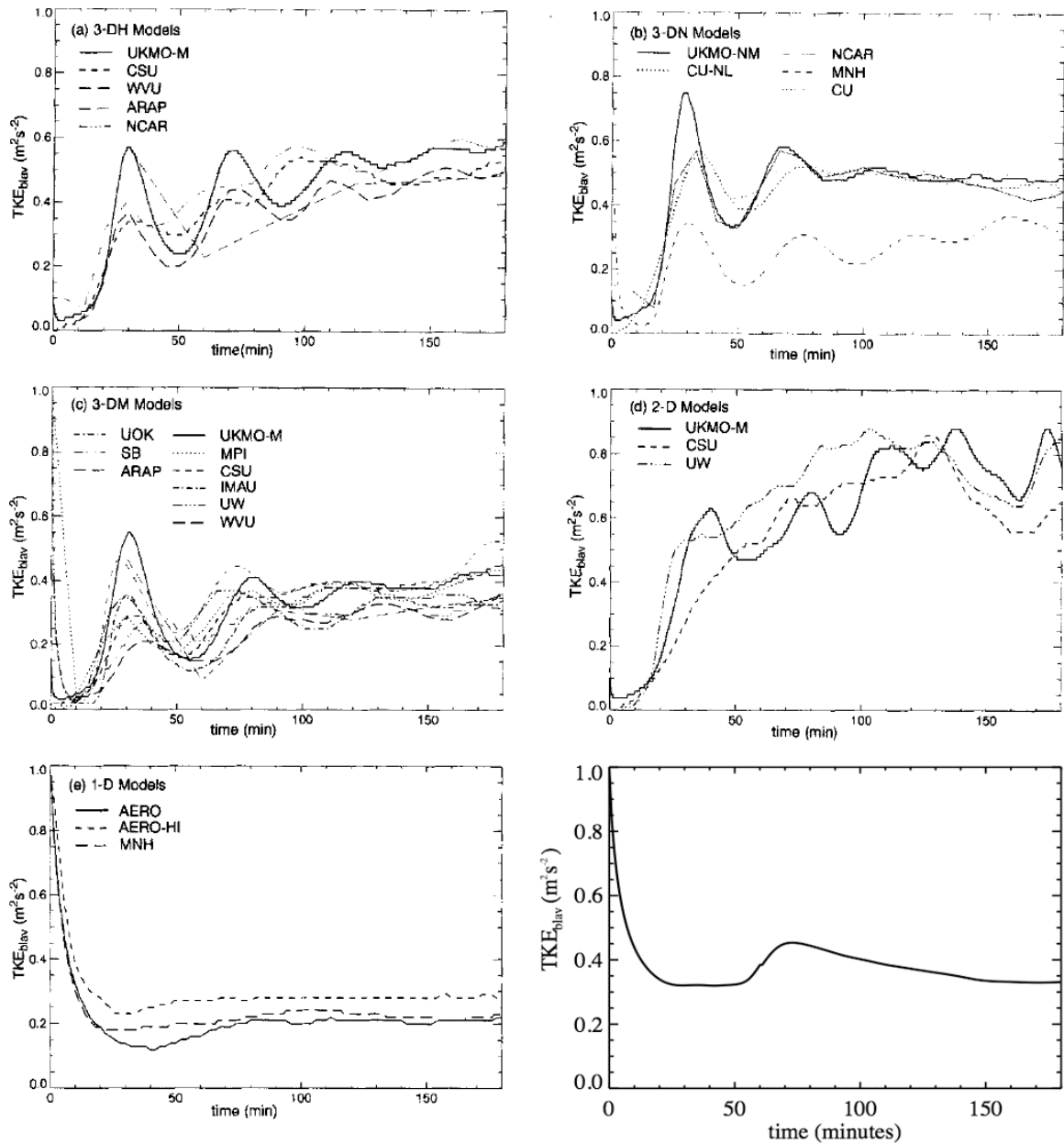


Figure 3.32 As in Figure 3.31 but for the boundary layer average TKE.

intercomparison study, with a steady state value reached quickly and without oscillations, but with a lower magnitude than the other types of models in general. The current model produces a higher boundary layer average TKE value than the other 1D models, and comes close to matching values from the monotone 3D models.

The time evolution of the other entrainment parameters is given in figure 3.33. The evolution of the entrainment rate, defined in equation (3.14), exhibits an interesting behavior. If one compares the time series of entrainment rate to the time-height cross-section of the smoke concentration, it is apparent that the boundary layer grows in somewhat discrete jumps due to the coarse grid size. The entrainment rate increases nonlinearly until the inversion jumps upward one grid level at which point the entrainment rate decreases to a baseline level. This anomalous phenomenon appears to happen twice during the integration: once around 50 minutes and a longer duration event near the end of the simulation. The evolution of the entrainment efficiency mirrors that of the entrainment rate, but this is to be expected since the quantities that make it up change little throughout the simulation except for the entrainment rate. The convective velocity reaches a somewhat steady-state value at 10 minutes into the simulation of about 0.8

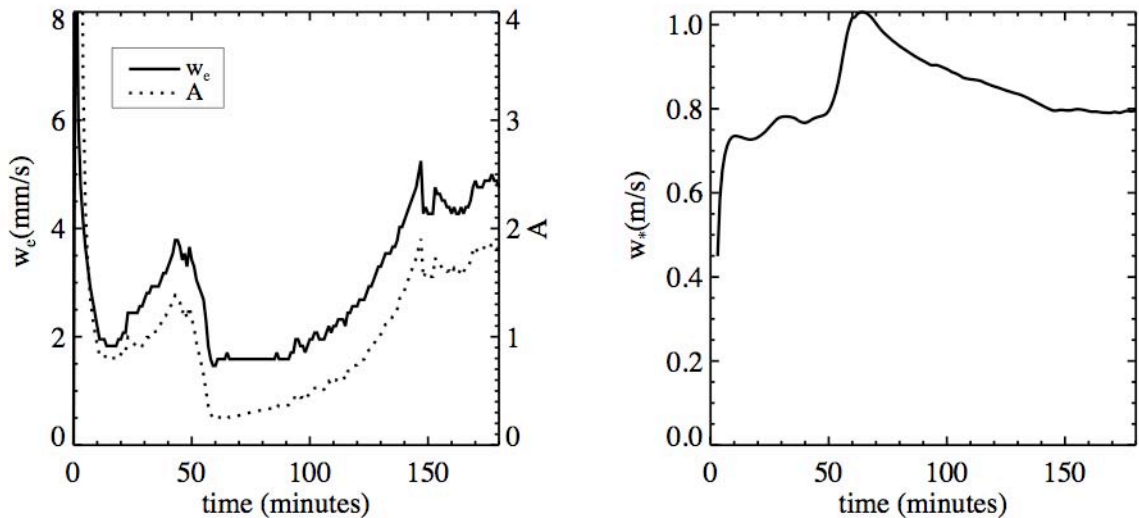


Figure 3.33 Time evolution of the entrainment rate (solid line, left), entrainment efficiency (dotted line, left), and convective velocity (right).

m s^{-1} , although a temporary increase coinciding with the increase in boundary layer average TKE is found near the one hour mark.

Figure 3.34 was obtained from Figures 3 and 13 of Bretherton et al. (1999) and shows the average values of entrainment rate, boundary layer average turbulent kinetic energy and entrainment efficiency for the last hour of the simulation for the different types of models. The plots have been modified to include values from the current model (red symbols in the 1D column). The entrainment rate plot (left) and entrainment efficiency plot (right) contain hatched areas that indicate the range of expected values from laboratory experiment analogs to this case (see Bretherton et al. 1999 for more details). The entrainment rate plot shows significant difference among the model types, with the high-resolution 3D LES models producing values closest to laboratory experiments. With the exception of two 3D models, the standard resolution 3D models,

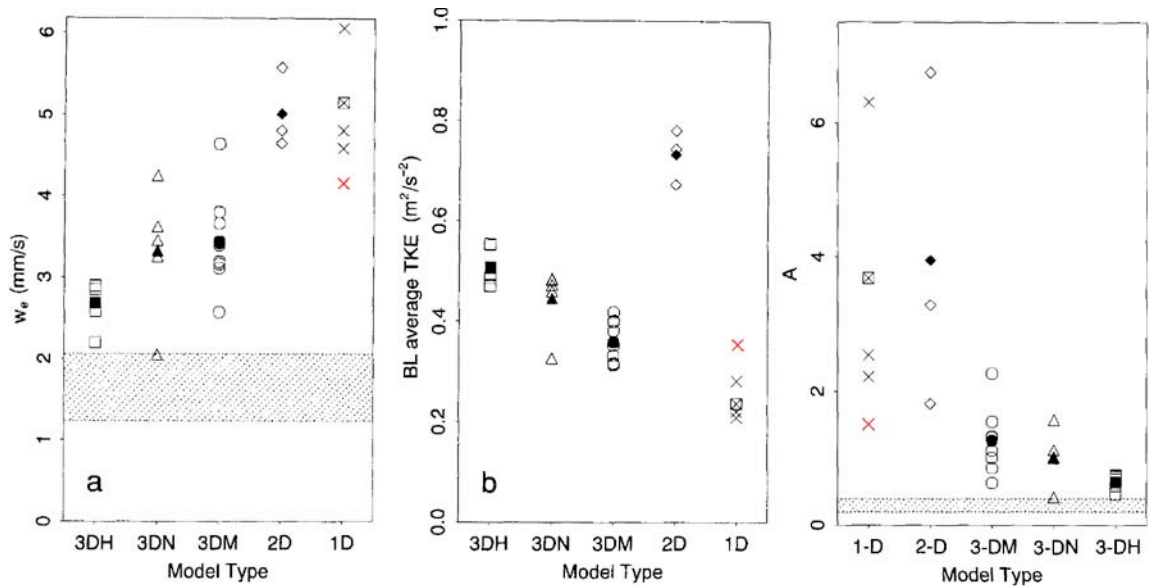


Figure 3.34 Comparison of the final hour average values of entrainment rate (left), boundary layer average TKE (center), and entrainment efficiency (right) grouped by model type. The current model's values are plotted as red x's in the 1D model column. Exact values for the current model are $w_e=4.14$ mm/s, $\text{TKE}_{\text{blav}}=0.34$ m^2/s^2 , and $A=1.46$.

2D models, and the 1D models all produce entrainment rates much higher than what laboratory experiments or the high-resolution 3D LES suggest. It is interesting to note, however, that the current model produces an entrainment rate smaller than the other 1D models, even approaching the range of entrainment rates produced by the 3D LES models. For boundary layer average TKE, the current model produces a value greater than the other 1D models, and generally inline with the range of values predicted by the monotone standard-resolution 3D LES models.

The values of the entrainment efficiency are interesting in context of the so-called “A-dilemma” presented in Bretherton et al. (1999). According to that paper, laboratory experiment analogs designed to study entrainment at the interface of two fluids with different densities show that the entrainment efficiency at the top of a smoke-filled boundary layer or stratocumulus-topped boundary layer should be between 0.2 and 0.4. Both numerical studies and observations suggest, however, that the entrainment efficiency of a stratocumulus-topped boundary layer is up to an order of magnitude larger. The reason for this discrepancy isn’t clear, but several hypotheses have been put forth, including the possibility that laboratory experiment analogs to this case are incorrect, that cloud-top evaporation is boosted by turbulence leading to enhanced entrainment, that entrainment efficiency is overestimated in stratocumulus layers due to their increased spatial complexity, and that the presence of clouds at the top of the boundary layer focuses TKE near the inversion and enhances the entrainment efficiency. The absence of liquid water and an irregular inversion for this case renders the last three explanations ineffective, yet the calculated entrainment efficiency in all models is still well above the values found in the laboratory experiments. In fact, an appreciable fraction

of the participant models display entrainment efficiencies an order of magnitude larger. The category of models that produces that entrainment efficiency closest to laboratory experiment range is the high-resolution 3D LES. Note that the current model calculated an entrainment efficiency well below the other 1D models and almost as close to the laboratory experiment range as some 3D LES models.

3.3.2.2 Selected second- and third-order moments

The profiles of the average heat flux for the last hour of the simulation are given in Figure 3.35. The general shape of the heat flux is in qualitative agreement for all models below the inversion. Indeed, Bretherton et al. (1999) explain that the particular shape is required by the imposed boundary conditions, radiative cooling, and the fact that the potential temperature in the mixed layer varies contiguously, so the agreement is not surprising. The main differences among the models are the magnitudes of the sub-inversion maximum and above-inversion minimum and whether or not a spurious positive heat flux exists above the inversion. The profile from the current model (lower right) displays a maximum heat flux of about 20 W m^{-2} below the inversion. This value is significantly greater than the other 1D models and seems to align well with the average standard resolution 3D LES. However, the maximum heat flux is underestimated compared to the high-resolution 3D LES. The magnitude of the negative heat flux minimum at the inversion and the spurious positive heat flux above in the current model are both similar to the standard resolution 3D LES with non-monotone advection, although the current model's spurious heat flux is much reduced compared to those models. In the current model, the spurious positive heat flux is a result of the buoyancy

term in the heat flux equation. These spurious values can be maintained when there is little dissipation above the inversion due to neutral stability there.

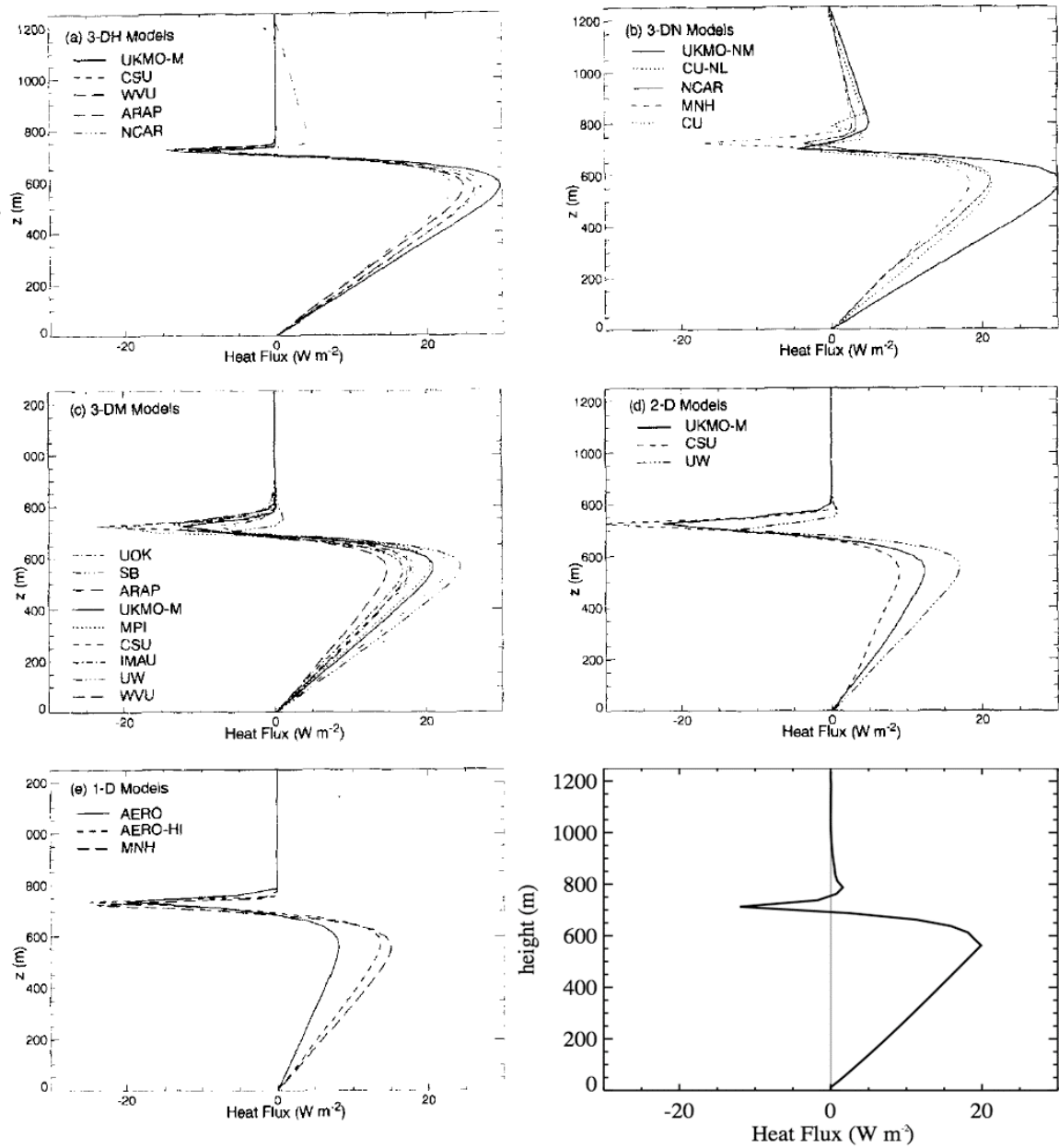


Figure 3.35 Profiles of the last hour average heat flux for the GCSS intercomparison models and the current model. The layout follows that of Figure 3.31.

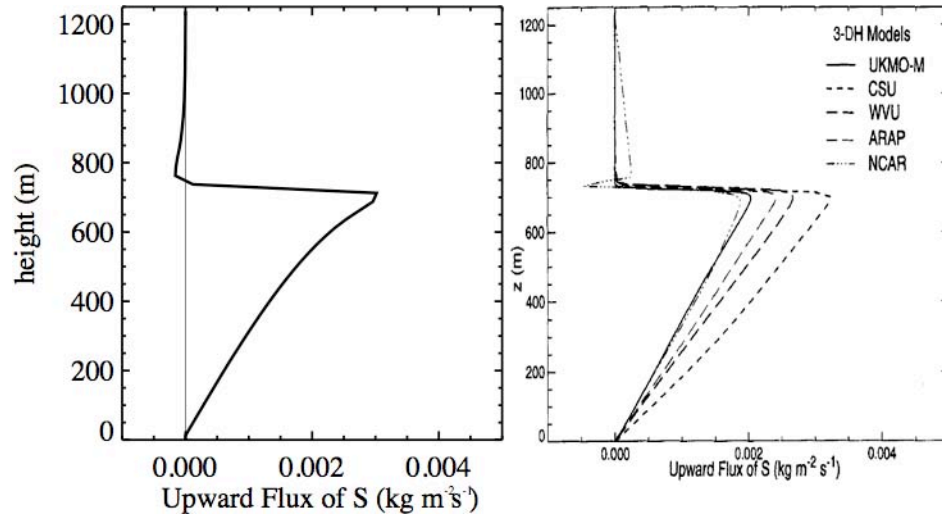


Figure 3.36 Average smoke flux profiles for the last hour for the current model (left) and the high-resolution 3D LES (right).

The average smoke flux profiles for the last hour of the simulation are shown for the current model and the high-resolution 3D LES in Figure 3.36. While qualitatively similar for much of the boundary layer, the same difficulties found in the heat flux profile are also visible in the smoke flux profile. Namely, the spurious negative smoke flux above the inversion is indicative of the same problem discussed with the heat flux: the buoyancy term in the smoke flux budget creates a negative smoke flux that is not damped properly due to the neutral layer above the inversion. Bretherton et al. (1999) did not publish the smoke flux profiles for all of the model types, but they submit that the non-monotone advection 3D LES models demonstrate similar problems as found with their heat flux profiles, and therefore share the same deficiency as the current model, but probably for different reasons having to do with their numerical discretization.

The average TKE profile for the last hour of the simulation for the current model and a representative mix of the GCSS intercomparison models is shown in Figure 3.37. General features include an absolute maximum next to the surface, a nearly uniform distribution throughout most of the boundary layer, a minor secondary maximum at the

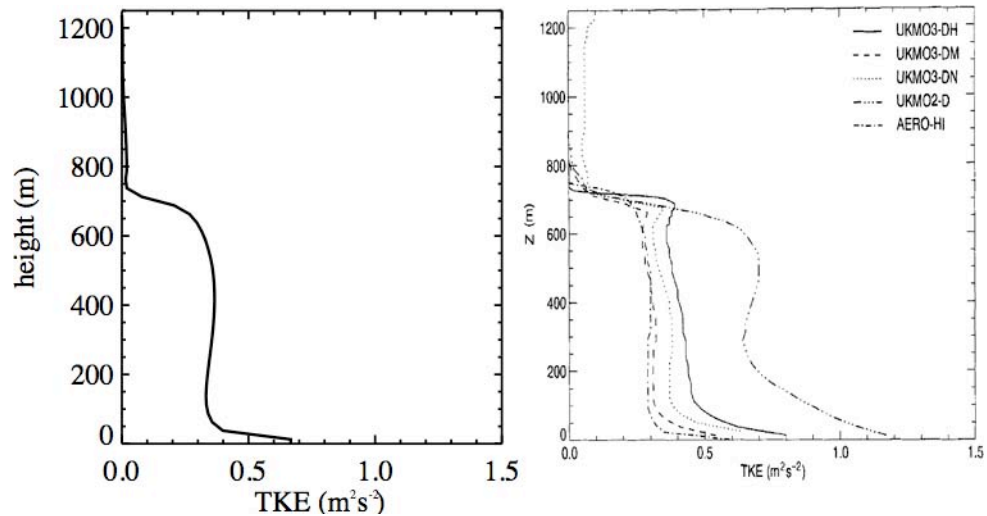


Figure 3.37 Profiles of average TKE for the last hour of the simulation for the current model (left) and models from the GCSS intercomparison representative of their groups.

inversion, and a second minor relative maximum above the inversion for those models with spurious convection there. Comparison between the current model and the GCSS intercomparison models shows that the current model produces a similar TKE profile to the standard resolution 3D LES models, although a broader secondary maximum in the upper half of the boundary layer is found. In addition, spurious weak TKE is found above the inversion for the same reason the heat and smoke flux profiles have spurious values there.

Lastly, the profiles of average vertical velocity skewness for the last hour of the simulation are shown in Figure 3.37 for the current model and the high-resolution 3D LES models from the GCSS intercomparison. The general characteristics show good agreement among the models: a small negative value from the surface to where the radiative cooling takes place and a small zone of positive skewness near the inversion. Values above the inversion show increased scatter due to the division by a small vertical velocity variance.

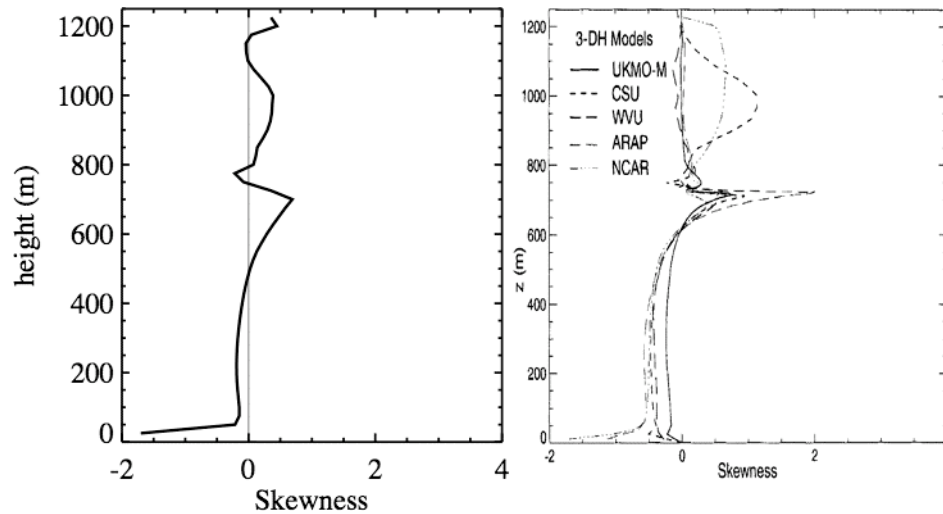


Figure 3.38 Average skewness profiles from the last hour of the simulation from the current model (left) and the high-resolution 3D LES from the GCSS intercomparison (right).

3.4 Drizzling Nocturnal Stratocumulus Case: DYCOMS II

The next test case to be considered is the nocturnal drizzling stratocumulus case of the GCSS BLCWG that was developed from data collected during the second research flight of the second Dynamics and Chemistry of Marine Stratocumulus field study (DYCOMS-II) that took place in a broad region of stratocumulus off the southern California coast during July of 2001. The second research flight measured conditions in two types of stratocumulus regimes: one that featured low drizzle rates and a solid cloud deck and a more broken cloud deck that featured pockets of open cells and higher drizzle rates. For the GCSS case, mean conditions from each of these stratocumulus regimes were averaged to obtain the initial conditions for the modeling test case.

Intercomparisons were performed for both LESs and SCMs that simulated this case and their results are published in Ackerman et al. (2009) and Wyant et al. (2007), respectively. Emphasis for the analyses was placed on the effect of drizzle and cloud

droplet sedimentation on the calculated liquid water path, entrainment rate, and overall boundary layer dynamics.

Within the context of this study, this case was performed to test the current model's ability to simulate a stratocumulus regime. This is the first of three cases to test the model under various boundary layer cloud regimes, and is the first to have the subgrid-scale condensation and subgrid-scale microphysics schemes active. It should be noted that stratocumulus regimes have historically been easier for boundary layer turbulence parameterizations to simulate given that the joint-Gaussian assumption for the thermodynamic variables is more relevant in this regime and that stratocumulus is generally more statistically stable through time.

3.4.1 Initial conditions

All initial and boundary conditions are given in Ackerman et al. (2009) and are as presented below. The mean profiles of θ_l (K), q_l (g kg^{-1}), u (m s^{-1}), and v (m s^{-1}) are given by

$$\theta_l = \begin{cases} 288.3 & z \leq z_i \\ 295 + (z - z_i)^{1/3} & z > z_i \end{cases} \quad (3.17)$$

$$q_l = \begin{cases} 9.45 & z \leq z_i \\ 5 - 3 \left(1 - e^{-\frac{z_i - z}{500}} \right) & z > z_i \end{cases} \quad (3.18)$$

$$u = 3 + \frac{4.3z}{1000} \quad (3.19)$$

$$v = -9 + \frac{5.6z}{1000} \quad (3.20)$$

where $z_i = 795$ m initially. The second- and third-order moments are all initialized to zero except for the TKE components below the inversion and all second-order moments at the surface. TKE is initially set to $1 \text{ m}^2\text{s}^{-2}$ and is assumed to be isotropic, so all three TKE components are initialized with an equal amount. The surface sensible and latent heat fluxes are held constant throughout the simulation at 16 and 93 W m^{-2} respectively. The vertical fluxes of momentum are parameterized according to

$$\overline{w'u'} = -\frac{\overline{uu_*^2}}{\sqrt{\overline{u^2} + \overline{v^2}}} \quad \text{and} \quad \overline{w'v'} = -\frac{\overline{vu_*^2}}{\sqrt{\overline{u^2} + \overline{v^2}}} \quad \text{where } u_* = 0.25 \text{ m s}^{-1} \text{ (constant)}. \quad \text{All other}$$

second order moments at the surface are treated according to Monin-Obukhov similarity theory as detailed for the Wangara case. The surface pressure is initialized to 1017.8 hPa, and the profiles of pressure and density are generated assuming hydrostatic equilibrium and an isentropic profile with $\theta_0 = 291.5$ K. In addition, pseudo-random perturbations of $[-0.1 \text{ K}, 0.1 \text{ K}]$ are added to the θ_l profile below the inversion.

To consider the effects of the atmosphere outside of the domain, two large-scale forcings are included. First, subsidence is calculated according to $\overline{w_{LS}} = -Dz$ where $D = 3.75 \times 10^{-6} \text{ s}^{-1}$ is the average divergence observed during the research flight. The subsidence acts on the thermodynamic variables to warm and dry the column. Second, a large-scale pressure gradient is included into the simulation by specifying profiles for the geostrophic wind. For this case, the initial mean wind profiles are used as the geostrophic values and the Coriolis parameter is calculated at latitude 31.5° N. In addition to the large-scale forcings, there are two associated with the inclusion of liquid clouds. The first is the net longwave radiative forcing. The net longwave flux is parameterized as a function of height and cloud water mixing ratio for each level as

$$F(z) = F_0 \exp[-Q(z, \infty)] + F_1 \exp[-Q(0, z)] + \alpha \rho_i c_p DH(z - z_i) \left[0.25(z - z_i)^{4/3} + z_i(z - z_i)^{1/3} \right] \quad (3.21)$$

where

$$Q(z_1, z_2) = \int_{z_1}^{z_2} \kappa \rho \bar{q}_l dz, \quad F_0 = 70 \text{ Wm}^{-2}, \quad F_1 = 22 \text{ Wm}^{-2}, \quad \kappa = 70 \text{ m}^2 \text{kg}^{-1}, \quad \alpha = 1 \text{ K m}^{1/3},$$

$\rho_i = 1.12 \text{ kg m}^{-3}$ is the density at the inversion, H is the Heaviside step function, and z_i is defined as the height at which $q_l = 8 \text{ g kg}^{-1}$. The second forcing associated with cloud water is the divergence of the cloud water sedimentation flux. While many bin microphysics schemes intrinsically account for this cloud droplet sedimentation, simpler schemes like the one included in the current model omit this process. This flux is parameterized according to

$$F_{sed}(z) = c \left(\frac{3}{4\pi\rho_l N_d} \right)^{2/3} (\rho \bar{q}_l)^{5/3} \exp\left[5(\ln \sigma_g)^2\right] \quad (3.22)$$

where $c = 1.19 \times 10^8 \text{ m}^{-1} \text{s}^{-1}$, $N_d = 55 \times 10^6 \text{ m}^{-3}$ (constant) is the cloud droplet concentration, and $\sigma_g = 1.5$ is the geometric standard deviation of the cloud droplet size distribution. Since the flux is defined as positive downwards, the forcing on the

thermodynamic variables is $\frac{\partial \bar{\theta}_l}{\partial t} \approx -\left(\frac{p_0}{p}\right)^\kappa \left(\frac{L_v}{\rho c_p}\right) \frac{dF_{sed}}{dz}$ and $\frac{\partial \bar{q}_l}{\partial t} \approx \left(\frac{1}{\rho}\right) \frac{dF_{sed}}{dz}$.

The simulation is run for 6 hours with a time step of 1 second. Sixty layers are used with a constant grid spacing of 25 m for a total domain depth of 1500 m. The results from the current model are compared mainly with the participant LES codes from Ackerman et al. (2009). The LES codes use a variable vertical grid size with maximum resolution of 5 m near the surface and the inversion with coarser resolution between and above the

inversion. The time steps used vary by model. The first two hours of the simulation is observed to be a “spin-up” period, so descriptive statistics are taken from the last 4 hours of the simulations where a quasi-steady state is observed. In addition, as in the LES study, a sensitivity test is performed where the cloud droplet sedimentation flux is neglected. These results are presented along with the standard test.

3.4.2 Results

3.4.2.1 Mean variables, cloudiness statistics, and precipitation

The mean profiles of the thermodynamic variables from the current model are shown in Figure 3.39 and compared with the LES participants of Ackerman et al. (2009). All models do an admirable job at maintaining the well-mixed boundary layer and sharp

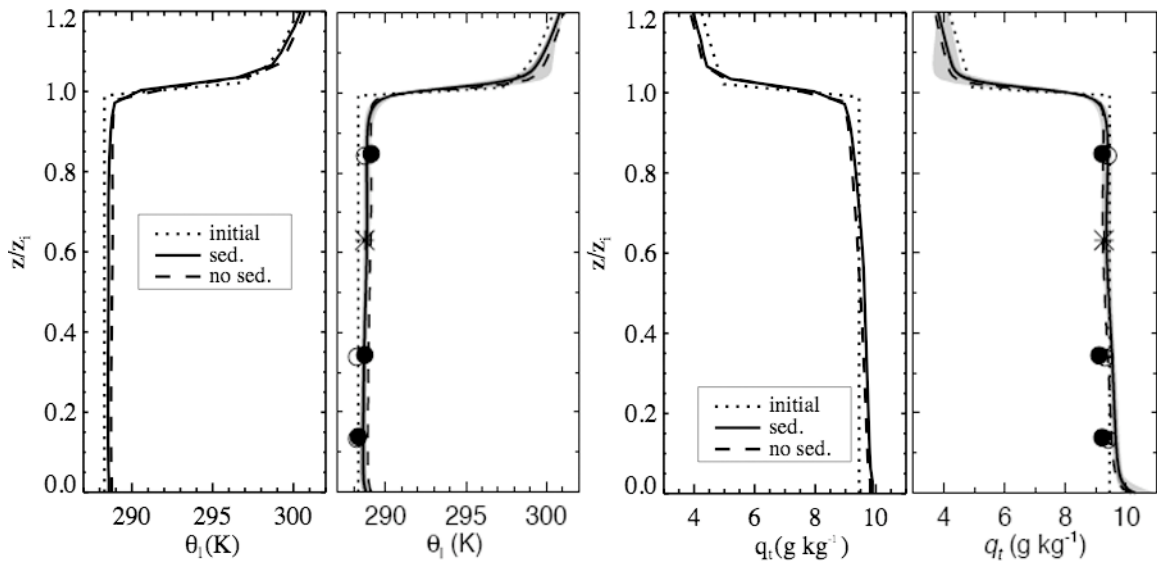


Figure 3.39 Mean profiles of $\bar{\theta}_i$ and \bar{q}_i for the current model (left in all plots) and the LES participants of Ackerman et al. (2009) (right in all plots). For all plots, the dotted line denotes the initial profile, the solid line denotes the average over the last 4 hours of the simulation, and the dashed line denotes results from the no cloud droplet sedimentation sensitivity test discussed in Section 3.4.2.3. The circular symbols denote observations, with the closed symbols representing the solid stratocumulus deck and the open symbols representing the open cellular stratocumulus.

inversion. The current model develops a $\bar{\theta}_l$ profile that is slightly less stratified at the top of the boundary layer, but otherwise, the agreement with LES is quite good. The mean \bar{q}_l for all models are slightly less well-mixed than $\bar{\theta}_l$ and the profiles show a slight drying of about a few tenths of one g kg^{-1} within the cloud layer and a slight moistening of the same magnitude below the cloud layer. The current model's profile matches the results from LES well, except for the lower half of the boundary layer is slightly too moist.

Of utmost interest for the first cloudy test case are the calculated cloud field and its properties. Profiles of cloud fraction and mean cloud liquid water are shown in Figure 3.40, while the liquid water path time series is shown in Figure 3.41. The agreement between the current model's results, the LES results, and observations is remarkably good. The maximum cloud fraction for the current model is about 98% versus the mean LES result of about 97%. The cloud thickness, defined as the thickness between where the cloud fraction first crosses 0.5 and where it crosses the same value near the boundary

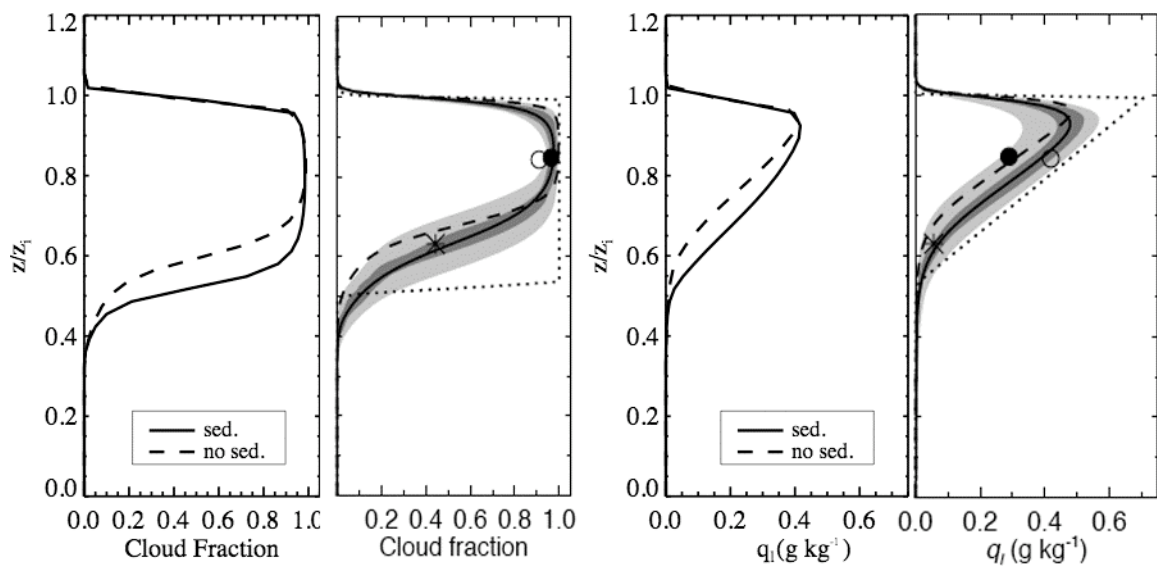


Figure 3.40 Profiles of cloud fraction and mean cloud liquid water for the current model (left panels) and LES participants (right panels). Lines and symbols are as in Figure 3.39.

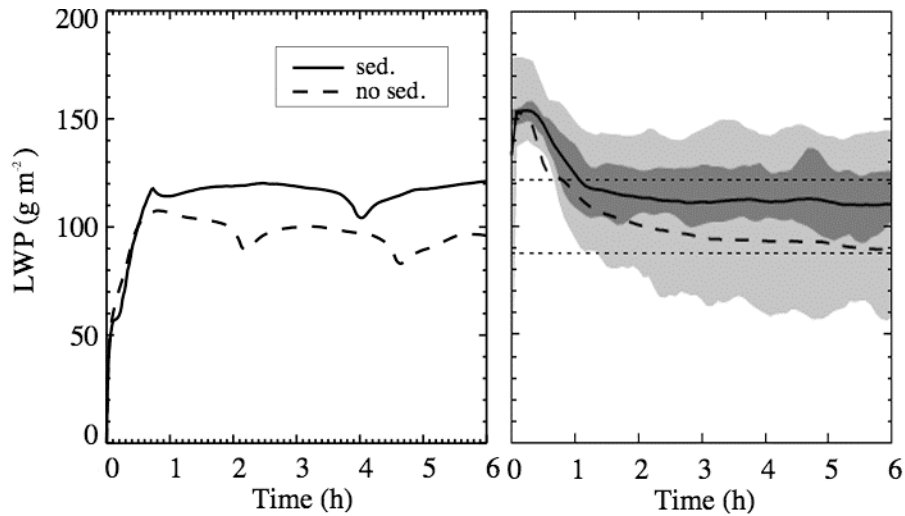


Figure 3.41 Time series of LWP for the current model (left) and the LES participants (right). Solid lines represent means for the standard case and dashed lines represent results from the no-sedimentation flux sensitivity test. Dotted lines on the LES figure denote the range of observations, while the dark and light shading represent the middle two quartiles and range of the LES results, respectively.

layer top, is slightly different between the models; the cloud deck in the current model occupies about 46% of the boundary layer, while the average LES cloud deck only occupies 37% of the boundary layer column. The cloud fraction profile shows that the extra cloud depth is found near cloud base. This is consistent with the lower half of the boundary layer being a little too moist in the current model. As with cloud fraction, the mean cloud liquid water specific humidity profiles compare really well between the current model and LES. The maximum values coincide to within 0.07 g kg^{-1} and the shapes of the profile are quite similar. Given that the current model calculates a slightly deeper cloud than the mean of the LES models, one might expect the liquid water path to be somewhat greater as well. Figure 3.41 demonstrates that this is indeed the case. After the two hour spin-up time, the liquid water path settles to a near-constant value around 120 g m^{-2} , compared with about 110 g m^{-2} for the LES participants. The current model's

results not only match the mean of the LES participants well, but also fall within the range of observations.

Given these results, it seems as though the SGS condensation scheme implemented in the current model can accurately capture the defining characteristics of a stratocumulus regime. With this accurate portrayal of the cloud field, can the SGS microphysics scheme also produce realistic results? Figure 3.42 shows the time-height cross-section of the total precipitation flux, which includes the parameterized cloud-droplet sedimentation flux. After a brief burst of relatively heavy precipitation during the spin-up period, the precipitation flux reaches a quasi-steady state that is maintained throughout the simulation except for a brief decrease associated with the inversion jumping one grid level upward. The spatial distribution of the precipitation flux matches what one would expect in a stratocumulus regime with the maximum precipitation flux collocated with the maximum cloud liquid water. Descending within the cloud, the

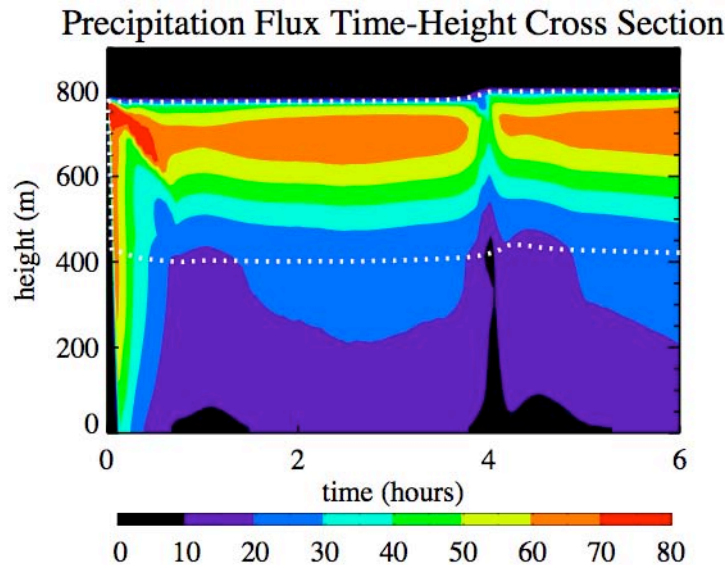


Figure 3.42 Time-height cross section of precipitation flux; contours units are $W m^{-2}$. The white dotted lines denote cloud top and cloud base.

precipitation flux decreases rapidly, and below cloud base, the precipitation flux is further depleted by evaporation.

Figures 3.43 and 3.44 show comparisons of the mean calculated precipitation flux profiles and the time series of surface precipitation with the LES results, respectively. Figure 3.43 also shows the separate components of the total precipitation flux: the rain flux diagnosed from the SGS microphysics scheme (solid blue line) and the parameterized cloud droplet sedimentation flux (solid red line). Through most of the cloud layer, the cloud droplet sedimentation flux dominates, but this is to be expected since this flux is proportional to $q_l^{-5/3}$, and the liquid water content increases with height in the cloud layer to the maximum value near the boundary layer top. As one descends through the cloud layer, the rain flux diagnosed from the SGS microphysics scheme increases due to cumulative autoconversion and collection and peaks at cloud base. Below this level, evaporation decreases the precipitation flux at a slower rate. Compared

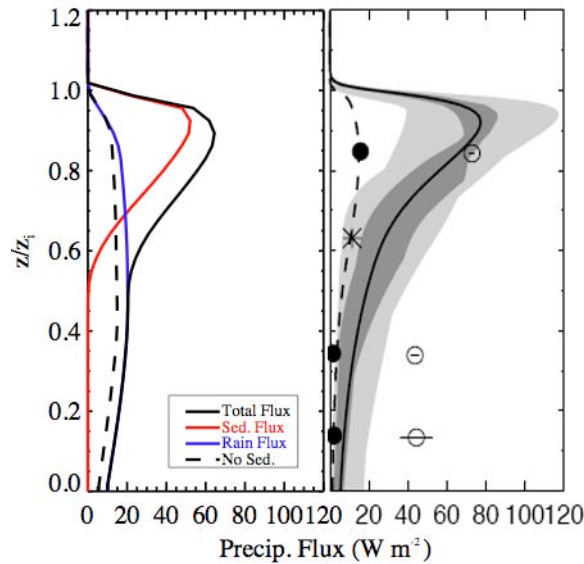


Figure 3.43 As in Figure 3.39, but for the precipitation flux. The red and blue solid lines for the current model plot indicate the cloud water sedimentation flux and the diagnosed rain flux.

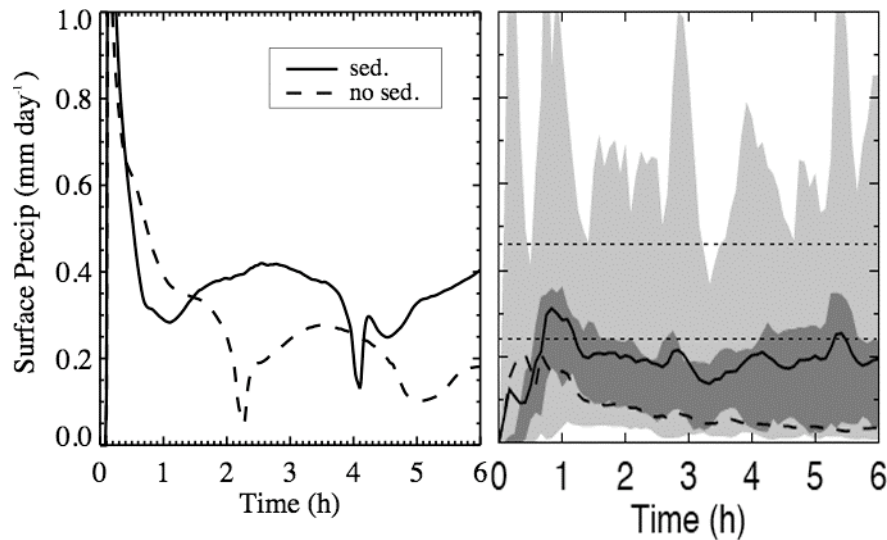


Figure 3.44 As in Figure 3.41, but for the surface precipitation flux.

with the LES results, the precipitation flux profile from the current model matches pretty well, with the maximum flux coinciding in placement and magnitude. The main difference between the two mean profiles is the shape near and below the transition from cloud layer to sub-cloud layer. This difference is probably attributed to differences in how evaporation of precipitation is handled. Compared with observations, the LES models' precipitation flux matches the open-cellular values in the cloud layer, but approaches the lower closed-cell values below the cloud layer, indicating the sub-cloud evaporation might be too strong. The current model calculates a precipitation flux that is greater than the LES results and closed-cellular values, but still considerably less than the observed open-cellular values. The time series of surface precipitation flux shows that the mean of the LES results slightly undershoots the observed range of 0.25-0.45 mm day⁻¹ while the current model generates surface precipitation that falls within the range of observations.

3.4.2.2 Turbulent moments and entrainment

Profiles of the total fluxes of the thermodynamic variables are shown in Figure 3.45. The total flux of $\overline{\theta}_t$ includes not only its vertical turbulent flux, but also the contributions from the radiative, precipitation, and cloud droplet sedimentation fluxes. Likewise, the total flux of \overline{q}_t includes its vertical turbulent flux and contributions from the precipitation and cloud droplet sedimentation fluxes. As with the Wangara case, the linear profiles are indicative of a well-mixed layer that warms or cools and moistens or dries in a constant way throughout the layer. The slightly negative constant slope of both profiles equates to a uniformly warming and moistening boundary layer. The basic shape of both profiles from the current model agrees with the results from LES, but there are important differences. For the total flux of $\overline{\theta}_t$, the slope is slightly more vertical. This is indicative of a boundary layer that doesn't warm as much as the one from LES, especially in the cloud layer (see Figure 3.39 for confirmation). Similarly, the slope of the total flux of \overline{q}_t profile is less vertical than the LES profile which is indicative of a moister boundary

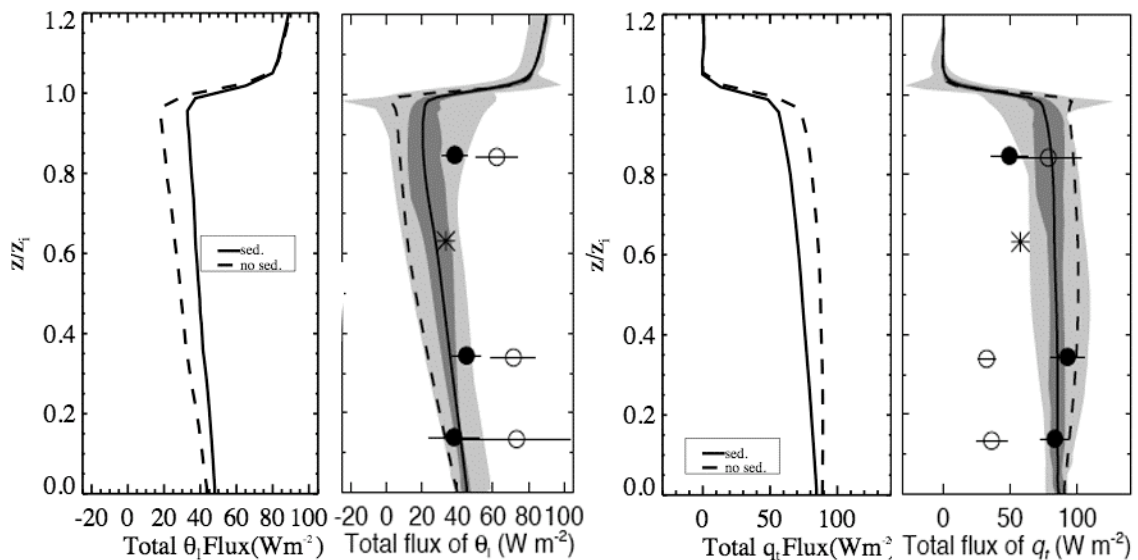


Figure 3.45 As in Figure 3.39 but for the total fluxes of $\overline{\theta}_t$ and \overline{q}_t .

layer (see Figure 3.39). All models, however, fail to accurately reproduce the observational values, particularly the values from the open-cellular convection. It is worth noting that the current model's results are slightly closer to the observed values than the LES results.

To gain a better perspective of the turbulent state of the modeled stratocumulus regime, mean profiles of the vertical velocity variance and buoyancy contribution to the TKE are shown in Figure 3.46. The buoyancy term profile matches nearly perfectly with both LES results and observations. The subcloud layer features a nearly linear profile consistent with clear convective boundary layers, and a significantly positive buoyancy flux is present in the cloud layer. Above the cloud layer is a thin layer of slightly negative buoyancy flux present in all models. The vertical velocity variance profiles show some disagreement, both between the current model and the LES and the LES participants themselves. The observations for both types of stratocumulus convection show a near parabolic shape that is consistent with well mixed convective boundary layers (see Figure

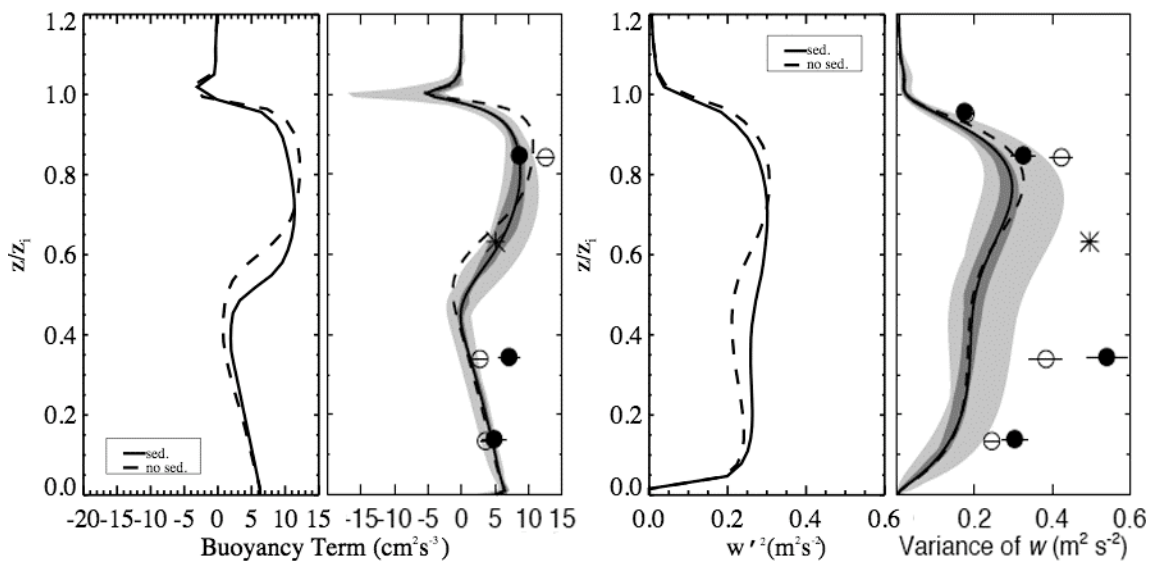


Figure 3.46 As in Figure 3.38 but for the buoyancy contribution to the TKE production and the vertical velocity variance.

3.18 of Section 3.2.2.2). The LES models produce profiles that are smaller in magnitude and that have two maxima, one below the cloud layer and one in the cloud layer. This double maximum profile is indicative of a cloud layer that has decoupled from the clear convective subcloud layer, which is not observed in this case. The profile from the current model is slightly better than the LES results, with a less pronounced local minimum near cloud base and higher values of vertical velocity variance below the cloud layer.

The time series for the maximum vertical velocity variance is shown in Figure 3.47 along with the time series of entrainment rate in Figure 3.48, where the entrainment rate is defined as $E = \frac{dz_i}{dt} - w_{LS}(z_i)$, or the time rate of change of the boundary layer depth minus the large scale subsidence at the inversion. As hinted in the vertical velocity variance profiles in Figure 3.46, the maximum vertical velocity variance is underestimated considerably in all models, although the current model is no worse than the LES participants. Despite this shortcoming, however, the models are still generally

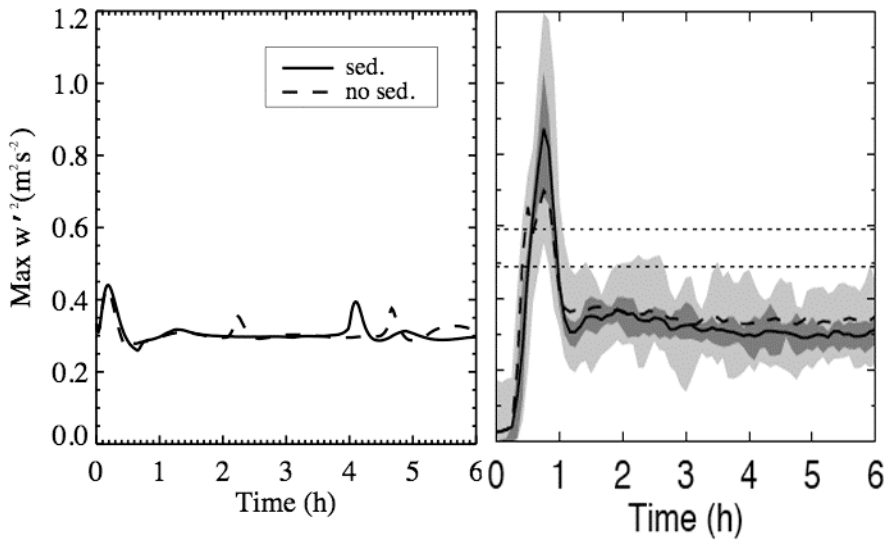


Figure 3.47 As in Figure 3.40 but for the maximum vertical velocity variance.

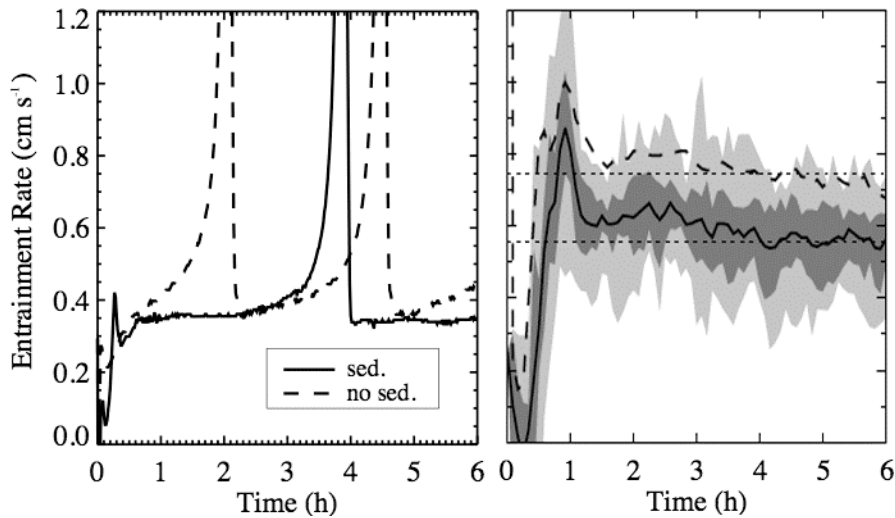


Figure 3.48 As in Figure 3.41 but for the entrainment rate.

able to reproduce an entrainment rate that is both reasonable and close to observations.

The current model’s entrainment rate is still generally underpredicted, though, and shows spikes associated with discrete inversion height changes.

3.4.2.3 Cloud Droplet Sedimentation Flux Omission Sensitivity Test

One of the goals of this GCSS intercomparison case was to study the effects of drizzle and cloud water sedimentation on boundary layer dynamics in a stratocumulus regime (Ackerman et al., 2009). These processes play an important role in the field of climate science due to their influence on indirect aerosol effects, particularly the “Twomey effect”. This phenomenon results from increased aerosol concentrations that provide more cloud condensation nuclei for water vapor to condense upon. This leads to more numerous but smaller cloud droplets that are able to reflect more shortwave radiation. The Twomey effect is thought to be enhanced by less efficient drizzle generation and increased cloud water sedimentation that also results from the smaller, more numerous droplets. For this reason, it is important for a model to accurately include

drizzle and cloud droplet sedimentation, and to understand how these processes affect other boundary layer variables.

Two previous studies by Ackerman et al. (2004) and Bretherton et al. (2007) demonstrate that the inclusion of cloud droplet sedimentation plays a critical role in decreasing the entrainment rate in stratocumulus regimes. The mechanism by which the reduction is created is debated between the two studies, however. Ackerman et al. (2004) postulate that cloud droplet sedimentation leads to a reduction in the moisture level of cloudy updrafts that robs moisture available for evaporation in downdrafts. This reduction in evaporative cooling reduces downdraft strength and results in decreased TKE and convective intensity within the cloud layer. The reduction in cloud layer TKE near the inversion hampers the boundary layers ability to entrain above-inversion air. Bretherton et al. (2007), on the other hand, found that TKE near the cloud top was unaffected by cloud droplet sedimentation. They propose that entrainment is reduced by two mechanisms both associated with the removal of liquid water from the entrainment zone. The first is the reduction in entrainment-enhanced evaporative cooling, and the second is the reduction in radiative cooling near cloud top as a result of the reduced liquid water. They also assert that the first mechanism is more important than the second.

As stated in the case setup, a sensitivity test was performed with the current model, in which cloud droplet sedimentation was neglected. All other model parameters and processes were left unchanged, including the microphysics scheme that was left on to produce drizzle by autoconversion. Figures 3.39 through 3.47 (with the exception of figure 3.42) all contain results from the no cloud droplet sedimentation sensitivity test (dashed lines). Compared to the standard case with cloud droplet sedimentation included,

the sensitivity test produced a boundary layer with nearly the same turbulence strength especially in the cloud layer (Figures 3.46 and 3.47), a slightly higher entrainment rate (2.18 mm/s vs. 1.69 mm/s) (Figure 3.48), a thinner cloud deck with a reduced liquid water path (116.80 g/m² vs. 94.97 g/m²) (Figures 3.40 and 3.41), and reduced surface precipitation (Figure 3.44). This is broadly consistent with the findings of Ackerman et al. (2004) and Bretherton et al. (2007), whereby cloud droplet sedimentation reduces entrainment, increases LWP, and increases precipitation.

This broad agreement is encouraging, but which mechanism for entrainment reduction was responsible? With the nontraditional subgrid-condensation scheme and diagnosed cloud liquid water content, the process of cloud water evaporation is completely absent in the current model. Therefore, it is impossible to confirm or refute the claim of Ackerman et al. (2004) that cloud droplet sedimentation leads to reduced evaporative cooling in cloudy downdrafts, reduced in-cloud TKE, and finally reduced entrainment. The fact that vertical velocity variance remains mostly unchanged in the cloud layer should not be interpreted as evidence that this mechanism does not take place in nature. Likewise, the first process proposed by Bretherton et al. (2007) of a reduction in entrainment-enhanced evaporative cooling due to cloud droplet sedimentation is also not represented in the current model. However, the second process of reduced cloud-top radiative cooling is represented. In support of Bretherton et al. (2007), Figure 3.49 shows that cloud droplet sedimentation reduces cloud water near the boundary layer top by up to 0.17 g kg⁻¹. This demonstrates that cloud droplet sedimentation does in fact reduce the liquid water available for evaporation and evaporative cooling by dry entrained air, even though this process is not represented in the model. In addition, the radiative cooling

profile shows a reduction in cloud-top radiative cooling of about 0.3 K/h when cloud droplet sedimentation is included. In addition, the position of the maximum radiative cooling has move downward somewhat. The difference in the two curves is plotted with a dotted line, and shows the downward displacement of maximum radiative cooling when sedimentation is included. A positive value on this curve indicates that the case run with sedimentation does not cool as much compared with the no-sedimentation sensitivity test. Further, Section 3.2.2.1 mentions that a potential mechanism for the increased entrainment efficiency, A , in stratocumulus regimes is the influence of enhanced evaporative and radiative cooling at cloud top. Bretherton et al. (2007) found that the entrainment efficiency was reduced when cloud droplet sedimentation was included and they interpret this finding as further evidence that the reduction of liquid water at cloud top is responsible for the reduction in entrainment rate. The current model supports this

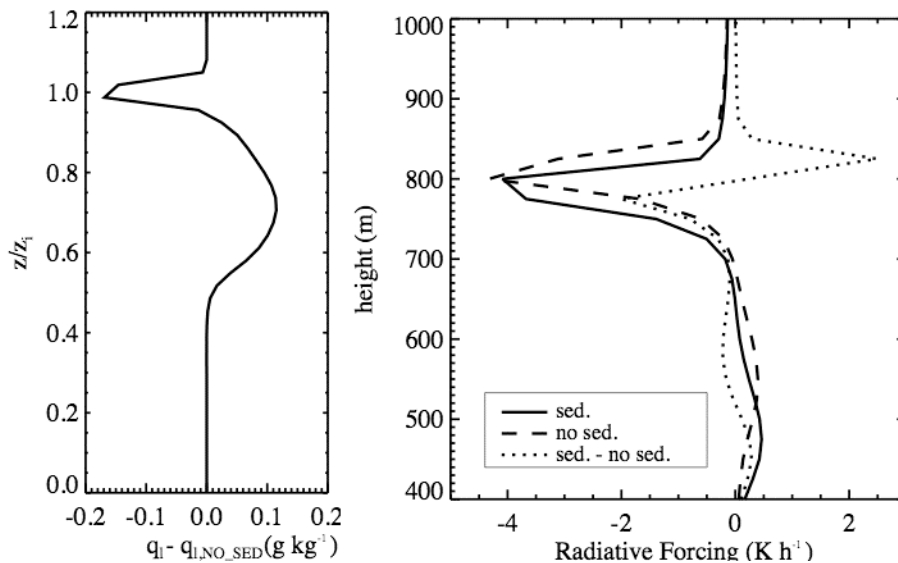


Figure 3.49 The profile on the left shows the difference between the no-sedimentation flux sensitivity test and the standard case. The profile on the right shows the difference in radiative forcing between the standard case (solid line) and the no-sedimentation flux sensitivity test (dashed line).

claim, at least for the cloud-top radiative cooling, since the entrainment efficiency, A , decreases about 34% from 0.53 to 0.35 when cloud droplet sedimentation is included.

3.5 Nonprecipitating trade-wind cumulus case: BOMEX

The fourth test case is based on mean conditions present during phase three of the Barbados Oceanographic and Meteorological Experiment (BOMEX) off the coast of Barbados in 1969, and is representative of steady-state non-precipitating maritime trade-wind cumulus. As with previous cases, the observational dataset chosen to create the test case was carefully chosen to minimize the effects of large-scale advection and other complicating factors in order to isolate processes of interest, namely shallow trade-wind cumulus convection. Also in accordance with the previous two cases, this case was developed for study by the BLCWG of GCSS. A detailed case description and results from a LES intercomparison are available in Siebesma et al. (2003). The main objectives of this case in the context of GCSS were to decipher how well the participant LES ensemble could reproduce the observed cloud structure and to what extent common cloud parameterizations could capture the relevant cloud dynamics.

In the context of the current study, the goal of using this test case aligns with the first objective of the GCSS BLCWG, namely to determine to what extent the current model is capable of reproducing a shallow trade-wind cumulus boundary layer regime. Recall in section 2.12 that subgrid-scale condensation schemes have historically been most useful for stratocumulus regimes and that cumulus regimes have proved to be a greater challenge. This is a product of the highly localized nature of the cloudy convective updrafts and expansive size of the broadly descending surrounding

environment leading to a highly skewed joint distribution of the thermodynamic variables. The precise PDF to use for a diagnostic subgrid-scale condensation scheme has yet to be determined, though many different forms have been tried with some success, including the one used in the current model. For this reason, it is reasonable to expect less favorable agreement between the current model's results and LES or observations.

3.5.1 Case setup

All initial and boundary conditions are given in Siebesma et al. (2003) and are presented below. The mean profiles of the thermodynamic and wind variables are

$$\bar{\theta}_t = \begin{cases} 298.7 & 0 < z \leq 520 \\ 298.7 + (302.4 - 298.7) \left(\frac{z - 520}{1480 - 520} \right) & 520 < z \leq 1480 \\ 302.4 + (308.2 - 302.4) \left(\frac{z - 1480}{2000 - 1480} \right) & 1480 < z \leq 2000 \\ 308.2 + 3.65 \times 10^{-3} (z - 2000) & z > 2000 \end{cases} \quad (3.23)$$

$$\bar{q}_t = \begin{cases} 17.0 + (16.3 - 17.0) \left(\frac{z}{520} \right) & 0 < z \leq 520 \\ 16.3 + (10.7 - 16.3) \left(\frac{z - 520}{1480 - 520} \right) & 520 < z \leq 1480 \\ 10.7 + (4.2 - 10.7) \left(\frac{z - 1480}{2000 - 1480} \right) & 1480 < z \leq 2000 \\ 4.2 - 1.2 \times 10^{-3} (z - 2000) & z > 2000 \end{cases} \quad (3.24)$$

$$\bar{u} = \begin{cases} -8.75 & 0 < z \leq 700 \\ -8.75 + 1.8 \times 10^{-3} (z - 700) & z > 700 \end{cases} \quad (3.25)$$

$$\bar{v} = 0 \quad (3.26)$$

where the momentum components have units of m s^{-1} , $\bar{\theta}_t$ is in K, and \bar{q}_t is in g kg^{-1} .

The initial second- and third-order moments are initialized to zero above the surface, except for the TKE components. The TKE profile is given by

$$TKE = 1.0 - \frac{z}{3000} \text{ (m}^2 \text{ s}^{-2}\text{)} \quad (3.27)$$

and is distributed isotropically over the three components. The surface sensible and latent

heat fluxes are held constant at $\overline{w'\theta'_{t,s}} = 8 \times 10^{-3} \text{ K m s}^{-1}$ and $\overline{w'q'_{t,s}} = 5.2 \times 10^{-5} \text{ m s}^{-1}$,

respectively. Surface momentum fluxes are parameterized according to

$$\overline{w'u'_s} = -u_*^2 \frac{\overline{u}}{\sqrt{\overline{u^2} + \overline{v^2}}} \text{ and } \overline{w'v'_s} = -u_*^2 \frac{\overline{v}}{\sqrt{\overline{u^2} + \overline{v^2}}} \text{ where } u_* = 0.28 \text{ m s}^{-1} \text{ is constant and the}$$

mean momentum values are taken from the lowest model level above the surface. All

other second-order moments are treated according to Monin-Obukhov similarity theory

as specified for the Wangara case. The surface pressure is initialized to 1015.0 hPa, and

the profiles of pressure and density are generated assuming hydrostatic equilibrium and

an isentropic profile with $\theta_0 = 299.1 \text{ K}$. In addition, pseudo-random perturbations in the

range of $[-0.1 \text{ K}, 0.1 \text{ K}]$ and $[-0.025 \text{ g kg}^{-1}, 0.025 \text{ g kg}^{-1}]$ are added to the $\overline{\theta_t}$ and

$\overline{q_t}$ profiles below 1500 m.

Large scale forcings include warming and drying from subsidence, radiative

cooling, large-scale moisture advection, and a large-scale pressure gradient through the

specification of geostrophic wind profiles. First, the subsidence is given by

$$\overline{w_{LS}} = \begin{cases} -0.0065 * \left(\frac{z}{1500} \right) & z \leq 1500 \\ -0.0065 + 0.0065 * \left(\frac{z - 1500}{2100 - 1500} \right) & 1500 < z \leq 2100 . \\ 0 & z > 2100 \end{cases} \quad (3.28)$$

The horizontal advection and radiative cooling rates are given by

$$ADV_{H,q_t} = \begin{cases} -1.2 \times 10^{-8} & z \leq 300 \\ -1.2 \times 10^{-8} + 1.2 \times 10^{-8} * \left(\frac{z-300}{500-300} \right) & 300 < z \leq 500 \\ 0 & z > 500 \end{cases} \quad (3.29)$$

$$-\frac{1}{\rho c_p} \frac{\partial \bar{F}}{\partial z} = \begin{cases} -2.0 & z \leq 1500 \\ -2.0 + 2.0 * \left(\frac{z-1500}{2500-1500} \right) & 1500 < z \leq 2500 \\ 0 & z > 2500 \end{cases} \quad (3.30)$$

where the horizontal advection term is in $\text{kg kg}^{-1} \text{s}^{-1}$ and the radiative cooling term is in K day^{-1} . The final forcing is the geostrophic wind, specified as

$$\begin{aligned} u_g &= -10 + 1.8 \times 10^{-3} z \quad (\text{m s}^{-1}) \\ v_g &= 0 \quad (\text{m s}^{-1}) \end{aligned} \quad (3.31)$$

The BOMEX observation area is located about 15°N , implying a Coriolis parameter of $f = 3.77 \times 10^{-5} \text{ s}^{-1}$.

A total of 30 grid levels at an even 100 m spacing are used, implying a domain depth of 3000 m. As in the previous DYCOMS RF02 case, the subgrid-scale condensation scheme is activated, but since this case is supposed to have non-precipitating cumulus, the subgrid-scale microphysics scheme is switched off. A time step of 1 s is used and the simulation is run for 6 hours. The results are compared with those from the LES participants as found in Siebesma et al. (2003). Unless stated otherwise, mean profiles are averaged over the last 3 hours of the simulation.

3.5.2 Results

3.5.2.1 Mean variables and cloudiness statistics

Mean profiles of the mean variables for the BOMEX case are shown in Figures 3.50, 3.51, and 3.52. In these plots, the mean profile represents an average over the last

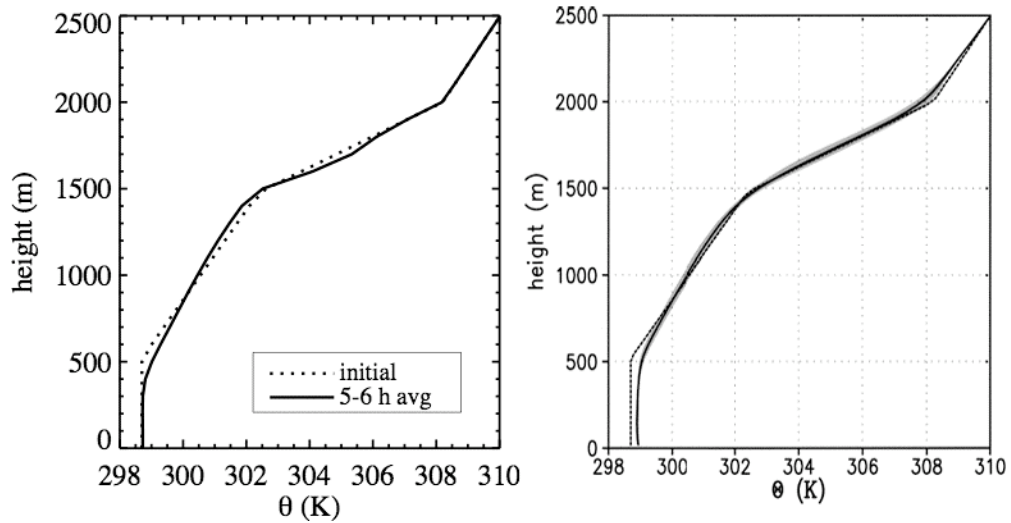


Figure 3.50 Mean profiles of $\bar{\theta}$ for the current model (left) and the LES participants (right). Solid lines indicate the mean profile from the last hour of the simulation, and the dotted lines indicate the initial profile. The shaded region for the LES plot indicates twice the standard deviation of the participants' results.

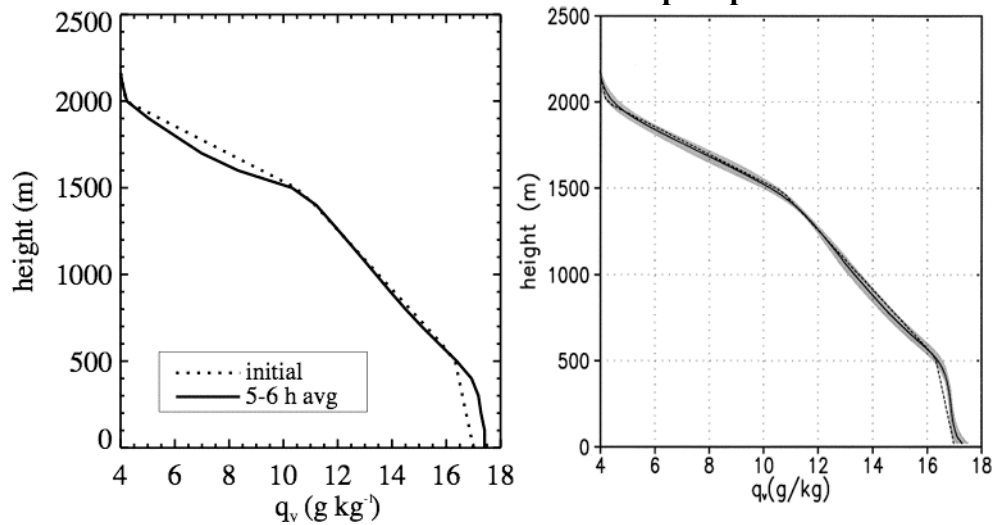


Figure 3.51 As in Figure 3.50, but for \bar{q}_v .

hour of the simulation. The LES results show little change in $\bar{\theta}$ from the initial profile to the end of the simulation. The lowest 700 m layer is slightly warmer, but the well-mixed layer maintains its depth. Other changes include minimal cooling between 1000 and 1500 m and a slight warming around 2000 m. The potential temperature profile from the current model matches the LES profile well, with a couple differences. The slight

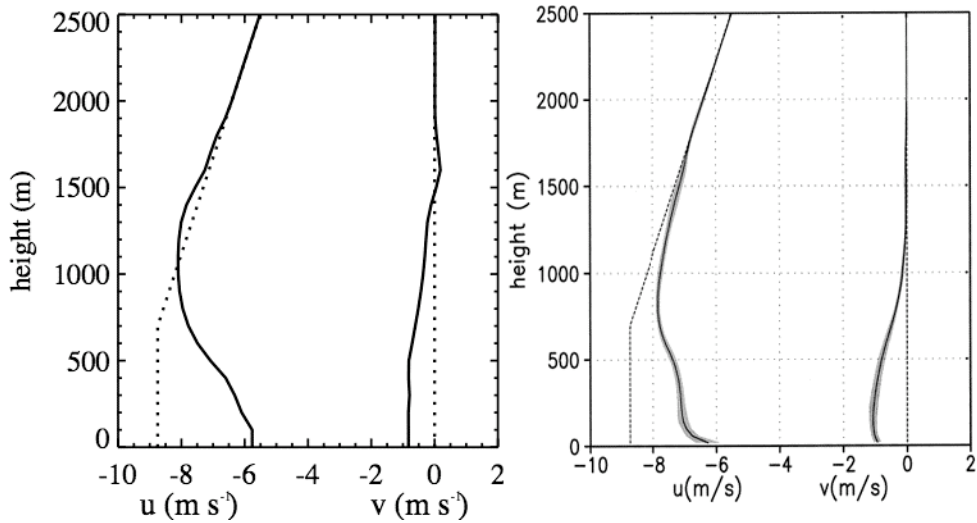


Figure 3.52 As in Figure 3.50, but for the mean wind components.

warming in the lowest 700 m is not reproduced, except for a thin layer from 300 m to 700 m. Cooling in the middle layer (800-1500 m) is slightly more pronounced, and warming above this layer creates a stronger inversion than existed at the beginning of the simulation. Similar discrepancies exist between the mean profiles of $\overline{q_v}$. The LES results show little change from the initial state, with a slight moistening below 500 m and slight drying from 700 – 1200 m and above 1400 m. The current model shows more moistening below 500 m and more drying above 1400 m, but matches LES extremely well in the cloud layer. The mean wind profiles in Figure 3.50 compare pretty well between the current model and LES, but both components are reduced a bit too much near the surface compared to LES.

Given the similarity of the mean profiles of the thermodynamic variables between the current model and LES, one might expect a commensurate cloud response. This response is evident in Figures 3.53, 3.54, and 3.55 which show the time-height cross-section of cloud fraction, mean profiles of cloud fraction, and mean profiles of cloud

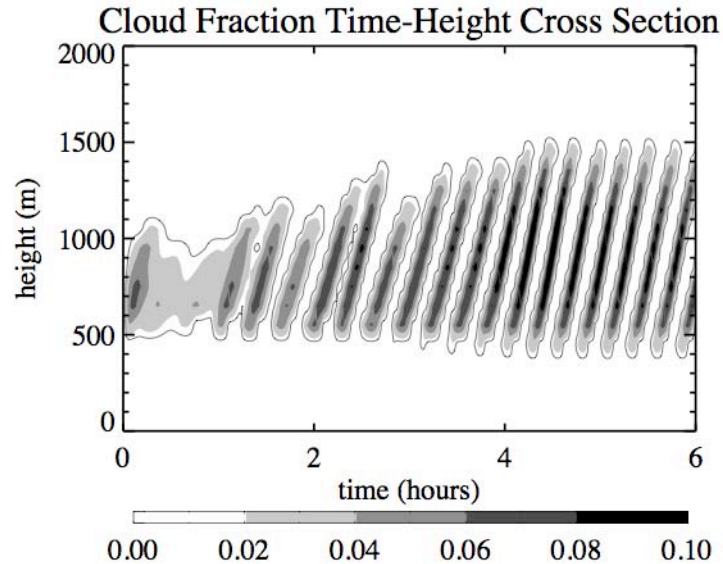


Figure 3.53 Time-height cross-section of cloud fraction for the current model.

water, respectively. The evolution of cloud fraction represented in Figure 3.53 shows some interesting features. First, while the cloud base remains steady in both observations and LES, it descends by about 100 m during the simulation in the current model. This anomalous feature is most likely a product of the increased subcloud layer moisture shown in Figure 3.51. Second, the current model produces what appears to be a succession of short-lived clouds that start at the LCL near 500 m and grow to a final height from 1300 to 1500 m. The complete lifetime of each cloud is about 30 – 40 min, although during its lifetime, it does not maintain a steady cloud base. The cloud base rises upward with the ascending thermal so that an individual’s cloud depth is only about 500 m. Before one cloud reaches its maximum height and dissipates, another discrete cloud forms near cloud base, so that a new cloud is being created at cloud base every 15 minutes or so. This cloud fraction oscillation is somewhat similar to how shallow cumuli operate in nature, although for a model that is attempting to simulate the mean state, this behavior is undesirable.

The spurious cloud water oscillation is not unique to the current model and has been investigated further by Cheng et al. (2004). The authors identified the source of the oscillation as the third-order moments involving the cloud liquid water [Equations (2.97)-(2.109)]. These moments are parameterized using the subgrid-scale condensation scheme and contribute to the buoyancy terms of the diagnostic third-order moments. Having come to the same conclusion that this oscillation is undesirable, the authors proposed three ways to dampen it. The first method involves adding ad hoc diffusion to the second-order moments. While this method is shown to dampen the oscillation and increase its period, the inclusion of ad hoc diffusion may have other consequences. For example, it may increase entrainment rates unrealistically or diffuse a sharp inversion. The second method involves using the modified turbulence length scale of Bougeault and André (1986). This effectively increases turbulence dissipation near cloud base. Cheng et al. (2004) show that when this method is combined with the first method, the cloud water oscillation is dampened further. Neither method one or two, or a combination thereof, completely damps the oscillation, however. The third method described in the study of Cheng et al. (2004) entails diagnostically determining the third-order moments involving cloud liquid water using the double-Gaussian PDF method of Golaz et al. (2002a). It is shown that method three is the only completely effective way to eliminate the cloud water oscillation, although its implementation constitutes a significant change to the subgrid-scale condensation scheme. While method two is employed in the current model, method one is not used due to its side effects. The third method is not used in the current model either, but will likely be put to use in future research.

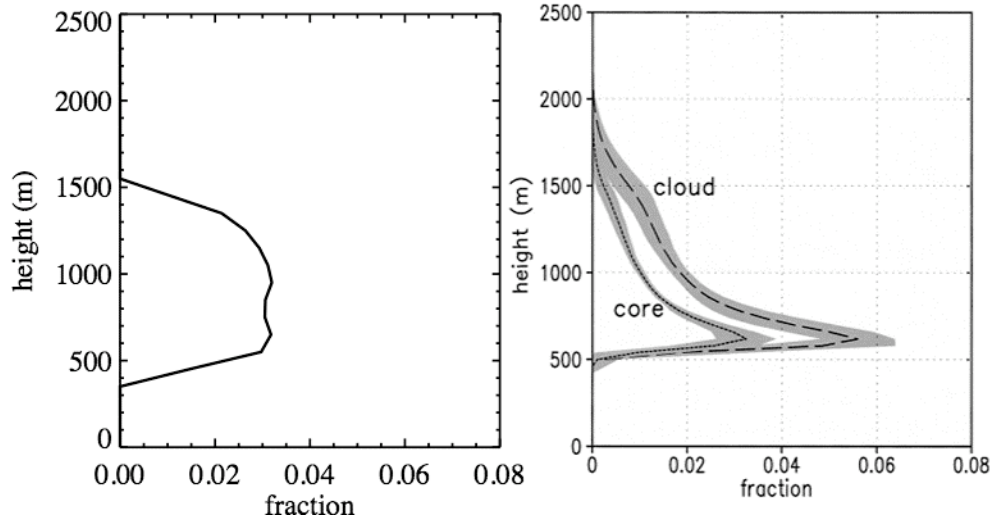


Figure 3.54 As in Figure 3.50, but for cloud fraction.

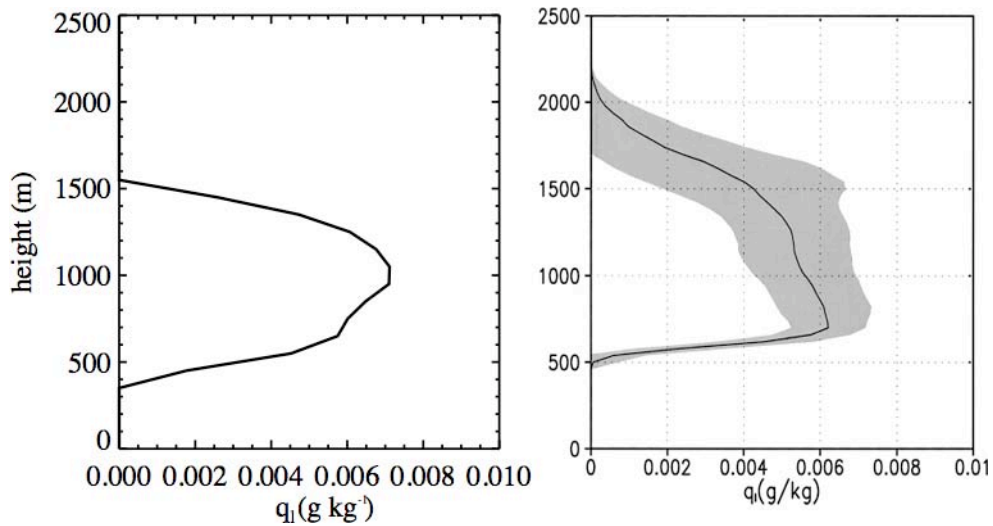


Figure 3.55 As in Figure 3.50, but for cloud liquid water mixing ratio.

The profiles of the mean cloud fraction shown in Figure 3.54 don't hint at the oscillation evident in the time-height cross section. It shows a more-or-less constant cloud fraction of 3% from about 500 to 1300 m with lesser amounts above and below. Most simulations of shallow cumulus, including this LES comparison, show that the maximum of the mean cloud fraction is found near cloud base, a result of the fact that most cumuli start at the lifted condensation level and reach various heights according to their buoyancy and other factors. The current model does not reproduce this behavior.

Further, the LES participants produce deeper clouds, up to nearly 2000 m, in contrast with the current model that only diagnoses clouds up to about 1500 m. The profiles of mean cloud water shown in Figure 3.55 are consistent with the cloud fraction profiles, and show that the current model slightly overestimates cloud water through much of the middle cloud layer, but underestimates the cloud water at cloud base and fails to produce any liquid water above 1550 m.

Despite the differences apparent in the spatial distribution of cloud as revealed by profiles, vertically integrated cloud statistics compare more favorably. Figure 3.56 shows time series of total cloud cover and LWP for the current model and the LES ensemble. Total cloud cover is often interpreted as the aerial extent of cloud cover as seen from a satellite, and for this reason could potentially influence radiative calculations. Since the current model is one-dimensional, there is no information about the spatial distribution of the cloud fraction that is diagnosed. However, the same cloud overlap assumption used for the microphysics scheme (Equation 2.119) is used to calculate cloud cover. The value

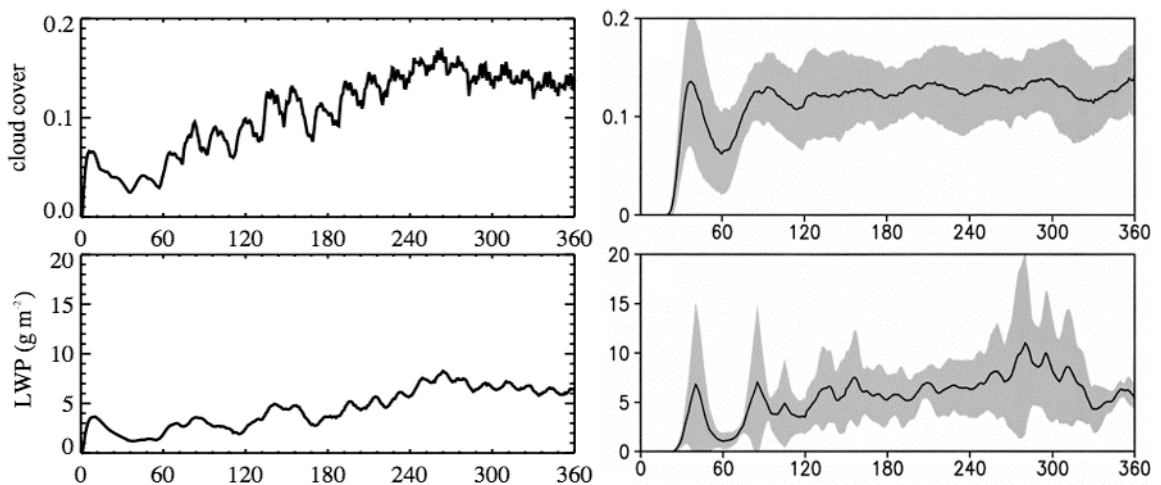


Figure 3.56 Time series of total cloud cover (top) and liquid water path (bottom) for the current model (left) and LES ensemble (right). As with the profiles from Siebesma et al. (2003), the shaded area denotes twice the standard deviation of the LES participants.

plotted in Figure 3.56 is the maximum cloud cover calculated from that equation. For the final three hours, cloud cover remains mostly steady between 10 and 15% for the current model, generally agreeing with the LES ensemble. The time series of LWP confirms the agreement in the cloud cover time series. Both the current model and the LES ensemble maintain a LWP between 5 and 8 g m⁻².

3.5.2.2 Turbulent moments

To examine how well the turbulent properties of a trade-wind cumulus boundary layer are represented in the current model, key turbulent moments are discussed. First, the time series and profile of TKE and its vertical velocity variance component are shown in Figures 3.57, 3.58, and 3.59, respectively. Figure 3.57 shows that the vertically integrated TKE increases slowly throughout the simulation, until about the last hour. The current model reproduces the increase, although it overestimates this quantity by about 100 kg m⁻¹ s⁻² compared with the LES ensemble mean after the spin-up period. The mean profiles of TKE over the last 3 hours of the simulation in Figure 3.58 show some important differences. The LES ensemble produces three maxima: one near the surface, one at the top of the subcloud layer, and one near the top of the cloud layer, but the current model does not reproduce the local maximum near the top of the subcloud layer. Also, TKE is considerably overestimated in the cloud layer compared with LES. Examination of the vertical velocity variance profile in Figure 3.59 shows that most of the overestimation in the cloud layer comes from this component. An examination of the TKE budget (not shown) indicates that the production of TKE by the buoyancy term in the cloud layer is too strong. Figure 3.62 shows the overestimation of the buoyancy flux.

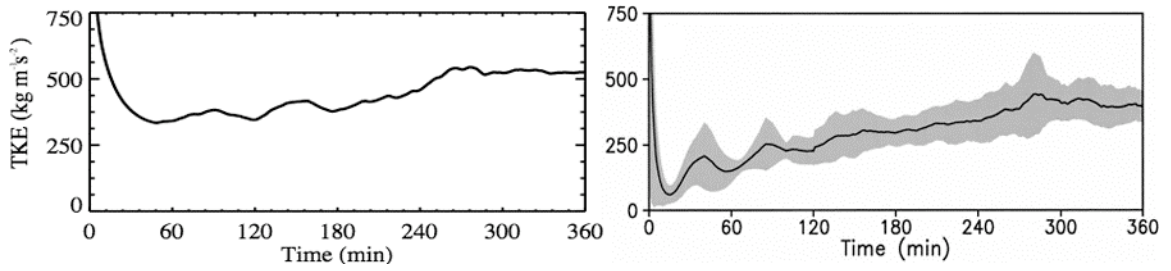


Figure 3.57 As in Figure 3.55 but for vertically integrated TKE.

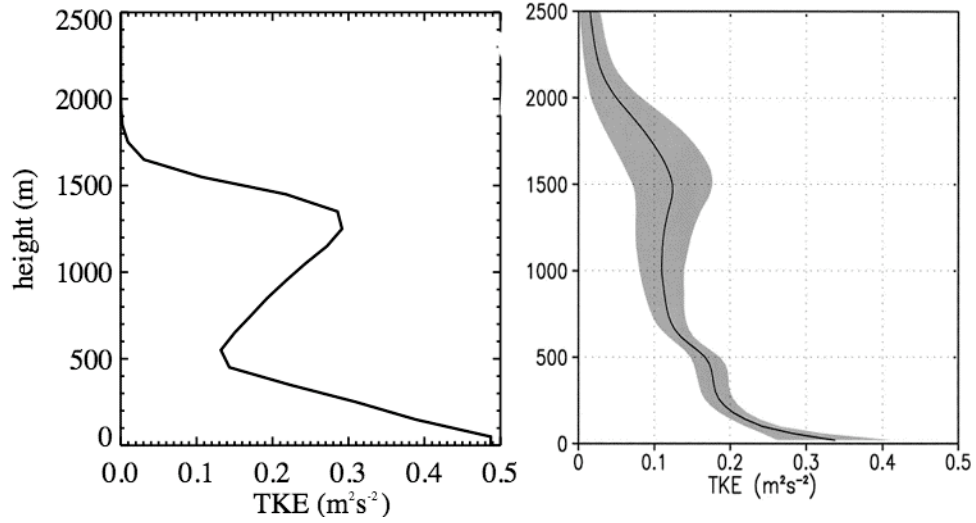


Figure 3.58 As in Figure 3.50, but for TKE.

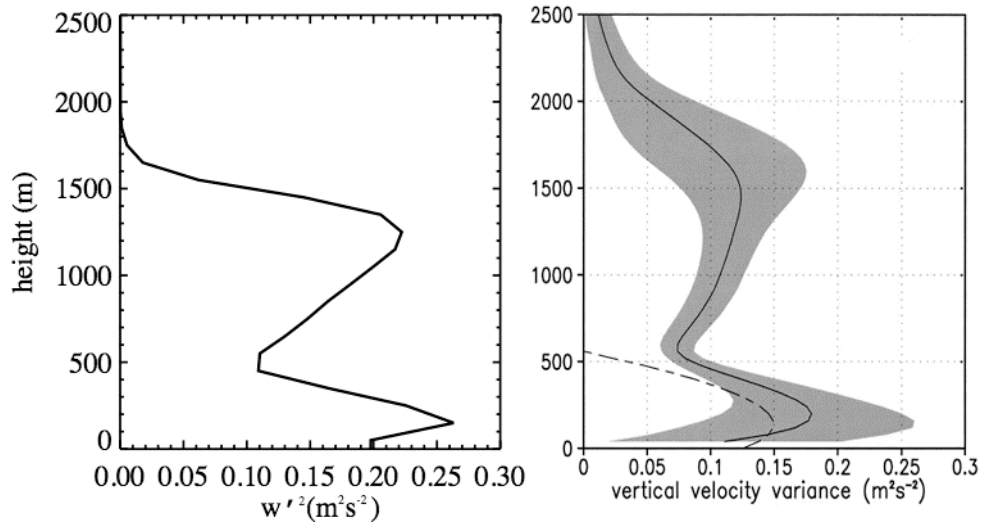


Figure 3.59 As in Figure 3.50, but for vertical velocity variance.

The mean profiles of the vertical turbulent fluxes of θ_l and q_l are shown in Figures 3.60 and 3.61. The mean profile of $\overline{w'\theta_l'}$ is in good agreement with LES as far as the magnitude and placement of the negative peak. However, the shape of the profile does not curve as smoothly as in the LES ensemble. The mean profile of $\overline{w'q_l'}$ for the

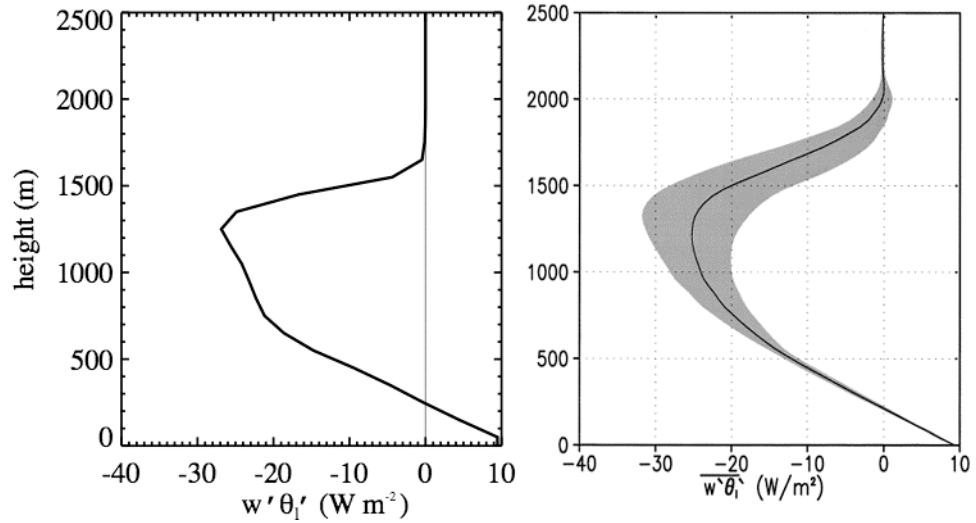


Figure 3.60 As in Figure 3.50, but for the vertical liquid water potential temperature flux.

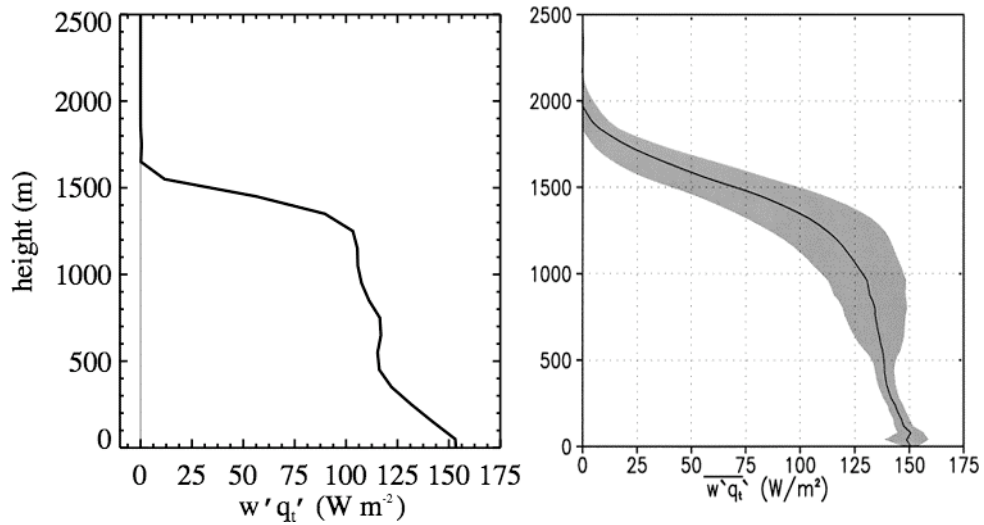


Figure 3.61 As in Figure 3.50, but for the vertical total water specific humidity flux.

current model has qualitative similarities to LES, but there are some important differences. First, the magnitude of decrease with height in the subcloud layer is too great, resulting in too much moisture convergence in this layer and ultimately to a cloud base that is 100 m too low. Additionally, in the bottom 200 m of the cloud layer (500 – 700 m), $\overline{w'q'_l}$ increases with height, indicating moisture flux divergence and drying of this layer. This feature could be responsible for the difference in shape between the current model's cloud fraction profile and LES.

Lastly, the mean buoyancy flux profile is presented in Figure 3.62. Compared with LES, the buoyancy flux is overestimated in the cloud layer. Recall that in the current model, the buoyancy flux is given by Equation 2.61, a combination of $\overline{w'\theta'_l}$, $\overline{w'q'_l}$, and $\overline{w'q'_v}$. These individual terms are plotted along with their total. Since the first two quantities don't differ enough from LES to account for an overestimate in the buoyancy flux, the culprit is the diagnosis of the liquid water flux from the subgrid-scale

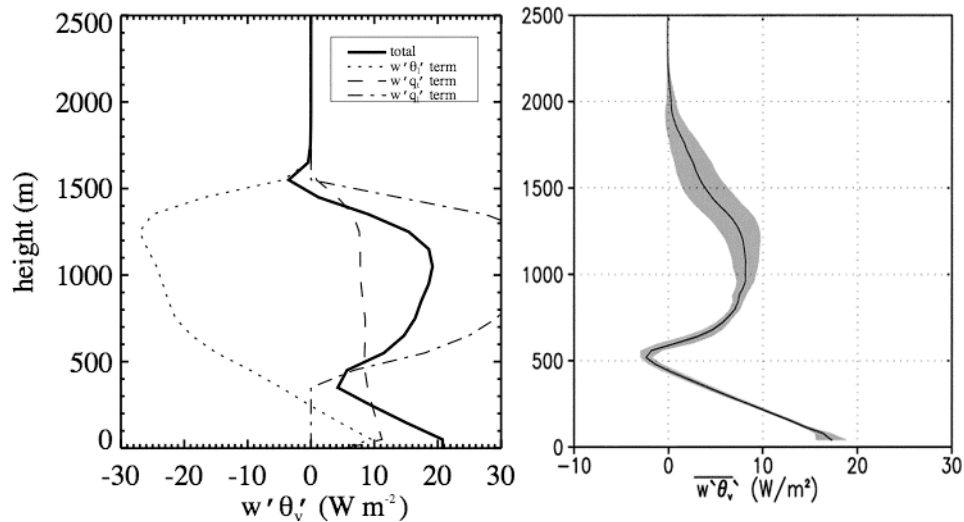


Figure 3.62 As in Figure 3.50, but for the vertical buoyancy flux.

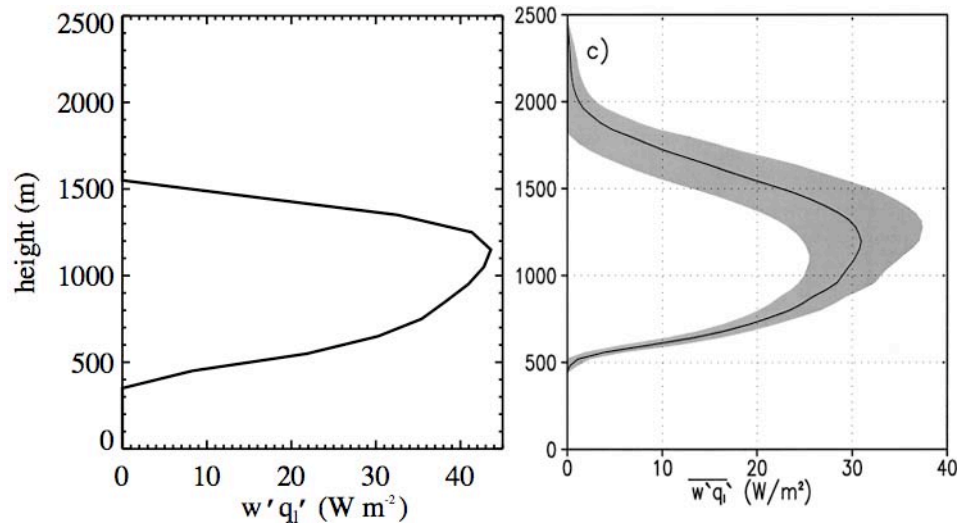


Figure 3.63 As in Figure 3.50, but for the liquid water flux.

condensation scheme. Figure 3.63 shows the mean liquid water flux compared to LES.

This quantity is overestimated in the current model by about 40% compared to LES.

3.6 Precipitating trade-wind cumulus case: RICO

The fifth and final test case is based on mean conditions during a three week undisturbed period of the Rain In Cumulus over the Ocean (RICO) field campaign in the winter of 2004-2005. The initial conditions are somewhat similar to the BOMEX case, but the conditionally unstable layer is deeper, implying somewhat deeper and potentially thicker clouds. In addition, many of the trade-wind cumuli produced light rainfall during the field campaign, so model participants were asked to leave their microphysics parameterizations active to see how well they could reproduce the observed rainfall of about 0.3 mm day^{-1} . In addition to testing whether the model participants accurately simulate the light precipitation, this intercomparison case also tests how well the participants capture the mean and turbulent properties of the boundary layer, as with the previous four cases. Results of the intercomparison have yet to be formally published,

although preliminary results and other case information may be found on the case website (<http://www.knmi.nl/samenw/rico>). Within the context of the current study, this case is run as a second challenging cumulus case, differing from BOMEX only by the initial and boundary conditions, large-scale forcings, and activated microphysics scheme.

3.6.1 Case setup

The initial profiles of the mean quantities are given by

$$\bar{\theta}_t = \begin{cases} 297.9 & 0 < z \leq 740 \\ 297.9 + (317.0 - 297.9) \left(\frac{z - 740}{4000 - 740} \right) & z > 740 \end{cases} \quad (K) \quad (3.32)$$

$$\bar{q}_t = \begin{cases} 16.0 + (13.8 - 16.0) \left(\frac{z}{740} \right) & 0 < z \leq 740 \\ 13.8 + (2.4 - 13.8) \left(\frac{z - 740}{3260 - 740} \right) & 740 < z \leq 3260 \\ 2.4 + (1.8 - 2.4) \left(\frac{z - 3260}{4000 - 3260} \right) & z > 3260 \end{cases} \quad (\text{g kg}^{-1}) \quad (3.33)$$

$$\bar{u} = -9.9 + 2.0 \times 10^{-3} * z \quad (\text{m s}^{-1}) \quad (3.34)$$

$$\bar{v} = -3.8 \quad (\text{m s}^{-1}) \quad (3.35)$$

All second- and third-order moments are initialized to zero above the surface except for TKE components, which receive an equal share of the initial TKE, defined as

$$TKE = 1.0 - \frac{z}{4000} \quad (\text{m}^2 \text{ s}^{-2}). \quad (3.36)$$

The surface fluxes are parameterized according to

$$\overline{w'\theta'_{t,s}} = -C_h \sqrt{\overline{u'^2} + \overline{v'^2}} (\bar{\theta}_t - \theta_{t,s}) \quad \text{K m s}^{-1} \quad (3.37)$$

$$\overline{w'q'_{t,s}} = -C_q \sqrt{\overline{u'^2} + \overline{v'^2}} (\bar{q}_t - q_s) \quad \text{kg kg}^{-1} \text{ m s}^{-1} \quad (3.38)$$

$$\overline{w'u'_s} = -C_m \bar{u} \sqrt{\bar{u}^{-2} + \bar{v}^{-2}} \text{ m}^2 \text{ s}^{-2} \quad (3.39)$$

$$\overline{w'v'_s} = -C_m \bar{v} \sqrt{\bar{u}^{-2} + \bar{v}^{-2}} \text{ m}^2 \text{ s}^{-2} \quad (3.40)$$

where mean values are taken from the first level above the surface and the constants are $C_h = 0.001094$, $C_q = 0.001133$, and $C_m = 0.001229$. Other second-order moments are calculated according to Monin-Obukhov similarity theory as in the Wangara case. The surface pressure is initialized to 1015.4 hPa, and the profiles of pressure and density are generated assuming hydrostatic equilibrium and an isentropic profile with $\theta_0 = 298.5 \text{ K}$. In addition, pseudo-random perturbations in the range of $[-0.1 \text{ K}, 0.1 \text{ K}]$ and $[-0.025 \text{ g kg}^{-1}, 0.025 \text{ g kg}^{-1}]$ are added to the $\bar{\theta}_t$ and \bar{q}_t profiles below 740 m.

Large scale forcings include warming and drying due to subsidence, horizontal advection of $\bar{\theta}_t$ and \bar{q}_t , radiative cooling, and the geostrophic wind. The subsidence profile is given by

$$\bar{w}_{LS} = \begin{cases} -0.005 * \left(\frac{z}{2260} \right) & z \leq 2260 \\ -0.005 & z > 2260 \end{cases} \quad (\text{m s}^{-1}), \quad (3.41)$$

the horizontal advection and radiative cooling terms are combined to a constant value independent of height of

$$ADV_{H,\theta_t} - \frac{1}{\rho c_p} \frac{\partial \bar{F}}{\partial z} = \frac{-2.5}{86400} \quad (\text{K s}^{-1}), \quad (3.42)$$

the horizontal advection of \bar{q}_t is given by

$$ADV_{H,q_t} = \begin{cases} -1.0 + 1.345 * \frac{z}{2980} & z \leq 2980 \\ 0.345 & z > 2980 \end{cases} \quad (\text{g kg}^{-1} \text{ day}^{-1}), \quad (3.43)$$

and the geostrophic wind profiles are identical to the initial mean wind profiles. The RICO observation area is 18° N implying a Coriolis parameter of $f = 4.5 \times 10^{-5} \text{ s}^{-1}$.

A total of 100 grid levels at an even 40 m spacing is used, implying a domain depth of 4000 m. As with the DYCOMS RF02 case, both subgrid-scale condensation and microphysics are activated. A time step of 5 s is used and the simulation is run for 24 hours. The results are compared with those from the preliminary analysis of the LES participants as found on the RICO case website mentioned in the introduction. Unless stated otherwise, mean profiles are averaged over the last 4 hours of the simulation.

3.6.2 Results

3.6.2.1 Mean variables, cloudiness statistics, and precipitation

To understand how the current model captures the mean thermodynamic state compared to LES, the mean profiles of the thermodynamic variables are shown in Figures 3.64 and 3.66 along with the change in the profiles from the initial conditions in Figures 3.65 and 3.67. Figure 3.64 shows that all model are adequately capable of resolving the transition from the initial shallow 700 m thick mixed layer to a boundary layer that is over 2 km deep that contains a conditionally unstable layer above a shallow well-mixed layer. However, Figure 3.65 is useful in pointing out differences among the models, and one major difference stands out. The cooling in the cloud layer (500 – 2100 m) is too strong compared with the LES ensemble mean. The maximum cooling in the current model is about 2.8 K near the inversion top versus a mean of about 2.1 K for the LES participants. The current model lies within the ensemble range, however.

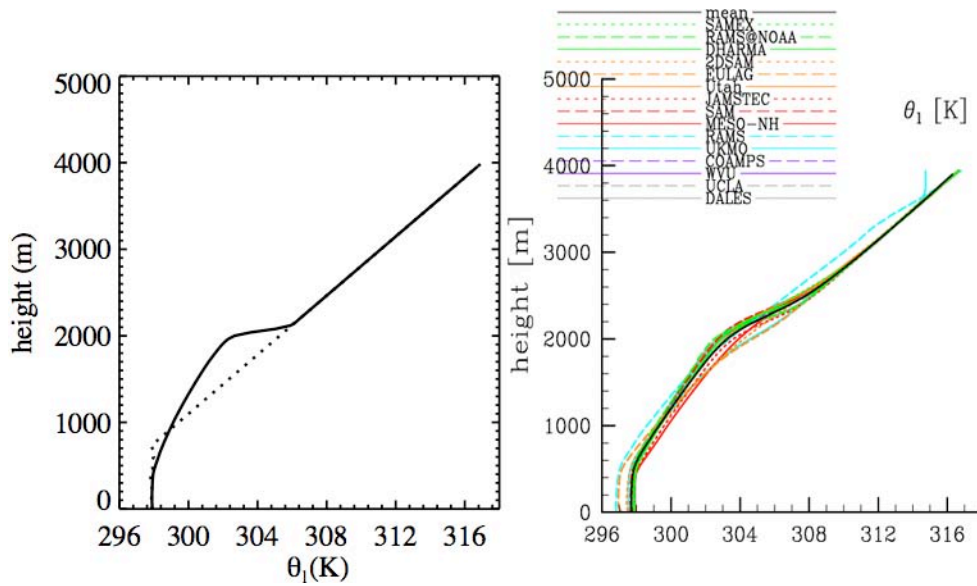


Figure 3.64 Mean profiles of $\bar{\theta}_1$ for the last four hours of the simulation for the current model (left) and the LES participants (right). The initial profile is given by the dotted line on the left plot. Each colored line indicates a particular LES participant result, and the solid black line represents the mean of the LES ensemble.

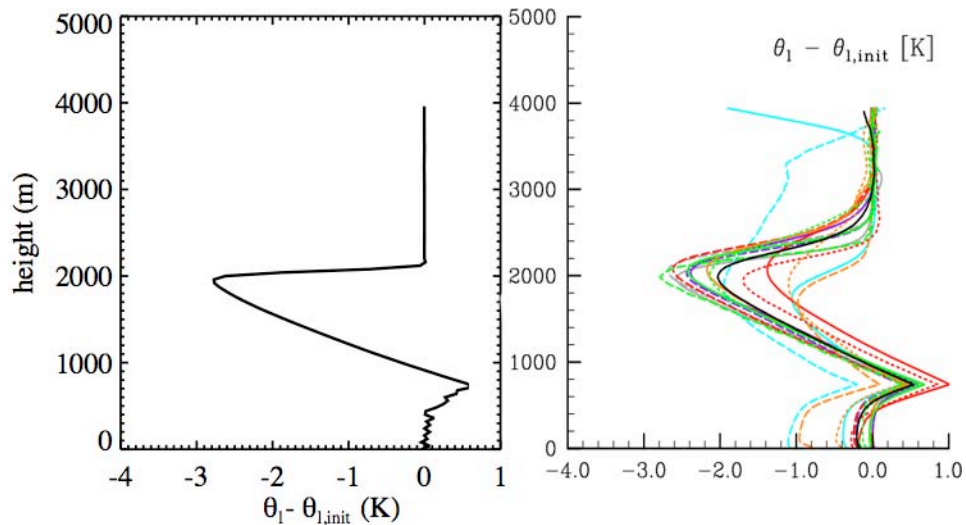


Figure 3.65 As in Figure 3.63, but for the change in $\bar{\theta}_1$ from the initial conditions to the profiles in Figure 3.63.

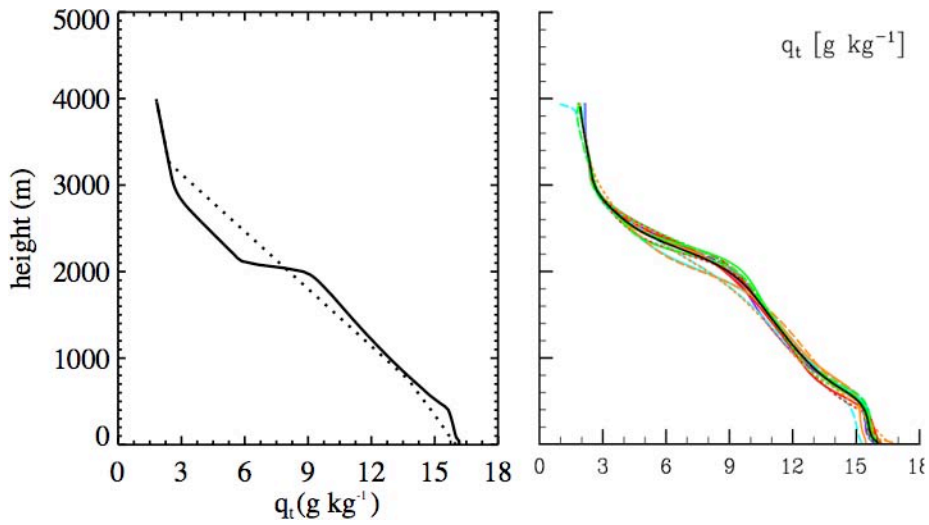


Figure 3.66 As in Figure 3.63, but for $\overline{q_t}$.

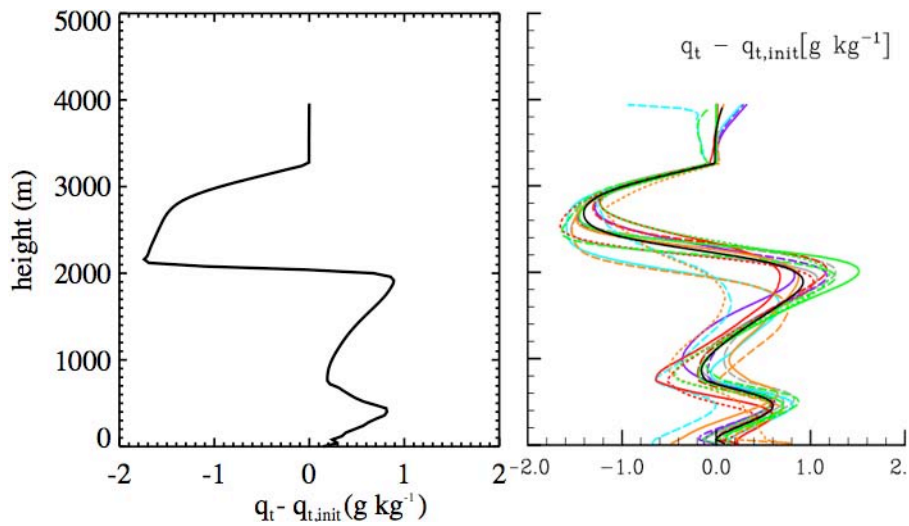


Figure 3.67 As in Figure 3.65, but for $\overline{q_t}$.

The mean profile of $\overline{q_t}$ in Figure 3.66 compares as favorably with the LES participants.

The moisture is shown to increase through the depth of the cloud layer, but particularly at cloud base and cloud top. Above cloud top, the gradient in moisture sharpens. The change in total water specific humidity profiles from the initial conditions to the final

state in Figure 3.67 shows a similar picture, although it demonstrates that the current model dries too much just above the inversion compared to LES.

The time-height cross-section of cloud fraction in Figure 3.68 shows the evolution of the cloud field throughout the simulation. The plot is surprisingly qualitatively different than the same plot for the BOMEX case. The cloud fraction slowly increases in height through the simulation, with a hint of an oscillation, but there are not discrete cumulus clouds as evident in the BOMEX case. In addition, the maximum cloud fraction is located toward the upper half of the cloud instead of near cloud base as in LES results and observations. Comparison of the cloud fraction profiles in Figures 3.69 shows that cloud fraction is overestimated substantially in the middle of the cloud layer, but underestimated near cloud base, and the depth of the cloud cover is underestimated. The maximum cloud fraction near cloud base for the mean of the LES results is around 6% versus the maximum cloud fraction of about 9% near 1700 m for the current model. While the cloud fraction profile still resembles cumulus due to its relatively low cloud

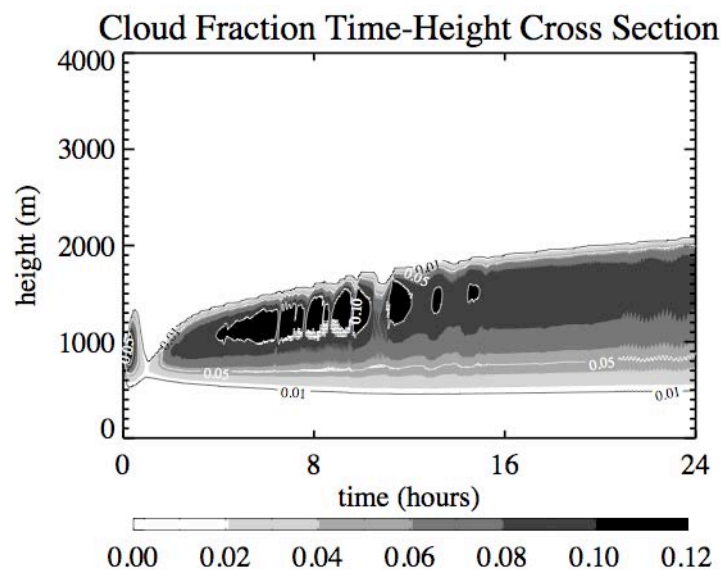


Figure 3.68 Time-height cross-section of cloud fraction.

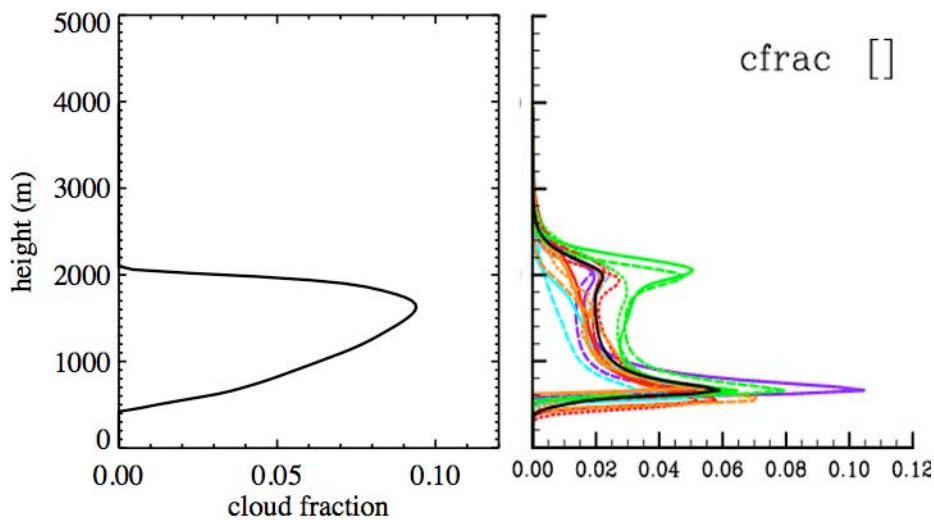


Figure 3.69 As in Figure 3.64, but for cloud fraction.

fraction, it demonstrates that there is still much room for improvement in the current model.

The mean profiles of precipitation flux are shown in Figure 3.70. Even with the overestimation of cloud fraction and cloud liquid water (not shown), the precipitation flux is underestimated compared to the mean LES results. The LES profiles suggest that rain production starts high within the cumulus ensemble, and reaches its maximum value at about 1500 m, roughly in the middle of the mean cloud deck. Below this point, precipitation is evaporated, even as it passes through the maximum cloud fraction near cloud base. The current model produces a different profile shape. As with LES, precipitation generation starts near cloud top, but unlike LES, the precipitation flux does not peak around mid-cloud. Instead, the precipitation flux is not reduced by evaporation until after it reaches cloud base. It is interesting to note that even with the differences in the precipitation flux profiles, the mean surface precipitation of the models is similar: 5 W m^{-2} for the current model and 7 W m^{-2} for the LES ensemble. Over the 24 hours of

compared to the LES ensemble mean. A look at the vertical velocity variance profile in Figure 3.69 identifies this component as a major contributor to this overestimation. Horizontal momentum variances are also overestimated by a similar amount (not shown). The overestimation of the vertical velocity variance is a direct result of the overestimation of the buoyancy flux (not shown) as in the BOMEX case.

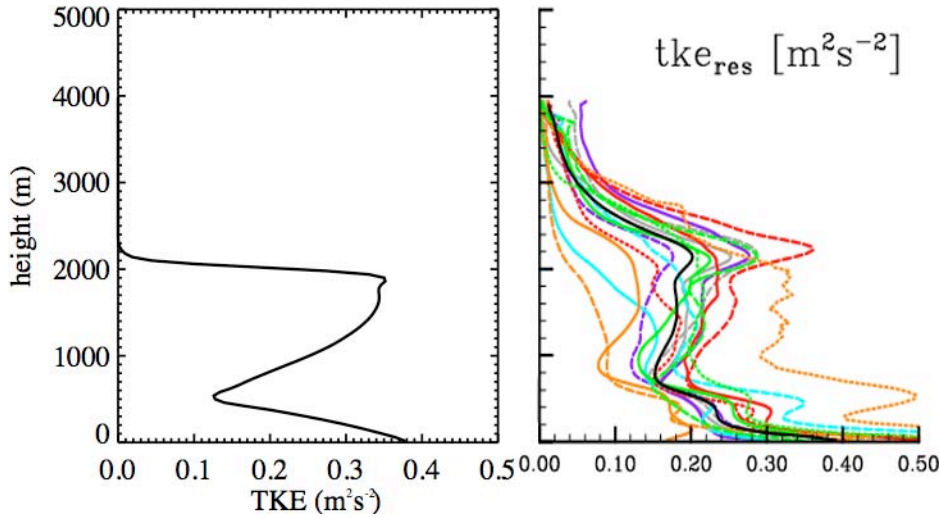


Figure 3.71 As in Figure 3.64, but for the TKE.

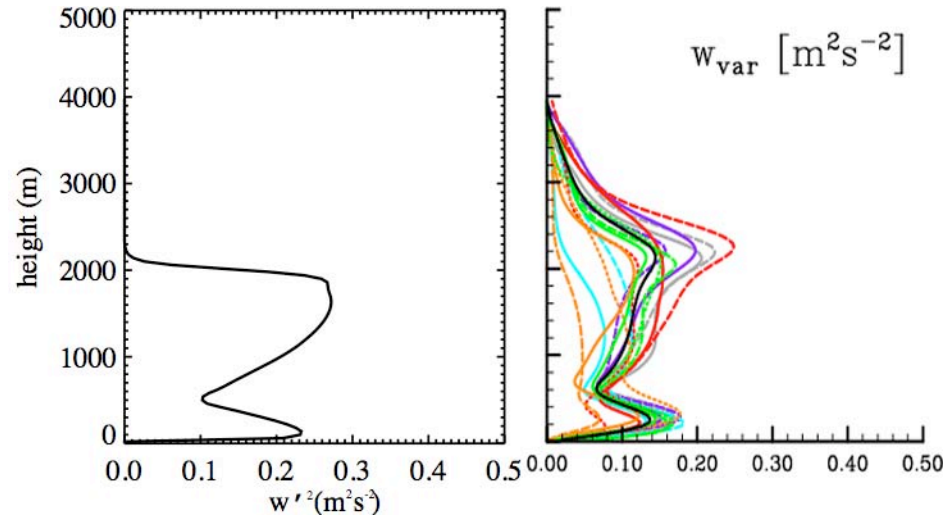


Figure 3.72 As in Figure 3.64, but for the vertical velocity variance.

The turbulent vertical fluxes of θ_i and q_i are shown in Figures 3.73 and 3.74, respectively. Both turbulent fluxes look qualitatively similar to their LES ensemble

counterparts, but a few important differences are noticeable. First, the current model produces slight curvature in the turbulent heat flux profile from the surface to the minimum point near 1800 m, whereas the LES ensemble mean profile is nearly linear here. Second, the current model has the moisture flux decreasing too quickly with height in the boundary layer, indicative of too much moistening.

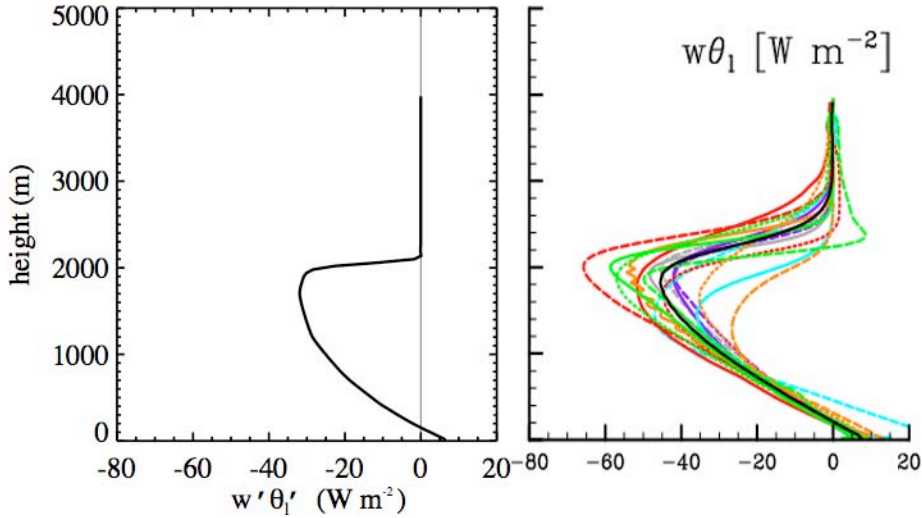


Figure 3.73 As in Figure 3.64, but for the vertical turbulent flux of θ_l .

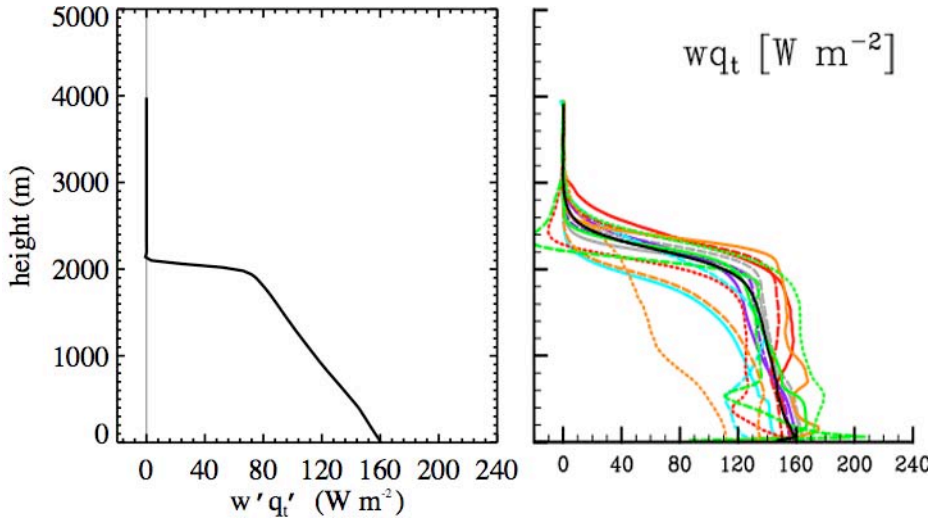


Figure 3.74 As in Figure 3.64, but for the vertical turbulent flux of q_t .

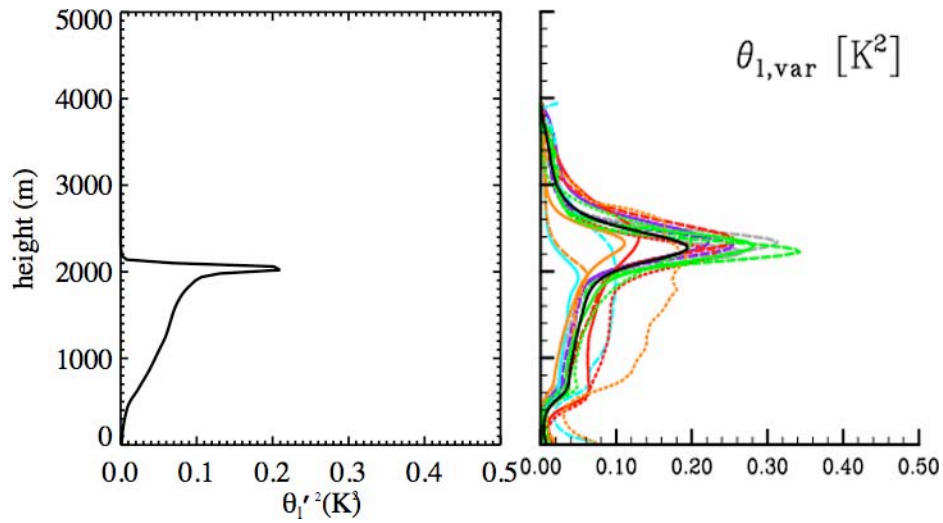


Figure 3.75 As in Figure 3.64, but for $\overline{\theta_t'^2}$.

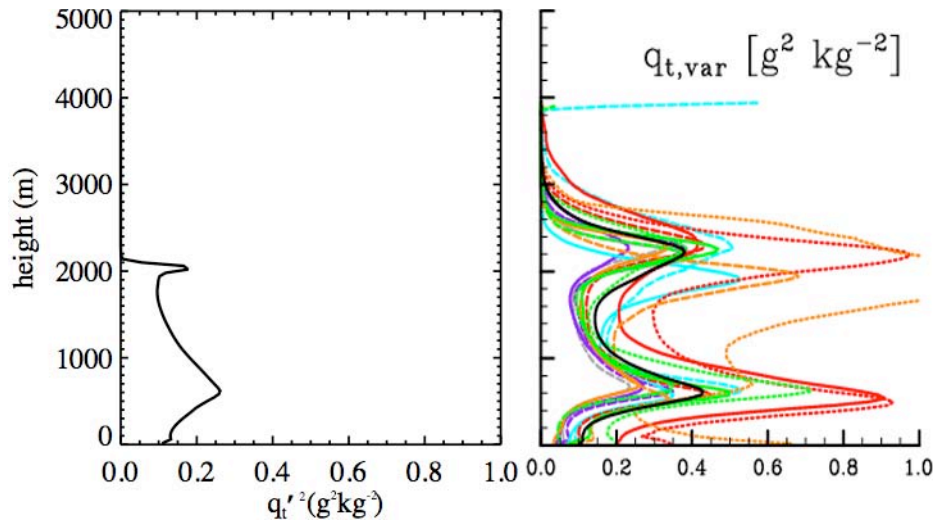


Figure 3.76 As in Figure 3.64, but for $\overline{q_t'^2}$.

Lastly, the variances of θ_t and q_t are shown in Figures 3.75 and 3.76, respectively. These two quantities play an important role in the buoyancy terms of the equations for the turbulent vertical fluxes of θ_t and q_t and are also needed to determine the normalized saturation deficit, Q_1 , and hence the cloud fraction and cloud liquid water content in the subgrid-scale condensation scheme. Qualitatively, the current model does a good job of matching the general shape of the LES ensemble mean profiles, with peaks in

variance near the boundary layer top for both quantities and another peak near cloud base for the moisture variance. The magnitude of the moisture variance peaks are slightly underestimated, but overall, the current model performs well compared to LES for these two quantities.

3.7 Notes on model execution time

All five cases were run on a dual 2 GHz PowerPC G5 Apple PowerMac. The processor time used by each model was calculated using the Unix “time” utility and the results are presented in Table 3.2.

Case Name	Process Execution Time
Wangara (Section 3.2)	0.40 s
Smoke Cloud (Section 3.3)	2.34 s
DYCOMS RF02 (Section 3.4)	4.31 s
BOMEX (Section 3.5)	1.18 s
RICO (Section 3.6)	5.32 s

Table 3.2 Processor time used for each model.

Chapter 4

Three-Dimensional Implementation and Results

4.1 Introduction

The results of the previous chapter demonstrate that the third-order closure turbulence model developed in this paper is capable of accurately modeling clear convective, stratocumulus-topped, and cumulus-containing boundary layers as well as approximating the entrainment process in a satisfactory fashion. Indeed, the current model has proven to be a valuable one-dimensional tool for studying cloudy boundary layers in general. Given this success, it is reasonable and fitting to couple the current model as a turbulence parameterization to a three-dimensional mesoscale model. While the current model could conceivably be coupled to any such model that requires the inclusion of vertical turbulent fluxes of heat, moisture, and momentum, a novel new three-dimensional model developed recently by Jung and Arakawa (2008) was chosen to be the recipient. The implementation of the coupling and the results produced from the resultant model are presented in this chapter.

4.2 Vector Vorticity Model (VVM)

The novelty of the host model, dubbed the Vector Vorticity Model (VVM), is attributed to its unique dynamical core. Rather than predicting the three momentum components as is traditionally done in GCMs and cloud models, VVM predicts the three-dimensional vorticity field. Specifically, only the two horizontal vorticity components are predicted at every grid point, while the vertical component of vorticity only needs to be predicted at one level. Its value at the remaining grid points can be diagnosed using the nondivergence of vector vorticity. Given the predicted vector vorticity field, the vertical velocity can be diagnosed with the solution of a three-dimensional elliptic equation. The horizontal velocity can also be diagnosed by splitting each component into its rotational and divergent parts and solving a two-dimensional elliptic equation for each part, at one specified level in the model. The remaining values at the other levels can be retrieved by integration and the definitions of horizontal vorticity components. Readers interested in the specifics of the dynamical core and its derivation are directed to Jung and Arakawa (2008) and Jung and Arakawa (2005).

The thermodynamic state is represented by the potential temperature and six species of water: vapor, cloud water, cloud ice, rain, snow, and graupel. Processes accounted for in the prediction of the thermodynamic variables include advection, radiation, microphysical transformations, fluxes due to turbulence, and large-scale forcings. The radiation terms are parameterized following the scheme of Fu et al. (1995) and the microphysics scheme follows Krueger et al. (1995), Lin et al. (1983), and Lord et al. (1984). The turbulence scheme used is the first-order closure scheme of Shutts and Gray (1994) with surface fluxes from Deardorff (1972). Finally, the advection scheme is

“an upstream-weighted partially third-order scheme” using an Eulerian space-difference scheme and the second-order Adams-Bashforth scheme in time (Jung and Arakawa 2008).

4.3 Coupling with VVM

Coupling the turbulence model presented in Chapter 2 to the VVM requires significant modification to both. First, for the same reasons mentioned in Section 2.2, the thermodynamic variables of the VVM are changed to match the moist-adiabatically conserved variables of the turbulence model, liquid water potential temperature and total water specific humidity. Rather than using six prognostic individual species of water as in the VVM, only three species of water are now considered: two prognostic rain water species from the subgrid-scale microphysics scheme and one diagnostic cloud water species from the subgrid-scale condensation scheme. With the change in thermodynamic variables it becomes more straightforward to use the output from the turbulence model that is formulated for the use of moist conservative variables. However, the buoyancy term found in the prognostic equations for the horizontal components of vorticity must be changed to reflect the new variable choice. Following Appendix B, the buoyancy term may be written in terms of the moist conservative variables as

$$B = \frac{g}{\theta_0} \left\{ \theta_l + \frac{(1 - \epsilon_0)}{\epsilon_0} \theta_0 q_t + \left[\frac{L_v}{c_p} \left(\frac{p_0}{p} \right)^{\kappa} - \frac{\theta_0}{\epsilon_0} \right] q_t \right\} \quad (4.1)$$

The next change is the replacement of the Shutts and Gray (1994) turbulence scheme with the current model. Other than porting the current model from Fortran 90 to Fortran 77 used in VVM, this switch is mostly straightforward. The integration of the current model’s output to VVM is accomplished by replacing all turbulence terms found

in VVM with the equivalent terms calculated from the turbulence model. The tendencies due to turbulence of the thermodynamic variables are calculated as

$$\frac{\partial \bar{\theta}_l}{\partial t_{TURB}} = -\frac{1}{\rho_0} \frac{\partial \overline{\rho_0 w' \theta'_l}}{\partial z} \quad (4.2)$$

$$\frac{\partial \bar{q}_l}{\partial t_{TURB}} = -\frac{1}{\rho_0} \frac{\partial \overline{\rho_0 w' q'_l}}{\partial z}. \quad (4.3)$$

Finally, the turbulence terms in the vorticity equation must be formulated from the available momentum fluxes calculated from the turbulence model. The turbulence terms for the ξ , η , and ζ components of vorticity are given by

$$\frac{\partial \xi}{\partial t_{TURB}} = \frac{\partial F_w}{\partial y} - \frac{\partial F_v}{\partial z} \quad (4.4)$$

$$\frac{\partial \eta}{\partial t_{TURB}} = -\frac{\partial F_w}{\partial x} + \frac{\partial F_u}{\partial z} \quad (4.5)$$

$$\frac{\partial \zeta}{\partial t_{TURB}} = \frac{\partial F_v}{\partial x} - \frac{\partial F_u}{\partial y} \quad (4.6)$$

where the F terms are the turbulent flux convergence terms from the momentum equations

$$F_u = -\frac{\partial \overline{u'^2}}{\partial x} - \frac{\partial \overline{u'v'}}{\partial y} - \frac{1}{\rho_0} \frac{\partial \overline{\rho_0 w' u'}}{\partial z}, \quad F_v = -\frac{\partial \overline{u'v'}}{\partial x} - \frac{\partial \overline{v'^2}}{\partial y} - \frac{1}{\rho_0} \frac{\partial \overline{\rho_0 w' v'}}{\partial z}, \quad \text{and}$$

$$F_w = -\frac{\partial \overline{w'u'}}{\partial x} - \frac{\partial \overline{w'v'}}{\partial y} - \frac{1}{\rho_0} \frac{\partial \overline{\rho_0 w'^2}}{\partial z}. \quad \text{Terms involving horizontal derivatives and fluxes are}$$

negligible compared with vertical derivatives and fluxes for grid configurations where the vertical grid spacing is considerably finer than the horizontal spacing, as is the case for

GCM's and the intended use of this coupled model. Therefore, these terms are neglected.

The resultant vorticity tendencies due to turbulence are then given by

$$\frac{\partial \xi}{\partial t}_{TURB} = -\frac{\partial}{\partial z} \left(-\frac{1}{\rho_0} \frac{\partial \overline{\rho_0 w'v'}}{\partial z} \right) \quad (4.7)$$

$$\frac{\partial \eta}{\partial t}_{TURB} = \frac{\partial}{\partial z} \left(-\frac{1}{\rho_0} \frac{\partial \overline{\rho_0 w'u'}}{\partial z} \right) \quad (4.8)$$

$$\frac{\partial \zeta}{\partial t}_{TURB} = 0 \quad (4.9)$$

(Note: The definition of η in the model code was multiplied by -1 by Jung and Arakawa, and therefore the RHS term of equation 4.8 should be multiplied by -1 in the model code.) As with the one-dimensional turbulence model, the surface fluxes are handled according to the specifications of each GCSS case. For the DYCOMS and BOMEX cases presented in this chapter, the surface heat and moisture fluxes are parameterized as a constant value and surface momentum fluxes are calculated from the same bulk formulas presented in Sections 3.4 and 3.5.

In addition to the replacement of the turbulence parameterizations, the other physical parameterizations of the VVM are changed by necessity. First, the use of a subgrid-scale condensation scheme and subgrid-scale microphysics scheme in the turbulence model obviates the need for the grid-scale microphysics scheme found in the regular VVM formulation. While the subgrid-scale microphysics scheme is considerably less complex without inclusion of ice processes, its consideration of partial cloudiness and warm rain processes are suitable for the intended purpose. While the radiation scheme could conceivably be used even with the given modifications, the scheme has

been switched off for the GCSS cases considered in this paper in favor of the simple parameterizations mentioned in the individual cases.

In Chapter 2, during the derivation of the turbulence model, it was deemed unnecessary, and indeed impossible, to include advection of the second-order moments in a one-dimensional framework and without a calculated vertical velocity. In a three-dimensional framework with a calculated vertical velocity, however, it becomes possible and prudent to include this process. In the interest of computational efficiency and for the reasons mentioned for the vorticity turbulence terms in the preceding paragraph, only vertical advection of the second-order moments are considered. The advection scheme for the second-order moments is replicated exactly as it is done for the main prognostic variables from VVM.

Finally, the position of variables on a three-dimensional grid is discussed. A schematic is shown in Figure 4.1. For the VVM, the vertical grid is described in Jung and Arakawa (2008) as being similar to the “Lorenz grid” for quasistatic models. Fortunately, the existing staggering of variables for VVM match well with the staggered grid for the turbulence model found in Figure 2.12, and as originally specified in Canuto et al. (1994). The second-order moments, cloud fraction, cloud liquid water, and precipitation flux remain at the same point, and are located at the “w-point” (also labeled “SOM” in Figure 4.1). The third-order moments are then located at the “ θ -point” (also labeled “TOM” in Figure 4.1).

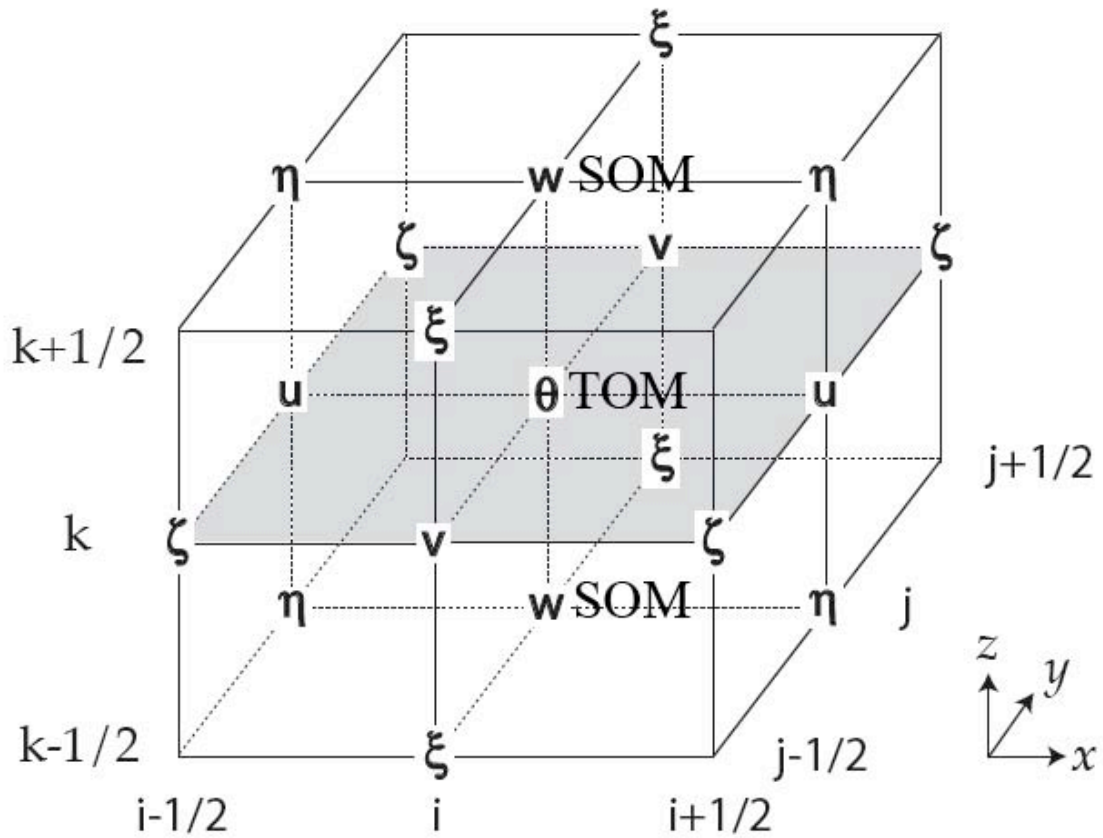


Figure 4.41 Placement of variables upon the grid.

4.4 Three-dimensional model results

As in Chapter 3, the coupled model is tested by running GCSS BLCWG test cases. For brevity, only two representative cases are considered: the nocturnal drizzling stratocumulus case from DYCOMS II RF02 and the non-precipitating shallow cumulus BOMEX case. In addition to comparing the coupled model's results to an LES ensemble and a few observations as is done in Chapter 3, they are also compared with results from the standard VVM with existing parameterizations. In this way, it is possible to decipher any improvement rendered by the inclusion of the new turbulence model and subgrid-

condensation and microphysics schemes. It is worth noting that the turbulence parameterization included in the standard version of the VVM was intended to be temporary and was mainly used for testing purposes for the VVM. In this context, one should expect a certain amount of improvement simply by replacing the temporary scheme with a more detailed one.

4.4.1 Drizzling nocturnal stratocumulus case: DYCOMS II

The first test case run with the coupled VVM is the same case presented in Section 3.4. As with the one-dimensional run, the subgrid-scale condensation and microphysics schemes are activated. For computational efficiency, a small 32 km x 32 km x 1.5 km domain is used with a horizontal grid spacing of 2 km and a constant vertical grid spacing of 25 m. The simulation is run for 6 hours with a 2 second time step. The standard VVM is run with the same setup using its conventional parameterizations

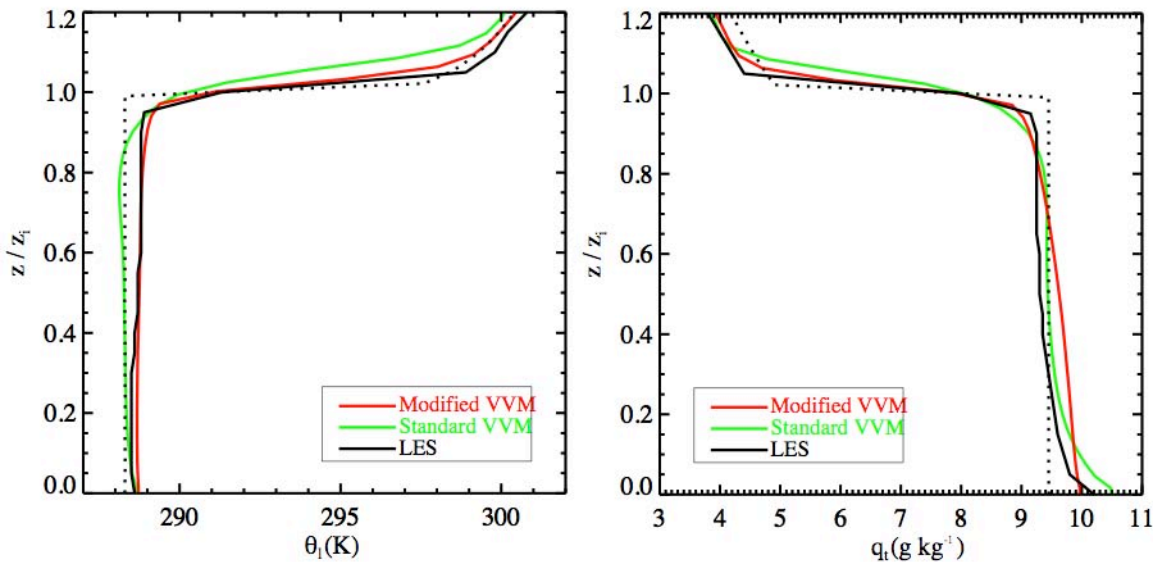


Figure 4.42 Mean profiles of liquid water potential temperature (left) and total water specific humidity (right). In this and subsequent Section 4.4.1 plots, red denotes the modified VVM, green denotes the standard VVM, and black represents results from the GCSS LES intercomparison of Ackerman et al. (2009) used in place of observations. Where appropriate, black dotted lines denote initial conditions.

except for the radiation scheme which is replaced by the case-mandated calculation. The results are presented in a similar format to those in Chapter 3.

The mean profiles of liquid water potential temperature and total water specific humidity are shown in Figure 4.2. From the initial conditions, the LES ensemble shows an increase in $\overline{\theta}_l$ of about 0.5 K and a decrease in \overline{q}_l of about 0.25 g kg^{-1} in the cloud region from $z/z_i = 0.5$ to 1.0. Below the cloud layer, the LES ensemble shows that $\overline{\theta}_l$ is only slightly warmer than the initial conditions whereas \overline{q}_l increases toward the surface where it moistens by over 0.5 g kg^{-1} . The performance of the modified VVM compared to the standard version is quite apparent for these thermodynamic fields. The coupled VVM matches the LES $\overline{\theta}_l$ profile nearly perfectly below the inversion, but tends to diffuse the inversion boundary and warm the lower boundary layer, while the standard VVM is slightly too cool through most of the boundary layer. Interestingly, the same improvement is not apparent in the moisture field. The modified VVM moistens the boundary layer too much below $\frac{z}{z_i} = 0.8$. Compared to both LES and the standard VVM, the modified version is worse. The only region where the modified VVM shows improvement over the standard VVM is below $\frac{z}{z_i} = 0.1$ where the standard VVM is considerably too moist.

To examine the cloud and precipitation fields, Figures 4.3 – 4.6 show the mean profiles of cloud fraction and cloud liquid water, time-height cross-sections of cloud fraction, time series of LWP, and mean profiles of the precipitation flux. The cloud fraction and cloud liquid water content profiles show some interesting differences. First,

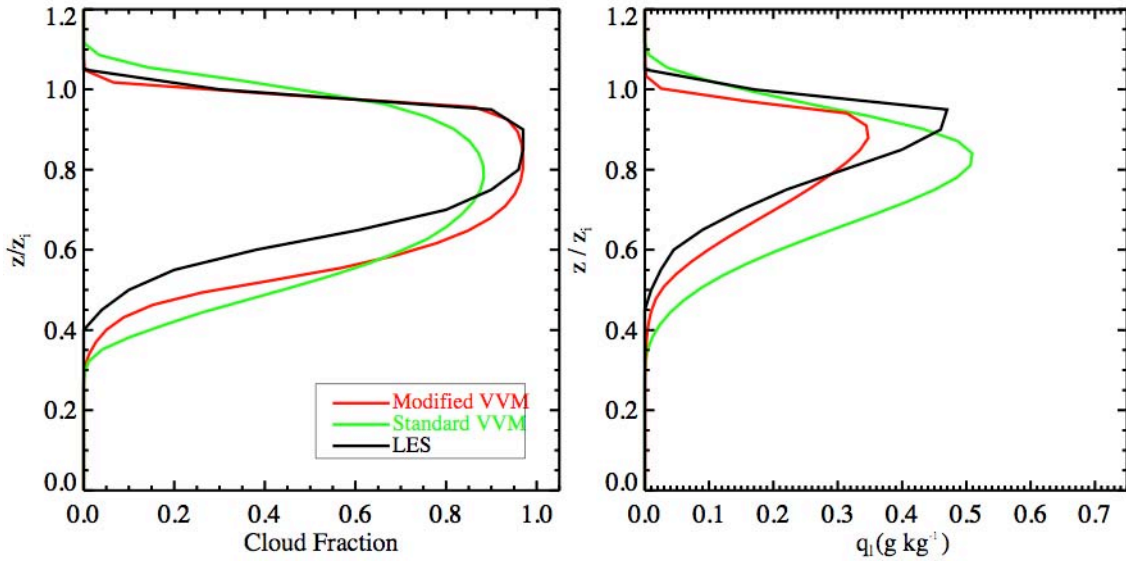


Figure 4.43 Mean cloud fraction and cloud liquid water profiles.

the modified VVM demonstrates good skill in calculating the magnitude and placement

of the cloud fraction peak, as its profile nearly matches the LES results above $\frac{z}{z_i} = 0.8$.

Below this height, however, the modified VVM produces too much cloud fraction as the cloud base is extended about 80 m. This is undoubtedly a result of the overly moist moisture profile in this region. The standard VVM, on the other hand, underestimates the peak cloud fraction by about 10%, but still has too deep of a cloud layer, like the modified version. The cloud liquid water content confusingly shows contradicting results.

Figure 4.3 shows that even though the modified VVM nearly matches the cloud fraction profile of the LES results, the liquid water specific humidity is underestimated by about 0.1 g kg^{-1} . In addition, even though the cloud fraction is significantly underestimated in the standard VVM, its liquid water content is overestimated, particularly in the lower cloud. The cloud fraction time-height cross-sections in Figure 4.4 show the time evolution of the cloud field for both the coupled and standard versions of the VVM. For

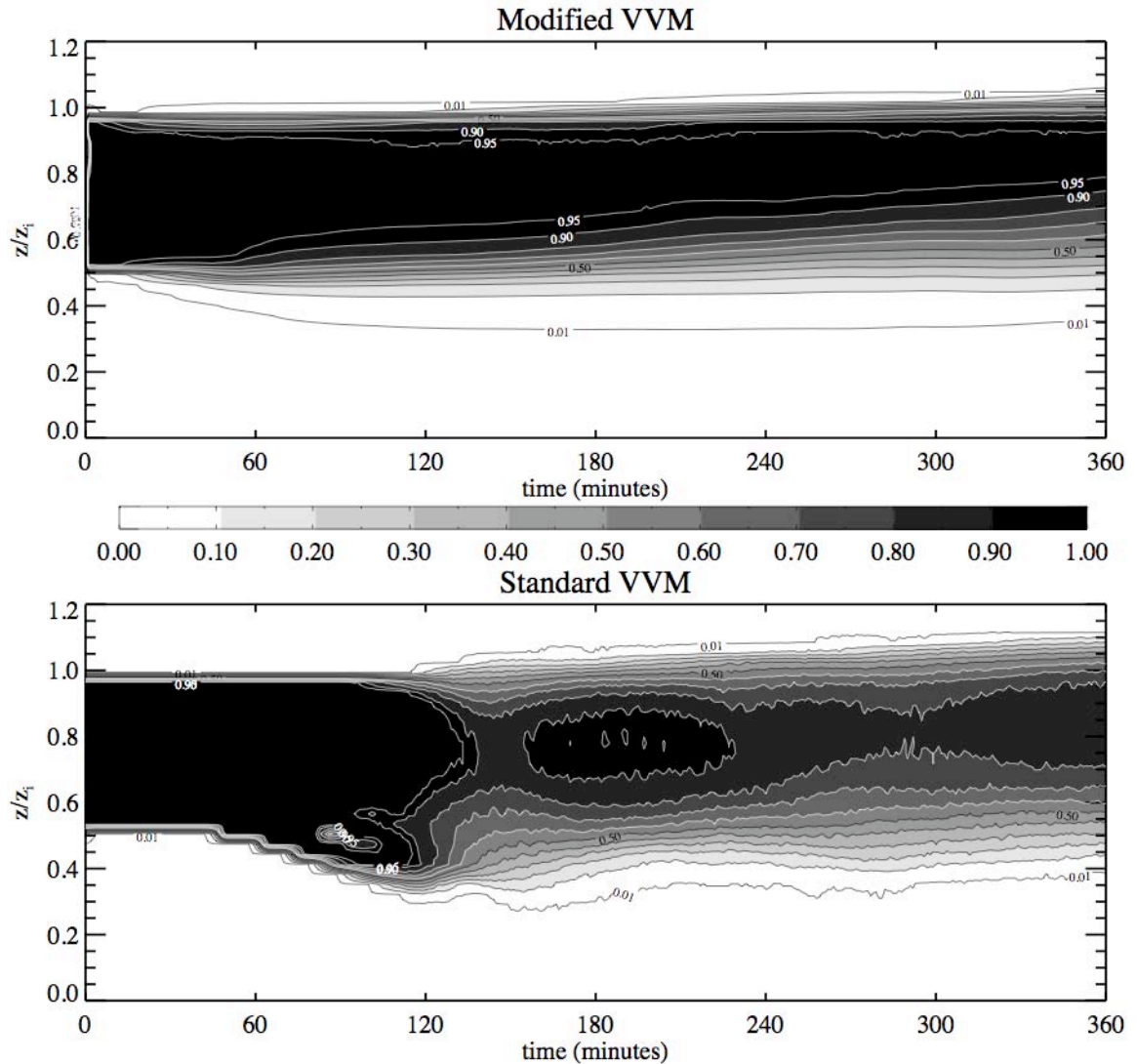


Figure 4.44 Time-height cross-sections of cloud fraction for the coupled VVM (top) and the standard VVM (bottom).

both models, the highest values of cloud fraction can be found near the beginning of the simulation, and the cloud fraction generally decreases through time. Diffusion of the cloud layer is evident in both models. As the values of cloud fraction decrease, the liquid water path is mostly steady as the cloud water is diluted into a greater volume. The standard VVM plot hints at an oscillatory evolution of the cloud fraction, and seems less statistically stable compared to the coupled VVM cloud fraction that varies smoothly in

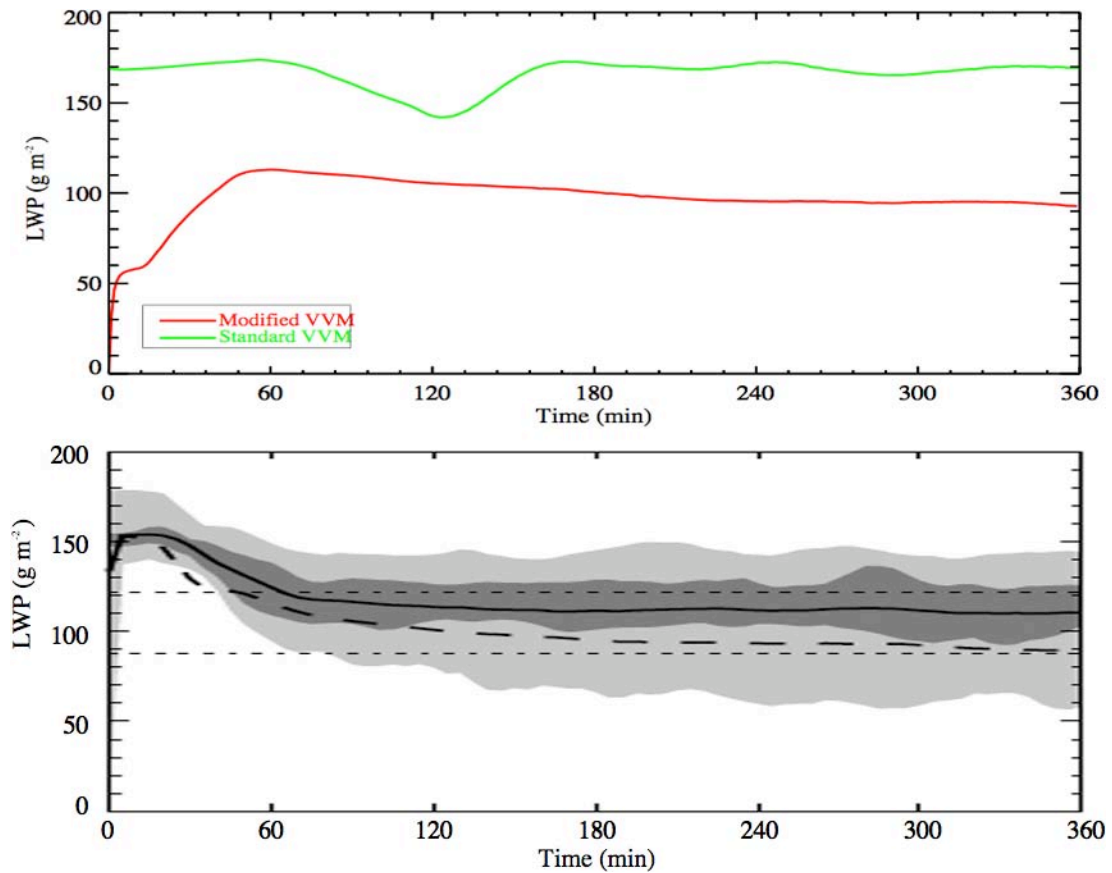


Figure 4.45 Time series of mean liquid water path for the VVMs (top) and the LES ensemble (bottom). Note that while the shading in both plots gives a measure of variability, the shading in the bottom plot denotes quartiles instead of standard deviation.

time. In accordance with the liquid water content profiles, the liquid water path time series shows that modified VVM produces a slight underestimate in liquid water path, although well within the range of observations. The standard VVM overestimates the liquid water path considerably, but this is to be expected given a cloud layer that is too deep and too thick as shown in Figure 4.3. It is also interesting to note that the mean liquid water path for the analogous one-dimensional test case in Section 3.4 found in Figure 3.41 is between 10 and 20 g m⁻² greater than the mean liquid water path calculated for the three-dimensional modified VVM.

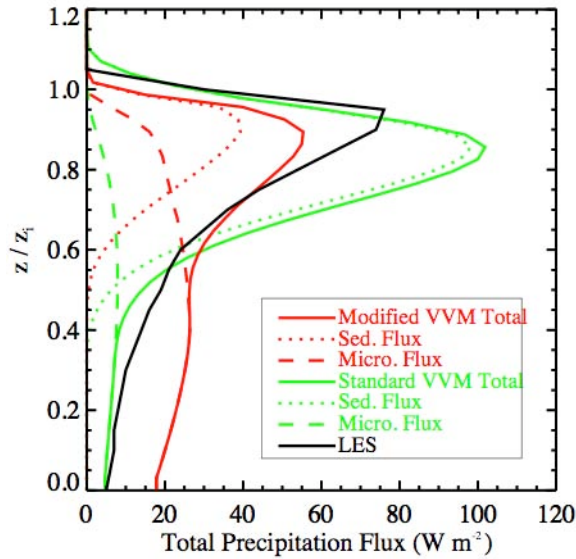


Figure 4.46 Mean profiles of the precipitation flux. The additional lines are explained in the text.

The mean total precipitation flux profiles are shown in Figure 4.6. The plot also includes the individual contributions from the cloud droplet sedimentation flux (dotted lines) and parameterized precipitation flux (dashed lines). The modified VVM significantly overestimates the total surface precipitation flux while the standard VVM matches the LES results. The overestimate found in the modified VVM is a product of a cloud layer that is too deep allowing too much collection of cloud water and a subcloud layer that is too moist, impeding evaporation. Not surprisingly, the standard VVM overestimates the sedimentation flux since this flux is parameterized from the cloud liquid water. The modified VVM does pretty well in the cloud layer due to its better representation of cloud water there.

The final two figures illuminate some of the turbulent properties of the standard and modified VVM compared to the LES ensemble. Figure 4.7 shows the mean total fluxes of $\overline{\theta}_t$ and \overline{q}_t . As in Section 3.4.2.2, the total fluxes include the subgrid and

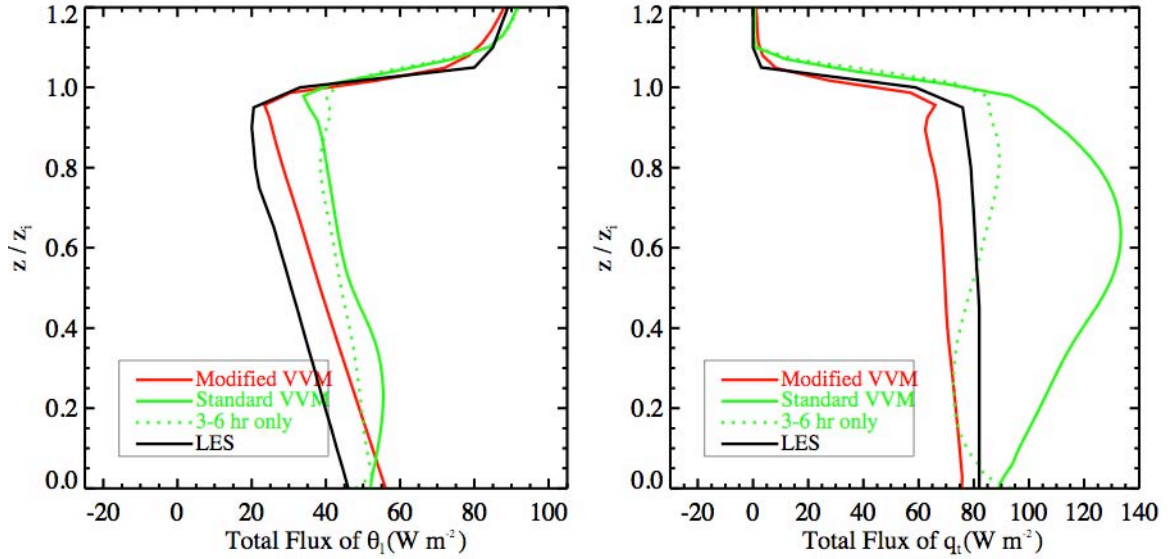


Figure 4.47 Total fluxes of liquid water potential temperature (left) and total water specific humidity (right). The green dotted lines represent average profiles for only the last three hours of the standard VVM simulation.

resolved turbulent fluxes, and contributions from radiation, precipitation, and cloud droplet sedimentation:

$$\overline{c_p \rho_0 w' \theta'_l}_{TOTAL} = \overline{c_p \rho_0 w' \theta'_l}_{RESOLVED} + \overline{c_p \rho_0 w' \theta'_l}_{SGS} + F_{RAD} + L_v P + L_v F_{SED}$$

$$\overline{L_v \rho_0 w' q'_t}_{TOTAL} = \overline{L_v \rho_0 w' q'_t}_{RESOLVED} + \overline{L_v \rho_0 w' q'_t}_{SGS} - L_v P - L_v F_{SED}$$

While the modified VVM profiles differ from the LES ensemble profiles by up to 10 W m⁻², this difference is largely attributed to the differences in precipitation fluxes found in Figure 4.6. Otherwise, the modified VVM profiles match the shape and slope of the LES profiles well, signifying that the flux divergence is similar for the modified VVM and LES. The shape of the standard VVM profiles is somewhat misleading. Recall that each of the profiles shown represents an average profile over the last four hours of the simulation. In Figures 4.4 and 4.5, it is apparent that the standard VVM has not completed its “spin up” time. It doesn’t appear that the standard VVM reaches a quasi-steady state until about 2.5 hours in the simulation. Thus for the first 30 minutes of the

averaging period, the standard VVM is still somewhat in a state of flux which skews the statistics. The mean profile of the total flux of $\overline{\theta}_t$ is mostly the right shape, but differs from LES by about 20 W m^{-2} . The mean profile of \overline{q}_t , on the other hand, displays a shape quite dissimilar from both LES and the modified VVM. The positive slope from the surface to $\frac{\bar{z}}{\bar{z}_i} = 0.6$ indicates a drying of this lower layer, something that is not observed from Figure 4.2. The time-height cross section of standard VVM cloud fraction in Figure 4.4 shows a considerable thinning of the stratocumulus deck from hour 2 to 2.5, which does provide evidence of temporary drying in this subcloud layer. Also plotted in Figure 4.7 are mean profiles of only the last three hours of the standard VVM simulation, when spin up has been completed. These profiles more closely resemble results from the modified VVM and LES intercomparison. The moisture flux profile in particular is much better, although it exhibits curvature not found in the other simulations, indicating a moistening of the lower subcloud layer and drying of the cloud layer.

The mean buoyancy flux and vertical velocity variance profiles are shown in Figure 4.8. The buoyancy flux profiles demonstrate reasonably good agreement between the modified VVM and LES, although the standard VVM is considerably worse. In the cloud layer, the modified VVM slightly overestimates the buoyancy flux but the standard VVM overestimates it by about a factor of two. In addition, the standard VVM has the wrong shape in the subcloud layer. This is due to the fact that this profile only represents the resolved buoyancy flux because the standard VVM does not calculate a subgrid-scale term. The vertical velocity variance profiles also show considerable disagreement. The standard VVM does not estimate this quantity at the subgrid scale and the resolved

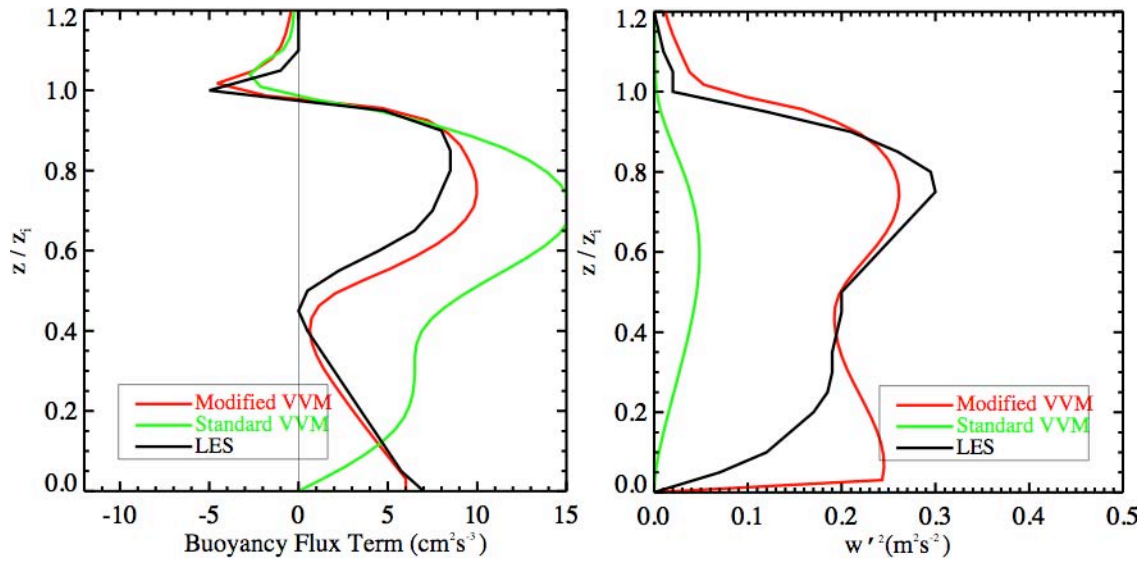


Figure 4.48 Mean profiles of the buoyancy flux term (left) and vertical velocity variance (right).

portion drastically underestimates the quantity throughout the boundary layer. The modified VVM does a good job matching the LES ensemble, particularly in the cloud layer. In the subcloud layer, the modified VVM overestimates vertical velocity variance compared to LES, but Figure 3.46 in Section 3.4.2.2 shows that the modified VVM is closer to actual observations. Both the LES ensemble and modified VVM show evidence of a spurious decoupling of the cloud layer from the subcloud layer, whereas the observed vertical velocity variance profile maintains a parabolic shape.

4.4.2 Nonprecipitating trade-wind cumulus case: BOMEX

The other test case run with the modified VVM is the same case presented in Section 3.5, the non-precipitating shallow cumulus case based on the BOMEX field campaign. As with the one-dimensional run, the subgrid-scale condensation scheme is activated, but the subgrid microphysics scheme is not. Once again, a limited domain of 32 km x 32 km x 3.0 km is used with a horizontal grid spacing of 2 km and a constant

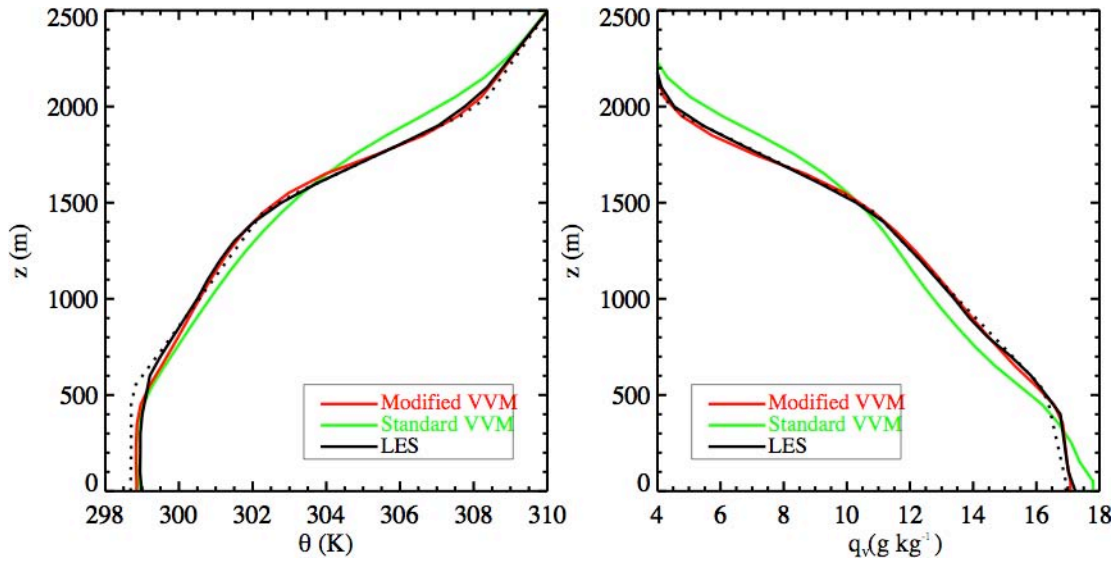


Figure 4.49 Mean profiles of potential temperature (left) and water vapor specific humidity (right). The colors denote the same models as in Section 4.4.1, but the black LES profiles represent the average of the LES intercomparison models from Siebesma et al. (2003).

vertical grid spacing of 100 m. The simulation is run for 6 hours with a 5 second time step. The standard VVM is run with the same setup using its conventional parameterizations except that the radiation scheme and the precipitation-generating portion of the microphysics scheme are switched off.

The profiles of the mean thermodynamic variables for the last three hours of the simulation are shown in Figure 4.9. The potential temperature profile is characterized by a shallow 400-500 m well-mixed layer below a roughly 1000 m thick conditionally unstable layer and a broad stably stratified layer above about 1600 m. The LES ensemble displays little change from the initial state except for slight cooling in the conditionally unstable layer, slight warming in the well-mixed layer, and a general “rounding” of the sharp corners of the initial profile. The modified VVM is able to match the LES ensemble almost exactly except for too little warming in the mixed layer. The standard VVM, on the other hand, generally warms too much below the inversion, cools above 1600 m, and greatly mixes out the sharp interfaces from the initial profile. A similar picture is found

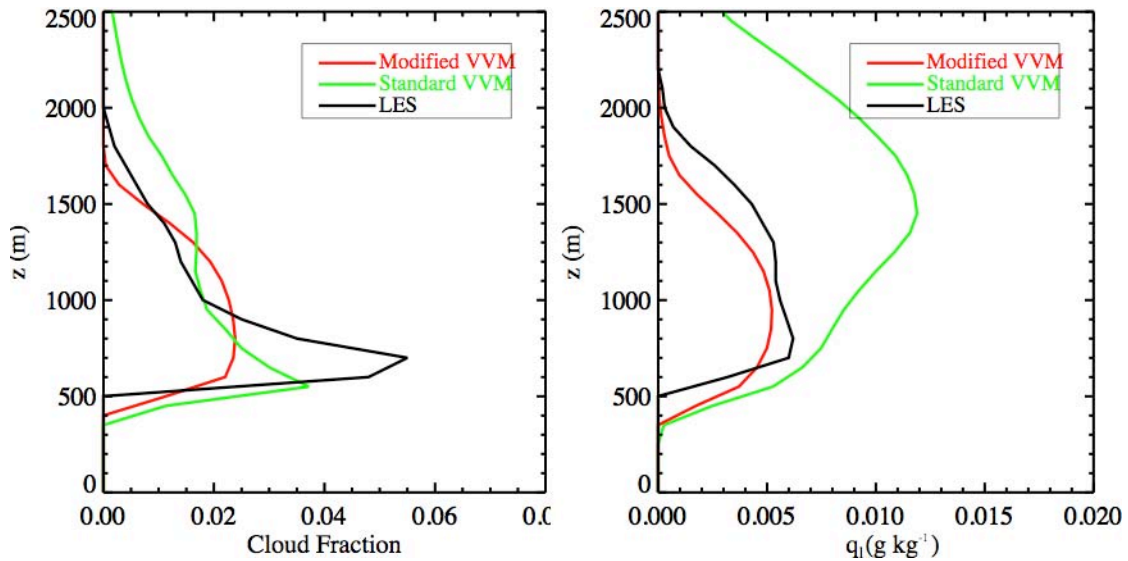


Figure 4.50 Mean profiles of cloud fraction (left) and liquid water specific humidity (right).

for the water vapor specific humidity. The modified VVM matches the LES ensemble particularly well throughout the column. The standard VVM again mixes out the sharp interfaces between layers in the moisture profile, creating a more linear profile from the surface to the inversion.

The simulated cloud field is examined with the mean profiles of cloud fraction and cloud liquid water in Figure 4.10, the time-height cross-section of cloud fraction in Figure 4.11, and the liquid water path time series in Figure 4.12. Figure 4.10 shows that the modified VVM underestimates the peak of cloud fraction near cloud base, but does a decent job of capturing the right cloud amount above 1000m. The cloud top height is still underestimated as it was for the one-dimensional model, but the VVM extends the cloud top height upward about 150 m compared to the one-dimensional model. The standard VVM captures more of a peak in cloud fraction at cloud base, but overestimates the cloud top height considerably. The cloud liquid water profiles show a more pronounced difference between the standard and modified VVMs. The modified VVM clearly does a

better job at estimating the cloud liquid water content despite it being slightly underestimated throughout the cloud layer. The standard VVM shows too much liquid water especially in the upper reaches of the cumulus cloud deck.

The time-height cross-sections of cloud fraction shown in Figure 4.11 show interesting differences in how cumulus clouds are represented in the two versions of VVM. The coupled VVM shows a relatively steady-state cloud fraction after the initial

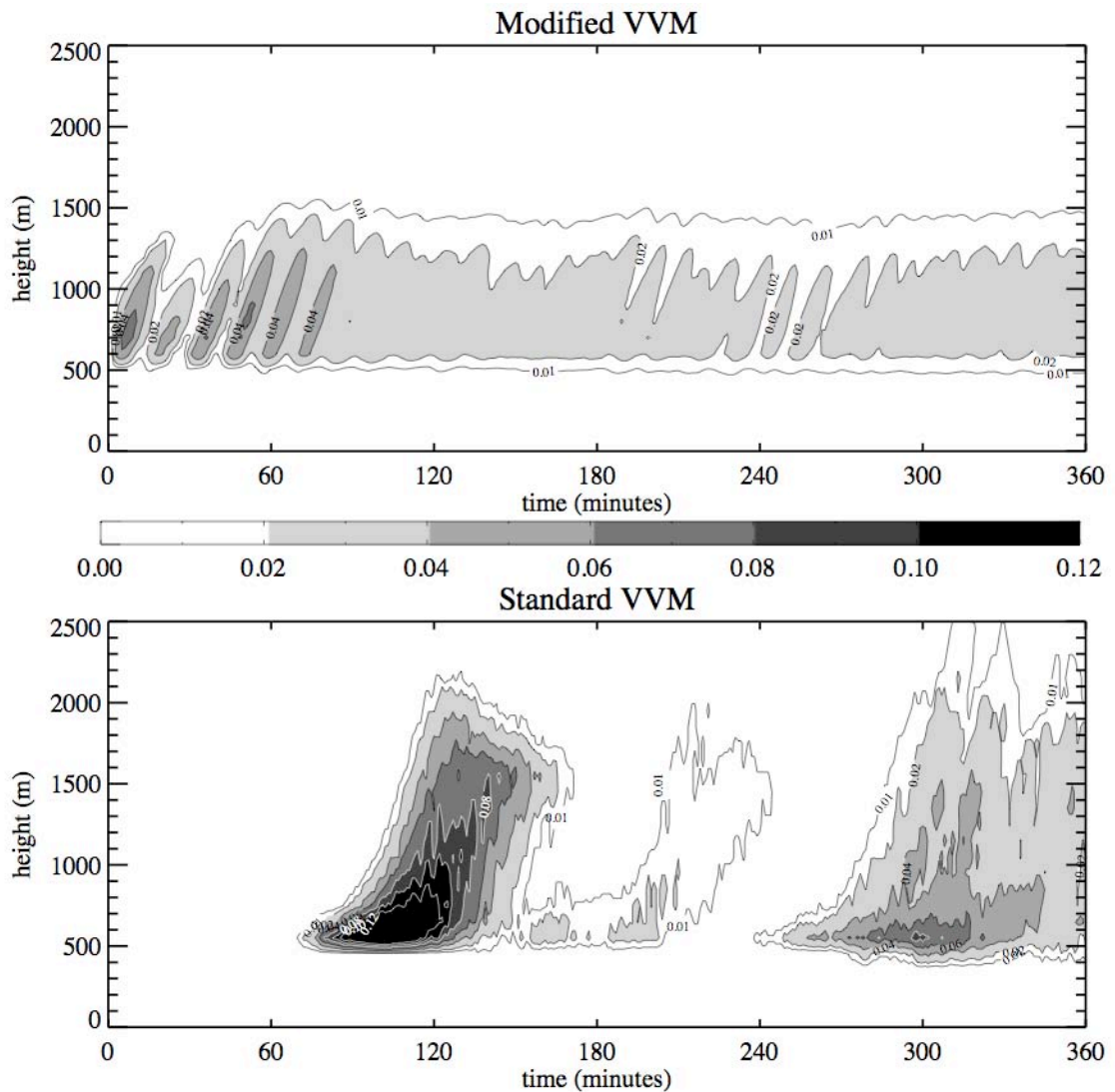


Figure 4.51 Time-height cross-section of cloud fraction for the coupled VVM (top) and the standard VVM (bottom).

spin-up period with slight undulations at regular intervals. The cloud thickness is mostly constant throughout the simulation, with a small cloud fraction from about 500 m to about 1500 m. The standard VVM demonstrates a different behavior. No clouds are observed to grow until about 90 minutes into the simulation when a sudden strong burst of clouds are created that extend well into the stable layer. After this long spin-up period, the growth of clouds is somewhat steadier, but continues to show cloud growth well above 1600 m. The time series of LWP tells a similar story. The modified VVM produces a steady LWP that evens out at about 6 g m^{-2} , reasonably close to the LES ensemble. The standard VVM shows large undulations in LWP that range from 0 to 50 g m^{-2} during the

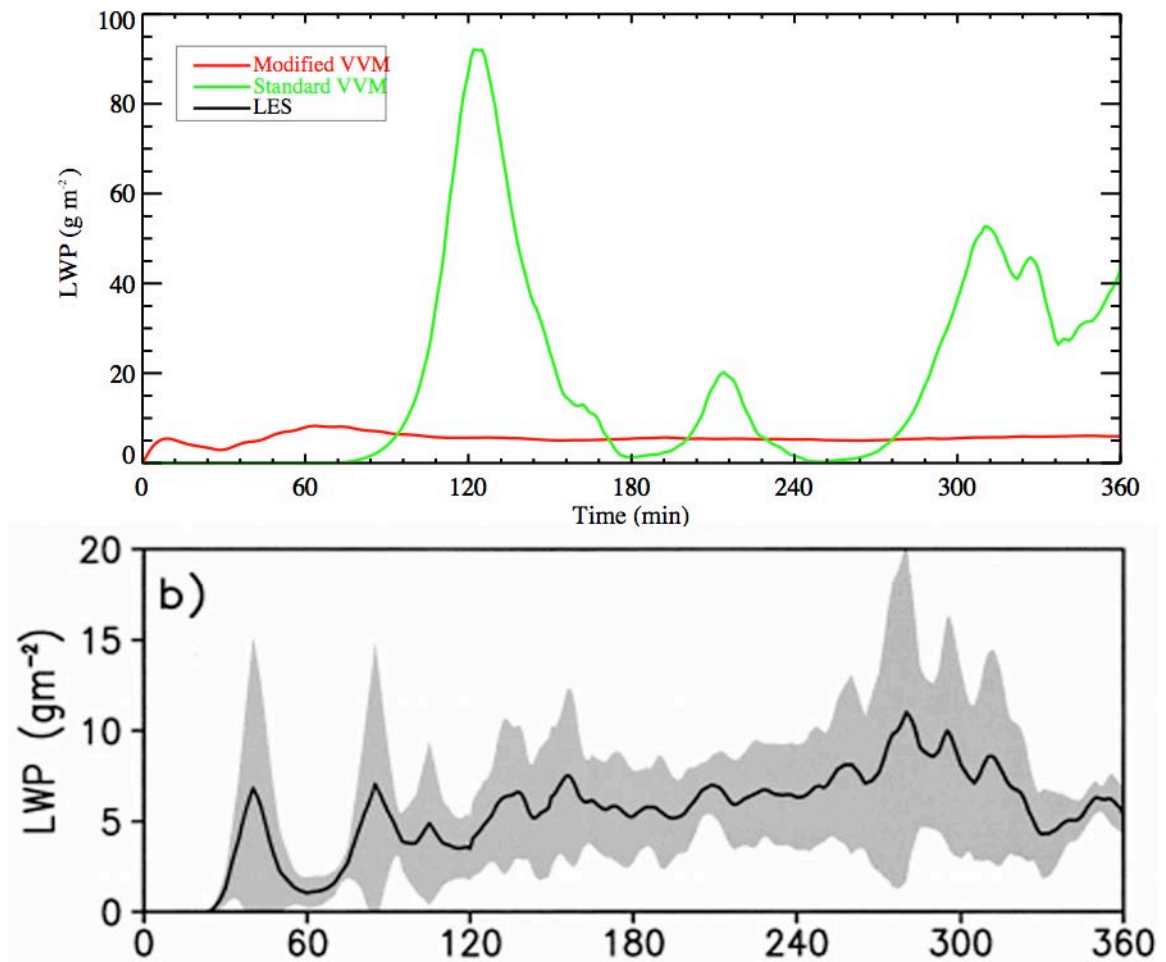


Figure 4.52 Mean LWP for the VVMs (top) and for the LES ensemble (bottom).

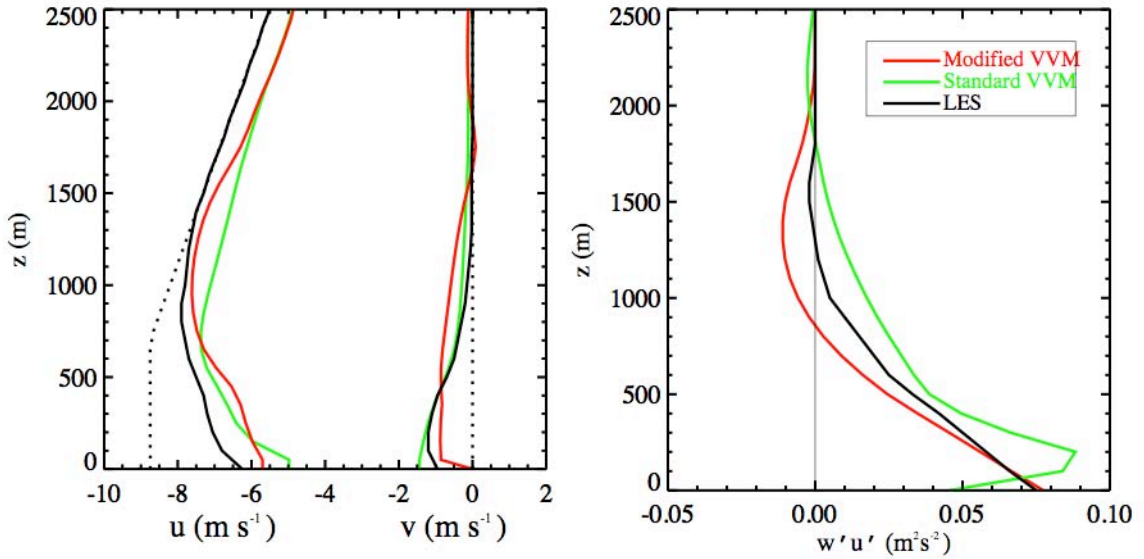


Figure 4.53 Mean profiles of the horizontal components of wind (left) and the total vertical flux of easterly momentum (right).

last three hours of the simulation, consistent with taller cumuli than were calculated by the LES ensemble.

The mean profiles of the horizontal winds and the vertical flux of easterly momentum are shown in Figure 4.13. Both models do a decent job of reproducing the LES ensemble winds, although both the modified and standard VVMs underestimate the easterly wind by about 1 m s^{-1} . Through most of the boundary layer, both VVM's reproduce the shape of the momentum flux profile reasonably well, but the modified version does a better job particularly near the surface.

Finally, the turbulent structure of the BOMEX boundary layer is examined. The mean profiles of the total vertical fluxes (subgrid-scale and resolved) of liquid water potential temperature and total water specific humidity are shown in Figure 4.14. For both variables, the modified VVM performs pretty well, matching the heat flux profile to within a few W m^{-2} and the moisture flux profile in shape and magnitude. Both quantities, however, are underestimated by about 25% in the cloud layer from 500 to

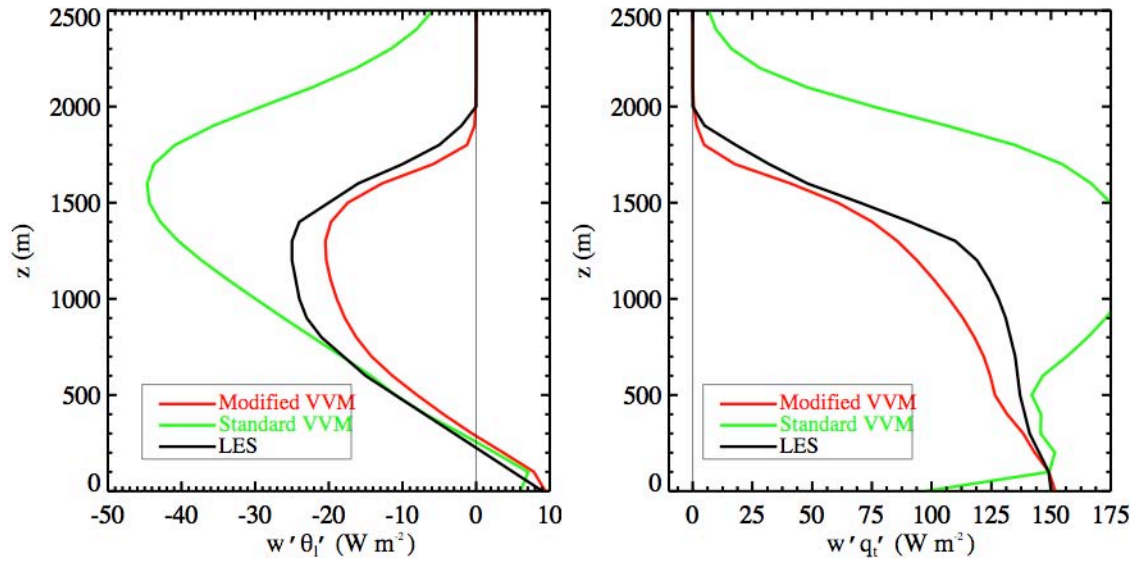


Figure 4.54 Mean profiles of the total turbulent fluxes of liquid water potential temperature (left) and total water specific humidity (right).

1500 m. This underestimate is a considerable improvement over the standard VVM, however. The standard VVM creates fluxes that are too large and extend higher in the column, consistent with taller, more vigorous cumuli. It is worth mentioning that the source of variability between the VVM versions differs markedly. The coupled VVM generates almost all variability on the subgrid scale from the turbulence parameterization, while the standard VVM generates most of its variability on the resolved scale.

The mean profiles of vertical velocity variance and TKE are shown in Figure 4.15. The vertical velocity variance profiles of the LES ensemble and the modified VVM both have the same qualitative shape with local maxima located in the middle of the subcloud and cloud layers. As with the one-dimensional turbulence model, the modified VVM overestimates both vertical velocity variance and TKE in the cloud layer. This overestimation is discussed in Section 3.5.2.2 and is attributed to the overestimation of the buoyancy flux in a cumulus regime. The standard VVM underestimates the vertical velocity variance throughout the column, except for where there is extraneous cumulus

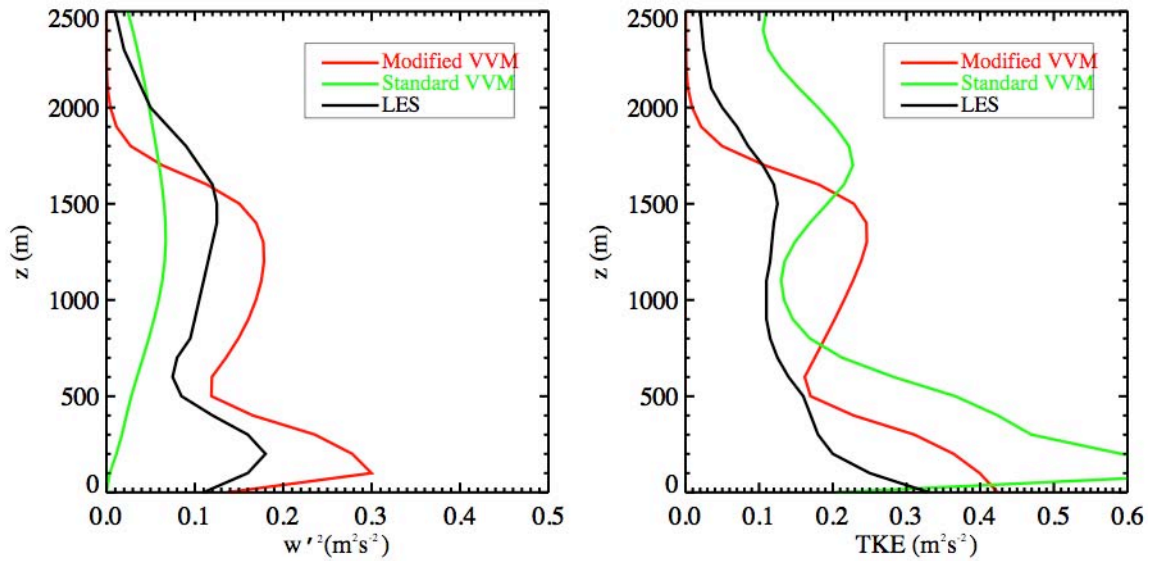


Figure 4.55 Mean profiles of total vertical velocity variance (left) and TKE (right). development above 2000 m. The considerable overestimate of TKE by the standard VVM in the subcloud and upper cloud layers together with an underestimate of the vertical velocity variance points to too much resolved horizontal velocity variance in that model.

4.5 Notes on Model Execution Time

Both control VVM runs and both modified VVM runs were executed on a dual 2 GHz PowerPC G5 Apple PowerMac. The processor time used by each model was calculated using the Unix “time” utility and the results are presented in Table 4.1.

Case Name	Standard Model Execution Time (HH:MM:SS)	Modified Model Execution Time (HH:MM:SS)	Execution Time Penalty for Using Modifications
DYCOMS RF02 (Section 4.4.1)	01:03:44	01:07:01	6.5 %
BOMEX (Section 4.4.2)	00:09:54	00:11:17	14.0%

Table 4.1 Processor time used for each model.

Chapter 5

Conclusion

Despite exciting progress in the succeeding decades after the first development of GCMs, there is a continual need for improvement in the parameterization of unresolvable processes. Boundary layer turbulence and cloudiness presents one ongoing challenge that has been addressed with increasing elegance and complexity during the progression of GCM development, and the goal of the current study in this context was to contribute to this process. Specifically, a new turbulence parameterization including subgrid-scale condensation and microphysics was created using a novel and more computationally efficient approach to calculating higher-order moments with the goal of achieving an accurate representation of boundary layer turbulence and cloudiness without undue computational expense. This study has presented the development of the new parameterization, testing of the new model in a one-dimensional configuration, the coupling of the new parameterization with an innovative three-dimensional cloud model, and testing of the resultant modified model.

The development of the new turbulence parameterization began with the work of Canuto et al. (1994) and Cheng et al. (2005). The first study demonstrated a novel way of retaining the strengths of a third-order closure turbulence model without having to prognose the third-order moments. The second study expanded upon the first, and

included new non-Gaussian fourth-order moments that improved the performance and efficiency of the Canuto et al. (1994) model. The derivation of the current model used the methods of these two studies to expand the model further to include moisture, moist conservative variables, momentum fluxes, additional necessary scalar second-order moments, and additional third-order moments. The inclusion of moisture allowed the possibility of including subgrid-scale condensation as first described by Sommeria and Deardorff (1977).

In order to create a general model more capable of simulating any type of cloudy boundary layer, ideas from studies expanding on Sommeria and Deardorff (1977) were used. Many studies concluded that the diagnosis of subgrid-scale cloud fraction and liquid water content depended on the cloud type being simulated since stratocumulus clouds and cumulus clouds have very different joint probability density functions of liquid water potential temperature and total water specific humidity. Similarly, other authors concluded that the buoyancy fluxes generated by the subgrid-scale cloudiness also differs based on cloud type and joint PDFs. Given these findings, using one type of PDF for all boundary layer cloud types seemed insufficient. Many subsequent authors have attempted to develop subgrid-scale cloudiness schemes for specific cloud types and for general use. The scheme used in the current study was based on these efforts.

Given subgrid-scale cloudiness, a conventional microphysics scheme must be adjusted to account for the lack of grid-scale condensation. As rain is produced within the cloudy areas of a grid cell, it must be allowed to fall through the column and interact with cloudy and clear areas. Unfortunately, the subgrid-scale condensation parameterization does not provide information on the spatial arrangement of the partial cloudiness, so

some assumption must be made about how the areas of partial cloudiness overlap. The work of Jakob and Klein (2000) presents a convenient framework for handling this problem. They split the precipitation flux into a cloudy and clear portion and define the interaction between the two. Although their scheme assumes an infinite fall speed, which is a poor assumption for models with shorter time steps, their idea can be adapted to include prognostic equations for cloudy and clear portions of the rain water specific humidity. All that remains to close the microphysics parameterization is to specify how to calculate the rates of change of rain water due to microphysical processes. Only warm rain processes such as autoconversion, collection, and evaporation are considered in this model and the bulk formulas from Khairoutdinov and Randall (2003) are used to calculate them.

The new turbulence model was tested by simulating five cases: one based on a clear convective boundary layer during the Wangara experiment commonly used in the literature and four cases from the GCSS BLCWG. The Wangara case was used to test the turbulence model core, without the complications of cloud cover or precipitation. The evolution of the mean variables was found to agree well with both past LES studies and observations. In fact, the evolution of the boundary layer height from the current model matched observations even better than high-resolution LES. For this case, it was found the LES often overestimated the vigor of turbulence and turbulent fluxes in the boundary layer while the current turbulence model represented them more accurately. The first GCSS case featured a stratocumulus-like thermodynamic profile without the inclusion of moisture. Instead, a radiatively active “smoke cloud” was used to generate cloud-top cooling and to drive turbulence and entrainment. The conclusion of this test showed that

the new turbulence parameterization can successfully simulate the entrainment process in this type of regime. It outperformed other one- and two-dimensional models used in the intercomparison study for many entrainment parameters, and even approached the performance of some of the three-dimensional models. The second GCSS case was based on the DYCOMS II field experiment and featured nocturnal precipitating stratocumulus. The new model produced results in remarkably good agreement with the LES ensemble and observations from the GCSS intercomparison study. A sensitivity test omitting cloud droplet sedimentation was conducted in accordance with the intercomparison study and the reduced entrainment rate, increased LWP, and increased precipitation were all consistent with previous studies. The last two GCSS cases featured cumulus regime boundary layers: one featured non-precipitating trade-wind cumulus with a low cloud fraction (BOMEX), and one featured precipitating trade-wind cumulus with a higher cloud fraction (RICO). In both cases, the turbulence model did reasonably well, but didn't match LES or observations as well as with the stratocumulus case. In particular, cloud fraction and liquid water content were overestimated through much of the cloud layer, while the cloud top height was underestimated. The profiles of most turbulent variables was satisfactory for these two cases, but the turbulent kinetic energy components were found to be overestimated in the cloud layer due to an overly active diagnostic buoyancy flux.

After testing in a one-dimensional configuration, the turbulence model was coupled to the Vector Vorticity Model (VVM) of Jung and Arakawa (2008) as a turbulence parameterization. Vertical advection of the second-order moments was added to the turbulence model and several modifications were made to VVM including the use

of moist conservative variables, replacement of the turbulence parameterization, and replacement of the microphysics parameterization. The coupled VVM was then tested by simulating the BOMEX trade-wind cumulus case and the DYCOMS II stratocumulus case. Results were compared to those from both the standard configuration of the VVM and the LES ensemble results found in the GCSS intercomparison studies. For both cases, the modified VVM performed considerably better than the standard VVM and matched the thermodynamic state, turbulent state, and cloud fields of the LES ensemble better. The three-dimensional modified VVM also performed better than the one-dimensional turbulence model alone.

This study demonstrates the usefulness of a new turbulence model, but future work is needed to improve upon it and further the progress of turbulence parameterization in GCMs. First, more work needs to be done to find a more general and elegant solution for the calculation of the buoyancy flux in the subgrid-scale condensation framework. The current solution of calculating the buoyancy flux based on the diagnosed cloud regime constitutes a quasi-trigger mechanism, and can probably be avoided, much like Cuijpers and Bechtold (1995) formulated a continuous function to calculate cloud fraction and liquid water content based on the normalized saturation deficit, without resorting to individualized PDF's based on cloud regime. Second, the number of prognostic second-order moments and diagnostic third-order moments was formulated for the current model based on the goal of accuracy of the turbulent state and thoroughness. It is quite possible that the number of prognostic or diagnostic variables might be reduced by using simpler formulations for some while maintaining the skill of the complete set, much like Mellor and Yamada (1974) developed degrees of

sophistication in their turbulence model. Third, like most turbulence parameterizations, there are many “tunable” parameters that must be specified throughout the model. A study by Golaz et al. (2007) demonstrates a way to find the best values of these parameters by comparing an ensemble of model runs with differing parameters to a reference LES dataset as well as helping to illuminate possible structural model errors. This technique would be extremely useful for improving the performance of the current model. Fourth, as with any atmospheric model running further test cases may always point out potential pitfalls and improvements, and should be performed. Finally, the new turbulence parameterization needs to be tested as part of a GCM, with coarser resolution and a global domain, longer time steps, and a longer integration period.

Appendix A

Solving For the Explicit Diagnostic Third-order Moments

The 28 algebraic third-order moment relations from equations (2.48)-(2.57) are:

$$\frac{c_8 + p_1}{\tau_1} \overline{w'^3} = 3(d_1 - 1) \overline{w'^3} \frac{\partial \overline{w}}{\partial z} - 3 \overline{w'^2} \frac{\partial \overline{w'^2}}{\partial z} + 3 \lambda \overline{w'^2 \theta'_v} \quad (\text{A1})$$

$$\begin{aligned} \frac{c_8 + p_2}{\tau_1} \overline{w'^2 \theta'_l} &= (d_2 - 1) \overline{w'^3} \frac{\partial \overline{\theta}_l}{\partial z} + 2(d_3 - 1) \overline{w'^2 \theta'_l} \frac{\partial \overline{w}}{\partial z} \\ &\quad - 2 \overline{w'^2} \frac{\partial \overline{w' \theta'_l}}{\partial z} - \overline{w' \theta'_l} \frac{\partial \overline{w'^2}}{\partial z} + 2 \lambda \overline{w' \theta'_l \theta'_v} \end{aligned} \quad (\text{A2})$$

$$\begin{aligned} \frac{c_8 + p_3}{\tau_1} \overline{w' \theta_l'^2} &= (d_4 - 2) \overline{w'^2 \theta'_l} \frac{\partial \overline{\theta}_l}{\partial z} + (d_5 - 1) \overline{w' \theta_l'^2} \frac{\partial \overline{w}}{\partial z} \\ &\quad - \overline{w'^2} \frac{\partial \overline{\theta_l'^2}}{\partial z} - 2 \overline{w' \theta'_l} \frac{\partial \overline{w' \theta'_l}}{\partial z} + \lambda \overline{\theta_l'^2 \theta'_v} \end{aligned} \quad (\text{A3})$$

$$\begin{aligned} \frac{c_8 + p_4}{\tau_1} \overline{w'^2 q'_l} &= (d_6 - 1) \overline{w'^3} \frac{\partial \overline{q}_l}{\partial z} + 2(d_7 - 1) \overline{w'^2 q'_l} \frac{\partial \overline{w}}{\partial z} \\ &\quad - 2 \overline{w'^2} \frac{\partial \overline{w' q'_l}}{\partial z} - \overline{w' q'_l} \frac{\partial \overline{w'^2}}{\partial z} + 2 \lambda \overline{w' q'_l \theta'_v} \end{aligned} \quad (\text{A4})$$

$$\begin{aligned} \frac{c_8 + p_5}{\tau_1} \overline{w' q_l'^2} &= (d_8 - 2) \overline{w'^2 q'_l} \frac{\partial \overline{q}_l}{\partial z} + (d_9 - 1) \overline{w' q_l'^2} \frac{\partial \overline{w}}{\partial z} \\ &\quad - \overline{w'^2} \frac{\partial \overline{q_l'^2}}{\partial z} - 2 \overline{w' q'_l} \frac{\partial \overline{w' q'_l}}{\partial z} + \lambda \overline{q_l'^2 \theta'_v} \end{aligned} \quad (\text{A5})$$

$$\begin{aligned} \frac{c_8 + p_6}{\tau_1} \overline{w'\theta'_l q'_l} &= (d_{10} - 1) \overline{w'^2 q'_l} \frac{\partial \overline{\theta}_l}{\partial z} + (d_{11} - 1) \overline{w'^2 \theta'_l} \frac{\partial \overline{q}_l}{\partial z} + (d_{12} - 1) \overline{w'\theta'_l q'_l} \frac{\partial \overline{w}}{\partial z} \\ &\quad - \overline{w'^2} \frac{\partial \overline{\theta'_l q'_l}}{\partial z} - \overline{w'\theta'_l} \frac{\partial \overline{w'q'_l}}{\partial z} - \overline{w'q'_l} \frac{\partial \overline{w'\theta'_l}}{\partial z} + \lambda \overline{\theta'_l q'_l \theta'_v} \end{aligned} \quad (\text{A6})$$

$$\frac{c_{10} + p_7}{\tau_1} \overline{\theta_l'^3} = (d_{13} - 3) \overline{w'\theta_l'^2} \frac{\partial \overline{\theta}_l}{\partial z} - 3 \overline{w'\theta_l'} \frac{\partial \overline{\theta_l'^2}}{\partial z} \quad (\text{A7})$$

$$\begin{aligned} \frac{c_{10} + p_8}{\tau_1} \overline{\theta_l'^2 q'_l} &= (d_{14} - 1) \overline{w'\theta_l'^2} \frac{\partial \overline{q}_l}{\partial z} + (d_{15} - 2) \overline{w'\theta_l' q'_l} \frac{\partial \overline{\theta}_l}{\partial z} \\ &\quad - 2 \overline{w'\theta_l'} \frac{\partial \overline{\theta'_l q'_l}}{\partial z} - \overline{w'q'_l} \frac{\partial \overline{\theta_l'^2}}{\partial z} \end{aligned} \quad (\text{A8})$$

$$\begin{aligned} \frac{c_{10} + p_9}{\tau_1} \overline{\theta_l' q_l'^2} &= (d_{16} - 1) \overline{w'q_l'^2} \frac{\partial \overline{\theta}_l}{\partial z} + (d_{17} - 2) \overline{w'\theta_l' q'_l} \frac{\partial \overline{q}_l}{\partial z} \\ &\quad - 2 \overline{w'q_l'} \frac{\partial \overline{\theta'_l q'_l}}{\partial z} - \overline{w'\theta_l'} \frac{\partial \overline{q_l'^2}}{\partial z} \end{aligned} \quad (\text{A9})$$

$$\frac{c_{10} + p_{10}}{\tau_1} \overline{q_l'^3} = (d_{18} - 3) \overline{w'q_l'^2} \frac{\partial \overline{q}_l}{\partial z} - 3 \overline{w'q_l'} \frac{\partial \overline{q_l'^2}}{\partial z} \quad (\text{A10})$$

$$\begin{aligned} \frac{c_8 + p_{11}}{\tau_1} \overline{w'u'^2} &= 2(d_{19} - 1) \overline{w'^2 u'} \frac{\partial \overline{u}}{\partial z} - (d_{20} - 1) \overline{w'u'^2} \frac{\partial \overline{w}}{\partial z} \\ &\quad - \overline{w'^2} \frac{\partial \overline{u'^2}}{\partial z} - 2 \overline{w'u'} \frac{\partial \overline{w'u'}}{\partial z} + \lambda \overline{u'^2 \theta'_v} \end{aligned} \quad (\text{A11})$$

$$\begin{aligned} \frac{c_8 + p_{12}}{\tau_1} \overline{u'^2 \theta'_l} &= (d_{21} - 1) \overline{w'u'^2} \frac{\partial \overline{\theta}_l}{\partial z} + 2(d_{22} - 1) \overline{w'u' \theta'_l} \frac{\partial \overline{u}}{\partial z} \\ &\quad - 2 \overline{w'u'} \frac{\partial \overline{u' \theta'_l}}{\partial z} - \overline{w' \theta'_l} \frac{\partial \overline{u'^2}}{\partial z} \end{aligned} \quad (\text{A12})$$

$$\begin{aligned} \frac{c_8 + p_{13}}{\tau_1} \overline{u'^2 q'_l} &= (d_{23} - 1) \overline{w'u'^2} \frac{\partial \overline{q}_l}{\partial z} + 2(d_{24} - 1) \overline{w'u' q'_l} \frac{\partial \overline{u}}{\partial z} \\ &\quad - 2 \overline{w'u'} \frac{\partial \overline{u' q'_l}}{\partial z} - \overline{w' q'_l} \frac{\partial \overline{u'^2}}{\partial z} \end{aligned} \quad (\text{A13})$$

$$\begin{aligned} \frac{c_8 + p_{14}}{\tau_1} \overline{w'v'^2} &= 2(d_{25} - 1) \overline{w'^2v'} \frac{\partial \bar{v}}{\partial z} - (d_{26} - 1) \overline{w'v'^2} \frac{\partial \bar{w}}{\partial z} \\ &\quad - \overline{w'^2} \frac{\partial v'^2}{\partial z} - 2 \overline{w'v'} \frac{\partial \overline{w'v'}}{\partial z} + \lambda \overline{v'^2 \theta'_v} \end{aligned} \quad (\text{A14})$$

$$\begin{aligned} \frac{c_8 + p_{15}}{\tau_1} \overline{v'^2 \theta'_l} &= (d_{27} - 1) \overline{w'v'^2} \frac{\partial \bar{\theta}_l}{\partial z} + 2(d_{28} - 1) \overline{w'v' \theta'_l} \frac{\partial \bar{v}}{\partial z} \\ &\quad - 2 \overline{w'v'} \frac{\partial v' \theta'_l}{\partial z} - \overline{w' \theta'_l} \frac{\partial v'^2}{\partial z} \end{aligned} \quad (\text{A15})$$

$$\begin{aligned} \frac{c_8 + p_{16}}{\tau_1} \overline{v'^2 q'_t} &= (d_{29} - 1) \overline{w'v'^2} \frac{\partial \bar{q}_t}{\partial z} + 2(d_{30} - 1) \overline{w'v' q'_t} \frac{\partial \bar{v}}{\partial z} \\ &\quad - 2 \overline{w'v'} \frac{\partial v' q'_t}{\partial z} - \overline{w' q'_t} \frac{\partial v'^2}{\partial z} \end{aligned} \quad (\text{A16})$$

$$\begin{aligned} \frac{c_8 + p_{17}}{\tau_1} \overline{w'^2 u'} &= (d_{31} - 1) \overline{w' u'^2} \frac{\partial \bar{w}}{\partial z} - 2(d_{32} - 1) \overline{w'^2 u'} \frac{\partial \bar{u}}{\partial z} \\ &\quad - 2 \overline{w'^2} \frac{\partial \overline{w' u'}}{\partial z} - \overline{w' u'} \frac{\partial \overline{w'^2}}{\partial z} + 2 \lambda \overline{w' u' \theta'_v} \end{aligned} \quad (\text{A17})$$

$$\begin{aligned} \frac{c_8 + p_{18}}{\tau_1} \overline{w' u' \theta'_l} &= (d_{33} - 1) \overline{w'^2 u'} \frac{\partial \bar{\theta}_l}{\partial z} + (d_{34} - 1) \overline{w'^2 \theta'_l} \frac{\partial \bar{u}}{\partial z} + (d_{35} - 1) \overline{w' u' \theta'_l} \frac{\partial \bar{w}}{\partial z} \\ &\quad - \overline{w'^2} \frac{\partial u' \theta'_l}{\partial z} - \overline{w' u'} \frac{\partial \overline{w' \theta'_l}}{\partial z} - \overline{w' \theta'_l} \frac{\partial \overline{w' u'}}{\partial z} + \lambda \overline{u' \theta'_l \theta'_v} \end{aligned} \quad (\text{A18})$$

$$\begin{aligned} \frac{c_8 + p_{19}}{\tau_1} \overline{w' u' q'_t} &= (d_{36} - 1) \overline{w'^2 u'} \frac{\partial \bar{q}_t}{\partial z} + (d_{37} - 1) \overline{w'^2 q'_t} \frac{\partial \bar{u}}{\partial z} + (d_{38} - 1) \overline{w' u' q'_t} \frac{\partial \bar{w}}{\partial z} \\ &\quad - \overline{w'^2} \frac{\partial u' q'_t}{\partial z} - \overline{w' u'} \frac{\partial \overline{w' q'_t}}{\partial z} - \overline{w' q'_t} \frac{\partial \overline{w' u'}}{\partial z} + \lambda \overline{u' q'_t \theta'_v} \end{aligned} \quad (\text{A19})$$

$$\begin{aligned} \frac{c_8 + p_{20}}{\tau_1} \overline{u' \theta'_l{}^2} &= (d_{39} - 2) \overline{w' u' \theta'_l} \frac{\partial \bar{\theta}_l}{\partial z} + (d_{40} - 1) \overline{w' \theta'_l{}^2} \frac{\partial \bar{u}}{\partial z} \\ &\quad - \overline{w' u'} \frac{\partial \theta'_l{}^2}{\partial z} - 2 \overline{w' \theta'_l} \frac{\partial u' \theta'_l}{\partial z} \end{aligned} \quad (\text{A20})$$

$$\begin{aligned} \frac{c_8 + p_{21}}{\tau_1} \overline{u'\theta'_i q'_i} &= (d_{41} - 1) \overline{w'u'q'_i} \frac{\partial \overline{\theta}_i}{\partial z} + (d_{42} - 1) \overline{w'u'\theta'_i} \frac{\partial \overline{q}_i}{\partial z} + (d_{43} - 1) \overline{w'\theta'_i q'_i} \frac{\partial \overline{u}}{\partial z} \\ &\quad - \overline{w'u'} \frac{\partial \overline{\theta'_i q'_i}}{\partial z} - \overline{w'\theta'_i} \frac{\partial \overline{u'q'_i}}{\partial z} - \overline{w'q'_i} \frac{\partial \overline{u'\theta'_i}}{\partial z} \end{aligned} \quad (\text{A21})$$

$$\begin{aligned} \frac{c_8 + p_{22}}{\tau_1} \overline{u'q_i'^2} &= (d_{44} - 2) \overline{w'u'q'_i} \frac{\partial \overline{q}_i}{\partial z} + (d_{45} - 1) \overline{w'q_i'^2} \frac{\partial \overline{u}}{\partial z} \\ &\quad - \overline{w'u'} \frac{\partial \overline{q_i'^2}}{\partial z} - 2 \overline{w'q'_i} \frac{\partial \overline{u'q'_i}}{\partial z} \end{aligned} \quad (\text{A22})$$

$$\begin{aligned} \frac{c_8 + p_{23}}{\tau_1} \overline{w'^2 v'} &= (d_{46} - 1) \overline{w'v'^2} \frac{\partial \overline{w}}{\partial z} - 2(d_{47} - 1) \overline{w'^2 v'} \frac{\partial \overline{v}}{\partial z} \\ &\quad - 2 \overline{w'^2} \frac{\partial \overline{w'v'}}{\partial z} - \overline{w'v'} \frac{\partial \overline{w'^2}}{\partial z} + 2 \lambda \overline{w'v'\theta'_v} \end{aligned} \quad (\text{A23})$$

$$\begin{aligned} \frac{c_8 + p_{24}}{\tau_1} \overline{w'v'\theta'_i} &= (d_{48} - 1) \overline{w'^2 v'} \frac{\partial \overline{\theta}_i}{\partial z} + (d_{49} - 1) \overline{w'^2 \theta'_i} \frac{\partial \overline{v}}{\partial z} + (d_{50} - 1) \overline{w'v'\theta'_i} \frac{\partial \overline{w}}{\partial z} \\ &\quad - \overline{w'^2} \frac{\partial \overline{v'\theta'_i}}{\partial z} - \overline{w'v'} \frac{\partial \overline{w'\theta'_i}}{\partial z} - \overline{w'\theta'_i} \frac{\partial \overline{w'v'}}{\partial z} + \lambda \overline{v'\theta'_i \theta'_v} \end{aligned} \quad (\text{A24})$$

$$\begin{aligned} \frac{c_8 + p_{25}}{\tau_1} \overline{w'v'q'_i} &= (d_{51} - 1) \overline{w'^2 v'} \frac{\partial \overline{q}_i}{\partial z} + (d_{52} - 1) \overline{w'^2 q'_i} \frac{\partial \overline{v}}{\partial z} + (d_{53} - 1) \overline{w'v'q'_i} \frac{\partial \overline{w}}{\partial z} \\ &\quad - \overline{w'^2} \frac{\partial \overline{v'q'_i}}{\partial z} - \overline{w'v'} \frac{\partial \overline{w'q'_i}}{\partial z} - \overline{w'q'_i} \frac{\partial \overline{w'v'}}{\partial z} + \lambda \overline{v'q'_i \theta'_v} \end{aligned} \quad (\text{A25})$$

$$\begin{aligned} \frac{c_8 + p_{26}}{\tau_1} \overline{v'\theta_i'^2} &= (d_{54} - 2) \overline{w'v'\theta'_i} \frac{\partial \overline{\theta}_i}{\partial z} + (d_{55} - 1) \overline{w'\theta_i'^2} \frac{\partial \overline{v}}{\partial z} \\ &\quad - \overline{w'v'} \frac{\partial \overline{\theta_i'^2}}{\partial z} - 2 \overline{w'\theta'_i} \frac{\partial \overline{v'\theta'_i}}{\partial z} \end{aligned} \quad (\text{A26})$$

$$\begin{aligned} \frac{c_8 + p_{27}}{\tau_1} \overline{v'\theta'_i q'_i} &= (d_{56} - 1) \overline{w'v'q'_i} \frac{\partial \overline{\theta}_i}{\partial z} + (d_{57} - 1) \overline{w'v'\theta'_i} \frac{\partial \overline{q}_i}{\partial z} + (d_{58} - 1) \overline{w'\theta'_i q'_i} \frac{\partial \overline{v}}{\partial z} \\ &\quad - \overline{w'v'} \frac{\partial \overline{\theta'_i q'_i}}{\partial z} - \overline{w'\theta'_i} \frac{\partial \overline{v'q'_i}}{\partial z} - \overline{w'q'_i} \frac{\partial \overline{v'\theta'_i}}{\partial z} \end{aligned} \quad (\text{A27})$$

$$\frac{c_8 + p_{28}}{\tau_1} \overline{v'q_t'^2} = (d_{59} - 2) \overline{w'v'q_t'} \frac{\partial \overline{q_t}}{\partial z} + (d_{60} - 1) \overline{w'q_t'^2} \frac{\partial \overline{v}}{\partial z} - \overline{w'v'} \frac{\partial \overline{q_t'^2}}{\partial z} - 2 \overline{w'q_t'} \frac{\partial \overline{v'q_t'}}{\partial z} \quad (\text{A28})$$

CEA2005 only determine values for the p_n and d_m constants given in Table A1 since they only consider 6 fourth-order moments. A logical extension to these constants for all 28 fourth-order moments in this model follows in Tables A2 and A3, where d's are assigned values so that they are in accordance with CEA2005 and so they eliminate the dependence of third-order moments on mean variable gradients. The p_n constants in CEA2005 are determined from LES data and are tunable. Increases in the p_n constants result in more damping of the third-order moment to which the constant applies.

p_1	p_2	p_3	p_7	p_{11}	p_{12}	d_2	d_4	d_{13}	d_{21}
4	4	2	1	0	0	1	2	3	1

Table A1 Constants for the fourth-order moments from Cheng et al. (2005)

d_1	d_2	d_3	d_4	d_5	d_6	d_7	d_8	d_9	d_{10}
1	1	1	1	1	1	1	2	1	1
d_{11}	d_{12}	d_{13}	d_{14}	d_{15}	d_{16}	d_{17}	d_{18}	d_{19}	d_{20}
1	1	3	1	2	1	2	3	1	1
d_{21}	d_{22}	d_{23}	d_{24}	d_{25}	d_{26}	d_{27}	d_{28}	d_{29}	d_{30}
1	1	1	1	1	1	1	1	1	1
d_{31}	d_{32}	d_{33}	d_{34}	d_{35}	d_{36}	d_{37}	d_{38}	d_{39}	d_{40}
1	1	1	1	1	1	1	1	1	1
d_{41}	d_{42}	d_{43}	d_{44}	d_{45}	d_{46}	d_{47}	d_{48}	d_{49}	d_{50}
1	1	1	1	1	1	1	1	1	1
d_{51}	d_{52}	d_{53}	d_{54}	d_{55}	d_{56}	d_{57}	d_{58}	d_{59}	d_{60}
1	1	1	2	1	1	1	1	2	1

Table A2 d Constants for the fourth-order moments

P_1	P_2	P_3	P_4	P_5	P_6	P_7	P_8	P_9	P_{10}
4	4	4	4	4	4	1	1	1	1
P_{11}	P_{12}	P_{13}	P_{14}	P_{15}	P_{16}	P_{17}	P_{18}	P_{19}	P_{20}
0	0	0	0	0	0	4	4	4	2
P_{21}	P_{22}	P_{23}	P_{24}	P_{25}	P_{26}	P_{27}	P_{28}		
2	2	4	4	4	2	2	2		

Table A3 p Constants for the fourth-order moments

Since equations (A1)-(A28) represent a system of 28 equations with 28 unknown third-order moments, it is possible to explicitly solve for the unknowns as the studies of Canuto et al. (1994) and CEA2005 have done. Equations (A1)-(A28) were put into a symbolic algebra program with the buoyancy terms parameterized following section 2.9.

Terms involving $\overline{u'\theta'_i}$, $\overline{u'q'_i}$, $\overline{v'\theta'_i}$, and $\overline{v'q'_i}$ were neglected since this model is only considering vertical fluxes. The results are shown as equations (A29)-(A56). Each third-order moment is a linear combination of vertical derivatives of the second-order moments with extensive coefficients. For organizational purposes, each coefficient has two indices separated by a period – the first one to denote which third-order moment the coefficient appears in and the second to indicate which second-order moment derivative the coefficient modifies. These coefficients are found in Table A4. In addition, 14 of the third-order moments have a third-order moment liquid water correlation term denoted as L 's and listed in Table A5. These liquid water correlations, if not neglected, need to be calculated in a subgrid-scale condensation scheme.

$$\begin{aligned} \overline{w'^3} = & -A_{1.3} \frac{\overline{\partial w'^2}}{\partial z} - A_{1.6} \frac{\overline{\partial w' \theta'_l}}{\partial z} - A_{1.7} \frac{\overline{\partial w' q'_t}}{\partial z} - A_{1.8} \frac{\overline{\partial \theta_l'^2}}{\partial z} \\ & - A_{1.9} \frac{\overline{\partial \theta'_l q'_t}}{\partial z} - A_{1.10} \frac{\overline{\partial q_t'^2}}{\partial z} + L_1 \end{aligned} \quad (\text{A29})$$

$$\begin{aligned} \overline{w'^2 \theta'_l} = & -A_{2.3} \frac{\overline{\partial w'^2}}{\partial z} - A_{2.6} \frac{\overline{\partial w' \theta'_l}}{\partial z} - A_{2.7} \frac{\overline{\partial w' q'_t}}{\partial z} - A_{2.8} \frac{\overline{\partial \theta_l'^2}}{\partial z} \\ & - A_{2.9} \frac{\overline{\partial \theta'_l q'_t}}{\partial z} - A_{2.10} \frac{\overline{\partial q_t'^2}}{\partial z} + L_2 \end{aligned} \quad (\text{A30})$$

$$\overline{w' \theta_l'^2} = -A_{3.6} \frac{\overline{\partial w' \theta'_l}}{\partial z} - A_{3.8} \frac{\overline{\partial \theta_l'^2}}{\partial z} - A_{3.9} \frac{\overline{\partial \theta'_l q'_t}}{\partial z} + L_3 \quad (\text{A31})$$

$$\begin{aligned} \overline{w'^2 q'_t} = & -A_{4.3} \frac{\overline{\partial w'^2}}{\partial z} - A_{4.6} \frac{\overline{\partial w' \theta'_l}}{\partial z} - A_{4.7} \frac{\overline{\partial w' q'_t}}{\partial z} - A_{4.8} \frac{\overline{\partial \theta_l'^2}}{\partial z} \\ & - A_{4.9} \frac{\overline{\partial \theta'_l q'_t}}{\partial z} - A_{4.10} \frac{\overline{\partial q_t'^2}}{\partial z} + L_4 \end{aligned} \quad (\text{A32})$$

$$\overline{w' q_t'^2} = -A_{5.7} \frac{\overline{\partial w' q'_t}}{\partial z} - A_{5.9} \frac{\overline{\partial \theta'_l q'_t}}{\partial z} - A_{5.10} \frac{\overline{\partial q_t'^2}}{\partial z} + L_5 \quad (\text{A33})$$

$$\overline{w' \theta'_l q'_t} = -A_{6.6} \frac{\overline{\partial w' \theta'_l}}{\partial z} - A_{6.7} \frac{\overline{\partial w' q'_t}}{\partial z} - A_{6.8} \frac{\overline{\partial \theta_l'^2}}{\partial z} - A_{6.9} \frac{\overline{\partial \theta'_l q'_t}}{\partial z} - A_{6.10} \frac{\overline{\partial q_t'^2}}{\partial z} + L_6 \quad (\text{A34})$$

$$\overline{\theta_l'^3} = -A_{7.8} \frac{\overline{\partial \theta_l'^2}}{\partial z} \quad (\text{A35})$$

$$\overline{\theta_l'^2 q'_t} = -A_{8.8} \frac{\overline{\partial \theta_l'^2}}{\partial z} - A_{8.9} \frac{\overline{\partial \theta'_l q'_t}}{\partial z} \quad (\text{A36})$$

$$\overline{\theta'_l q_t'^2} = -A_{9.9} \frac{\overline{\partial \theta'_l q'_t}}{\partial z} - A_{9.10} \frac{\overline{\partial q_t'^2}}{\partial z} \quad (\text{A37})$$

$$\overline{q_t'^3} = -A_{10.10} \frac{\overline{\partial q_t'^2}}{\partial z} \quad (\text{A38})$$

$$\overline{w'u'^2} = -A_{11.1} \frac{\partial \overline{u'^2}}{\partial z} - A_{11.4} \frac{\partial \overline{w'u'}}{\partial z} + L_{11} \quad (\text{A39})$$

$$\overline{u'^2 \theta'_i} = -A_{12.1} \frac{\partial \overline{u'^2}}{\partial z} \quad (\text{A40})$$

$$\overline{u'^2 q'_i} = -A_{13.1} \frac{\partial \overline{u'^2}}{\partial z} \quad (\text{A41})$$

$$\overline{w'v'^2} = -A_{14.2} \frac{\partial \overline{v'^2}}{\partial z} - A_{14.5} \frac{\partial \overline{w'v'}}{\partial z} + L_{14} \quad (\text{A42})$$

$$\overline{v'^2 \theta'_i} = -A_{15.2} \frac{\partial \overline{v'^2}}{\partial z} \quad (\text{A43})$$

$$\overline{v'^2 q'_i} = -A_{16.2} \frac{\partial \overline{v'^2}}{\partial z} \quad (\text{A44})$$

$$\begin{aligned} \overline{w'^2 u'} = & -A_{17.3} \frac{\partial \overline{w'^2}}{\partial z} - A_{17.4} \frac{\partial \overline{w'u'}}{\partial z} - A_{17.6} \frac{\partial \overline{w'\theta'_i}}{\partial z} - A_{17.7} \frac{\partial \overline{w'q'_i}}{\partial z} \\ & - A_{17.8} \frac{\partial \overline{\theta_i'^2}}{\partial z} - A_{17.9} \frac{\partial \overline{\theta'_i q'_i}}{\partial z} - A_{17.10} \frac{\partial \overline{q_i'^2}}{\partial z} + L_{17} \end{aligned} \quad (\text{A45})$$

$$\overline{w'u'\theta'_i} = -A_{18.4} \frac{\partial \overline{w'u'}}{\partial z} - A_{18.6} \frac{\partial \overline{w'\theta'_i}}{\partial z} - A_{18.8} \frac{\partial \overline{\theta_i'^2}}{\partial z} - A_{18.9} \frac{\partial \overline{\theta'_i q'_i}}{\partial z} + L_{18} \quad (\text{A46})$$

$$\overline{w'u'q'_i} = -A_{19.4} \frac{\partial \overline{w'u'}}{\partial z} - A_{19.7} \frac{\partial \overline{w'q'_i}}{\partial z} - A_{19.9} \frac{\partial \overline{\theta'_i q'_i}}{\partial z} - A_{19.10} \frac{\partial \overline{q_i'^2}}{\partial z} + L_{19} \quad (\text{A47})$$

$$\overline{u'\theta_i'^2} = -A_{20.8} \frac{\partial \overline{\theta_i'^2}}{\partial z} \quad (\text{A48})$$

$$\overline{u'\theta'_i q'_i} = -A_{21.9} \frac{\partial \overline{\theta'_i q'_i}}{\partial z} \quad (\text{A49})$$

$$\overline{u'q_i'^2} = -A_{22.10} \frac{\partial \overline{q_i'^2}}{\partial z} \quad (\text{A50})$$

$$\begin{aligned} \overline{w'^2 v'} = & -A_{23.3} \frac{\overline{\partial w'^2}}{\partial z} - A_{23.5} \frac{\overline{\partial w' v'}}{\partial z} - A_{23.6} \frac{\overline{\partial w' \theta'_i}}{\partial z} - A_{23.7} \frac{\overline{\partial w' q'_i}}{\partial z} \\ & - A_{23.8} \frac{\overline{\partial \theta_i'^2}}{\partial z} - A_{23.9} \frac{\overline{\partial \theta'_i q'_i}}{\partial z} - A_{23.10} \frac{\overline{\partial q_i'^2}}{\partial z} + L_{23} \end{aligned} \quad (\text{A51})$$

$$\overline{w' v' \theta'_i} = -A_{24.5} \frac{\overline{\partial w' v'}}{\partial z} - A_{24.6} \frac{\overline{\partial w' \theta'_i}}{\partial z} - A_{24.8} \frac{\overline{\partial \theta_i'^2}}{\partial z} - A_{24.9} \frac{\overline{\partial \theta'_i q'_i}}{\partial z} + L_{24} \quad (\text{A52})$$

$$\overline{w' v' q'_i} = -A_{25.5} \frac{\overline{\partial w' v'}}{\partial z} - A_{25.7} \frac{\overline{\partial w' q'_i}}{\partial z} - A_{25.9} \frac{\overline{\partial \theta'_i q'_i}}{\partial z} - A_{25.10} \frac{\overline{\partial q_i'^2}}{\partial z} + L_{25} \quad (\text{A53})$$

$$\overline{v' \theta_i'^2} = -A_{26.8} \frac{\overline{\partial \theta_i'^2}}{\partial z} \quad (\text{A54})$$

$$\overline{v' \theta'_i q'_i} = -A_{27.9} \frac{\overline{\partial \theta'_i q'_i}}{\partial z} \quad (\text{A55})$$

$$\overline{v' q_i'^2} = -A_{28.10} \frac{\overline{\partial q_i'^2}}{\partial z} \quad (\text{A56})$$

Third-Order Moment	Coefficients
$\overline{w'^3}$	$A_{1.3} = \frac{3\tau_1}{b_1} \overline{w'^2} + \frac{3\lambda\tau_1^2}{b_1 b_2} \overline{w' \theta'_i} + \frac{3C_{T_0} \lambda \tau_1^2}{b_1 b_4} \overline{w' q'_i}$ $A_{1.6} = \frac{6\lambda\tau_1^2}{b_1 b_2} \overline{w'^2} + \frac{12\lambda^2\tau_1^3}{b_1 b_2 b_3} \overline{w' \theta'_i} + \frac{6C_{T_0} \lambda^2 \tau_1^3}{b_1 b_6} \left(\frac{1}{b_4} + \frac{1}{b_2} \right) \overline{w' q'_i}$ $A_{1.7} = \frac{6C_{T_0} \lambda \tau_1^2}{b_1 b_4} \overline{w'^2} + \frac{6C_{T_0} \lambda^2 \tau_1^3}{b_1 b_6} \left(\frac{1}{b_4} + \frac{1}{b_2} \right) \overline{w' \theta'_i} + \frac{12C_{T_0}^2 \lambda^2 \tau_1^3}{b_1 b_4 b_5} \overline{w' q'_i}$ $A_{1.8} = \frac{6\lambda^2\tau_1^3}{b_1 b_2 b_3} \overline{w'^2} + \frac{18\lambda^3\tau_1^4}{b_1 b_2 b_3 b_7} \overline{w' \theta'_i} + \frac{6C_{T_0} \lambda^3 \tau_1^4}{b_1 b_8} \left(\frac{1}{b_4 b_6} + \frac{1}{b_2 b_6} + \frac{1}{b_2 b_3} \right) \overline{w' q'_i}$ $A_{1.9} = \frac{6C_{T_0} \lambda^2 \tau_1^3}{b_1 b_6} \left(\frac{1}{b_4} + \frac{1}{b_2} \right) \overline{w'^2} + \frac{12C_{T_0} \lambda^3 \tau_1^4}{b_1 b_8} \left(\frac{1}{b_4 b_6} + \frac{1}{b_2 b_6} + \frac{1}{b_2 b_3} \right) \overline{w' \theta'_i}$ $+ \frac{12C_{T_0} \lambda^3 \tau_1^4}{b_1 b_9} \left(\frac{1}{b_4 b_5} + \frac{1}{b_4 b_6} + \frac{1}{b_2 b_6} \right) \overline{w' q'_i}$ $A_{1.10} = \frac{6C_{T_0}^2 \lambda^2 \tau_1^3}{b_1 b_4 b_5} \overline{w'^2} + \frac{6C_{T_0}^2 \lambda^3 \tau_1^4}{b_1 b_9} \left(\frac{1}{b_4 b_6} + \frac{1}{b_2 b_6} \right) \overline{w' \theta'_i} + \frac{18C_{T_0}^3 \lambda^3 \tau_1^4}{b_1 b_4 b_5 b_{10}} \overline{w' q'_i}$

$\overline{w'^2\theta'_i}$	$A_{2.3} = \frac{\tau_1 \overline{w'\theta'_i}}{b_2}$ $A_{2.6} = \frac{2\tau_1 \overline{w'^2}}{b_2} + \frac{4\lambda\tau_1^2 \overline{w'\theta'_i}}{b_2 b_3} + \frac{2C_{T_0} \lambda\tau_1^2 \overline{w'q'_i}}{b_2 b_6}$ $A_{2.7} = \frac{2C_{T_0} \lambda\tau_1^2 \overline{w'\theta'_i}}{b_2 b_6}$ $A_{2.8} = \frac{2\lambda\tau_1^2 \overline{w'^2}}{b_2 b_3} + \frac{6\lambda^2\tau_1^3 \overline{w'\theta'_i}}{b_2 b_3 b_7} + \frac{2C_{T_0} \lambda^2\tau_1^3 \left(\frac{1}{b_6} + \frac{1}{b_3}\right) \overline{w'q'_i}}{b_2 b_8}$ $A_{2.9} = \frac{2C_{T_0} \lambda\tau_1^2 \overline{w'^2}}{b_2 b_6} + \frac{4C_{T_0} \lambda^2\tau_1^3 \left(\frac{1}{b_6} + \frac{1}{b_3}\right) \overline{w'\theta'_i}}{b_2 b_8} + \frac{4C_{T_0}^2 \lambda^2\tau_1^3 \overline{w'q'_i}}{b_2 b_6 b_9}$ $A_{2.10} = \frac{2C_{T_0}^2 \lambda^2\tau_1^3 \overline{w'\theta'_i}}{b_2 b_6 b_9}$
$\overline{w'\theta'_i{}^2}$	$A_{3.6} = \frac{2\tau_1 \overline{w'\theta'_i}}{b_3}$ $A_{3.8} = \frac{\tau_1 \overline{w'^2}}{b_3} + \frac{3\lambda\tau_1^2 \overline{w'\theta'_i}}{b_3 b_7} + \frac{C_{T_0} \lambda\tau_1^2 \overline{w'q'_i}}{b_3 b_8}$ $A_{3.9} = \frac{2C_{T_0} \lambda\tau_1^2 \overline{w'\theta'_i}}{b_3 b_8}$
$\overline{w'^2 q'_i}$	$A_{4.3} = \frac{\tau_1 \overline{w'q'_i}}{b_4}$ $A_{4.6} = \frac{2\lambda\tau_1^2 \overline{w'q'_i}}{b_4 b_6}$ $A_{4.7} = \frac{2\tau_1 \overline{w'^2}}{b_4} + \frac{2\lambda\tau_1^2 \overline{w'\theta'_i}}{b_4 b_6} + \frac{4C_{T_0} \lambda\tau_1^2 \overline{w'q'_i}}{b_4 b_5}$ $A_{4.8} = \frac{2\lambda^2\tau_1^3 \overline{w'q'_i}}{b_4 b_6 b_8}$ $A_{4.9} = \frac{2\lambda\tau_1^2 \overline{w'^2}}{b_4 b_6} + \frac{4\lambda^2\tau_1^3 \overline{w'\theta'_i}}{b_4 b_6 b_8} + \frac{4C_{T_0} \lambda^2\tau_1^3 \left(\frac{1}{b_5} + \frac{1}{b_6}\right) \overline{w'q'_i}}{b_4 b_9}$ $A_{4.10} = \frac{2C_{T_0} \lambda\tau_1^2 \overline{w'^2}}{b_4 b_5} + \frac{2C_{T_0} \lambda^2\tau_1^3 \left(\frac{1}{b_5} + \frac{1}{b_6}\right) \overline{w'\theta'_i}}{b_4 b_9} + \frac{6C_{T_0}^2 \lambda^2\tau_1^3 \overline{w'q'_i}}{b_4 b_5 b_{10}}$
$\overline{w'q'_i{}^2}$	$A_{5.7} = \frac{2\tau_1 \overline{w'q'_i}}{b_5}$ $A_{5.9} = \frac{2\lambda\tau_1^2 \overline{w'q'_i}}{b_5 b_9}$

	$A_{5.10} = \frac{\tau_1 \overline{w'^2}}{b_5} + \frac{\lambda \tau_1^2 \overline{w'\theta'_l}}{b_5 b_9} + \frac{3C_{T_0} \lambda \tau_1^2 \overline{w'q'_t}}{b_5 b_{10}}$
$\overline{w'\theta'_l q'_t}$	$A_{6.6} = \frac{\tau_1 \overline{w'q'_t}}{b_6}$ $A_{6.7} = \frac{\tau_1 \overline{w'\theta'_l}}{b_6}$ $A_{6.8} = \frac{\lambda \tau_1^2 \overline{w'q'_t}}{b_6 b_8}$ $A_{6.9} = \frac{\tau_1 \overline{w'^2}}{b_6} + \frac{2\lambda \tau_1^2 \overline{w'\theta'_l}}{b_6 b_8} + \frac{2C_{T_0} \lambda \tau_1^2 \overline{w'q'_t}}{b_6 b_9}$ $A_{6.10} = \frac{C_{T_0} \lambda \tau_1^2 \overline{w'\theta'_l}}{b_6 b_9}$
$\overline{\theta'_l{}^3}$	$A_{7.8} = \frac{3\tau_1 \overline{w'\theta'_l}}{b_7}$
$\overline{\theta'_l{}^2 q'_t}$	$A_{8.8} = \frac{\tau_1 \overline{w'q'_t}}{b_8}$ $A_{8.9} = \frac{2\tau_1 \overline{w'\theta'_l}}{b_8}$
$\overline{\theta'_l q'_t{}^2}$	$A_{9.9} = \frac{2\tau_1 \overline{w'q'_t}}{b_9}$ $A_{9.10} = \frac{\tau_1 \overline{w'\theta'_l}}{b_9}$
$\overline{q'_t{}^3}$	$A_{10.10} = \frac{3\tau_1 \overline{w'q'_t}}{b_{10}}$
$\overline{w'u'^2}$	$A_{11.1} = \frac{\tau_1 \overline{w'^2}}{b_{11}} + \frac{\lambda \tau_1^2 \overline{w'\theta'_l}}{b_{11} b_{12}} + \frac{C_{T_0} \lambda \tau_1^2 \overline{w'q'_t}}{b_{11} b_{13}}$ $A_{11.4} = \frac{2\tau_1 \overline{w'u'}}{b_{11}}$
$\overline{u'^2 \theta'_l}$	$A_{12.1} = \frac{\tau_1 \overline{w'\theta'_l}}{b_{12}}$
$\overline{u'^2 q'_t}$	$A_{13.1} = \frac{\tau_1 \overline{w'q'_t}}{b_{13}}$
$\overline{w'v'^2}$	$A_{14.2} = \frac{\tau_1 \overline{w'^2}}{b_{14}} + \frac{\lambda \tau_1^2 \overline{w'\theta'_l}}{b_{14} b_{15}} + \frac{C_{T_0} \lambda \tau_1^2 \overline{w'q'_t}}{b_{14} b_{16}}$ $A_{14.5} = \frac{2\tau_1 \overline{w'v'}}{b_{14}}$

$\overline{v'^2 \theta'_l}$	$A_{15.2} = \frac{\tau_1}{b_{15}} \overline{w' \theta'_l}$
$\overline{v'^2 q'_t}$	$A_{16.2} = \frac{\tau_1}{b_{16}} \overline{w' q'_t}$
$\overline{w'^2 u'}$	$A_{17.3} = \frac{\tau_1}{b_{17}} \overline{w' u'}$ $A_{17.4} = \frac{2\tau_1}{b_{17}} \overline{w'^2} + \frac{2\lambda\tau_1^2}{b_{17}b_{18}} \overline{w' \theta'_l} + \frac{2C_{T_0}\lambda\tau_1^2}{b_{17}b_{19}} \overline{w' q'_t}$ $A_{17.6} = \frac{2\lambda\tau_1^2}{b_{17}b_{18}} \overline{w' u'}$ $A_{17.7} = \frac{2C_{T_0}\lambda\tau_1^2}{b_{17}b_{19}} \overline{w' u'}$ $A_{17.8} = \frac{2\lambda^2\tau_1^3}{b_{17}b_{18}b_{20}} \overline{w' u'}$ $A_{17.9} = \frac{2C_{T_0}\lambda^2\tau_1^3}{b_{17}b_{21}} \left(\frac{1}{b_{19}} + \frac{1}{b_{18}} \right) \overline{w' u'}$ $A_{17.10} = \frac{2C_{T_0}^2\lambda^2\tau_1^3}{b_{17}b_{19}b_{22}} \overline{w' u'}$
$\overline{w' u' \theta'_l}$	$A_{18.4} = \frac{\tau_1}{b_{18}} \overline{w' \theta'_l}$ $A_{18.6} = \frac{\tau_1}{b_{18}} \overline{w' u'}$ $A_{18.8} = \frac{\lambda\tau_1^2}{b_{18}b_{20}} \overline{w' u'}$ $A_{18.9} = \frac{C_{T_0}\lambda\tau_1^2}{b_{18}b_{21}} \overline{w' u'}$
$\overline{w' u' q'_t}$	$A_{19.4} = \frac{\tau_1}{b_{19}} \overline{w' q'_t}$ $A_{19.7} = \frac{\tau_1}{b_{19}} \overline{w' u'}$ $A_{19.9} = \frac{\lambda\tau_1^2}{b_{19}b_{21}} \overline{w' u'}$ $A_{19.10} = \frac{C_{T_0}\lambda\tau_1^2}{b_{19}b_{22}} \overline{w' u'}$

$\overline{u'\theta_i'^2}$	$A_{20.8} = \frac{\tau_1}{b_{20}} \overline{w'u'}$
$\overline{u'\theta_i'q_i'}$	$A_{21.9} = \frac{\tau_1}{b_{21}} \overline{w'u'}$
$\overline{u'q_i'^2}$	$A_{22.10} = \frac{\tau_1}{b_{22}} \overline{w'u'}$
$\overline{w'^2v'}$	$A_{23.3} = \frac{\tau_1}{b_{23}} \overline{w'v'}$ $A_{23.5} = \frac{2\tau_1}{b_{23}} \overline{w'^2} + \frac{2\lambda\tau_1^2}{b_{23}b_{24}} \overline{w'\theta_i'} + \frac{2C_{T_0}\lambda\tau_1^2}{b_{23}b_{25}} \overline{w'q_i'}$ $A_{23.6} = \frac{2\lambda\tau_1^2}{b_{23}b_{24}} \overline{w'v'}$ $A_{23.7} = \frac{2C_{T_0}\lambda\tau_1^2}{b_{23}b_{25}} \overline{w'v'}$ $A_{23.8} = \frac{2\lambda^2\tau_1^3}{b_{23}b_{24}b_{26}} \overline{w'v'}$ $A_{23.9} = \frac{2C_{T_0}\lambda^2\tau_1^3}{b_{23}b_{27}} \left(\frac{1}{b_{25}} + \frac{1}{b_{24}} \right) \overline{w'v'}$ $A_{23.10} = \frac{2C_{T_0}^2\lambda^2\tau_1^3}{b_{23}b_{25}b_{27}} \overline{w'v'}$
$\overline{w'v'\theta_i'}$	$A_{24.5} = \frac{\tau_1}{b_{24}} \overline{w'\theta_i'}$ $A_{24.6} = \frac{\tau_1}{b_{24}} \overline{w'v'}$ $A_{24.8} = \frac{\lambda\tau_1^2}{b_{24}b_{26}} \overline{w'v'}$ $A_{24.9} = \frac{C_{T_0}\lambda\tau_1^2}{b_{24}b_{27}} \overline{w'v'}$
$\overline{w'v'q_i'}$	$A_{25.5} = \frac{\tau_1}{b_{25}} \overline{w'q_i'}$ $A_{25.7} = \frac{\tau_1}{b_{25}} \overline{w'v'}$ $A_{25.9} = \frac{\lambda\tau_1^2}{b_{25}b_{27}} \overline{w'v'}$

	$A_{25.10} = \frac{C_{T_0} \lambda \tau_1^2}{b_{25} b_{27}} \overline{w'v'}$
$\overline{v'\theta_i'^2}$	$A_{26.8} = \frac{\tau_1}{b_{26}} \overline{w'v'}$
$\overline{v'\theta_i'q_i'}$	$A_{27.9} = \frac{\tau_1}{b_{27}} \overline{w'v'}$
$\overline{v'q_i'^2}$	$A_{28.10} = \frac{\tau_1}{b_{28}} \overline{w'v'}$

Table A4 Coefficients for the diagnostic third-order moments

Third-order Moment Liquid Water Correlation Terms

$$L_1 = \frac{3D\lambda\tau_1}{b_1} \left(\overline{w'^2 q'_i} + \frac{2\lambda\tau_1}{b_2} \overline{w'\theta'_i q'_i} + \frac{2\lambda^2\tau_1^2}{b_2 b_3} \overline{\theta_i^2 q'_i} + \frac{2C_{T_0}\lambda\tau_1}{b_4} \overline{w'q'_i q'_i} \right. \\ \left. + \frac{2C_{T_0}\lambda^2\tau_1^2}{b_6} \left(\frac{1}{b_4} + \frac{1}{b_2} \right) \overline{\theta'_i q'_i q'_i} + \frac{2C_{T_0}^2\lambda^2\tau_1^2}{b_4 b_5} \overline{q_i^2 q'_i} \right)$$

$$L_2 = \frac{2D\lambda\tau_1}{b_2} \left(\overline{w'\theta'_i q'_i} + \frac{\lambda\tau_1}{b_3} \overline{\theta_i^2 q'_i} + \frac{C_{T_0}\lambda\tau_1}{b_6} \overline{\theta'_i q'_i q'_i} \right)$$

$$L_3 = \frac{D\lambda\tau_1}{b_3} \overline{\theta_i^2 q'_i}$$

$$L_4 = \frac{2D\lambda\tau_1}{b_4} \left(\overline{w'q'_i q'_i} + \frac{\lambda\tau_1}{b_6} \overline{\theta'_i q'_i q'_i} + \frac{C_{T_0}\lambda\tau_1}{b_5} \overline{q_i^2 q'_i} \right)$$

$$L_5 = \frac{D\lambda\tau_1}{b_5} \overline{q_i^2 q'_i}$$

$$L_6 = \frac{D\lambda\tau_1}{b_6} \overline{\theta'_i q'_i q'_i}$$

$$L_{11} = \frac{D\lambda\tau_1}{b_{11}} \overline{u'^2 q'_i}$$

$$L_{14} = \frac{D\lambda\tau_1}{b_{14}} \overline{v'^2 q'_i}$$

$$L_{17} = \frac{2D\lambda\tau_1}{b_{17}} \left(\overline{w'u'q'_i} + \frac{\lambda\tau_1}{b_{18}} \overline{u'\theta'_i q'_i} + \frac{C_{T_0}\lambda\tau_1}{b_{19}} \overline{u'q'_i q'_i} \right)$$

$$L_{18} = \frac{D\lambda\tau_1}{b_{18}} \overline{u'\theta'_i q'_i}$$

$$L_{19} = \frac{D\lambda\tau_1}{b_{19}} \overline{u'q'_i q'_i}$$

$$L_{23} = \frac{2D\lambda\tau_1}{b_{23}} \left(\overline{w'v'q'_i} + \frac{\lambda\tau_1}{b_{24}} \overline{v'\theta'_i q'_i} + \frac{C_{T_0}\lambda\tau_1}{b_{25}} \overline{v'q'_i q'_i} \right)$$

$$L_{24} = \frac{D\lambda\tau_1}{b_{24}} \overline{v'\theta'_i q'_i}$$

$$L_{25} = \frac{D\lambda\tau_1}{b_{25}} \overline{v'q'_i q'_i}$$

Table A5 Liquid water correlation terms in the diagnostic third-order moments

Upon inspection of the coefficients in Tables A4 and A5, it is apparent that many terms contain multiples of the turbulent timescale to the third or fourth power. These terms originate during the process of solving the extensive system of 28 equations, and the power associated with the turbulent timescale is an indication of the dependence of a

particular third-order moment on the term the coefficient modifies. Higher powers indicate more distant relationships. Since the turbulent timescale is somewhat of an artificial parameterized quantity, terms containing its third or fourth power can be considered more highly parameterized and potentially less accurate. For this reason in addition to the destabilizing influence of terms containing higher-order multiples, it is prudent to consider neglecting these terms as a simplifying assumption. Table A6 and A7 list the simplified coefficients and third-order liquid water correlations, and these are the relations used in the current model.

Third-Order Moment	Coefficients
$\overline{w'^3}$	$A_{1.3} = \frac{3\tau_1 \overline{w'^2}}{b_1} + \frac{3\lambda\tau_1^2 \overline{w'\theta'_l}}{b_1 b_2} + \frac{3C_{T_0} \lambda\tau_1^2 \overline{w'q'_l}}{b_1 b_4}$ $A_{1.6} = \frac{6\lambda\tau_1^2 \overline{w'^2}}{b_1 b_2}$ $A_{1.7} = \frac{6C_{T_0} \lambda\tau_1^2 \overline{w'^2}}{b_1 b_4}$ $A_{1.8} = 0$ $A_{1.9} = 0$ $A_{1.10} = 0$
$\overline{w'^2 \theta'_l}$	$A_{2.3} = \frac{\tau_1 \overline{w'\theta'_l}}{b_2}$ $A_{2.6} = \frac{2\tau_1 \overline{w'^2}}{b_2} + \frac{4\lambda\tau_1^2 \overline{w'\theta'_l}}{b_2 b_3} + \frac{2C_{T_0} \lambda\tau_1^2 \overline{w'q'_l}}{b_2 b_6}$ $A_{2.7} = \frac{2C_{T_0} \lambda\tau_1^2 \overline{w'\theta'_l}}{b_2 b_6}$ $A_{2.8} = \frac{2\lambda\tau_1^2 \overline{w'^2}}{b_2 b_3}$ $A_{2.9} = \frac{2C_{T_0} \lambda\tau_1^2 \overline{w'^2}}{b_2 b_6}$ $A_{2.10} = 0$
$\overline{w'\theta'_l{}^2}$	$A_{3.6} = \frac{2\tau_1 \overline{w'\theta'_l}}{b_3}$

	$A_{3.8} = \frac{\tau_1 \overline{w'^2}}{b_3} + \frac{3\lambda\tau_1^2 \overline{w'\theta'_l}}{b_3 b_7} + \frac{C_{T_0} \lambda \tau_1^2 \overline{w'q'_l}}{b_3 b_8}$ $A_{3.9} = \frac{2C_{T_0} \lambda \tau_1^2 \overline{w'\theta'_l}}{b_3 b_8}$
$\overline{w'^2 q'_l}$	$A_{4.3} = \frac{\tau_1 \overline{w'q'_l}}{b_4}$ $A_{4.6} = \frac{2\lambda\tau_1^2 \overline{w'q'_l}}{b_4 b_6}$ $A_{4.7} = \frac{2\tau_1 \overline{w'^2}}{b_4} + \frac{2\lambda\tau_1^2 \overline{w'\theta'_l}}{b_4 b_6} + \frac{4C_{T_0} \lambda \tau_1^2 \overline{w'q'_l}}{b_4 b_5}$ $A_{4.8} = 0$ $A_{4.9} = \frac{2\lambda\tau_1^2 \overline{w'^2}}{b_4 b_6}$ $A_{4.10} = \frac{2C_{T_0} \lambda \tau_1^2 \overline{w'^2}}{b_4 b_5}$
$\overline{w'q'_l{}^2}$	$A_{5.7} = \frac{2\tau_1 \overline{w'q'_l}}{b_5}$ $A_{5.9} = \frac{2\lambda\tau_1^2 \overline{w'q'_l}}{b_5 b_9}$ $A_{5.10} = \frac{\tau_1 \overline{w'^2}}{b_5} + \frac{\lambda\tau_1^2 \overline{w'\theta'_l}}{b_5 b_9} + \frac{3C_{T_0} \lambda \tau_1^2 \overline{w'q'_l}}{b_5 b_{10}}$
$\overline{w'\theta'_l q'_l}$	$A_{6.6} = \frac{\tau_1 \overline{w'q'_l}}{b_6}$ $A_{6.7} = \frac{\tau_1 \overline{w'\theta'_l}}{b_6}$ $A_{6.8} = \frac{\lambda\tau_1^2 \overline{w'q'_l}}{b_6 b_8}$ $A_{6.9} = \frac{\tau_1 \overline{w'^2}}{b_6} + \frac{2\lambda\tau_1^2 \overline{w'\theta'_l}}{b_6 b_8} + \frac{2C_{T_0} \lambda \tau_1^2 \overline{w'q'_l}}{b_6 b_9}$ $A_{6.10} = \frac{C_{T_0} \lambda \tau_1^2 \overline{w'\theta'_l}}{b_6 b_9}$
$\overline{\theta'_l{}^3}$	$A_{7.8} = \frac{3\tau_1 \overline{w'\theta'_l}}{b_7}$
$\overline{\theta'_l{}^2 q'_l}$	$A_{8.8} = \frac{\tau_1 \overline{w'q'_l}}{b_8}$

	$A_{8,9} = \frac{2\tau_1}{b_8} \overline{w'\theta'_i}$
$\overline{\theta'_i q'_i{}^2}$	$A_{9,9} = \frac{2\tau_1}{b_9} \overline{w'q'_i}$ $A_{9,10} = \frac{\tau_1}{b_9} \overline{w'\theta'_i}$
$\overline{q'_i{}^3}$	$A_{10,10} = \frac{3\tau_1}{b_{10}} \overline{w'q'_i}$
$\overline{w'u'^2}$	$A_{11,1} = \frac{\tau_1}{b_{11}} \overline{w'^2} + \frac{\lambda\tau_1^2}{b_{11}b_{12}} \overline{w'\theta'_i} + \frac{C_{T_0}\lambda\tau_1^2}{b_{11}b_{13}} \overline{w'q'_i}$ $A_{11,4} = \frac{2\tau_1}{b_{11}} \overline{w'u'}$
$\overline{u'^2\theta'_i}$	$A_{12,1} = \frac{\tau_1}{b_{12}} \overline{w'\theta'_i}$
$\overline{u'^2q'_i}$	$A_{13,1} = \frac{\tau_1}{b_{13}} \overline{w'q'_i}$
$\overline{w'v'^2}$	$A_{14,2} = \frac{\tau_1}{b_{14}} \overline{w'^2} + \frac{\lambda\tau_1^2}{b_{14}b_{15}} \overline{w'\theta'_i} + \frac{C_{T_0}\lambda\tau_1^2}{b_{14}b_{16}} \overline{w'q'_i}$ $A_{14,5} = \frac{2\tau_1}{b_{14}} \overline{w'v'}$
$\overline{v'^2\theta'_i}$	$A_{15,2} = \frac{\tau_1}{b_{15}} \overline{w'\theta'_i}$
$\overline{v'^2q'_i}$	$A_{16,2} = \frac{\tau_1}{b_{16}} \overline{w'q'_i}$
$\overline{w'^2u'}$	$A_{17,3} = \frac{\tau_1}{b_{17}} \overline{w'u'}$ $A_{17,4} = \frac{2\tau_1}{b_{17}} \overline{w'^2} + \frac{2\lambda\tau_1^2}{b_{17}b_{18}} \overline{w'\theta'_i} + \frac{2C_{T_0}\lambda\tau_1^2}{b_{17}b_{19}} \overline{w'q'_i}$ $A_{17,6} = \frac{2\lambda\tau_1^2}{b_{17}b_{18}} \overline{w'u'}$ $A_{17,7} = \frac{2C_{T_0}\lambda\tau_1^2}{b_{17}b_{19}} \overline{w'u'}$ $A_{17,8} = 0$ $A_{17,9} = 0$ $A_{17,10} = 0$

$\overline{w'u'\theta'_i}$	$A_{18.4} = \frac{\tau_1}{b_{18}} \overline{w'\theta'_i}$ $A_{18.6} = \frac{\tau_1}{b_{18}} \overline{w'u'}$ $A_{18.8} = \frac{\lambda\tau_1^2}{b_{18}b_{20}} \overline{w'u'}$ $A_{18.9} = \frac{C_{T_0} \lambda\tau_1^2}{b_{18}b_{21}} \overline{w'u'}$
$\overline{w'u'q'_i}$	$A_{19.4} = \frac{\tau_1}{b_{19}} \overline{w'q'_i}$ $A_{19.7} = \frac{\tau_1}{b_{19}} \overline{w'u'}$ $A_{19.9} = \frac{\lambda\tau_1^2}{b_{19}b_{21}} \overline{w'u'}$ $A_{19.10} = \frac{C_{T_0} \lambda\tau_1^2}{b_{19}b_{22}} \overline{w'u'}$
$\overline{u'\theta_i'^2}$	$A_{20.8} = \frac{\tau_1}{b_{20}} \overline{w'u'}$
$\overline{u'\theta'_i q'_i}$	$A_{21.9} = \frac{\tau_1}{b_{21}} \overline{w'u'}$
$\overline{u'q_i'^2}$	$A_{22.10} = \frac{\tau_1}{b_{22}} \overline{w'u'}$
$\overline{w'^2 v'}$	$A_{23.3} = \frac{\tau_1}{b_{23}} \overline{w'v'}$ $A_{23.5} = \frac{2\tau_1}{b_{23}} \overline{w'^2} + \frac{2\lambda\tau_1^2}{b_{23}b_{24}} \overline{w'\theta'_i} + \frac{2C_{T_0} \lambda\tau_1^2}{b_{23}b_{25}} \overline{w'q'_i}$ $A_{23.6} = \frac{2\lambda\tau_1^2}{b_{23}b_{24}} \overline{w'v'}$ $A_{23.7} = \frac{2C_{T_0} \lambda\tau_1^2}{b_{23}b_{25}} \overline{w'v'}$ $A_{23.8} = 0$ $A_{23.9} = 0$ $A_{23.10} = 0$
$\overline{w'v'\theta'_i}$	$A_{24.5} = \frac{\tau_1}{b_{24}} \overline{w'\theta'_i}$

	$A_{24.6} = \frac{\tau_1 \overline{w'v'}}{b_{24}}$ $A_{24.8} = \frac{\lambda \tau_1^2 \overline{w'v'}}{b_{24} b_{26}}$ $A_{24.9} = \frac{C_{T_0} \lambda \tau_1^2 \overline{w'v'}}{b_{24} b_{27}}$
$\overline{w'v'q'_t}$	$A_{25.5} = \frac{\tau_1 \overline{w'q'_t}}{b_{25}}$ $A_{25.7} = \frac{\tau_1 \overline{w'v'}}{b_{25}}$ $A_{25.9} = \frac{\lambda \tau_1^2 \overline{w'v'}}{b_{25} b_{27}}$ $A_{25.10} = \frac{C_{T_0} \lambda \tau_1^2 \overline{w'v'}}{b_{25} b_{27}}$
$\overline{v'\theta'_t{}^2}$	$A_{26.8} = \frac{\tau_1 \overline{w'v'}}{b_{26}}$
$\overline{v'\theta'_t q'_t}$	$A_{27.9} = \frac{\tau_1 \overline{w'v'}}{b_{27}}$
$\overline{v'q'_t{}^2}$	$A_{28.10} = \frac{\tau_1 \overline{w'v'}}{b_{28}}$

Table A6 Simplified coefficients for the diagnostic third-order moments

Third-order Moment Liquid Water Correlation Terms
$L_1 = \frac{3D\lambda\tau_1}{b_1} \left(\overline{w'^2 q'_t} + \frac{2\lambda\tau_1}{b_2} \overline{w'\theta'_t q'_t} + \frac{2C_{T_0} \lambda \tau_1}{b_4} \overline{w'q'_t q'_t} \right)$
All other third-order moment liquid water correlations are the same as in Table A5

Table A7 Simplified third-order moment liquid water correlations

Appendix B

Virtual potential temperature as a function of conservative variables

The virtual potential temperature is defined as the potential temperature a parcel of dry air would need to have in order to have the same density as a parcel that includes moisture, written mathematically as

$$\theta_v = \theta \left[1 + \left(\frac{1 - \varepsilon_0}{\varepsilon_0} \right) q_v - q_l \right] \quad (\text{B1})$$

where θ is the potential temperature, q_v is the water vapor specific humidity, q_l is the liquid water specific humidity, and $\varepsilon_0 = \frac{R_d}{R_v}$ is the ratio of the dry air gas constant to the

water vapor gas constant. We wish to write the virtual potential temperature in terms of the conserved variables θ_l and q_l . This may be accomplished by adding and subtracting

$$\text{the term } \theta \frac{1 - \varepsilon_0}{\varepsilon_0} q_l + \frac{L_v}{c_p} \left(\frac{p_0}{p} \right)^\kappa q_l \quad (\text{B2})$$

to the right-hand side of equation (B1):

$$\theta_v = \theta \left[1 + \left(\frac{1 - \varepsilon_0}{\varepsilon_0} \right) q_v - q_l \right] + \theta \frac{1 - \varepsilon_0}{\varepsilon_0} q_l + \frac{L_v}{c_p} \left(\frac{p_0}{p} \right)^\kappa q_l - \theta \frac{1 - \varepsilon_0}{\varepsilon_0} q_l - \frac{L_v}{c_p} \left(\frac{p_0}{p} \right)^\kappa q_l \quad (\text{B3})$$

Group the terms as follows:

$$\theta_v = \theta \left[\left(\frac{1 - \varepsilon_0}{\varepsilon_0} \right) (q_v + q_l) - \left(1 + \frac{1 - \varepsilon_0}{\varepsilon_0} \right) q_l \right] + \left(\theta - \frac{L_v}{c_p} \left(\frac{p_0}{p} \right)^\kappa q_l \right) + \frac{L_v}{c_p} \left(\frac{p_0}{p} \right)^\kappa q_l \quad (\text{B4})$$

Simplify, using the fact that $\theta_l = \theta - \frac{L_v}{c_p} \left(\frac{p_0}{p} \right)^\kappa q_l$ and $q_l = q_v + q_l$:

$$\theta_v = \theta_l + \theta \left(\frac{1 - \varepsilon_0}{\varepsilon_0} \right) q_l + \left[\frac{L_v}{c_p} \left(\frac{p_0}{p} \right)^\kappa - \left(\frac{\theta}{\varepsilon_0} \right) \right] q_l \quad (\text{B5})$$

REFERENCES

- Abdella, K., and N. McFarlane, 2001: Modeling boundary-layer clouds with a statistical cloud scheme and a second-order turbulence closure. *Bound.-Layer Meteor.*, **98**, 387-410.
- Ackerman, A. S., M. P. Kirkpatrick, D. E. Stevens, and O. B. Toon, 2004: The impact of humidity above stratiform clouds on indirect aerosol climate forcing. *Nature*, **432**, 1014-1017.
- , M. C. vanZanten, B. Stevens, V. Savic-Jovicic, C. S. Bretherton, A. Chlond, J.-C. Golaz, H. Jiang, M. Khairoutdinov, S. Krueger, M. Zulauf, A. Lock, C.-H. Moeng, K. Nakamura, M. D. Petters, J. R. Snider, and S. Weinbrecht, 2009: Large-eddy simulations of a drizzling, stratocumulus-topped marine boundary layer. *Mon. Wea. Rev.*, **137**, 1083-1110.
- André, J. C., G. De Moor, P. Lacarrère, G. Therry, and R. Du Vachat, 1976: Turbulence approximation for inhomogeneous flows: Part I. The clipping approximation. *J. Atmos. Sci.*, **33**, 476-481.
- , G. De Moor, P. Lacarrère, G. Therry, and R. Du Vachat, 1978: Modeling the 24-hour evolution of the mean and turbulent structures of the planetary boundary layer. *J. Atmos. Sci.*, **35**, 1861-1883.
- Bechtold, P., C. Fravallo, and J. P. Pinty, 1992: A model of marine boundary-layer cloudiness for mesoscale applications. *J. Atmos. Sci.*, **49**, 1723-1744.
- , W. M. Cuijpers, P. Mascart, and P. Trouilhet, 1995: Modeling of trade wind cumuli with a low-order turbulence model: Toward a unified description of Cu and Sc clouds in meteorological models. *J. Atmos. Sci.*, **52**, 455-463.
- , and P. Siebesma, 1998: Organization and representation of boundary layer clouds. *J. Atmos. Sci.*, **55**, 888-895.
- Betts, A. K., 1973: Non-precipitating cumulus convection and its parameterization. *Quart. J. Roy. Meteor. Soc.*, **99**, 178-196.
- Bougeault, P., 1981a: Modeling the trade-wind cumulus boundary layer. Part I: Testing the ensemble cloud relations against numerical data. *J. Atmos. Sci.*, **38**, 2414-2428.

- , 1981b: Modeling the trade-wind cumulus boundary layer. Part II: A high-order one-dimensional model. *J. Atmos. Sci.*, **38**, 2429-2439.
- , 1982: Cloud-ensemble relations based on the gamma probability distribution for the higher-order models of the planetary boundary layer. *J. Atmos. Sci.*, **39**, 2961-2700.
- , 1985: The diurnal cycle of the marine stratocumulus layer: A higher-order model study. *J. Atmos. Sci.*, **42**, 2826-2843.
- , and J. C. André, 1986: On the stability of the third-order turbulence closure model for the modeling of the stratocumulus-topped boundary layer. *J. Atmos. Sci.*, **43**, 1574-1581.
- , and P. Lacarrère, 1989: Parameterization of orography-induced turbulence in a mesobeta-scale model. *Mon. Wea. Rev.*, **117**, 1872-1890.
- Bretherton, C. S., M. K. MacVean, P. Bechtold, A. Chlond, W. R. Cotton, J. Cuxart, H. Cuijpers, M. Khairoutdinov, B. Kosovic, D. Lewellen, C.-H. Moeng, P. Siebesma, B. Stevens, I. Sykes, and M. C. Wyant, 1999: An intercomparison of radiatively driven entrainment and turbulence in a smoke cloud, as simulated by different numerical models. *Quart. J. Roy. Meteor. Soc.*, **125**, 391-423.
- , P. N. Blossey, and J. Uchida, 2007: Cloud droplet sedimentation, entrainment efficiency, and subtropical stratocumulus albedo. *Geophys. Res. Lett.*, **34**, L03813.
- Brown, A. R., R. T. Cederwall, A. Chlond, P. G. Duynkerke, J.-C. Golaz, M. Khairoutdinov, D. C. Lewellen, A. P. Lock, M. K. Macvean, C.-H. Moeng, R. A. J. Neggers, A. P. Siebesma, and B. Stevens, 2002: Large-eddy simulation of the diurnal cycle of shallow cumulus convection over land. *Quart. J. Roy. Meteor. Soc.*, **128**, 1075-1093.
- Canuto, V. M., 1992: Turbulent convection with overshooting: Reynolds stress approach. *Astrophys. J.*, **392**, 218-232.
- , F. Minotti, C. Ronchi, and R. M. Ypma, 1994: Second-order closure PBL model with new third-order moments: Comparison with LES data. *J. Atmos. Sci.*, **51**, 1605-1618.
- Cheng, A., K. M. Xu, and J.-C. Golaz, 2004: The liquid water oscillation in modeling boundary layer cumuli with third-order turbulence closure models. *J. Atmos. Sci.*, **61**, 1621-1629.

- Cheng, Y., V. M. Canuto, and A. M. Howard, 2005: Nonlocal convective PBL model based on new third- and fourth-order moments. *J. Atmos. Sci.*, **62**, 2189-2204.
- Clarke, R. H., A. J. Dyer, R. R. Brook, D. G. Reid, and A. J. Troup, 1971: The Wangara experiment: Boundary layer data. Tech. Pap. No. 19, CSIRO Div. Meteor. Phys., Melbourne, 340 pp.
- Cuijpers, J. W. M., and P. Bechtold, 1995: A simple parameterization of cloud water related variables for use in boundary layer models. *J. Atmos. Sci.*, **52**, 2486-2490.
- Cuxart, J., P. Bougeault, and J.-L. Redelsperger, 2000: A turbulence scheme allowing for mesoscale and large-eddy simulations. *Quart. J. Roy. Meteor. Soc.*, **126**, 1-30.
- Deardorff, J. W., 1972: Parameterization of the planetary boundary layer for use in general circulation models. *Mon. Wea. Rev.*, **100**, 93-106.
- , 1974a: Three-dimensional numerical study of the height and mean structure of a heated planetary boundary layer. *Bound.-Layer Meteor.*, **7**, 81-106.
- , 1974b: Three-dimensional numerical study of turbulence in an entraining mixed layer. *Bound.-Layer Meteor.*, **7**, 199-226.
- , 1976a: Usefulness of liquid-water potential temperature in a shallow-cloud model. *J. Appl. Meteor.*, **15**, 98-102.
- , 1976b: On the entrainment rate of a stratocumulus-topped mixed layer. *Quart. J. Roy. Meteor. Soc.*, **102**, 563-582.
- , 1980: Stratocumulus-capped mixed layers derived from a three-dimensional model. *Bound.-Layer Meteor.*, **18**, 495-527.
- Fu, Q., S. K. Krueger, and K. N. Liou, 1995: Interactions of radiation and convection in simulated tropical cloud clusters. *J. Atmos. Sci.*, **52**, 1310-1328.
- Golaz, J.-C., V. E. Larson, and W. R. Cotton, 2002a: A PDF-based model for boundary layer clouds. Part I: Method and Model Description. *J. Atmos. Sci.*, **59**, 3540-3551.
- , V. E. Larson, J. A. Hansen, D. P. Schanen, and B. M. Griffin, 2007: Elucidating model inadequacies in a cloud parameterization by use of an ensemble-based calibration framework. *Mon. Wea. Rev.*, **135**, 4077-4096.
- Hartmann, D. L., M. E. Ockert-Bell, and M. L. Michelsen, 1992: The effect of cloud type on earth's energy balance: Global analysis. *J. Climate*, **5**, 1281-1304.

- Jakob, C., and S. A. Klein, 2000: A parameterization of the effects of cloud and precipitation overlap for use in general-circulation models. *Quart. J. Roy. Meteor. Soc.*, **126**, 2525-2544.
- Jung, J.-H., and A. Arakawa, 2005: A three-dimensional cloud model based on the vector vorticity equation. Colorado State University Atmospheric Science Paper 762, 57 pp.
- , and A. Arakawa, 2008: A three-dimensional anelastic model based on the vorticity equation. *Mon. Wea. Rev.*, **136**, 276-294.
- Klemp, J. B., and R. B. Wilhelmson, 1978: The simulation of three-dimensional convective storm dynamics. *J. Atmos. Sci.*, **35**, 1070-1096.
- Krueger, S. K., 1988: Numerical simulation of tropical cumulus clouds and their interaction with the subcloud layer. *J. Atmos. Sci.*, **45**, 2221-2250.
- , Q. Fu, K. N. Liou, and H.-N. Chin, 1995: Improvements of an ice-phase microphysics parameterization for use in numerical simulations of tropical convection. *J. Appl. Meteor.*, **34**, 281-287.
- Larson, V. E., J. C. Golaz, and W. R. Cotton, 2002: Small-scale and mesoscale variability in cloudy boundary layers: Joint probability density functions. *J. Atmos. Sci.*, **59**, 3519-3539.
- Lenderink, G., and A. A. M. Holtslag, 2004: An updated length-scale formulation for turbulent mixing in clear and cloudy boundary layers. *Quart. J. Roy. Meteor. Soc.*, **130**, 3405-3427.
- Lewellen, W. S., and S. Yoh, 1993: Binormal model of ensemble partial cloudiness. *J. Atmos. Sci.*, **50**, 1228-1237.
- Lilly, D. K., 1968: Models of cloud-topped mixed layers under a strong inversion. *Quart. J. Roy. Meteor. Soc.*, **94**, 292-309.
- Lin, Y.-L., R. D. Farley, and H.D. Orville, 1983: Bulk parameterization of the snow field in a cloud model. *J. Climate Appl. Meteor.*, **22**, 1065-1092.
- Lord, S. J., H. E. Willoughby, and J. M. Piotrowicz, 1984: Role of a parameterized ice-phase microphysics in an axisymmetric nonhydrostatic tropical cyclone model. *J. Atmos. Sci.*, **41**, 2836-2848.
- Marht, L., 1976: Mixed layer moisture structure. *Mon. Wea. Rev.*, **104**, 1403-1407.
- Mellor, G. L., and T. Yamada, 1974: Heirarchy of turbulence closure models for planetray boundary layers. *J. Atmos. Sci.*, **31**, 1791-1806.

- , 1977a: The Gaussian cloud model relations. *J. Atmos. Sci.*, **34**, 356-358.
- , 1977b: Corrigenda. *J. Atmos. Sci.*, **34**, 1483-1484.
- Moeng, C.-H., and D. A. Randall, 1984: Problems in simulating the stratocumulus-topped boundary layer with a third-order closure model. *J. Atmos. Sci.*, **41**, 1588-1600.
- , 1986: Large-eddy simulation of a stratus-topped boundary layer. Part I: Structure and budgets. *J. Atmos. Sci.*, **43**, 2886-2900.
- , W. R. Cotton, B. Stevens, C. Bretherton, H. A. Rand, A. Chlond, M. Khairoutdinov, S. Krueger, W. S. Lewellen, M. K. MacVean, J. R. M. Pasquier, A. P. Siebesma, and R. I. Sykes, 1996: Simulation of a stratocumulus-topped planetary boundary layer: Intercomparison among different numerical codes. *Bull. Amer. Met. Soc.*, **77**, 261-278.
- Nakanishi, M., 2001: Improvement of the Mellor-Yamada turbulence closure model based on large-eddy simulation data. *Bound.-Layer Meteor.*, **99**, 349-378.
- Randall, D. A., 1987: Turbulent fluxes of liquid water and buoyancy in partly cloudy layers. *J. Atmos. Sci.*, **44**, 850-858.
- , S. Krueger, C. Bretherton, J. Curry, P. Duynkerke, M. Moncrieff, B. Ryan, D. Starr, M. Miller, W. Rossow, G. Tselioudis, and B. Wielicki, 2003: Confronting models with data: The GEWEX cloud systems study. *Bull. Amer. Met. Soc.*, **84**, 455-469.
- Redelsperger, J. L., and G. Sommeria, 1986: Three-dimensional simulation of a convective storm: Sensitivity studies on subgrid parameterization and spatial resolution. *J. Atmos. Sci.*, **43**, 2619-2635.
- Schubert, W. H., 1976: Experiments with Lilly's cloud-topped mixed layer model. *J. Atmos. Sci.*, **33**, 436-446.
- , J. S. Wakefield, E. J. Steiner, and S. K. Cox, 1979: Marine stratocumulus convection. Part I: Governing equations and horizontally homogeneous solutions. *J. Atmos. Sci.*, **36**, 1286-1307.
- Shutts, G. J., and M. E. B. Gray, 1994: A numerical modeling study of the geostrophic adjustment process following deep convection. *Quart. J. Roy. Meteor. Soc.*, **120**, 1145-1178.
- Siebesma, A. P., C. S. Bretherton, A. Brown, A. Chlond, J. Cuxart, P. G. Duynkerke, H. Jiang, M. Khairoutdinov, D. Lewellen, C.-H. Moeng, E. Sanchez, B. Stevens, D.

- E. Stevnes, 2003: A large eddy simulation intercomparison study of shallow cumulus convection. *J. Atmos. Sci.*, **60**, 1201-1219.
- Slingo, A., 1990: Sensitivity of the earth's radiation budget to changes in low clouds. *Nature*, **343**, 49-51.
- Sommeria, G., 1976: Three-dimensional simulation of turbulent processes in an undisturbed trade wind boundary layer. *J. Atmos. Sci.*, **33**, 216-241.
- , and J. W. Deardorff, 1977: Subgrid-scale condensation in models of nonprecipitating clouds. *J. Atmos. Sci.*, **34**, 344-355.
- Stevens, B., C.-H. Moeng, A. S. Ackerman, C. S. Bretherton, A. Chlond, S. De Roode, J. Edwards, J.-C. Golaz, H. Jiang, M. Khairoutdinov, M. P. Kirkpatrick, D. C. Lewellen, A. Lock, F. Muller, D. E. Stevens, E. Whelan, P. Zhu, 2005: Evaluation of large-eddy simulations via observations of nocturnal marine stratocumulus. *Mon. Wea. Rev.*, **133**, 1443-1462.
- Stull, R. B., 1988: *An Introduction to Boundary Layer Meteorology*. Kluwer Academic, 666 pp.
- Sun, W., and Y. Ogura, 1980: Modeling the evolution of the convective planetary boundary layer. *J. Atmos. Sci.*, **37**, 1558-1572.
- Sundqvist, H., E. Berge, and J. E. Kristjánsson, 1989: Condensation and cloud parameterization studies with a mesoscale numerical weather prediction model. *Mon. Wea. Rev.*, **117**, 1641-1657.
- Tiedtke, M., 1993: Representation of clouds in large-scale models. *Mon. Wea. Rev.*, **121**, 3040-3061.
- Tompkins, A. M., 2002: A prognostic parameterization for the subgrid-scale variability of water vapor and clouds in large-scale models and its use to diagnose cloud cover. *J. Atmos. Sci.*, **59**, 1917-1942.
- Willis, G. E., and J. W. Deardorff, 1974: A laboratory model of the unstable planetary boundary layer. *J. Atmos. Sci.*, **31**, 1297-1307.
- Wyant, M. C., C. S. Bretherton, A. Chlond, B. M. Griffin, H. Kitagawa, C.-L. Lappen, V. E. Larson, A. Lock, S. Park, S. R. deRoode, J. Uchida, M. Zhao, A. S. Ackerman, 2007: A single-column model intercomparison of a heavily drizzling stratocumulus-topped boundary layer. *J. Geophys. Res.*, **112**, D24204.
- Wyngaard, J. C., and O. R. Coté, 1974: The evolution of a convective planetary boundary layer – A higher-order-closure model study. *Bound.-Layer Meteor.*, **7**, 289-308.

- Yamada, T., and C.-Y. J. Kao, 1986: A modeling study on the fair weather marine boundary layer of the GATE. *J. Atmos. Sci.*, **43**, 3186-3199.
- , and G. L. Mellor, 1975: A simulation of the Wangara atmospheric boundary layer data. *J. Atmos. Sci.*, **32**, 2309-2329.
- Zeman, O., and J. L. Lumley, 1976: Modeling buoyancy driven mixed layers. *J. Atmos. Sci.*, **33**, 1974-1988.
- , 1979: Buoyancy Effects in Entraining Turbulent Boundary Layers: A Second-Order Closure Study. *Turbulent Shear Flows, Vol. I*. Springer-Verlag, 295-306.